ThermoSolar and Photovoltaic Hybridization for Small Scale Distributed Generation: Applications for Powering Rural Health

by

Matthew S. Orosz

Submitted to the Department of Civil and Environmental Engineering
in partial fulfillment of the requirements for the degree of

Doctor of Philosophy in Civil and Environmental Engineering

at the

MASSACHUSETTS INSTITUTE OF TECHNOLOGY

June 2012

Author .....
Department of Civil and Environmental Engineering
May 4, 2012

Certified by .....
Harold F. Hemond
William E. Leonhard Professor of Civil and Environmental Engineering
Thesis Supervisor

Accepted by .....
Heidi M. Nepf
Chair, Departmental Committee for Graduate Students

ThermoSolar and Photovoltaic Hybridization for Small Scale Distributed Generation: Applications for Powering Rural Health

by
Matthew S. Orosz

Submitted to the Department of Civil and Environmental Engineering
on May 4, 2012, in partial fulfillment of the
requirements for the degree of
Doctor of Philosophy in the field of Civil and Environmental Engineering

Abstract

The problem of provisioning a remote health clinic or school with electricity, heating and cooling (trigeneration) is considered from an engineering design and optimization standpoint. A baseline technical-economic review of existing options is performed, and a novel alternative is proposed: micro-Concentrating Solar Power (CSP), featuring an Organic Rankine Cycle (ORC) using repurposed HVAC scroll compressors as expanders. The design of the μ-CSP technology is informed by a semi-empirical steady state multi-physics sizing and performance model (SORCE) which predicts system output, efficiency, and specific costs as a function of geoposition. Empirical validation of key mechanical and electrical components is performed to parameterize the model. On a levelized cost basis, μ-CSP is shown to outperform standard equipment for trigeneration applications at remote sites.

Scroll expander development is identified as an opportunity for enhanced performance, and a computationally efficient method for selecting optimal thermo-mechanical geometries for a scroll expander is described. Tradeoffs between concentration ratio, power block size and thermal storage are examined, and the key role of thermal capacity in the system is highlighted. A semi-dynamic version of SORCE is developed to support optimization amongst system components in a simulated operating environment including insolation and thermal transients; this offers preliminary insights into control decisions that influence cost and performance, such as timing and power management of ORC operation.

Finally, the concept of synergies between concentrating solar photovoltaic (CPV) and CSP architecture is explored. A semi-empirical diode model is developed using experimental data from commercially available a-SI and c-Si solar cells and incorporated into PV-SORCE (where the μ-CSP thermal absorber is replaced with a PV heat collection element). Optimization of design parameters influencing figures of merit (system efficiency and specific costs) indicates that an optimal configuration is highly sensitive to the PV properties; as such, further optimization of the hybrid system parameters is recommended.

This research also involved lab and field (Lesotho, southern Africa) prototyping of small solar ORC units. Relevant design parameters and further development of the μ-CSP concept is discussed in the context of field experiences.

Thesis Supervisor: Harold F. Hemond
Title: William E. Leonhard Professor of Civil and Environmental Engineering

Acknowledgments

When I reflect on the events that led me to this moment in my life, it occurs to me that a full account of the debt that I owe to family, friends and colleagues, would require an undertaking of a magnitude far exceeding the accomplishments of this doctoral thesis. In this note, I can only hope to sketch the briefest outline of the many encounters for which I am grateful, in roughly chronological order and necessarily leaving out a great number of details and inspiring people.

In the beginning, when I was small and reportedly precocious, I was not really cognizant of how blessed I was to be surrounded by a family that nurtured and challenged me, and within their means provided me with every opportunity to explore and imbibe the world: from my father's ancestral homeland in the Carpathian basin to the white cliffs of Narragansett Bay behind Geoffrey's Family Restaurant and the frog ponds and library bookshelves of my maternal hometown of Bridgewater, MA. I dedicate this work to my family. To my mom, Janet, for the ineffable gift of raising me and surrounding me with love. To my father, Árpád, for emphasizing education and knowledge in navigating the challenges of an uncertain world. To my brother John, who was teaching me the importance of having a team long before I realized it. To my grandparents, Kay (Ma) and Armand (Pépère) Gendreau and Dr. Árpád (Nagypapa) and Anna (Nagymama) Orosz, for their abiding warmth and generosity. I was luckiest to be their first grandchild; and to share in their heritage. To my aunts and uncles and cousins, who knit the family together and unflinchingly supported me through all my stages of growth.

There are many roads diverging in the yellow wood, and along the way friends and teachers profoundly influenced the course I charted. In grade school Gail Caisson fanned the flames of my creativity, and Tom Flangheddy, possibly the most inspirational high school teacher ever, taught me the sublime importance of words and meaning. My senior year of high school, when my good friend Matt Ozug put an application to Dartmouth College in my hands, I took the road that maybe made all the difference. At Dartmouth two professors and a coach had a huge impact on my thinking and being in the world. Sandy Ford-Centonze honed not just my sprinting ability, but my ability to reach down to my core and find the reserve strength to keeping moving forward against any odds. Alexander Wendt helped me formalize my understanding of political systems, and Dana Meadows showed me how these systems, all systems in fact, are rooted in the philosophy of the natural world. Dana had influenced me before I ever sat in her classroom, having read her book "Beyond the Limits" while living next to my (amazing!) aunt Dalma and studying economics in Budapest on a semester abroad in 1998. Dana's perspective single-handedly shifted the center of gravity of my worldview, and on returning to Dartmouth I changed my major to environmental studies. The example of her brilliance, kindness, and steadfast ethic for working towards a better world gave me strength of purpose that I draw on to this day. I learned of her illness and tragic death midway through my Peace Corps service; she had encouraged me to serve and wrote my recommendation. Her passing was an inconsolable loss for me and the world.

As a Peace Corps volunteer I think I was meant to teach; in practice it worked the other way: I owe countless Basotho friends and colleagues for what I learned, and continue to learn, working in Lesotho. My first brush with concentrated solar power was as a PCV, from a parabolic cooker designed by Ivan Yaholnitsky, founder of the Bethel Business and Community Development Center (BBCDC) in Mohale's Hoek. I put my hand in the focus, got burned, and was promptly hooked on solar engineering.

My first year at MIT resembled a kind of engineering bootcamp. I covered my walls with brown paper and with a magic marker I filled my room with all of the equations from my classes. I survived this pressure cooker with my sanity intact thanks to my friends, and Polski FIAT: ELK, JGO and roadie Joe (10 years 3 albums and over 70 shows!). To everyone in M.Eng, TPP, Parsons, to anyone

who helped me work through problem sets, got me out hiking, drank a beer with me - THANK YOU. You kept me human.

My course at MIT was forever altered when I enrolled in Amy Smith's D-lab class in 2004. D-lab was the springboard from which I was able to create a path through the metabolism of MIT that could lead me back to the beginning: the desire to solve the kinds of infrastructure problems that plagued my village in Lesotho (where I had lived for two years without running water or electricity). Through D-lab, the connections I made there, and the development and public service ecosystem at MIT, I was able to return to Lesotho for the first time and begin to put my engineering ideas into practice. I pitched the micro-CSP concept to Prof. David Wallace's 2.009 class, and a team of MechE students spent a semester evolving it, with Headley Jacobus and Toni Ferreira following up with fieldwork in Lesotho. By 2006, I had founded the non-profit STG International and a team of us spent a year prototyping micro-CSP at BBCDC with funding from the World Bank, including myself, Amy Mueller, Libby Wayman, and Headley from MIT and Tumelo Makhetha, Makoanyane Khakhanyo and Motlatsi Sekhesa from Lesotho. Bryan Urban led a G-lab contingent to Lesotho that developed our first market assessment and solidified our partnership with the Appropriate Technology Services of the Government of Lesotho. We owe a debt to Dennis Phakisi, Kopano Tsenoli, Lengeta Mabea and the ATS team for their continued support of this work.

Without the persistent and compelling guidance of my advisor Prof. Harry Hemond, I never would have returned to MIT for a PhD. As all of his students know, Harry is a brilliant, kind soul with a sprawling erudition and an uncanny talent for combining environmental science, field research and engineering design. Despite my perhaps unconventional pivot from nitrogen biogeochemistry to solar energy, Harry welcomed me back to his lab in 2007: to say that his support for this work has been crucial is an understatement. Harry is an incomparably wise and enthusiastic mentor, collaborator and friend. Words cannot express my gratitude for what I've gained through knowing him.

I thank also my committee, including Prof. Ghoniem and Prof. Buonassisi, for their insight into thermodynamics and photovoltaics and for their support throughout my doctoral studies. In addition, many undergraduate research assistants contributed to this work, especially Jing Han, Cynthia Lin, Adam Love and Peter Lu, as well as visiting students Christian Muller and Alex Fanderl from TUM. Visiting researchers Dr. Sylvain Quoilin and Bertrand Dechesne from the University of Liége played a major role in driving the ORC research forward, as well as challenging me to continually improve my understanding of thermodynamics and mechanics. I am also grateful to Mercedes Ibarra of Plataforma Solar de Almería for hosting our SFERA research visit to study their solar ORC. Thank you to Andrej Lenert for use of the Wang lab solar simulator, and for Joe Sullivan for training me on Buonassisi lab equipment. I am especially grateful to Prof. Dave Perreault for the use of the LEES generator dynamometer rig, and to Prof. David Hastings for facilitating our solar ORC test site at Eckerd College. Without the generous assistance and support of these colleagues, my progress in this thesis would have been meager. Any failings or mistakes in this work, however, are entirely my own.

As usual I have left the most difficult task for last, with the margin fast approaching. Amy Mueller ...is not just an esteemed colleague, fellow founder of STG, and a great hiking/motorcycle adventure companion. She is my best friend, the unswerving foundation on which this thesis, and everything else in my life, is built. She easily deserves a second PhD for the amount of herself she has dedicated to mine. To Amy I can only say:

Édes szerelmem, te vagy a legnagyobb kaland. A lelkem keresés az egesz szépség minden a világon, Találom te elsö és mindig.

Contents

List of Figures

List of Tables

Chapter 1

Introduction

1.1 Generating Power in Remote Areas: Personal Motivation

As a Peace Corps volunteer, I lived on the wrong side of the mighty Senqu River (opposite from the main paved road and easy transport) for two years, in the small village of Tlokoeng in Lesotho. Like everyone else in my village, I wondered when the government was going to build a bridge, improve the roads, and get electricity and running water to the communities. It dawned on me that we might be waiting for the rest of our lives. I decided to become a civil engineer and figure out how to better design infrastructure to meet the challenges of remote areas. It has been my good fortune to have had the opportunity to study engineering and pursue this goal at MIT.

Although building a bridge would have topped my priorities as a Peace Corps volunteer, at MIT I was drawn to sustainable energy as a foundational prerequisite for economic development. Not only the economy but everything in the ecosystem depends on sustained energy flows, the ultimate source of which is the sun. Access to energy is potentially transformative in every context; without it there is no growth, no information, and no life. In this thesis I was determined to acquire the technical knowledge that, had I possessed it as a volunteer in Lesotho, would have enabled my community to systematically approach building their own solar power plant.

1.2 Background

Solar thermal power, also known as concentrating solar power (CSP), had been a tantalizing possibility since the invention of the heat engine and was put to practical commercial use as early as 1913 when U.S. engineer Frank Shuman installed a 55kW solar thermal powered pumping station on the Nile at Maedi in Egypt (Fig. 1-1). Even earlier, in 1872, John Ericsson had been interested in solar power, inventing a displacer type air engine powered by a parabolic trough (Fig. 1-1), but he found little commercial interest in his device at the time. The rise of the petroleum industry in the 20th century led to widely available, relatively inexpensive energy, effectively sidelining the use of CSP for nearly 60 years.

1.3 Concentrating solar power and photovoltaics: relative advantages and potential synergies

Utility scale (Megawatt), grid tied CSP-based thermal-electric generation has been online in the US since the 1980s, and today there is nearly a gigawatt of installed capacity globally with more than

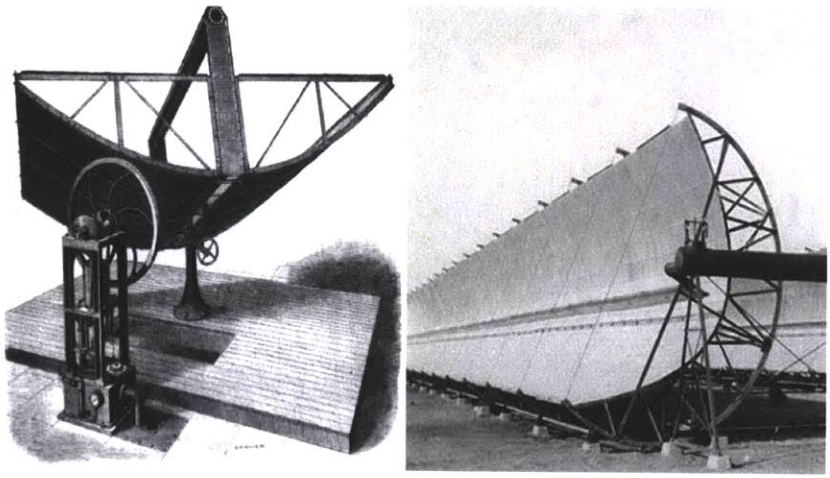

J.Ericsson, *Nature*, 3 January 1884 Maedi Egypt pumping plant, 1913

Figure 1-1: Historical examples of solar driven engine concepts. Left: Ericsson's solar hot air engine. Right: Frank Shuman's 55kW pumping station on the Nile.

an additional 2 GW under construction. Both CSP generation and solar photovoltaics (PV) utilize a free energy resource, but whereas the latter is limited to a capacity factor below 0.25 on earth, CSP offers advantages in the relative ease to which it can be integrated with cost-efficient thermal storage (typically a thermocline tank using phase change materials, with nitrate salts among the common formulations [32]) or hybridized with combustion-based infrastructure, both of which can serve to raise the plant capacity factor to near unity.

Historically, CSP has been used for large, multi-MW applications whereas photovoltaic modules were considered the optimal solution at the scale of a few kilowatts. The steeply dropping cost of PV, however, has vastly increased its market share (20GW shipped in 2010), and today it seems likely that these distinctions will soon be blurred.

In searching for a technology appropriate for rural areas of the developing world, the choice of CSP cuts against conventional wisdom because of scale and the expected cost advantages of PV. At average module efficiencies of 15% and cost per watt of less than $2 in 2012, PV is indeed a preeminent technology for renewable energy. These prices are, however, strongly dependent on geography and market, and US costs for the base panels are not generally representative of those seen in developing countries, nor are the installation costs comparable to those experienced by users in rural areas that may be extremely difficult to access. In contrast, some small high temperature CSP systems have exceeded 30% conversion efficiency [88], but these also remain much too costly for underserved areas. In this thesis, a third option is explored whereby lower temperature CSP using an organic Rankine cycle (ORC) is explored, sacrificing conversion efficiency in favor of lower specific cost ($/W).

In addition to offering a potentially lower specific cost, the calculus further tilts in favor of CSP when other human activities that require thermal energy (space and water heating, space cooling) in addition to electricity are considered. At sunlight to thermal conversion efficiencies reaching 60-70%, CSP is both an efficient and cost effective solution for heating and even cooling (using absorption technology), whereas PV can only provide these services via the inefficient conversion of photons to electricity and then back to heat. This advantage of CSP is not likely to be erased by PV efficiency improvements in the near future. This energy context thus provides the backdrop for

the investigation of small-scale, low-temperature CSP pursued in this doctoral project.

Finally, there are advantages and drawbacks to the use of either PV or CSP, and this thesis explores the potential synergies in combining the technologies. The main challenge to overcome in PV-CSP hybridization is the negative correlation of PV cell efficiency with temperature, whereas the efficiency of a Carnot engine increases with temperature. Temperature of operation is thus the key parameter to consider for optimization of a PV-thermal system.

In Chapter 2, the energy needs for a typical rural health clinic are examined both as a case study and to develop specifications for designing a practical energy source. These facilities are highlighted due to the relatively high social impact expected from energy access, and because the agencies operating them can engage in the type of long term planning in which levelized costs are considered (a key determinant in evaluating renewable or fossil-fuel based generation projects). Chapters 3 and 4 present the thermodynamic, mechanical, and economic analyses utilized in the process of designing a micro-CSP system for remote power generation, and experimental results are presented. In Chapter 5, the approach is extended to consider thermal storage and the resultant dynamic behavior of the system, which presents further opportunities for optimization (by reducing the size of the power island, shifting energy production to match the load curve, and operating to take advantage of diurnal ambient temperature differentials). In Chapter 6, the hybridization of CSP with PV is explored via a semi-empirical application of the "5 parameter" diode model, design tradeoffs are considered, and the key role of cell properties and areal specific costs are highlighted. Finally, Chapter 7 presents a methodology for designing scroll expanders optimized for a micro-CSP system.

Chapter 2

Technologies for heating, cooling and powering rural health facilities in sub-Saharan Africa

The text in this chapter is being prepared for submission to the Journal of Power and Energy, IMechE. Additional authors are Sylvain Quoilin and Harold Hemond.

Abstract

This paper highlights technical and economic choices for rural electrification in Africa and presents the rationale for trigeneration (capability for electricity, heating and cooling) in health and education applications. An archetypal load profile for a rural health clinic (25 $kWh_e \cdot day^{-1}$ and 118-139 kWh_t) is described, and a regional analysis is performed for sub Saharan Africa by aggregating NASA meteorological data (insolation, temperature, and heating and cooling degree days) using correlates to latitude. As a baseline for comparison, the technical, economic (using discounted cash flow) and environmental aspects of traditional electrification approaches, namely photovoltaic (PV) systems and diesel generators, are quantified and options for meeting heating and cooling loads (e.g. gas-fired heaters, absorption chillers, or solar water heaters) are evaluated alongside an emerging micro-scale Concentrating Solar Power (CSP) technology featuring a solar thermal Organic Rankine Cycle (ORC). Photovoltaics hybridized with LPG/Propane and μ-CSP trigeneration are the lowest cost alternatives for satisfying important but often overlooked thermal requirements, with cost advantages for μ-CSP depending on latitudinal variation in insolation and thermal parameters. For a 15-year project lifetime, the net present cost for meeting clinic energy needs varied from 44-55k USD, with specific levelized electricity costs of 0.26-0.31 USD kWh^{-1}. In comparison, diesel generation of electricity is both costly and polluting (94 tons CO_2 per site over 15 years), while LPG/Propane based heating and cooling results in 160-400 tons CO_2 emittted. The comparative analysis of available technologies indicates that where the energy demand includes a mixture of electrical and thermal loads, as in typical health and education outposts, μ-CSP trigeneration approaches are cost effective and non-carbon emitting.

2.1 Introduction

Extending energy supplies to the nearly 1.6 billion people that lack access to electricity is an enduring challenge of the 21st century, one which is implicitly interconnected to the unfolding impacts of climate change. In some regions, centralized grid infrastructure strains to keep pace with demand growth, and as a result, power outages and "load shedding" can impair energy availability [13]. In rural areas with dispersed communities or in sparsely inhabited mountainous areas, the cost of extending the electricity grid is generally prohibitive for distances exceeding 5-10 km at over 20k USD·km^{-1} [50]. Communities in these areas may rely on biomass, petroleum-based generators, or renewable resources (hydro-power, wind or solar) if available and cost effective [142]. In many cases electrification lags behind other forms of public infrastructure, such as water supply, roads, and the establishment of health and education facilities [31]. The latter facilities represent a unique case study for the application of decentralized mini-grid power systems, which is the focus of this paper.

Electrification of healthcare and educational facilities is prerequisite for meeting the objectives of the Millenium Development Goals (MDGs) [110]. The benefits of modern forms of energy in health facilities are well understood [36, 35]: electricity is required for specialized medical diagnostic and treatment equipment (x-ray machines, ultrasound, centrifuges, etc.) [17], computers, electronic medical recordkeeping (EMR) and telemedicine programs. Supporting loads include lighting (for increased hours of operation and security), cold storage of medicines and vaccines as part of the "cold chain" climate control (rarely), and the powering of staff quarters, the latter having implications for the attraction and retention of qualified professionals to work in remote areas [57, 82, 17]. In addition to electricity, the need for thermal energy, in the form of heating the clinic facility in cold seasons and provision of hot water, is often overlooked in the electrification literature (exceptions are [36, 76]) despite clear impacts on operations and hygiene. Sourcing power for thermal needs is usually separated from the planning for electrification, mainly because electricity from diesel generators and PV systems is expensive and the electrical supply is thus limited in comparison to potential thermal loads. Supplementary technologies used to meet thermal needs for space heating include biomass or coal combustion stoves and LPG or propane heaters. LPG, propane and/or solar thermal water heaters are generally selected for domestic water services where indoor plumbing is available. In comparing available energy systems for health clinics in section 5, we take a holistic approach where both electric and thermal loads are considered.

Progress in electrification proceeds slowly, and the benefits of off-grid electrification projects are seldom fully realized once executed [17]. A review of one UNDP-GEF project in Zimbabwe, for example, indicated that 48% of installed systems were faulty (of these faulty systems 33% had battery failure, 23% had lighting failures, and 12% had charge controller failures) [45]. An extensive literature reports on the technical and non-technical reasons why clinic power systems frequently fail [145, 31, 50, 9, 15]. According to [15] writing in 2003: "It is quite possible that over half of the institutional systems installed over the past decade are not functional."

2.2 Technical Specifications for Powering Rural Health Centers

2.2.1 Estimation methods

The first step towards health center electrification is to determine the technical specifications of the application, with the ideal that a standardized but flexible design can evolve to meet the range of identified needs. The principal design specification is the demand load, quantified in terms of instantaneous power requirements (kW) and energy over time (kWh), including both electric and

thermal components. In order to evaluate the demand load, a profile of a representative clinic was developed through a combination of literature survey [145, 35] and local inquiries (site visits and interviews with clinic staff) at remote clinics ($n = 11$) in Lesotho (≈27°S 29°E) operated by either the Lesotho Ministry of Health (MoH) or the U.S. based NGO, Partners in Health (PIH). These participatory assessments (and the ensuing technology design and testing phases) were conducted by a team of collaborators from the NGO STG International, the Massachusetts Institute of Technology, the University of Liege, and the Appropriate Technology Services of the Government of Lesotho from 2008-2010.

Interviews of health workers revealed a strong preference for greater access to energy regardless of the electrification status of the facility. Additionally, four of the clinics (MoH) reported that previously installed (via a World Bank program) solar PV panels had been stolen, and six reported that previously installed solar hot water heaters had broken down. At the time of evaluation (July-September 2009) three of the clinics (PIH) were equipped with 3ϕ 1.4 kW PV energy systems installed by the Solar Electric Light Fund (SELF), and of those, two were equipped with backup 3ϕ diesel generators (30 kVA). The clinics are seasonally heated by coal-burning stoves or LPG heaters, and a mixture of LPG and solar hot water heaters are in use.

The existence of energy supplies at a subset of clinics presents an opportunity to compare the results of an audit (measured loads) in the field to typical demand load estimation methodologies (e.g., undertaken by the clinic operators or using a specialized version of the software tool HOMER [89]). Estimation typically involves counting the number of unique loads, noting their instantaneous power consumption in Watts, and multiplying by the number of hours of usage to obtain Watt-hours [35]. The energy audit was conducted over a period of 6 weeks at three of the clinics (Nkau, Bobete, and Methaleneng) using SmartWatt SW25020 logging power meters connected inline to each phase in the main junction box at the clinics (sampling period = 20 mins). The daily outputs of the 1.4 kW PV systems were recorded at the system controller (Mate II, Outback), and a 42-day average yield of 6.3 kWh·day^{-1} was logged for the period of load monitoring. The measured average clinic demand load curves at sites with PV systems for weekdays (6.8 kWh·day^{-1}) and weekends (5kWh·day^{-1}) are shown in Fig. 2-1. The load factors (LF, percent of full capacity used) for the PV systems were 107% and 79% for weekdays and weekends respectively (essentially 100% combined). The load curves for the diesel-only site ranged from 2-5 kWh·day^{-1}, with a load factor below 3%, which severely degrades fuel economy (Fig. 2-2) [1, 73].

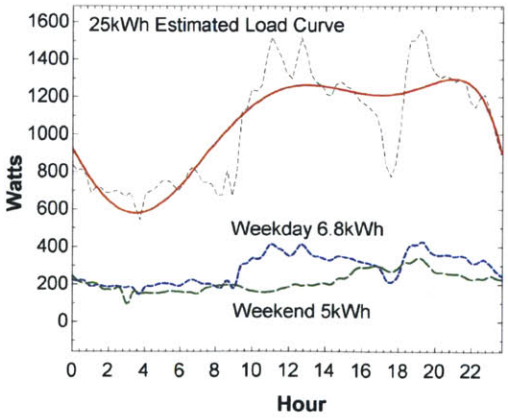

Figure 2-1: Measured and estimated health clinic load profiles

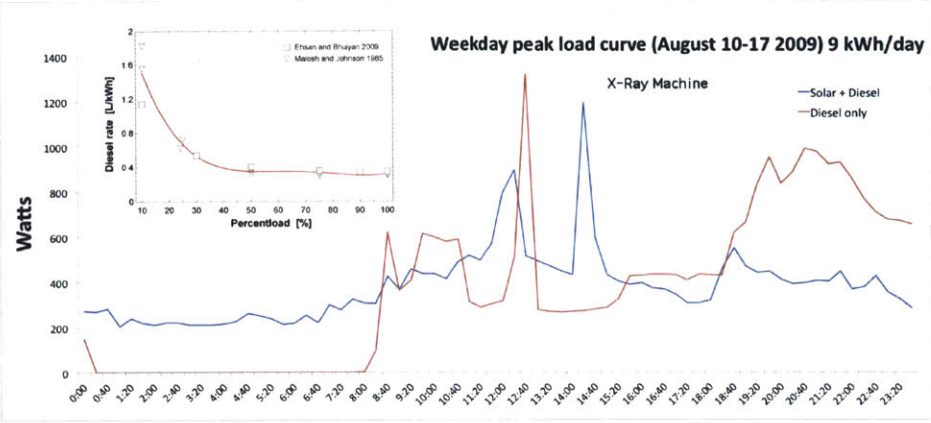

Figure 2-2: Measured PV and Diesel clinic loads with part load fuel economy derived from [72, 54]

The maximum power consumption observed in the dataset is 1330 W, while the averaged load curve is 283W, for an average-to-peak load ratio of 4.7. The operational profile and demand load estimation (20 kWh day^{-1}) for the archetypal clinic is described in Fig. 2-3. Estimated and measured loads differ by a factor of three, which might be anticipated given the $LF = 99\%$ for the PV systems, i.e. the investigated energy systems are undersized compared to demand (in the case of the diesel–only site the fuel supply, rather than the generator capacity, is the limiting factor). During the monitoring period the PV system energy supply was exhausted almost daily, usually tripping the low battery voltage protection late at night or in the early morning. It is interesting to note that only ~3 kWh day^{-1} was consumed during the operating hours (8 a.m.–5 p.m.) of the clinic, which indicates that on average only 33% of the available energy is used for strictly defined operational purposes. This could indicate a mismatch between estimation methodologies and actual operational needs, an implicit clinic staff preference for allocating energy towards personal uses, or a combination of the two.

A conclusive answer to the question "How much electricity does the average clinic need?" is thus not possible on the basis of this dataset alone, although in the case of a 99% load factor at 6.3 kWh·day^{-1} the qualitative answer is 'more.' Estimation methods assuming a high level of care (using PIH equipment inventory as a benchmark) produce an average of 20 kWh·day^{-1} for a clinic fitting the profile of Fig. 2-3 with a possible peak load of 5 kW, although these estimations focus on operational loads whereas in practice off-design loads are routinely observed. An upper bound on energy consumption could be extrapolated from the global peak load curve (12 kWh·day^{-1}) but this may still underestimate loads due to energy supply constraints affecting the sites (the Diesel only site was allocated 205 L fuel per month, equivalent to 3 kWh·day^{-1} at the part load conditions represented by their peak load curve (Fig. 2-2).

2.3 Baseline Clinic Load Specifications

2.3.1 Electrical load

To establish a baseline power consumption for comparisons between alternatives, in Fig. 2-3 we estimate that 20 kWh·day^{-1} is sufficient for typical operational and staff uses. Given holidays and a design availability factor of 0.9, we recommend sizing systems at 25 kWh·day^{-1} to accommodate 25% future growth in demand. For a baseline capacity estimate, we use the extrapolated load

Clinic Load Estimation

		19.7 kWh/day
Lighting	**Number**	**kWh/Day**
Clinic	10	0.3
Ward/ISO	16	0.4
Lab/X-ray	9	0.2
Staff Housing	40	1.5
		2.4
Equipment		
Medical		7.6
Centrifuge-QBC	1	0.5
Auto Read	1	0.2
Vscan Ultrasound	1	0.1
Biochem visual	1	0.1
Kyosha printer	1	0.1
Autoclave	1	1.3
Microscope	1	0.1
O2 concentrator	1	1.3
Nebulizer	1	1.4
X-ray GE ANX4+	1	0.6
UV disinfection lights	12	2.0
Communications		4.2
Modem	1	1.2
Outdoor Unit	1	0.3
Wireless Access Points	2	0.4
Cisco Router	1	1.4
Switch	2	0.4
Radio/Cell Phones	2	0.4
IT		2.7
Computer	5	2.5
Printers	2	0.2
Climate control		2.8
Fans	10	2.8

'Average' Clinic Profile

Buildings:	**6**	Seasonal Heating	70GJt/year
Personnel:	**5**	Hot Water	300L @ 35°C /day
Patients:	**100/day**		30MJt/day

Degree Days (16°C baseline) Source: FABL Bloemfontein Airport, ZA (26.30E,29.09S)

Jan	Feb	Mar	Apr	May	Jun	Jul	Aug	Sep	Oct	Nov	Dec
1	4	17	76	162	286	234	214	94	57	21	14

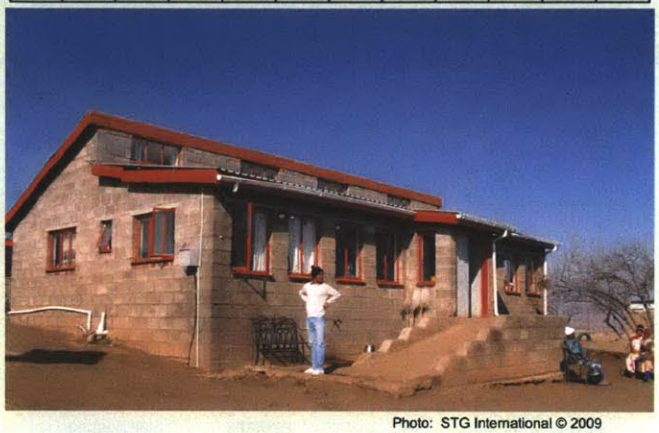

Photo: STG International © 2009

Figure 2-3: Estimation of clinic loads using the USAID HOMER inventory cross referenced to a PIH inventory and site surveys at 11 clinics in Lesotho.

curve of Fig. 2-1, which indicates a nominal inverter output of 2 kW and peak capacity of 5 kW based on a 4.7 average to peak ratio. The annual target for 330 days of operation per year is 8250 kWh of electricity for the alternatives compared below. These estimates generally agree with previously published clinic power needs estimates [82, 145], although further data collection at clinic sites having relatively unconstrained power supplies (e.g., continuously fueled generators) would be informative. For reference, 25 kWh·day^{-1}, while generous by the standards of currently deployed clinic power supplies, represents the capacity to treat thousands of rural patients per year with a high level of care at a power consumption rate roughly equivalent to the average U.S. home [18].

2.3.2 Thermal loads for clinic climate control and hot water

2.3.3 Target thermal conditions

Whereas the importance of electrification is recognized and prioritized in the planning for clinic energy infrastructure, supplementary energy demands for cooking, climate control, and hot water are sometimes overlooked. These needs vary considerably with geo-position and altitude and are cost prohibitive to supply via electricity from a micro-grid given lower cost alternatives. (For example, a thermal kWh obtained from LPG (retail in South Africa in 2012) costs about 0.02 USD, approximately 17 times less than an equivalent thermal kWh obtained from the PV or diesel generator systems discussed above [6].) Indoor climate control in remote health clinics is frequently neglected [145], possibly due to wide variation in thermal needs, cost and design difficulties encountered in the field, or a perception that climate control is a luxury in remote, underserved areas. Whatever the causes, the requirements for climate control in a health facility setting are codified in e.g. ASHRAE Standards [22, 23], and these codes can also be applied where high quality health

care or education is practiced in remote areas. Affects of high temperature and humidity, according to the heat index [138] include: lapses in judgment, fatigue, mold, bacterial infection of open wounds, and possible damage to electronics. At low temperatures effects range from discomfort to hypothermia, functional impairment, reduced hygiene maintenance, immune system depression, and in extreme cases damage to electronics. Indoor climate extremes thus affect health, safety, productivity, and potentially jeopardize sensitive equipment and the overall operational mission.

2.3.4 Estimating thermal loads with a building envelope model

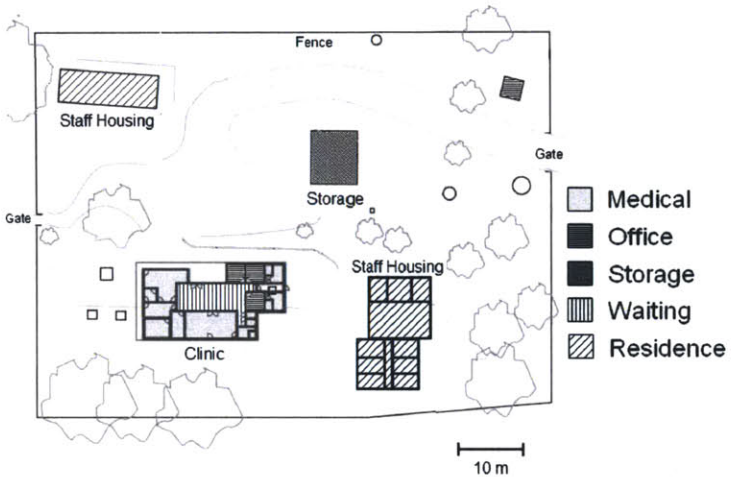

Figure 2-4: An example of a typical clinic complex in Lesotho

To estimate the combined heating, cooling, and hot water loads for clinics, we develop a simple thermal model for a typical clinic complex (Fig. 2-4). For climate control and hot water requirements, the relevant estimates are calculated on the basis of degree-days above and below set design temperatures, based on a combined clinic building footprint of 200 m^2, and a peak heating load [$W \cdot m^{-2}$] based on assumed insulation characteristics and design temperatures described below [12]. Water requirements are calculated directly assuming a consumption rate of 60 L hot water at 45°C per person per day (assumed to be heated from the average ambient temperature). These calculations are highly sensitive to initial assumptions (location, climate, building construction, thermal efficiencies of equipment, etc.), and latitude in particular is an essential parameter for establishing realistic estimates for clinic heating loads.

As a first approximation, we take the change in heating degree days (HDD) below 18°C and cooling degree days (CDD) above a humidity dependent design temperature (Eq. 2.1) with latitude across a representative region of Africa by averaging grid data from 15°E to 30°E [8] (Fig. 2-5) and plotting the regressions, normalizing CDD to a design temperature T_{cool} calculated as a function of the heat index [138]:

$$T_{cool} = 58.4 - 7.1 \cdot ln(RH)\ [C] \tag{2.1}$$

where the average relative humidity (RH) for sub-Saharan Africa is found as a function of the absolute value of latitude using a second order polynomial fit for the longitude-averaged dataset [8]:

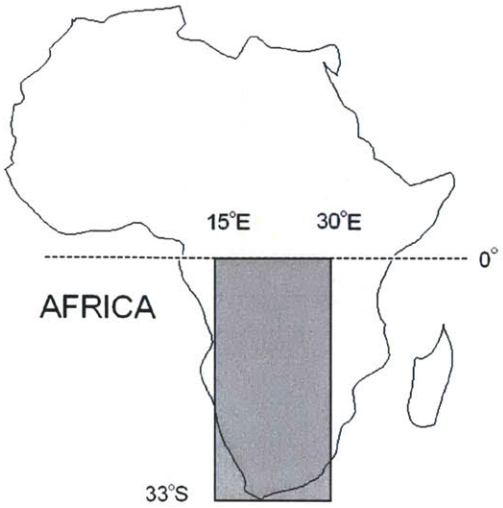

Figure 2-5: Longitudinally Averaged Meteorological Data

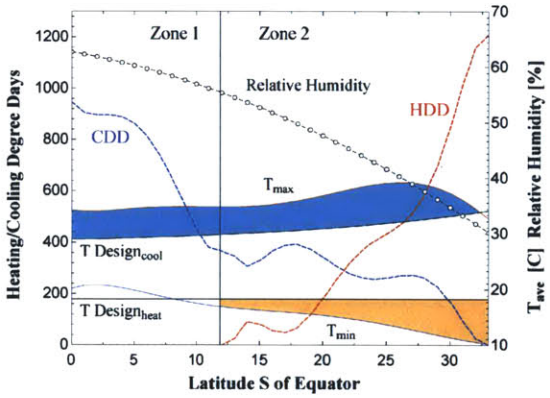

Figure 2-6: Latitudinal degree-day and temperature profiles for Africa

$$RH = 62.7 - 0.4 \cdot latitude - 0.0177 \cdot latitude^2 \ [\%] \tag{2.2}$$

Noting that the number of HDDs for latitudes 12°N to -12°S is zero, we separate our analysis of clinic thermal load profiles into two zones: (1) those with exclusively cooling loads (equatorial region) and (2) those with both heating and cooling loads outside the 12°equatorial band (Fig. 2-6).

The thermal load for climate control is proportional to degree-days and calculated according to a peak load based on the difference between average ambient and design temperatures. The thermal model of the clinic assumes generally poor insulation: masonry (concrete block) walls (R value of 0.6 $m^2\ K^{-1}\ W^{-1}$) and a drop ceiling, wood joist supported corrugated iron roof (R value of 0.8 $m^2\ K^{-1}\ W^{-1}$) [33] (Fig. 2-7). Assuming wall and roof-to-footprint surface area ratio of 1.44:1 and 1.2:1 respectively, a three-meter single story height, and approximately 7 air changes per hour (ACH) using estimates from Table 2.1, the peak heating load [W m^{-2}] is found for a given ΔT_{design} according to the following best fit curve ($R^2 = 0.99$):

Table 2.1: Estimated fractional usage of floorspace by type at a remote clinic, with recommended minimum number of air changes per hour [3]

Usage Type	Areal Fraction	Minimum recommended ACH	SubTotal
Waiting Room	0.1	4	0.4
Storage	0.15	2	0.3
Medical	0.2	8	1.6
Office	0.05	3	0.15
Residential	0.5	10	5
		Total	**7.45**

$$Max_{HL/CL} = -3.4 + 10.6 \cdot \Delta T_{design}\ [W \cdot m^{-2}] \tag{2.3}$$

where Δ T_{design} is design temperature (18°C) minus the average minimum ambient temperature for heating loads or the average maximum ambient temperature minus the design temperature (T $Design_{cool}$) for cooling loads. Maximum and minimum temperatures are derived from polynomial curve fits (Table 2.2) of satellite based measurements available from [8].

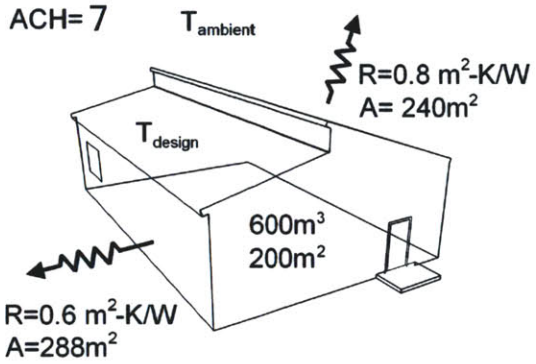

Figure 2-7: Simple heat loss model for clinic with 7 air changes per hour

2.3.5 Heating and cooling loads as a function of latitude

Peak heating and cooling loads are normalized to degree days for the latitude-specific temperatures by multiplying by 24 hours and dividing by Δ T_{design}. The total annual thermal load (HL/CL) is then:

$$Load = PeakLoad_{norm} \cdot Area \cdot DD\ [kWh\ year^{-1}] \tag{2.4}$$

Total load corresponds to number of degree-days for heating and cooling, while peak loading depends on ambient temperature and heat transfer in the thermal model (Fig. 2-8). The magnitude of peak loading multiplied by the footprint specifies the maximum capacity of heating and cooling systems required.

It should be stressed that this approach yields only a first approximation of the heating load for an archetypal poorly-insulated clinic campus. Actual heating and cooling loads will depend on

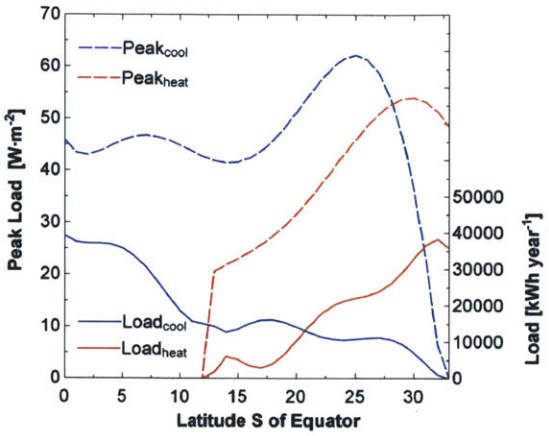

Figure 2-8: Latitudinal variation in Heating and Cooling Loads and Peak Capacity

significant variation in local climate due to e.g. coastal proximity or altitude, precipitation etc. and the specific thermal properties and form factors of the clinic buildings.

2.4 The Cost of Powering Rural Health Clinics

The standard procedure in rural electrification uses discounted cash flow analysis to select the preferred technology [103, 43]. Levelized costs are a solid foundation for an energy plan that should also include environmental and sustainability metrics, e.g. CO_2 avoidance.

For electricity generation we contrast widely used diesel generators and solar PV with the novel micro-CSP cogeneration system described in [128], featuring single-axis tracking parabolic trough solar concentrators, an air-cooled Organic Rankine Cycle (ORC) power block, and sensible heat storage. LPG/Propane and solar thermal configurations for heating and cooling are compared in Fig. 2-10 for the range of heating and cooling loads shown in Fig. 2-6. The analysis is limited to cases where application of distributed generation equipment is more cost-effective than extension of the centralized grid. In the study area, connection fees for utilities range from 20–1,000 USD, and extension of the grid costs between 3k-20k USD·km^{-1} [11, 132, 50, 58, 86]. The levelized cost of a grid extension investment is thus a function of both distance and consumption density (demand km^{-1}), meaning that the break-even point for grid extension vs. a fixed cost micro-grid at a given clinic site will depend on distance, the surrounding population density, and their ability to pay for electricity. Chakrabarti [40] calculated this break-even point for India (population density $>$ 350 km^{-2} [19]) and determined a distance of 16 km, below which grid extension is more appropriate than distributed generation.

For sub-Saharan Africa (population density $<$ 80 km^{-2} [111]) a conservative approach is to evaluate the centralized vs. decentralized question for sites within a 5–15 km radius of the grid (based on the NPC of systems discussed below and at 3k USD·km^{-1}), and proceed on the supposition that below and above that range grid extension and micro-grids respectively are otherwise preferable. For meeting thermal load specifications we focus on LPG/propane fuels, evacuated tube solar thermal hot water heaters, and micro-Concentrating Solar Power (CSP). For thermal loads, a solar fraction (amount of total load supplied by solar) of 85% is assumed, and the specified availability factor is $>$0.9. The service lifetime of the reciprocating generator is 25,000 hours and battery replacement is required at 5 year intervals [73]. PV panel 2012 wholesale prices in sub Saharan

are approximately 2–3 USD·W^{-1} [61, 15, 156], while diesel generators are available at 0.2–1.6 USD·W^{-1} depending on size, features and accessories [85, 50, 73].

For the electrical generators (diesel and solar) the design autonomy duration (availability to supply loads when not generating power) used in sizing the battery storage capacity is one day plus the non-illuminated portions of adjacent days based on the 25 kWh load curve of Fig. 2-1, (i.e., the total time between sunset on day 1 and sunrise on day 3 with no insolation on day 2). For solar thermal loads, storage is sized according to the average daily thermal requirement in the larger of the seasonal modes (heating or cooling), with backup capacity supplied by LPG/Propane. Redistribution of daytime solar energy collection is necessary, and we assume a solar evacuated tube-LPG hybrid system having 1 day thermal storage autonomy. Thermal storage is modeled as a 1D vertically stratified tank using the Schumann equations via Hughes method [53] with a glycol heat transfer fluid (HTF) in the pore space ($porosity = 0.3$) of a packed bed of quartzite rock, as described in [117]. The cost of deep cycle sealed lead acid batteries in 2011 remains above 150 USD·kWh^{-1} [20, 73, 1, 145], while for sub-MWh systems the cost for sensible thermal storage at 150°C in a cylindrical tank quartzite pebble bed ranges between 20–100 USD·kWh$_t^{-1}$ (Fig. 2-9).

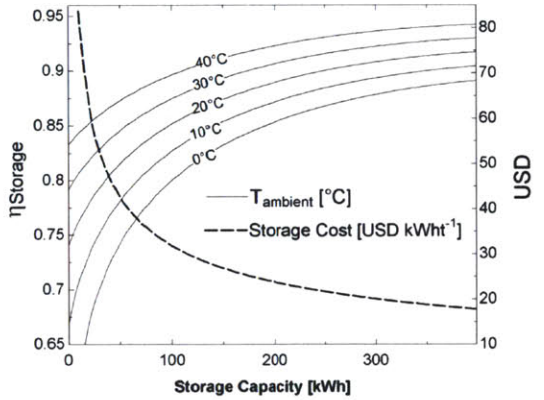

Figure 2-9: Efficiency and cost of insulated (3.5 m^2·W^{-1}·K^{-1}) sensible pebble bed storage type curves as a function of ambient temperature and storage capacity [116]

The economic objective function is minimized net present costs (NPC), generalized for energy systems as follows:

$$NPC = I_o + \sum_{t=0}^{n} \frac{O_t + M_t}{(1+r)^t} \tag{2.5}$$

where I_o is the initial cost of the equipment, n is the service life in years, O_t and M_t represent Operating and Maintenance costs in year t, and r is the discount rate. Operating costs are a unique function of the technology, but maintenance costs can be generalized as a function of the initial costs in two components – a constant annual service component and a linear function for repairs due to wear with age:

$$M_t = \frac{f \cdot a \cdot I_o}{n} + \frac{f \cdot (1-a) \cdot I_o}{n^2} \cdot (2t-1) \tag{2.6}$$

where f is the fraction of total maintenance costs with respect to initial costs, and a is a coefficient expressing the fraction of regular service costs with respect to total maintenance costs (including

incremental repairs). In this study a is taken to be 0.25 for all the investigated technologies. For diesel generators $f = 1.25$ [73]; for the other systems $f = 0.25$ is assumed.

The NPC of capital, operating and maintenence expenses shown in Fig. 2-11 are calculated assuming a 15 year lifetime for a total of 124,000 kWh electricity and latitude-dependent thermal loads (Eq. 2.4) at a discount rate of 4%. The discount rate should approximate the difference between the central bank interest rate and inflation; in practice interest rates and inflation in developing countries are often too volatile to derive a meaningful difference [28]. In this analysis, we selected the mean discount rate from a 2001 survey of 2160 economists for problems involving a long-term environmental component (in this case creating new energy infrastructure in the context of climate change) [64]. Further assumptions and equations are described in Table 2.2 with coefficients listed in Table 2.3. Calculations are performed using Engineering Equation Solver (EES) V8.962 [83].

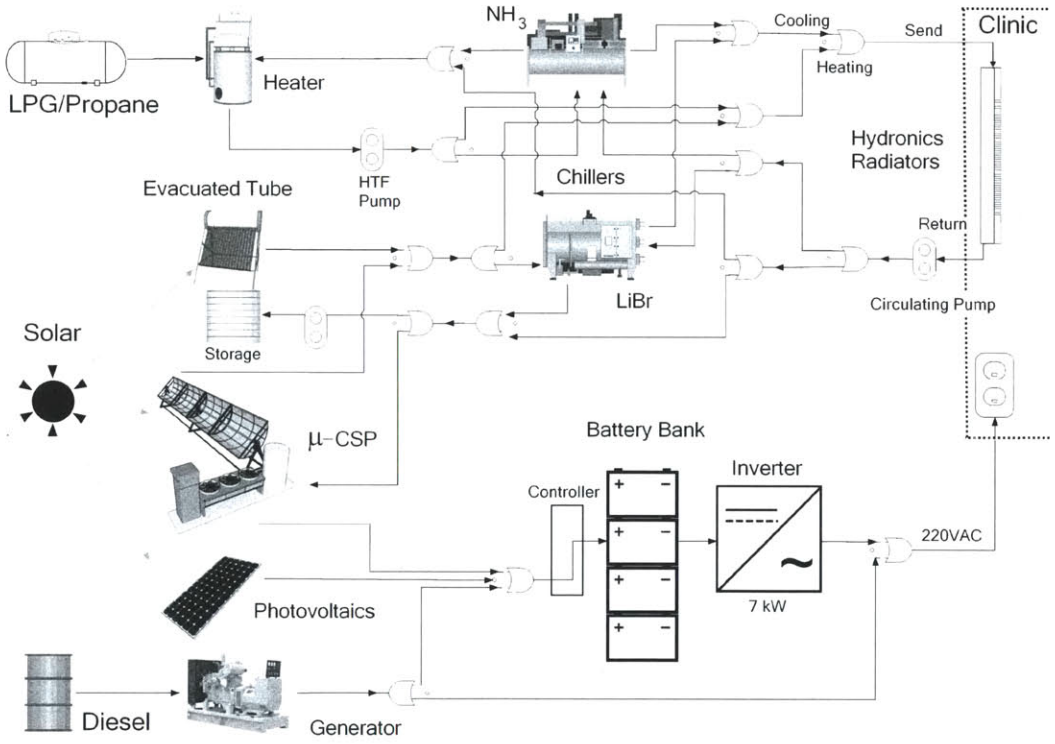

Figure 2-10: Configurations for heating, cooling and powering rural health facilities (X-OR gates used to represent represent where fluid and electrical circuits can be exclusively supplied from either of two sources)

Table 2.2: Equations used in calculating NPC for diesel, PV and micro-CSP energy systems. Parameters used are: $Cost_{fuel} = 1.3$ [USD·L^{-1}] (15); $\eta_{batt} = 0.85$, $\eta_{inv} = 0.95$ (16); $\eta_{heater} = 0.85$, $\eta_{chiller} = 0.64$ (18).

Number	Equation	Sources
(7)	$CDD_{0-12} = \frac{a_o + \sum_{j=1}^{4} a_j \cdot Latitude^j}{TDesign_{cool}}$ (R^2 99.75)	[8]
(8)	$CDD_{12-33} = \frac{b_o + \sum_{j=1}^{6} b_j \cdot Latitude^j}{TDesign_{cool}}$ (R^2 98.41)	[8]
(9)	$HDD_{12-33} = c_o + \sum_{j=1}^{6} c_j \cdot Latitude^j$ (R^2 99.49)	[8]
(10)	$T_{max} = d_o + \sum_{j=1}^{6} d_j \cdot Latitude^j$ [C] (R^2 96.19)	[8]
(11)	$T_{min} = e_o + \sum_{j=1}^{6} e_j \cdot Latitude^j$ [C] (R^2 97.51)	[8]
(12)[a]	$I_{tilt} = f_o + \sum_{j=1}^{6} f_j \cdot Latitude^j$ [kWh m^{-2} day^{-1}] (R^2 99.7)	[8]
(13)[b]	$Load_{clinic} = g_o + \sum_{j=1}^{6} g_j \cdot Hour^j$ [W]	[116]
(14)[c]	$L_{kWh} = h_o + \sum_{j=1}^{4} h_j \cdot \%_{Load}{}^e$ (R^2 98.25)	[72, 54]
(15)	$O_t = kWh_t \cdot \frac{L_{kWh} \cdot Cost_{fuel}}{\eta_{system}}$	[2]
(16)[d]	$\eta_{system} = 0.42 + 0.58 \cdot \eta_{batt} \cdot \eta_{inv}$	[50, 139]
(17)[e]	$kW = \frac{kWh \cdot day^{-1} \cdot \frac{Operating_{days}}{Operating_{days} - Autonomous_{days}}}{(I_{Tilt} \cdot (0.59 \cdot \eta_{batt} \cdot \eta_{inv} + 0.41 \cdot \eta_{inv})}$	
(18)	$kWh_{fuel} = \frac{kWh_{cool}}{\eta_{chiller}} + \frac{kWh_{heat}}{\eta_{heater}} + \frac{kWh_{hw}}{\eta_{heater}}$	[60]
(19)	$Area_{evac\_tube\ Solar} = \frac{kWh_{day}}{I_{Tilt} \cdot \eta_{evac\_tube\ Solar}}$	
(20)[f]	$\eta_{evac\_tube\ Solar} = 0.82 - \frac{7.884 * (T_{in} - T_{ave})}{(I_{Tilt}}$	[24]
(21)[g]	$\eta_{coefficient} = 3.2 - 0.068 * (T_{max} - T_{cool} + 2 * T_{pinch} + 12.5)$	[116]
(22)	$Cost_{heater} = 100 + (13 - 1.06 \cdot ln(kWh_{heat})) \cdot kWh_{heat}$	[5]
(23)	$Cost_{chiller} = 145 \cdot kWh_{cool}(LPG)$ *or* $550 \cdot kWh_{cool}(Solar)$	[7]
(24)[h]	$Cost_{Radiators} = 48.8 + 72 \cdot Max_{HL/CL}$	[4]
(25)	$Cost_{evac\_tube\ Solar} = 54 + 432 \cdot Area_{evac\_tube\ Solar}$	[16]
(26)	$Cost_{kWh\_storage} = i_o + \sum_{j=1}^{6} i_j \cdot Latitude^j$ (R^2 100)	[116]

[a] Global irradiance on a latitude tilted surface.
[b] 25kWh load curve shape extrapolated from measured loads (Fig. 2-1).
[c] Percent load is derived from the 25kWh load curve and the diesel generator capacity (7kW in stand alone or 3kW with battery and inverter).
[d] Efficiency distribution due to fraction of energy passing through of battery/inverter.
[e] Assume 55 days of autonomy - 59% energy routes through battery and 41% is direct solar to inverter. $Operating_{days} = 330 year^{-1}$
[f] Insolation is converted to kJ.
[g] Efficiency modifier reflecting the variation in chiller operating conditions. The T_{pinch} is assumed constant (10 °C) for radiators and air condensers, and 12.5 represents the nominal return line temperature (°C).
[h] The maximum load (in kW) is used to size the radiators for heating or cooling.

Table 2.3: Coefficients used in equations given in Table 2.2

Coef	Value	Coef	Value	Coef	Value	Coef	Value	Coef	Value	Coef	Value	Coef	Value	Coef	Value	Coef	Value
a_0	2.54E+03	b_0	3.44E+05	c_0	-1.63E+05	d_0	3.43E+01	e_0	2.02E+01	f_0	4.82E+00	g_0	9.23E+02	h_0	3.12E+00	i_0	1.08E+02
a_1	-1.59E+02	b_1	-1.00E+05	c_1	4.79E+04	d_1	-3.99E-01	e_1	7.45E-01	f_1	-2.69E-02	g_1	-1.76E+02	h_1	-1.82E-01	i_1	-2.36E+00
a_2	7.23E+01	b_2	1.19E+04	c_2	-5.73E+03	d_2	1.91E-01	e_2	-2.62E-01	f_2	9.76E-03	g_2	8.86E+00	h_2	4.37E-03	i_2	2.69E-02
a_3	-1.25E+01	b_3	-7.38E+02	c_3	3.58E+02	d_3	-2.72E-02	e_3	2.49E-02	f_3	1.10E-03	g_3	6.49E+00	h_3	-4.52E-05	i_3	-1.55E-04
a_4	5.52E-01	b_4	2.51E+01	c_4	-1.23E+01	d_4	1.67E-03	e_4	-1.09E-03	f_4	-1.49E-04	g_4	-8.88E-01	h_4	1.70E-07	i_4	4.71E-07
		b_5	-4.45E-01	c_5	2.20E-01	d_5	-4.45E-05	e_5	2.20E-05	f_5	5.34E-06	g_5	4.17E-02			i_5	-7.18E-10
		b_6	3.22E-03	c_6	-1.61E-03	d_6	4.18E-07	e_6	-1.68E-07	f_6	-6.26E-08	g_6	-6.70E-04			i_6	4.32E-13

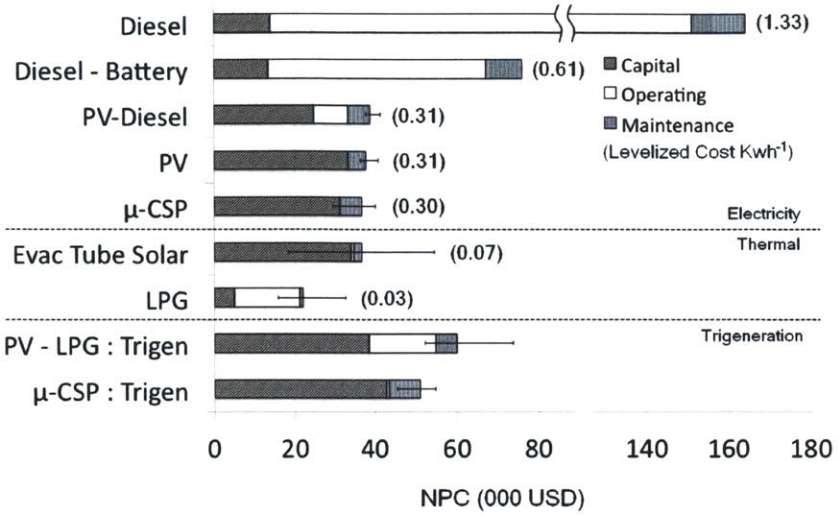

Figure 2-11: Net Present Cost (NPC) of distributed generation technologies meeting a typical clinic specification (25 kWh_e, 118-139 $kWh_t \cdot day^{-1}$, 330 $days \cdot year^{-1}$). Latitudinal variance due to thermal loads is indicated by bars where appropriate.

2.5 Discussion

2.5.1 Relative costs of available technologies

The estimated net present cost (NPC) for supplying electricity to remote health clinics and maintaining indoor climate between 18 and approximately 30°C (depending on relative humidity) at the archetypal African clinic ranges from 50k USD near the equator to a local maximum of 55k at 5-6°S (mainly Congo, DRC, and Tanzania) and a local minimum of 44k USD at latitudes 10-15°S (approximately parts of Angola, Zambia, Tanzania and Mozambique) over a 15 year project lifetime. The ranking of technology options by NPC and levelized cost is illustrated in Fig. 2-11, with bars indicating variation due to climate factors. The lowest cost trigeneration solution depends on the local heating and cooling loads (Fig. 2-8). μ-CSP with trigeneration using an LiBr-H_2O chiller-hydronic system is cost effective at latitudes with strong to mild cooling demand from 0-20°S, and photovoltaics combined with an LPG-fired NH_4-H_2O chiller and hydronics offer similar economies at higher heating loads found >20°S (Fig. 2-12). Our analysis indicates a potential role for μ-CSP trigeneration at remote outposts with substantial thermal requirements (for standalone electricity generation, PV-solar is cost-effective and more mature). Unlike a PV-LPG hybrid, μ-CSP is a completely renewable energy based approach, and the technology is comparatively simple and scaleable using manufacturing methods already available in sub-Saharan Africa. Localized manufacturing may induce positive spillover effects where μ-CSP is deployed.

2.5.2 The persistence of diesel and falling PV panel prices

The results of Fig. 2-11 raise the question of the persistance of diesel as a stationary power plant. We note the high levelized cost of standalone diesel electricity generation is largely due to poor fuel economy at part load operation, whereas the addition of battery storage and derating the generator

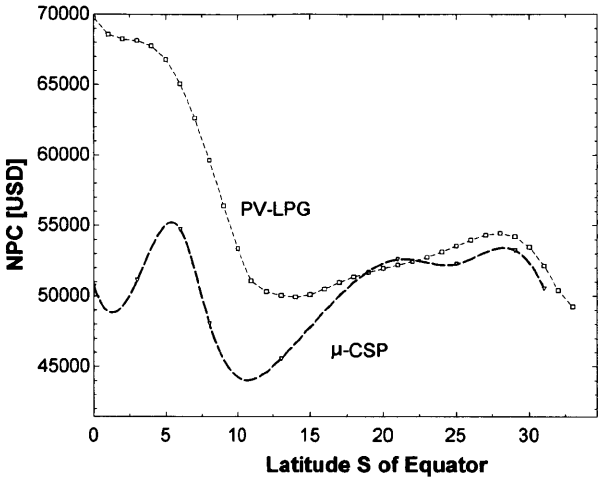

Figure 2-12: NPC variation with latitude for μ-CSP and PV-LPG trigeneration systems

can reduce costs by over 50%, although this is rarely done [129]. Due to steadily decreasing prices of PV panels (9 USD·W^{-1} in 1987 to almost 1 USD·W^{-1} in 2012, or -7%·yr^{-1} adjusting for inflation) [106, 87], solar power has inexorably become cost competitive with diesel. Nevertheless, recent growth in diesel capacity in Africa has been prodigious (30% in 2008, adding ~2 GW·yr^{-1}) [14]. As of 2002, total installed capacity of off-grid PV in Africa was no more than 125 MW [106], and the most ambitious growth projections (including grid-tie solar PV) call for less than 1 GW additional capacity per year [61]. Balance of System (BOS) costs, including the batteries, charge controller, inverter and structural support systems have not declined as quickly as solar panel costs, and now represent about half of installed costs [30]. We believe the discrepancy between procurement choices and high levelized costs in the case of diesel can be ascribed to their several advantages in micro-grid applications: they are quickly dispatchable (energy on demand), have a high power availability (>90%) and power quality, are commercially available in capacities of 2.5 kVA to several MVA, use a common pay-as-you-go fuel with a global supply chain, occupy a small footprint compared with renewable energy equipment, and are perceived as robust and well understood by local technicians. The low initial cost of a diesel generator compared to renewables is also a decisive factor.

2.5.3 Site specific factors

The foregoing analyses ignore any labor cost or security differentials between the examined projects: for example, unlike a solar array, a skid-mounted genset can be installed in one day, and installation costs for hydronic climate control systems will depend on features of the existing clinic structures. Cost savings can be achieved by designing new clinic sites with consideration for energy systems and insulation, but necessary upgrades to existing facilities will require site-specific specialized structures for e.g. mounting PV systems or housing generators and protecting fuel supplies. Theft of diesel fuel, solar panels, and batteries is endemic in off-grid areas [56], and this risk is not reflected in a simple economic analysis.

2.5.4 The influence of carbon finance

The comparison of Fig. 2-11 does not include costing the benefits of 94 tons of avoided diesel CO_2 emissions over the service lifetime of the project in the case of a solar-eletric system (or 78 avoided tons for a solar-diesel hybrid). The life-cycle emissions for the thermal systems range from 160 to 400 tons CO_2 depending on climatic factors. The embodied carbon footprints of the systems are as follows: PV electricity – 12–22 g CO_2-eq·kWh$_t^{-1}$; diesel electricity – 800 g CO_2-eq·kWh$_t^{-1}$ [75, 160]; heating and cooling loads – 280–660 g CO_2-eq·kWh$_t^{-1}$ (this study).

A robust market for carbon offsets under the Clean Development Mechanism (Kyoto Protocol) has yet to emerge, but projecting a price of 15 USD ton^{-1} CO_2 [11] earned over the lifetime of the project and discounted by 4%, present costs for μ-CSP trigeneration could potentially be reduced by 5k USD per health clinic, or about 10% of total NPC. Development of carbon markets could further expand the climate domain where μ-CSP holds a cost advantage over PV-LPG.

2.5.5 Sources of uncertainty in projecting future energy costs

A major source of uncertainty in this assessment is the assumption of a constant fuel price over a 15 year project life. The trajectory of LPG prices is highly uncertain, but may positively or negatively influence the tradeoff between PV-LPG and μ-CSP. The historical price of diesel fuel from 1994 to 2011 climbed nearly monotonically from 0.3 USD L^{-1} to 1 USD L^{-1} [18] (almost 8% per year). This rate is higher than our discount rate and highlights the significant risk to investment in petroleum-based energy generation schemes. A final source of uncertainty is the use of historical meteorology data to project thermal loads in a future where climate patterns may be disrupted.

2.6 Conclusion

In this paper we present an assessment of heating, cooling and electrification technologies designed to meet an achetypal remote African health clinic specification for 25kWh$_e$·day^{-1}. Thermal loading of 118–139 kWh$_t$·day^{-1} was estimated using a simple building envelope heat loss model and parameter correlations based on historical geographic meteorology data. The net present cost (NPC) of trigeneration power systems was calculated as a function of latitude with variation due to aggregated climate factors affecting the available insolation for the solar collectors, ambient temperature for heat loss and heat rejection, and the heating and cooling load throughout the year based on degree days and maintenance of a 18–30°C indoor temperature profile modified by the humidex (humidity heat index). Calculated NPC varied from 50k USD at the equator to about 50k USD at the southern tip of Africa, with a local maxima and minima of 55 and 44k USD at latitudes of 5–6°S and 10–15°S for μ-CSP with trigeneration.

Using commonly available technologies, we find that the lowest cost configuration is sensitive to the extent of heating as compared to cooling loads. At latitudes above 20°S a PV system with LPG based hydronic heating and cooling via an NH_3-H_2O chiller is cost-effective, but emerging technologies such as μ-CSP (using an LiBr chiller) can be more economical depending on local thermal parameters, LPG costs, and carbon finance availability.

Chapter 3

Performance and design optimization of a low-cost solar organic Rankine cycle for remote power generation

by S. Quoilin, M. Orosz, H. Hemond and V. Lemort, Published in Solar Energy Vol. 85, 2011

Abstract

Recent interest in small-scale solar thermal combined heat and power (CHP) power systems has coincided with demand growth for distributed electricity supplies in areas poorly served by centralized power stations. One potential technical approach to meeting this demand is the parabolic trough solar thermal collector coupled with an organic Rankine cycle (ORC) heat engine. The paper describes the design of a solar organic Rankine cycle being installed in Lesotho for rural electrification purpose. The system consists of parabolic though collectors, a storages tank, and a small-scale ORC engine using scroll expanders.

A model of each component is developed taking into account the main physical and mechanical phenomena occurring in the cycle and based on experimental data for the main key components.

The model allows sizing the different components of the cycle and evaluates the performance of the system. Different working fluids are compared, and two different expansion machine configurations are simulated (single and double stage).

Nomenclature

A	area, m^2
c	specific heat, $J/(kgK)$
D	diameter (m)
FF	filling factor, -
h	heat transfer coefficient, $W/(m2K)$
h	specific enthalpy, $J/(kgK)$
k	conductivity (W/mK)
L	length (m)
M	mass, kg
$\dot{M}$	mass flow rate, kg/s
n	number of nodes
N_p	number of plates
N_{rot}	rotating speed, rpm
p	pressure, Pa
pinch	pinch point value, (K)
$\dot{Q}$	Heat power, W
$\dot{q}$	linear heat flux, W/m
r	ratio, -
$r_{v,in}$	Internal built-in volume ratio, -
S_{beam}	beam solar insolation (W/m^2)
T	temperature, $°C$
U	heat transfer coefficient, $W/(m^2K)$
v	specific volume, m^3/kg
V	velocity, m/s
V_s	swept volume, m^3
$\dot{V}$	volume flow rate, m^3/s
w	specific work, J/kg
W	width (m)
Greek symbols	
α	absorptivity
ε	effectiveness
ε	emissivity
η	efficiency
ρ	density, kg/m^3
ρ	reflectivity, -
τ	transmittance -
Subscripts and superscripts	
abs	absorber
amb	ambient
cd	Condenser
col	Collector
ev	Evaporator
ex	Exhaust
exp	Expander
i	Relative to cell i
htf	Heat transfer fluid
hx	Heat exchanger
l	Liquid
opt	Optical
p	Pressure
pp	Pump
rec	recuperator
su	Supply
sf	Secondary fluid
tp	Two-phase
tot	total
v	Vapor
v	Volume

3.1 Introduction

Concentrating Solar Power (CSP) systems have been implemented with a variety of collector systems such as the parabolic trough, the solar dish, the solar tower or the Fresnel linear collector. However, most of the currently installed CSP plants use a steam Rankine cycle in the power block. This technology requires a minimum power of a few MWe in order to be competitive and involves high collector temperatures.

Particularly in the case of small-scale systems, an Organic Rankine Cycle (i.e. a Rankine cycle using an organic fluid instead of water) may show a number of advantages over the steam cycle. These include a lower working temperature, the absence of droplets during the expansion, the low maintenance requirements and the simplicity (fewer components). According to McMahan [101], those advantages make the ORC technology more economically attractive when used at small and medium power scales.

Solar ORCs have been studied both theoretically [120, 123] and experimentally [105] as early as in the 70s and with reported overall efficiencies varying between 2.52 and 7%. Experimental studies usually involved the use of vane expanders ([26] multi-vane expanders, [120]), and high Ozone Depleting Potential (ODP) refrigerants such as R11 or R13 were often used. Recent studies have tended to emphasize optimization of fluid selection for different cycle architectures and collecting temperatures [154, 101, 51, 34, 52, 149]. It is interesting to note, however, that no single fluid has been identified as optimal for the ORC. This is mainly due to the strong interdependence between the optimal working fluid, the working conditions and the cycle architecture. It follows that the study of the working fluid candidates should be integrated into the design process of any ORC system.

Few studies have provided experimental data from operational solar ORC systems: Kane [78] studied the coupling of linear Fresnel collectors with a cascaded 9-kWe ORC, using R123 and R134a as working fluids. An overall efficiency (solar to electricity) of 7.74% was obtained, with a collector efficiency of 57%. Manolakos [98] studied a 2kWe low-temperature solar ORC with R134a as working fluid and evacuated tube collectors: an overall efficiency below 4% was obtained. Wang [151] studied a 1.6 kWe solar ORC using a rolling piston expander. An overall efficiency of 4.2 % was obtained with evacuated tube collectors and 3.2% with flat-plate collectors. The difference in terms of efficiency was explained by lower collector efficiency (71% for the evacuated tube vs. 55% for the plate technology) and lower collection temperature.

Detailed models of such systems are also scarce in the scientific literature: McMahan [101] proposed a detailed model and an optimization of the ORC cycle for solar applications, but this model was not coupled to a solar collector model; Forristall [59] proposed a model of the solar collectors validated with the SEGS plants data, independent of a power cycle model. Jing [74] developed a model of an ORC cycle using R123 as working fluid and coupled to CPC collectors: the predicted overall efficiency was about 7.9% for a solar insolation of 800 W/m^2 and an evaporating temperature of 147 $°C$. Kane [77] developed a model of a cascaded ORC using scroll expanders and coupled to a collector model. This model was used to conduct a thermoeconomic optimization on the system.

Most of the above mentioned studies show that the ORC efficiency is significantly improved by inclusion of a recuperator, of cascaded cycles, or of reheating [101, 77, 121].

At present, only one commercial solar ORC power plant is reported in the technical literature: the 1 MWe Saguaro Solar ORC plant in Arizona, USA. This plant uses n-pentane as working fluid and shows an overall efficiency of 12.1%, for a collector efficiency of 59% [38].

If medium-scale solar ORCs are already commercially available, work remains to be done for very small-scale units (a few kWe), especially to reduce the specific investment costs and to control

the system in order to avoid the need of an on-site operator.

3.2 System description

Researchers at MIT and University of Liége have collaborated with the non-governmental organization STG International for the purpose of developing and implementing a small scale solar thermal technology utilizing medium temperature collectors and an ORC. A first unit was installed by STG in 2007, and is shown in Fig. 3-1.

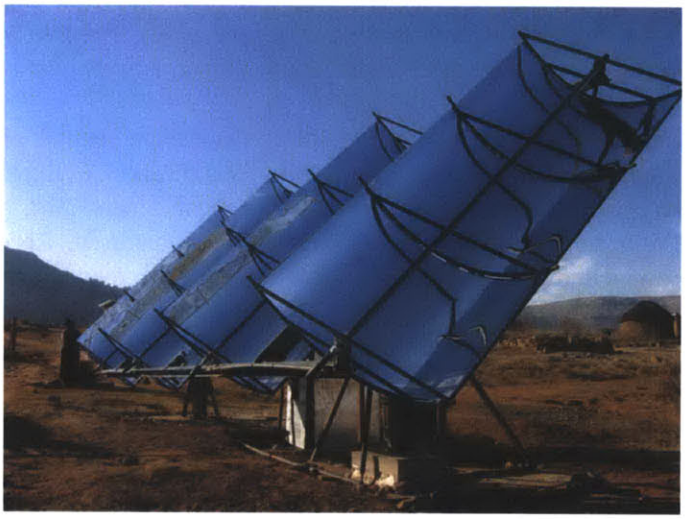

Figure 3-1: Solar ORC prototype installed by STG in Lesotho.

The goal is to provide rural areas of developing countries with a system that can be manufactured and assembled locally (unlike PV collectors) and can replace or supplement diesel generators in off grid areas, by generating clean power at a lower levelized cost [117].

At the core of this technology is a solar thermal power plant consisting of a field of parabolic solar concentrating collectors and a vapor expansion power block for generating electricity. An electronic control unit is added for autonomous operation as sub-megawatt scale plants cannot justify the staffing of operating personnel. Operating at a lower cycle temperatures ($< 200°C$) and Carnot efficiency is an example of a design tradeoff for maintaining low cost at small scales. For a given level of output power, lower temperatures enable cost savings in the materials and manufacture of the absorber units, heat exchangers, fluid manifolds and parabolic troughs.

Because no thermal power blocks are currently manufactured in the kilowatt range a small-scale ORC has to be designed for this application. The design is based on modified commercially available components e.g. HVAC scroll compressors (for the expander), and industrial pumps and heat exchangers. It should be noted that the main challenge for ORC development is the high cost of specially designed expander-generator equipment. At present, no volumetric expander is available on the market. In order to reduce the cost of a practicable system, the expander is obtained by adapting an off-the-shelf hermetic scroll compressor to run in reverse, as proposed and successfully tested by Lemort et al. [95]. Scroll machines show the advantage of being widely available, reliable and with a limited number of moving parts [159].

The goal of this paper is to design and dimension an improved solar ORC unit to be installed

in a rural clinic in Berea District of Lesotho and to evaluate its performance with different working fluids. The main characteristics of this unit are the following:

- Target net output power: 3 kWe.
- Collector field: $75m^2$ single-axis parabolic trough, using Miro aluminum reflectors and a Heat Collection Element (HCE) with selective coating and air-filled annulus between absorber pipe and glazing.
- ORC: One or two stage expansion of R245fa using modified commercial HVAC compressors, brazed plate heat exchangers for high pressure heat transfer, and commercial HVAC tubes-and- fins air condenser for heat rejection.
- Heat transfer fluid (HTF): Monoethylene glycol (MEG) with thermal buffering in a thermal storage tank with a 2 m^3 packed bed of 19 mm quartzite pebble bed.

The heat transfer fluid is heated up in the collector field and driven to the evaporator by the heat transfer fluid pump. A thermal storage is installed in order to attenuate the fast fluctuations of solar irradiation during the day and to maintain stable operation of the ORC engine (See Fig. 3-2).

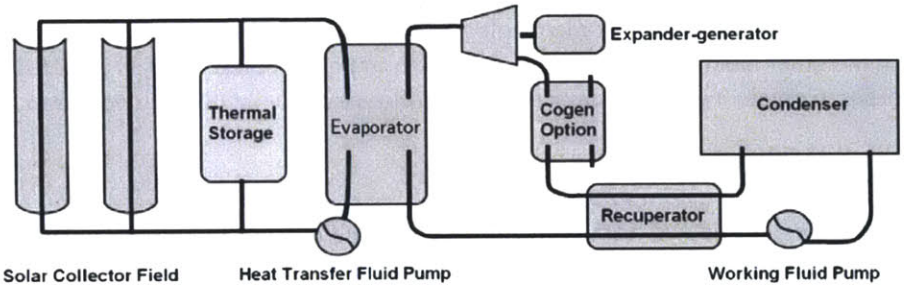

Figure 3-2: Conceptual scheme of the solar ORC.

The main components in the classical Rankine cycle include an evaporator, expander, a condenser and a recirculation pump. In an ORC with a "dry" fluid, recuperation from the superheated exhaust to the subcooled liquid is typically achieved with a heat exchanger interposed between the expander exhaust and the pump outlet. This superheated exhaust is also readily exploitable for cogeneration, requiring an additional heat exchanger which can be positioned in series with or parallel to the recuperator.

In the proposed system the cycle heat exchangers (evaporator, recuperator and condenser) are sized in order to obtain the required pinch point and pressure drop. The working fluid is condensed in an air condenser in order to avoid unnecessary water consumption (but at the expense of non-negligible fan consumption) and then repressurized in a piston pump The expansion process is performed by one or two modified HVAC scroll machines configured in series. Cogeneration is obtained with the additional plate heat exchanger installed between the expander and the recuperator in order to produce hot water in addition to electricity, depending on the local demand.

3.3 Modeling

In this section, a steady-state model of the system presented in Figure 3-2 is developed, for the rating and sizing of the different components and to optimize the working conditions on a nominal point.

The transient behavior of the solar source is not taken into account here and an average insolation is utilized. It is assumed that the storage is sized in such a way to maintain almost constant heat transfer fluid flow rate and temperature during the operating time of the system: the ORC engine is assumed to stand by in case of insufficient solar insolation for meeting temperature requirements and in order to avoid part load conditions that might reduce the cycle efficiency. In practice this means that during periods of low insolation, the time to charge the storage to the set operational point is longer than the operating time of the ORC engine. In light of this steady state hypothesis, the storage tank is not modeled. The water heating heat exchanger is also neglected, since the main goal of the model is to evaluate the electricity generation potential of the system.

The solar ORC is model within the EES environment [83]: a model is developed for each subcomponent and included into a module. These modules are further interconnected to obtain the global model of the system.

The proposed global model cannot be validated experimentally because of the lack of experimental data. However, it was shown in a previous publication that connecting validated component submodels in order to build a global ORC model can lead to an acceptable overall error lower than 10% compared to experimental data [127].

Since a nominal size (or power) must be set, the proposed model is a hybrid between a simulation model and a sizing model: on one hand, the design, the size and the parameters of the collector are set according to the collector technology developed by STG International and installed in Lesotho. On the other hand, the size of the ORC cycle and of its components is recalculated by the model in order to obtain a good match between collector power and ORC engine power.

3.3.1 Parabolic trough model

The trough module, largely adapted from Forristall [59], is a one-dimensional energy balance model around a Heat Collection Element (HCE) of user specified dimensions and materials: Radiation impinges on a reflector element with user- input focal length, reflective coefficient, and aperture. The energy is correspondingly reduced (e.g. due to a reflective coefficient ¡1) and concentrated onto a nodal area of the HCE, where it is transmitted through a glass envelope and a gas annulus, and finally absorbed or reflected at the surface of the HCE.

Depending on the absorptivity and emissivity characteristics of the selective coating and the temperature of the HTF flowing through the HCE at a given node, some amount of absorbed energy is transferred through the HCE wall into the HTF (process 2-1 in Fig. 3-3) with a heat exchange coefficient calculated from the fluid thermal properties and flow regime parameters.

The remaining absorbed heat is lost at the HCE outer surface, via convection and radiation back through the annulus (3-4), conduction through the envelope (4-5), radiation between the envelope and the sky (5-7) and convection to the ambient air (5-6).

This process is repeated for each node, where the input for each node is the output of the previous node, resulting in an overall enthalpy and temperature gain for the focal line length specified by the user. The collector module thus derives a thermal efficiency and outputs a heat flux and temperature gain for the HTF at the user specified flow rate and initial temperature.

The different heat transfer relations used to compute the heat flows are provided in Table 3.1.

The amounts of radiation absorbed by the collector and by the glass enveloped are respectively given by [59]:

$$q_{sun,3} = q_{sun} \cdot \eta_{opt} \cdot \tau_{env} \cdot \alpha_{coating} \tag{3.1}$$

$$q_{sun,5} = q_{sun} \cdot \eta_{opt} \cdot \alpha_{env} \tag{3.2}$$

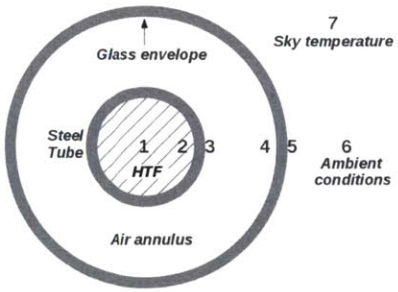

Figure 3-3: Heat transfer in the absorber.

	Heat transfer type	Heat transfer law
1-2	Convection	Gnielinski correlation for turbulent heat transfer in pipes [71] $q_{23} = 2\pi k_{23} \frac{T_2 - T_3}{ln(D_3/D_2)}$
2-3	Conduction	k_{23} is the assumed-to-be-constant steel conductivity: $k_{23} = 50\ W/mK$
	Convection	Hollands correlation for natural convection in an annular space between horizontal cylinders [68].
3-4	Radiation	$q_{34,rad} = \frac{\sigma \pi D_3 (T_3^4 - T_4^4)}{\frac{1}{\varepsilon_3} + \frac{1-\varepsilon_4}{\varepsilon_4} \frac{D_3}{D_4}}$
4-5	Conduction	$q_{45} = 2\pi k_{45} \frac{T_4 - T_5}{ln(D_5/D_4)}$
5-6	Free convection	Churchill and Chu correlation for laminar convection from a horizontal cylinder [71].
5-6	Forced convection	Zhukauskas' correlation for external forced convection flow normal to an isothermal cylinder [71].
5-7	Radiation	$q_{57,rad} = \sigma \pi D_5 (T_5^4 - T_7^4)$, T_7 is taken 8° below the ambient temperature

Table 3.1: Absorber heat transfer models.

Where $q_{sun} = S \cdot W_{col}$ is the linear beam insolation. And

$$\eta_{opt} = \rho_{mirror} \cdot \eta_{shadowing} \cdot \eta_{tracking} \cdot \eta_{geometry} \cdot \eta_{unaccounted} \tag{3.3}$$

η_{opt} is the optical efficiency, lumping different sources of losses such as mirror reflectivity (ρ_{mirror}), tracking losses ($\eta_{tracking}$), shadowing ($\eta_{shadowing}$), geometrical effects ($\eta_{geometry}$) and other unaccounted losses ($\eta_{unaccounted}$). The values of the different efficiencies are the ones recommended by Forristall [59], except for $\eta_{tracking}$ and $\eta_{geometry}$, where a significantly lower efficiency is selected. This conservative hypothesis is made in order to account for the relatively lower optical intercept factor ($\tilde{0}.9$) resulting from the low-cost design of the collector, which could reduce the performance of the system.

In order to reduce the magnitude of $q_{34,rad}$, a selective coating is applied on the collector tube, maximizing the solar absorptivity and minimizing the infra-red emissivity. This emissivity is calculated according to Forristall recommendation for a "Solar UAV cermet" coating:

$$\varepsilon_{coating} = 2.249 \cdot 10^{-7} \cdot T_3^2 + 1.039 \cdot 10^{-4} \cdot T_3 + 5.599 \cdot 10^{-2} \tag{3.4}$$

For each cell of the discretized collector (having a length equal to the total focal line length divided by the number of nodes) the different energy balance equations can be applied:

$$T_{ex,cell} = T_{su,cell} + \frac{\dot{q}_{12} \cdot \Delta x}{\dot{M}_{htf} \cdot \bar{cp}_{htf}} \tag{3.5}$$

$$\dot{q}_{45} = \dot{q}_{34,conv} + \dot{q}_{34,rad} \tag{3.6}$$

$$\dot{q}_{56,conv} = \dot{q}_{45} + \dot{q}_{sun,5} - \dot{q}_{57} \tag{3.7}$$

$$\dot{q}_{12,conv} = \dot{q}_{23} \tag{3.8}$$

$$0 = \dot{q}_{23} + \dot{q}_{34,conv} + \dot{q}_{34,rad} - \dot{q}_{sun,3} \tag{3.9}$$

Moreover, a pressure drop in the heat transfer fluid can be computed in each cell using the following equation:

$$\Delta p_{cell} = \frac{f \cdot \Delta L \cdot G_{htf}^2}{2 \cdot D_2 \cdot \rho} \tag{3.10}$$

where f is the friction factor, calculated with the Gnielinski correlation [71]. The different parameters used for the modeling of the solar collected are summarized in table 3.2.

Parameter	Description	Value
ρ_{mirror}	Mirror reflectivity	0.94
$\eta_{tracking}$	Tracking error	0.92
$\eta_{shadowing}$	Shadowing error	0.98
$\eta_{geometry}$	Geometry error	0.93
$\eta_{unaccounted}$	Unaccounted losses	0.96
D_2	absorber tube inner diameter	66 mm
D_3	absorber tube outer diameter	70 mm
D_4	envelope inner diameter	80 mm
D_4	envelope outer diameter	88 mm
L_{col}	Total collector length	46 m
W_{col}	Collector width	2.5 m
τ_{env}	envelope transmissivity	0.96
α_{env}	envelope absorbtivity	0.04
$\alpha_{coating}$	coating absorbtivity	0.96
ε_{env}	envelope emissivity	0.86
N	Number of node	15

Table 3.2: Collector model parameters.

3.3.2 Evaporator model

The evaporator is modeled by means of the Logarithmic Mean Temperature Difference (LMTD) method for counter-flow heat exchangers. The heat exchanger is subdivided into 3 moving- boundaries zones, each of them being characterized by a heat transfer area A and a heat transfer coefficient U [127]. The heat transfer coefficient U is calculated by considering two convective heat transfer resistances in series (secondary fluid and refrigerant sides).

$$\frac{1}{U} = \frac{1}{h_r} + \frac{1}{h_{sf}} \tag{3.11}$$

The total heat transfer area of the heat exchanger is given by:

$$A_{tot} = A_l + A_{tp} + A_v = (N_p - 2) \cdot L \cdot W \tag{3.12}$$

N_p the number of plates, L the plate length and W the plate width.

Single-phase

Forced convection heat transfer coefficients are evaluated by means of the non-dimensional relationship:

$$Nu = C \cdot Re^m \cdot Pr^n \tag{3.13}$$

where the influence of temperature-dependent viscosity is neglected.

The parameters C, m and n are set according to Thonon's correlation for corrugated plate heat exchangers [25]. The pressure drops are computed with the following relation:

$$\Delta p = \frac{2 \cdot f \cdot G^2}{\rho \cdot D_h} \cdot L \tag{3.14}$$

Where f is the friction factor, calculated with the Thonon correlation, G is the mass velocity $(kg/s\ m^2)$, ρ is the mean fluid density, D_h is the hydraulic diameter and L is the plate length.

Boiling heat transfer coefficient

The overall boiling heat transfer coefficient is estimated by the Hsieh correlation, established for the boiling of refrigerant R410a in a vertical plate heat exchanger. This heat exchange coefficient is considered as constant during the whole evaporation process and is calculated by [69]:

$$h_{tp} = C h_l Bo^{0.5} \tag{3.15}$$

Where Bo is the boiling number and h_l is the all-liquid non-boiling heat transfer coefficient. The pressure drops are calculated in the same manner as in eq. 3.14, using the Hsieh correlation for the calculation of the friction factor.

Heat exchanger sizing

For a given corrugation pattern (amplitude, chevron angle, and enlargement factor), two degrees of freedom are available when sizing a plate heat exchanger: the length and the total flow width. The total flow width is given by the plate width multiplied by the number of channels:

$$W_{tot} = W_{hx} \cdot \frac{N_p - 1}{2} \tag{3.16}$$

The two degrees of freedom are fixed by the heat exchange area requirement and the limitation on the pressure drop on the working fluid side:

- Increasing the total width decreases the Reynolds number. This leads to a lower pressure drop and to a higher required heat transfer area, since the heat transfer coefficient is also decreased.

- Increasing the plate length leads to a higher pressure drop.

Therefore, by imposing a pinch point and a pressure drop, it is possible to define the total width and the length of the plate heat exchanger. The flow chart of the sizing process is shown in Fig. 3-4.

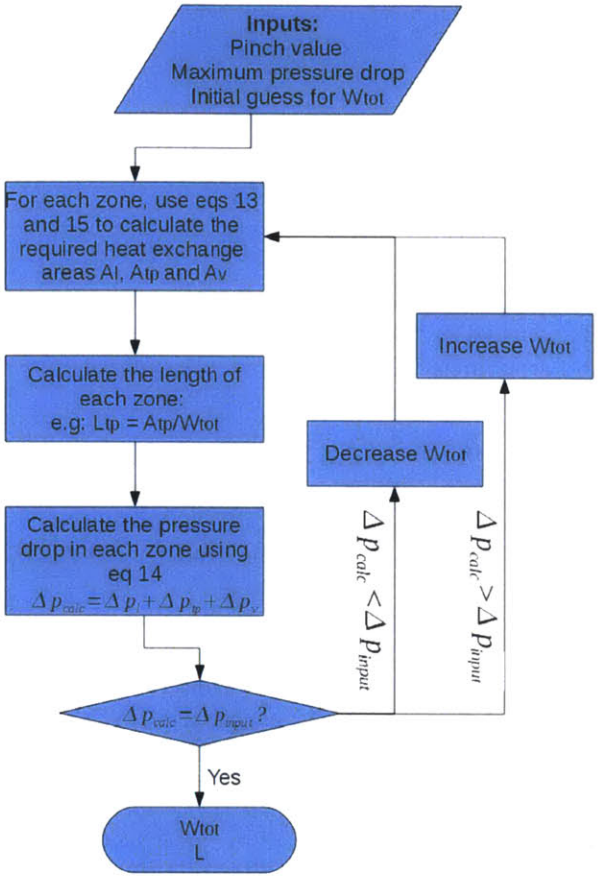

Figure 3-4: Plate heat exchangers sizing process.

The imposed parameters of the evaporator model are presented in Table 3.3.

Parameter	Description	Value
D_h	Hydraulic diameter	2 mm
$\beta_{chevron}$	Chevron angle	45 °

Table 3.3: Evaporator model parameters.

3.3.3 Recuperator model

The recuperator model is similar to the evaporator model, with one zone (single phase) instead of three. The inputs of the model are the maximum pressure drop and the heat exchanger efficiency, which allows sizing the exchanger in terms of total width and length.

3.3.4 Expander model

Volumetric expanders, such as the scroll, screw or reciprocating technologies present an internal built-in volume ratio ($r_{v,in}$) corresponding to the ratio between the inlet pocket volume and the outlet pocket volume. This can generate two types of losses if the system specific volume ratio is not equal to the expander nominal volume ratio:

Under-expansion occurs when the internal volume ratio of the expander is lower than the system specific volume ratio. In that case, the specific volume in the expansion chambers at the end of the expansion process (Pin) is lower than the specific volume in the discharge line.

Likewise Over-expansion occurs when the internal volume ratio imposed by the expander is higher than the system specific volume ratio.

These two effects can considerably reduce the efficiency of the expansion process. Other sources of losses include friction losses, supply pressure drop, internal leakage and heat transfers [95].

Since no off-the-shelf small-scale expansion machine is currently available on the market, the expander was obtained by modifying a scroll compressor to make it run in reverse. This allows keeping the expander cost low, hermetic compressors being very common components in HVAC applications. On the other hand, since the device is not optimized for expander applications, experimental results by Lermort et al. showed that the efficiency is reduced by about 10% when working in expander mode (about 60% efficiency) compared to the compressor mode (typically 70%). In this work, the considered expander is a hermetic scroll expander tested and modeled by Lemort et al [94].

A semi-empirical thermodynamic model such as the one proposed by Lemort et al. is not suitable for the purpose of this work since it was developed for one machine in particular. Here, a sizing model is needed, that can predict the performance of scroll expanders with very different swept volumes.

If ambient heat losses are neglected, scroll expanders can be modeled by their isentropic efficiency and by their filling factor, respectively defined by [94]:

$$\varepsilon_{exp} = \frac{\dot{W}_{exp}}{\dot{M} \cdot (h_{su,exp} - h_{ex,exp,s}} \tag{3.17}$$

and:

$$FF = \frac{60 \cdot \dot{M}}{\rho_{su} \cdot V_s \cdot N_{rot}} \tag{3.18}$$

Where V_s is the swept volume of the expander and N_{rot} its rotational speed (assumed to be constant at 3000 rpm). where $\dot{W}_{exp}$ the electrical power generated by the expander and $h_{ex,exp,s}$ is the isentropic exhaust enthalpy. It should be noted that the given efficiency is an electrical and not a mechanical isentropic efficiency, i.e. electromechanical losses in the generator have already been accounted for.

In order to simulate realistic performance close to the actual experimental data, the model developed by Lemort et al. [94] is used to express ε and FF as a polynomial law of the main working conditions. The two selected working conditions are the fluid inlet density ρ_{su} and pressure ratio over the expander r_p since they turned out to be the two main representative variables of the working conditions. The polynomial fits are expressed in the following form:

$$\varepsilon = \sum_{i=0}^{n-1}\sum_{j=0}^{n-1} a_{ij} \cdot ln(r_p)^i \cdot \rho_{su}^j + a_{n0} \cdot ln(r_p)^n + a_{0n} \cdot \rho_1^n = f(r_p, \rho_{su}) \tag{3.19}$$

For ε,a 4^{th}-order ($n = 4$) polynomial fit is used, while for FF a second-order ($n = 2$) polynomial fit turned out to be sufficient. The correlations have been established on the basis of the validated model for 800 different working points inside of the following operating conditions:

$$30 < \rho_{su} < 200; 1.2 < r_p < 12 \tag{3.20}$$

The values of ε and FF were respectively predicted by the polynomial fit with $R^2 = 99.98\%$ and $R^2 = 99.96\%$. It is assumed that, when changing the scale of the expander (and thus the swept volume), the isentropic efficiency and the filling factor remain similar if the pressure ratio and the inlet density are kept equal.

Double-stage expander

As mentioned above, volumetric expanders are optimized for a given specific volume ratio. It appears that the specific volume ratios involved in refrigeration for which the scroll compressors are designed is typically much lower than the specific volume ratios involved in ORC cycles. When the expander is obtained from a modified scroll compressor, under-expansion losses can therefore become prohibitive for high specific volume ratios (typically higher than 10). A possible solution consists in using two expanders assembled in series, as shown in Fig 3-5.

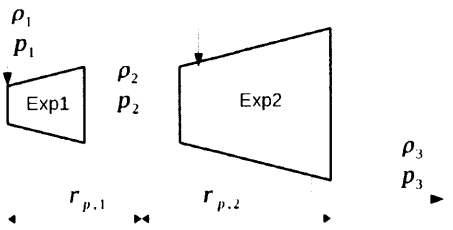

Figure 3-5: Two-stage expander

When sizing a double-stage expander, it is important to define carefully the two swept volumes in order to optimize the intermediate pressure p_2. If the expander efficiency was only dependent on the pressure ratio, the optimal single-stage pressure ratio would be defined as the square root of the overall pressure ratio ($r_{p,1} = r_{p,2} = \sqrt{r_p}$). However, the efficiency also depends on the flow rate going through the expander because a higher flow rate entails a higher output power and makes the constant losses (e.g. friction losses) relatively smaller. In the polynomial correlations, the influence of the flow rate is reflected by the dependence in terms of supply vapor density.

In order to determine the optimal first-stage pressure ratio, the overall isentropic efficiency is maximized using the following equation:

$$\frac{d\varepsilon}{dr_{p,1}} = \frac{d}{dr_{p,1}}\left[\frac{h_1 - h_s}{h_1 - h_{ss}}\right] \tag{3.21}$$

This can be done numerically or analytically. For the latter solution,ε must be expressed in

terms of $r_{p,1}$, which can be achieved using the ideal gas hypothesis.

3.3.5 Condenser model

Since air condensers are well-known components in HVAC applications, a simplified model based on manufacturer data [153] is used to compute the condenser performance and fan consumption.

The two inputs are the pinch point, defined as the difference between the condensing temperature and the ambient temperature, and the condensing power.

Special attention is paid to the fan consumption since it can amount for a non-negligible share of the generated power. The fan consumption is computed as a function of the heat transfer power and of the pinch point with the following relation:

$$\dot{W}_{fan,cd} = 54.5 + 0.0185 \cdot Q_c d \cdot \frac{8.333}{pinch_{cd}} \tag{3.22}$$

3.3.6 Pump model

Two pump consumptions are taken into account: the heat transfer fluid pump and the working fluid pump. They are modeled by their isentropic efficiency, defined by [127]:

$$\varepsilon_{pp} = \frac{v_{su,pp} \cdot (p_{ex,pp} - p_{su,pp})}{h_{ex,pp} - h_{su,pp}} \tag{3.23}$$

For the HTF pump, the pressure difference is given by the sum of the pressure drops in the evaporator and in the collector. A constant, realistic value of 70% is assumed for the pump efficiency [96].

3.3.7 Cycle model

The global model of the system is obtained by interconnecting each subcomponent model according to Fig. 3-6.

Several performance indicators can be defined.
The overall collector efficiency:

$$\eta_{col} = fracM_{htf} \cdot \bar{cp}_{htf} \cdot (T_{htf,ex,col} - T_{htf,su,col}) S_{beam} \cdot L_{col} \cdot W_{col} \tag{3.24}$$

The net electrical output power:

$$W_{net} = W_{exp} - W_{pp} - W_{fans} - W_{pp,htf} \tag{3.25}$$

The ORC cycle efficiency

$$\eta_{ORC} = \frac{W_{net}}{Q_{ev}} \tag{3.26}$$

The overall system efficiency:

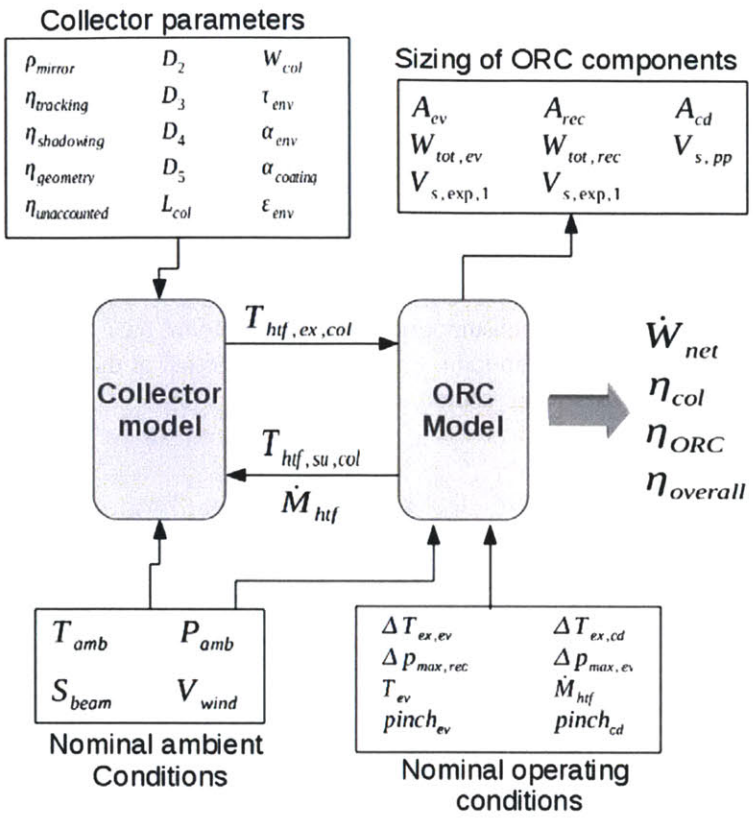

Figure 3-6: Global model parameters, inputs and outputs

$$\eta_{overall} = \frac{W_{net}}{S_{beam} \cdot L_{col} \cdot W_{col}} = \eta_{col} \cdot \eta_{ORC} \tag{3.27}$$

In this work, the pinch points are set to 8K, the superheating at the expander inlet is set to 10K, the subcooling at the condenser outlet is set to 5K, and the maximum pressure drop on the refrigerant side of each heat exchanger is set to 75 mbar.

3.4 System performance and fluid comparison

This section aims at understanding the influence of different cycle parameters on the system and to compare several working fluids and cycle architectures. For that purpose, nominal ambient conditions are imposed and are kept constant for all the simulations performed below:

$$\begin{cases} T_{amb} &= 15^oC \\ p_{amb} &= 0.83\ bars \\ S_{beam} &= 800\ W/m^2 \\ V_{wind} &= 2\ m/s \end{cases}$$

These conditions are typical of the mid-season or winter time conditions in the highlands of

Lesotho.

Three main degrees of freedom are available to control the working conditions of the cycle: the heat transfer fluid flow rate, the working fluid flow rate and the expander swept volume or rotational speed. Setting the working fluid flow rate and the expander speed allows defining the evaporating temperature and the superheating [127]. Setting the heat transfer fluid flow rate allows defining the temperature glide in the collector. According to Yamamoto [157], the superheating should be maintained as low as possible when using high molecular weight working fluids. The two remaining degrees of freedom (evaporating temperature and collector temperature glide) can be determined optimally, as shown in the next sections.

3.4.1 Influence of the temperature glide in the collector.

Modifying the heat transfer fluid flow rate entails two main antagonist effects: on the one hand, the overall temperature level in the collector is modified (Fig. 3-7), which will impact its thermal efficiency via the various heat loss mechanisms.

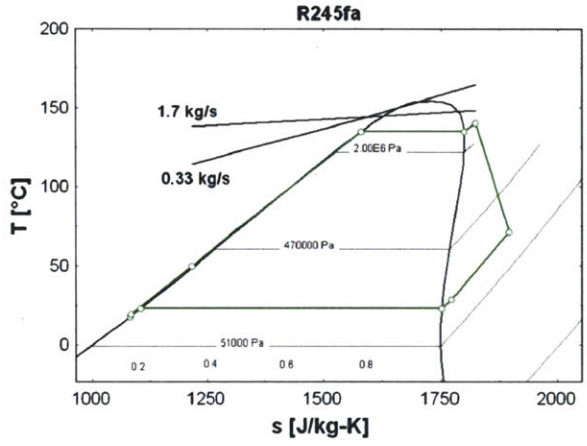

Figure 3-7: T-s diagram of the ORC process.

On the other hand, changing the fluid flow rate affects the heat transfer coefficient between the heat transfer fluid and the absorber, which also impacts the collector efficiency.

Fig. 3-8 shows that the second effect is predominant: For very low temperature glides, the overall efficiency is reduced because of the very high HTF fluid pumping consumption. For high temperature glides, the overall efficiency is lowered by the low heat transfer coefficient in the collector. An optimum is obtained for a temperature glide of 15K, corresponding to a heat transfer fluid flow rate of 1.2 kg/s.

In the following parametric studies, the temperature glide value will always be set to its optimal value for each computed working point. This value is obtained with the "Golden Section Search" algorithm.

3.4.2 Influence of the evaporating pressure

The selection of the optimal evaporating temperature results in a tradeoff between collector efficiency and cycle efficiency. In the particular case of an ORC using volumetric expanders, increasing the evaporation temperature also increases the under-expansion losses and reduces the cycle efficiency, which constitutes an additional influence.

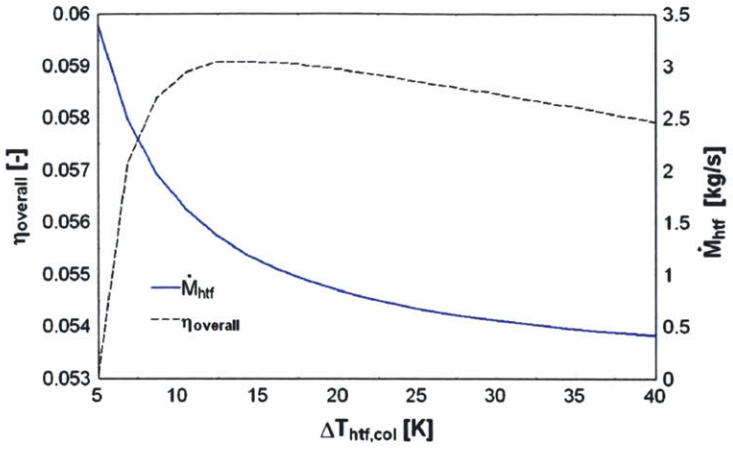

Figure 3-8: Influence of the HTF temperature glide.

The goal of this section is to illustrate the influence of the evaporating temperature on different cycle parameters and performance indicators. For that purpose, an arbitrary working point is selected: the selected working fluid is R245fa, with a two-stage expander, an optimized heat transfer fluid temperature glide, a superheating of 5K, and a subcooling of 5K.

As shown in Fig. 3-9, increasing the evaporating temperature leads to higher cycle efficiency and to lower collector efficiency. An optimal overall efficiency is stated around 150 $°C$, which is just below the critical point (154$°C$ for R245fa).

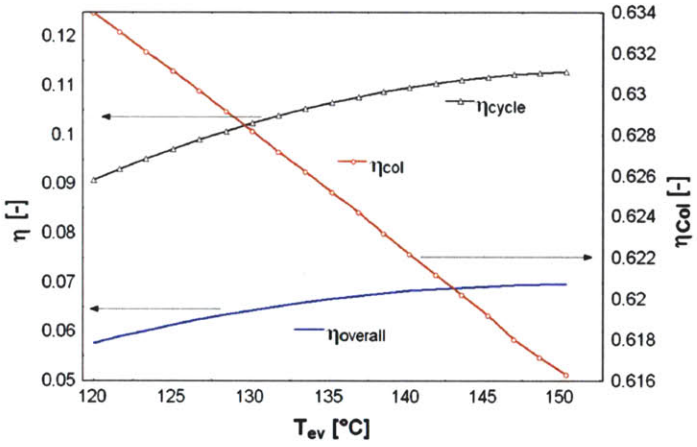

Figure 3-9: Influence of the evaporation temperature on the performance.

The evaporating temperature also has an impact on the size of the different components. Fig. 3-10 shows that with high evaporating temperature levels, smaller swept volumes are needed for both expanders since the inlet densities are higher. This is an appreciable advantage since the cost of the expanders is reduced.

A similar effect is stated for the heat transfer area of the evaporator (Fig. 3-11): for a given pressure drop, a higher vapor density allows reducing the passage area, which in turns reduces the required area. Fig. 3-11 also shows that a modification of the evaporating temperature has a very

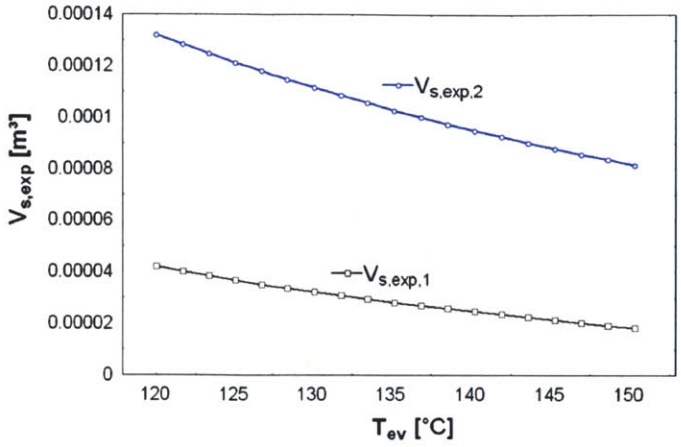

Figure 3-10: Required swepts volumes vs. evaporating temperature.

limited effect on the required recuperator area. Although those calculations were performed for R245fa, a similar behavior is stated for alternative working fluids.

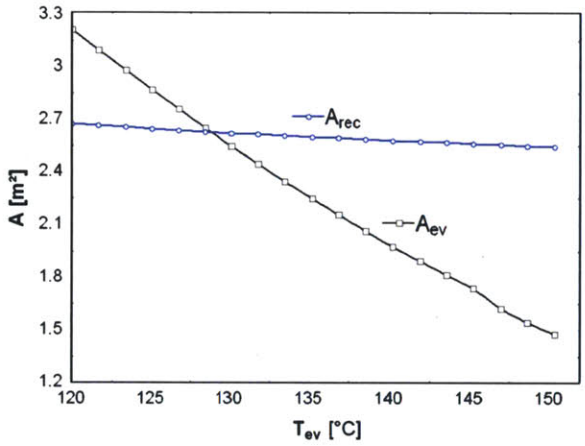

Figure 3-11: Required heat transfer area vs. evaporating temperature.

3.4.3 Working fluid and architecture comparison

In order to compare a reasonable amount of working fluids, a pre-screening is performed with the following conditions:

- The critical point of the working fluid should be similar to the target temperature range (100 to 200°C).
- The working fluid should be a well known-fluid in state-of-the-art ORC applications or in the scientific literature dealing with working fluid selection (See [126] for a review). This criterion ensures that several conditions such as the toxicity, the cost or the flammability are fulfilled.

- The working fluid should have a null Ozone Depleting Potential (ODP) in order to avoid the phasing-out of the Montreal Protocol.

Four fluids have been selected using this methodology: R134a, R245fa, Solkatherm (SES36) and n-Pentane.

One of the main influences of the working fluid on the cycle architecture lieays in the specific volume ratio: generally speaking, the higher the critical temperature, the higher the specific volume ratio over the expander. The scroll expanders considered in this work are designed for a volume ratio close to 3. As discussed above, when used at much higher specific volume ratios, their effectiveness is reduced. Fig. 3-12 shows that the specific volume ratio remains acceptable for single stage expansion only for R134a and R245fa (at low evaporating temperature). In the simulations, R134a is therefore used with single-stage expansion architecture. Solkatherm and n-pentane are simulated with a double-stage expansion. R245fa is simulated with both architectures.

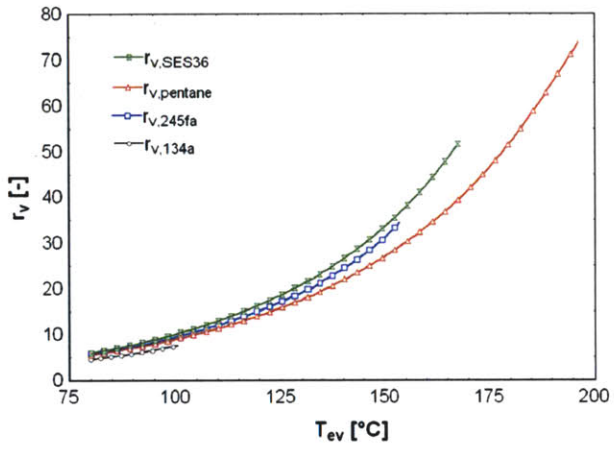

Figure 3-12: Specific volume ratio vs. evaporating temperature.

Fig. 3-13 shows the overall efficiency of the system with the four different fluids. A maximum appears in terms of evaporating temperature when the single-stage architecture is selected. This is explained by the very high under-expansion losses that reduce the expander effectiveness at high evaporating temperature. On the contrary, when using a two-stage expansion, the efficiency is limited by the critical temperature or by unrealistic working conditions such as very high specific volume ratios. Solkatherm is the fluid showing the highest efficiency, with a maximum close to 8%. It should however be noted that refrigeration compressors are not designed for temperatures higher than $150°C$, which might reduce their lifetime. If this limit is applied, the maximum overall efficiency is 7.5% for Solkatherm and 7% for R245fa.

Additional parameters to the sole efficiency must be taken into account when comparing working fluids. Table 3.4 shows the more relevant cycle parameters for a few selected optimal points. The bold characters indicate the most advantageous value for each column. If Solkatherm is the most efficient fluid, it is also the one requiring the biggest expander, with a suction swept volume (in expander mode) of 180.7 cm^3 for the second stage of expansion and an evaporating temperature of $150°C$. R245fa on the contrary shows very advantageous swept volumes, which could reduce the cost of the system. n-pentane must be run at very high temperature to show a good efficiency. Its required evaporator area is advantageous, but the required recuperator area is very high due to the low density and the very high pressure drops in the low-pressure vapor.

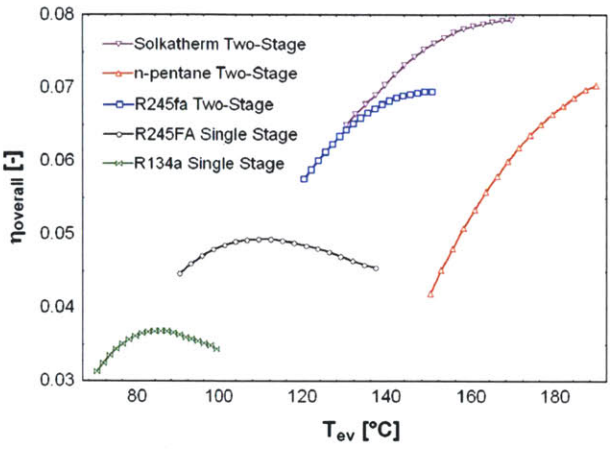

Figure 3-13: Overall efficiency for different working fluids.

	$T_{ev}(°C)$	$\Delta T_{HTF}(°C)$	$\eta_{col}(\%)$	$\eta_{ORC}(\%)$	$\eta_{overall}(\%)$	$\varepsilon_{exp}(\%)$	$V_{s,1}\ (cm^3)$	$V_{s,2}\ (cm^3)$	$A_{ev}\ (m^2)$	$A_{rec}\ (m^2)$
n-Pentane	189	31.6	59.1	11.9	7.0	47.2	22.2	98.9	**0.95**	3.53
SES36	169	19.5	60.4	**13.1**	**7.9**	54.9	27.1	137.3	1.1	**1.24**
SES36	150	14.0	61.6	12.3	7.5	55.0	44.9	180.7	1.71	1.29
R245fa	150	22.9	61.6	11.2	6.9	58.7	**20.8**	**92.8**	1.48	2.54
R245fa	109	12.8	**63.9**	7.7	4.9	50.3	59.9	0	4.02	2.73
R134a	**85**	17.1	65.1	5.6	3.6	**59.7**	37.2	0	2.7	1.53

Table 3.4: Simulations resuts for different working fluids.

3.4.4 Influence of the working conditions

The developments proposed above were conducted for nominal conditions, defined in section 4. However, the selection of these working conditions can have a non-negligible influence on the simulation results.

A parametric study is performed to evaluate the influence of the nominal working conditions on the overall efficiency: this study is performed for the SES36 working fluid and an evaporating temperature imposed at 150 $°C$ (third line in Table 3.4). Fig 3-14 shows the influence of the wind speed, of the ambient temperature and on the solar beam insolation. The influence of the wind speed is straightforward: the higher the speed, the lower the overall efficiency since the heat transfer coefficient from the collector to the ambient is increased. The same trend is stated for the beam insolation: a higher value makes the ambient losses of the collector proportionally smaller, and the overall efficiency is increased. The ambient temperature influences the cycle performance in two different ways: the ambient heat losses of the collector are increased with a lower ambient temperature, and the cycle efficiency is increased because of a lower condensing temperature. Fig 3-14 shows that this second influence is predominant: for a 3 to 30$°C$ evolution of the ambient temperature, the collector efficiency is decreased by 2%, while the ORC cycle efficiency is decreased by 15%, resulting in a 13% increase of the overall efficiency.

3.5 Conclusions

Small-scale solar Organic Cycles are well adapted for remote off-grid areas of developing countries. Compared to the main competitive technology, the PV collector, Solar ORCs have an advantage of

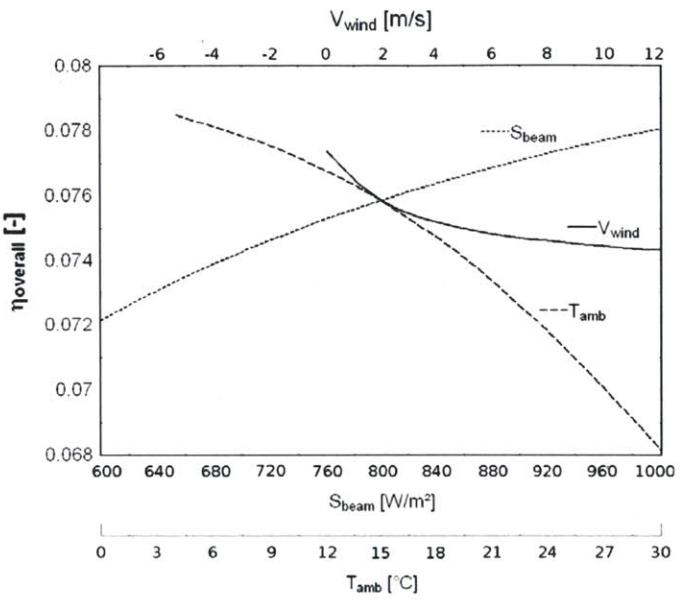

Figure 3-14: Influence of the working condition on the efficiency.

being manufacturable locally. They are also more flexible and allow the production of hot water as a by-product.

This work focused on the evaluation of the thermodynamic performance of the system. With conservative hypotheses, and real expander efficiency curves, it was shown that an overall electrical efficiency between 7 and 8% can be reached. This efficiency is a steady-state efficiency at a nominal working point. In order to evaluate the yearly energy output, a dynamic model is needed. In particular, the behavior of the storage tank should be modeled to perform a one-year simulation.

It should be noted that these calculations were performed for off-the-shelf components, especially the expander, whose combined electro-mechanical efficiency did not exceed 60%. Components specifically developed for the target applications (e.g. a high volume ratio expander, optimized for the ORC working fluid) could significantly increase the system performance.

The comparison between working fluids showed that the most efficient fluid is Solkatherm. However, it is also the fluid requiring the highest expander swept volumes, which increases the cost of the system. R245fa also shows a good efficiency and has the advantage of requiring much smaller equipment.

Even though part-load conditions were not simulated in the present work, the proposed model allows computing the performance of the system for a wide range of working and ambient conditions.

Chapter 4

Component testing and Validation of the SORCE solar ORC model

Parts of this chapter are drawn from the EUROSUN 2010 conference proceedings paper "SORCE: A Design Tool for Solar Organic Rankine Cycle Systems in Distributed Generation Applications" with co-authors Sylvain Quoilin and Harold Hemond [117]. As this paper was preliminary to the work of Chapter 3, some redundancies are excised and what follows is an extension of the work to include more detailed information on thermal storage and preliminary model validation using experimental systems.

EUROSUN 2010 Abstract

Recent interest in small-scale solar thermal combined heat and power (CHP) power systems has coincided with demand growth for distributed electricity supplies in areas unserved by centralized power stations. One approach to meeting this demand is the parabolic trough solar thermal collector coupled with an organic Rankine cycle (ORC) heat engine. Much existing research touches on aspects of the underlying physics and mechanics of this technology, but a holistic treatment including economic evaluation is lacking. Design and analysis tools are needed to specify the solar collector and power block configurations for meeting performance and financial targets for a range of applications in disparate environments. In this paper we present the Solar Organic Rankine Cycle Economic (SORCE) model combining semi-empirical multi-physics computation modules for solar resource and site environmental characterization along with optical, thermal and electromechanical performance prediction of trough collectors and ORC systems with technical specifications and costs of standard system equipment. The model is tested with data from experimental solar ORC systems at MIT and deployed in Lesotho, southern Africa (29°12'48.44"S, 27°51'37.36"E). SORCE is available for download as an executable program derived from Engineering Equation Solver (EES) that enables site-specific evaluation of a solar ORC system for performance and cost comparison with alternatives (e.g. wind, solar PV, diesel, etc.).

4.1 Introduction

The demand for distributed energy supplies is growing globally at an unprecedented rate. In areas of the developing world where service from centralized power stations is unreliable or unavailable, the relatively high cost of power generation using diesel fuel (>\$0.50 kWh^{-1}) or photovoltaic (PV)

(>\$0.30 kWh^{-1}) systems has motivated the search for alternatives, e.g., the scaled-down solar thermal power plants of this study.

A solar ORC power generation system is conceptually similar to the many steam Rankine solar thermal power plants in operation around the globe, with the exception of scale: an ORC is potentially advantageous well below the range of currently planned commercialized installations. At the time of writing the only commercial solar thermal using the ORC is the 1 MW Saguaro Solar ORC plant in Arizona, USA. Technical variations employed at a small scale are driven by cost considerations and may include differences in the operating thermophysical regimes, the apparatus geometries and materials, working fluid selection, and system component (heat exchanger and fluid machinery) size and type. Design and analysis tools are useful for specifying the solar collector and power block configurations to meet performance and cost targets. Several investigators have made an economic analysis of a particular ORC system, e.g., [27, 133], but relatively few attempts have been made to create explicit integrated thermo-physical and economic models for an ORC system using some specified or unspecified thermal source [143, 102]. To date no comprehensive general model (including thermodynamic, mechanical, electrical and economics components) for a solar thermal driven ORC, with its unique thermal source fluctuation characteristics, has been developed. To bridge this gap, we introduce here a physical and economic model, called SORCE (Solar Organic Rankine Cycle Economic model), developed in the context of a research scale 3kW Solar ORC for distributed power applications.

4.2 SORCE Model Overview

The main modules in the SORCE model include numerically solved systems of equations for calculating the following:

1. Available solar energy at a user-specified location
2. Stepwise energy conversion to electricity through optical and thermal apparatus in the solar ORC

Relevant parameters (Fig. 4-1) are specified via a graphical user interface (GUI) in the diagram windows of Engineering Equation Solver. SORCE modules are based on equations and approaches derived from several literature sources, especially [59], combined with empirical datasets and regressions for phenomena, e.g., cloud cover, fluid machinery isentropic efficiency, and generator electromechanical efficiency, that are computationally intensive to model. The output of these semi-empirical multi-physics modules are referenced to industry and literature-derived cost data for the specified materials and components, enabling cost assessment on a capital (\$) or specific cost (\$/kW) basis. In its most basic default configuration, a user of SORCE can specify a location on earth, and the program will calculate the efficiency and power output for a 3kW Solar ORC which is scaled to an average daily energy output (by multiplying by average time between sunrise and sunset). Annual outputs are extrapolated from the average daily output and levelized cost calculations are performed using user input parameters such as project lifetime, fraction of labor costs, and discount rate. An advanced user can manipulate the variables in the diagram window to explore alternative configurations of system size, working fluids, temperatures, collector geometries, expanders, etc. and likewise calculate relevant parameters such as performance, cost, and specifications for major equipment (e.g. heat exchange area and parasitic power consumption).

SORCE comprises multiple sub-modules that are explained in more detail in the following section. Although EES is a non-ordered simultaneous equation solver, the SORCE program conceptually begins with a solar resource calculation, then passes that information into a solar collector

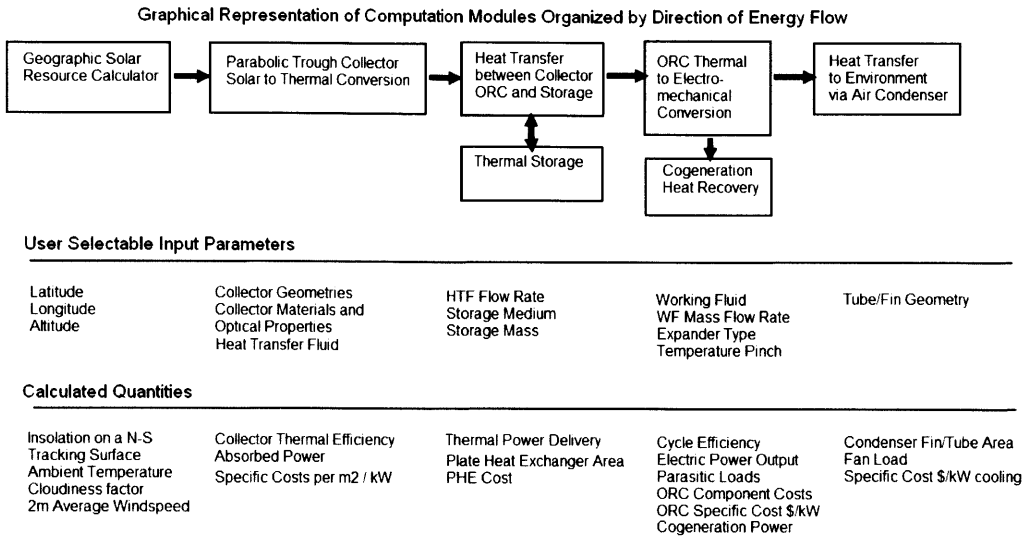

Figure 4-1: User defined SORCE inputs and calculated outputs

module which calculates a heat gain in a heat transfer fluid. The final node temperature of the collector module is the start node temperature for the storage/buffer module, which creates a temperature profile in the packed bed; the last node temperature of the HTF in the packed bed is the input temperature for the ORC module. The ultimate difference between the ORC output temperature and the initial temperature for the solar collector module reflects the residual in the energy balance indicating whether the storage/buffer unit is charging or discharging. Finally note that, while SORCE was developed in EES, it is also available for download as a free standalone Windows-executable program online at [115]. In addition to the executable program, a detailed document displaying all formatted equations and logic used in SORCE, and listing appropriate references, is available at [114].

4.3 SORCE Reference System

The SORCE model is intended to be a general and open source platform for calculating the quantities of interest and predicting the performance of a small scale Solar ORC. In practice, the range of design parameters and potential configurations possible in this complex type of system are fairly extensive, and a comprehensive model can only be defined for a system within reasonable limits. SORCE was co-developed in the context of an engineering design process for a prototype 3kW Solar ORC system, and the computational model reflects the major design decisions: e.g. parabolic trough collectors, positive displacement expanders, etc. SORCE can readily be used to explore alternative configurations and scales to about 10kW; however, profound departures from the reference case require consideration of implicit assumptions within the system of equations that may be invalidated e.g. maintaining the heat transfer fluid (glycol or Therminol 55) below its boiling point, capacity of available HVAC expanders, etc.. To explore e.g. alternative concentrator architectures or power block devices the program should be altered by the user to model the changes appropriately. The reference 3kW$_e$ Solar ORC prototype is described in [119] and has the following features:

1. Location - 29°12'48.44"S, 27°51'37.36"E (Matjotjo Clinic in Berea District of Lesotho)

2. Solar Collector - 75m^2 single-axis parabolic trough with a 150°C design operating point, using Miro aluminum reflectors and a Heat Collection Element (HCE) with an air-filled annulus between absorber pipe and glazing. Solec Hi/Sorb II selective coating is used on the absorber pipe [?].

3. ORC - Two stage expansion of R245fa using modified commercial HVAC compressors each with a fixed volume ratio of 2.8, brazed plate heat exchangers for high pressure heat transfer, and commercial HVAC air condenser coils for heat rejection.

4. Heat transfer fluid (HTF) - Monoethylene glycol (MEG) with thermal buffering in a 2.4 m^3 thermal storage tank with a packed bed of 19mm quartzite aggregate.

The piping and instrumentation diagram for an identical pilot system using SopoNova collectors at Eckerd College in St. Petersburg FL is shown in Fig. 4-2.

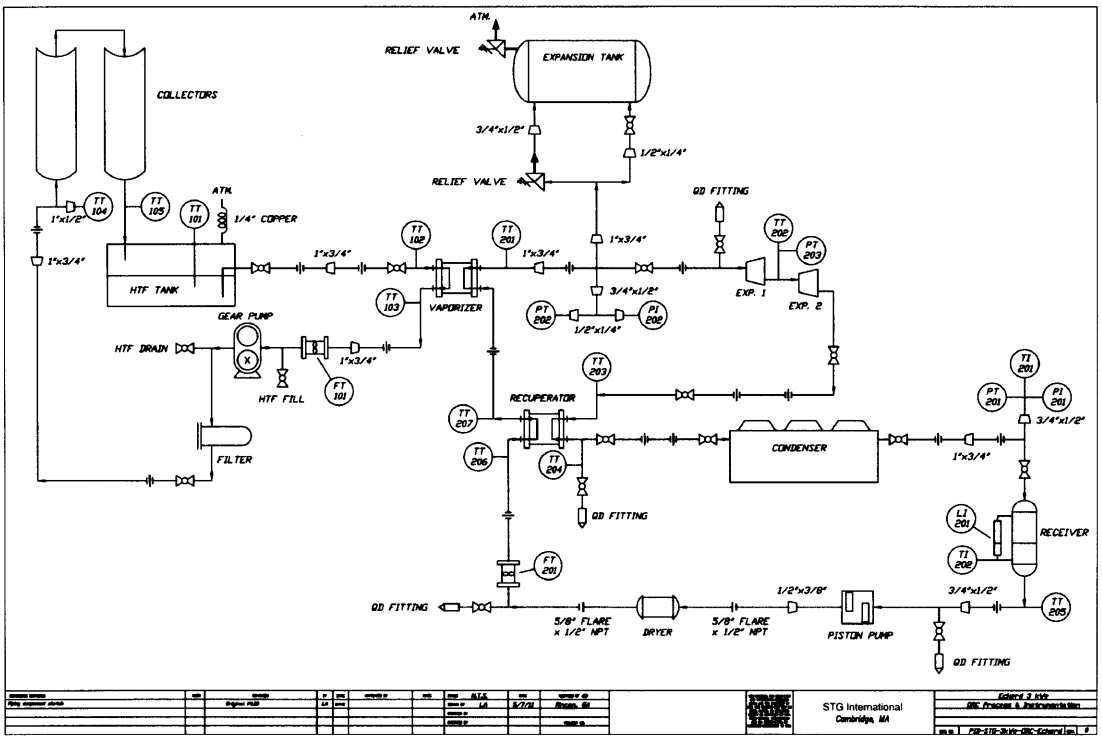

Figure 4-2: Piping and Instrumentation Diagram (PID) for 3kWe Solar ORC

4.4 SORCE Modules

4.4.1 Solar Resource Model

The initial task of SORCE is to calculate the amount of beam radiation available to a single-axis tracking (N-S axis) surface at an arbitrary location. Input variables are latitude, longitude, altitude,

and time difference (in hours) from GMT. Starting from the solar constant and using well known geometric and trigonometric relationships for the earth's rotation and orbit around the sun [53, 90], the incidence angle and interposing air mass are calculated for the tracking surface on an hourly basis over the entire year. This results in an estimate for annual integrated insolation accounting for absorption in the absence of other (non air mass) atmospheric factors. The latter, particularly cloud cover, is estimated from a NASA meteorological dataset [8] for the specified location, and beam radiation is reduced accordingly. In addition to calculating average direct irradiance (W m^{-2}) and average duration of daylight (hours), the maximum and minimum beam radiation for the location is available for modeling at the extremes. The module also outputs average wind speed and local ambient temperature for use in computing heat loss in the collector module.

4.4.2 Parabolic Trough Model

The trough module, largely adapted from [59], accepts as inputs the minimum, maximum, or average insolation values calculated by the solar resource module. It then conducts a one-dimensional energy balance around a Heat Collection Element (HCE) of user-specified dimensions and materials, which is translated to the axial dimension of fluid flow through coupled sequential 1-D nodes. Radiation impinges on a reflector element with user input focal length, reflective coefficient, and aperture. The energy is correspondingly reduced (e.g. due to a reflective coefficient < 1) and concentrated onto a nodal area of the HCE, where it is transmitted through a glass envelope and a gas (or vacuum) annulus, and finally absorbed or reflected at the surface of the HCE. Depending on the absorptivity and emissivity characteristics of the user-chosen selective coating and the temperature of the HTF flowing through the HCE at a given node, some amount of absorbed energy is transferred through the HCE wall into the HTF via the appropriate heat exchange coefficient, calculated from the fluid thermal properties and flow regime parameters. The remaining absorbed heat is lost at the HCE outer surface, via either (1) radiation back through the annulus and envelope to the sky, or (2) convection through the annulus to the envelope, conduction through the envelope, and convection to the ambient air. This process is repeated for each node, where the input temperature for each node is the output temperature of the previous node, resulting in an overall enthalpy and temperature gain for the focal line length specified by the user. The collector module thus derives a thermal efficiency and outputs a heat flux and temperature gain for the HTF at the user-specified flow rate and initial temperature. The collector module can be used with parameters for commercially available medium temperature collectors such SopoNova and NEP1200 as well as collectors designed by STG for the pilot system in Lesotho in N-S or E-W tracking orientations. The dimensions corresponding to the STG parabolic trough collectors (E-W tracking, focal point axis of rotation) at the reference site are shown in Fig. 4-3, and the HCE dimensions are listed in table 4.1.

4.4.3 Storage/Buffer Model

The thermal capacity of a small Solar ORC is too low to prevent large temperature swings during insolation transients (e.g., a passing cloud), which can be problematic for stable ORC operation. To overcome this, additional thermal buffering capacity is needed, e.g. in the form of a tank of HTF or, to save on the cost of HTF, a tank partially-filled with inexpensive but high thermal capacity filler material such as quartzite rock (Fig. 4-4). Alternative buffering or storage technologies (phase change materials, concrete, etc.) have been extensively reviewed in the literature [66], however cost is currently minimized with a packed bed implementation. The essential principle of the storage module is an implementation of the Schumann equations described in [53] for heat transfer between a fluid and solid matrix, assuming constant solid properties, 1D plug flow and no temperature

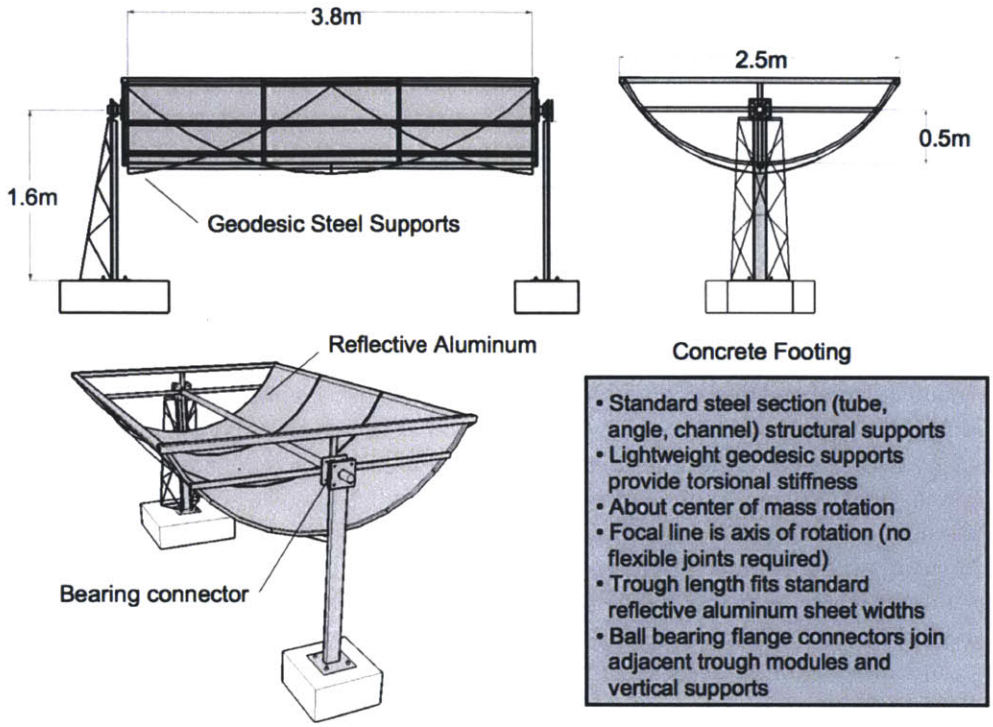

Figure 4-3: Solid model and description of STG parabolic troughs constructed for Matjotjo pilot solar ORC. Drive mechanism (not shown) is a 100:1 24VDC 1725RPM 0.75kW worm gearmotor with 3:1 ANSI #40 final chain drive

Table 4.1: Dimensions for STG parabolic troughs deployed at Matjotjo health clinic

HCE Envelope	**Diameter[m]**
Absorber ID	0.053
Absorber OD	0.065
Glass ID	0.08
Glass OD	0.088
Collector	**Attribute**
Reflectance	0.91
Axial Length	30 [m]
Focal Length	0.5 [m]
Tracking	E-W

gradients within the solids:

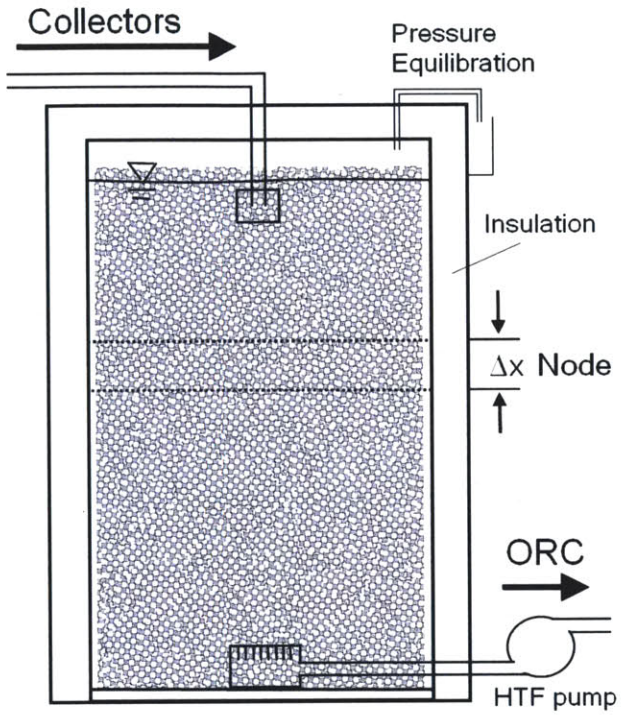

Figure 4-4: Cutaway view of an unpressurized packed bed thermal storage tank using rock solids and thermal oil in the void space. The tank is modeled as a 1D axial plug flow control volume divided into nodes of Δx where $\Delta x = \frac{height_{tank}}{\#_{nodes}}$.

$$(\rho C_p)_f \epsilon \frac{\delta T_f}{\delta t} = -\frac{(\dot{m} C_p)_f}{A} \frac{\delta T_f}{\delta x} + h_v (T_s - T_f) \tag{4.1}$$

where ϵ is the porosity, h_v is the volumetric heat transfer coefficient between solid and fluid, and the timestep t is derived by relating flow through a single node to the node volume:

$$t = \frac{vol_{HTFnode} \cdot \rho_{HTF}}{\dot{m}_{HTF}} \tag{4.2}$$

This is frequently modeled using air as the working fluid [131], however in this case where thermal oil is used, the fluid heat capacity term cannot be neglected [101]. Furthermore, the infinite number of transfer units (NTU) assumption is made following the observation of [70] that the performance ratio of a finite to infinite NTU bed converges to unity for NTU >25 and is above 0.95 even at a NTU of 10.

$$NTU = \frac{h_v V}{\dot{m}(C_p)_f} \tag{4.3}$$

Table 4.2: Parameters for the storage tank in the reference system

Storage Tank Parameter	Value	Units
Number of nodes	10	
Porosity	0.3	$\frac{m^3}{m^3}$
Quartzite conductivity	6.4	W m^{-1} K^{-1}
Quartzite diameter	19	mm
Tank height	2.2	m
Tank Diameter	1.2	m
Insulation	20	m

For a high conductivity, small diameter solid, temperature gradients within bed particles and pore volumes can be neglected and the infinite NTU assumption is justified for the purposes of establishing a computationally efficient storage tank energy balance and temperature profile. The equilibrated temperature at each consecutive node *i* is then determined through Equation 4.4:

$$T_i = \frac{T_{i-1} \cdot \dot{m}_{HTF} \cdot Cp_{HTF} \cdot timestep + T_{sop,i} \cdot m_s \cdot Cp_s}{\dot{m}_{HTF} \cdot Cp_{HTF} \cdot timestep + m_s \cdot Cp_s} \tag{4.4}$$

The user defines tank geometry, porosity, and the number of nodes to use in calculations. For the reference case the values are listed in Table 4.2. The module accepts the collector final output temperature as the charging temperature, develops the thermal profile during charging, operation, and discharging, and provides an outlet temperature as the implied stable input to the ORC. The height of the tank is added to the collector piping head losses for the HTF pump work calculation.

4.4.4 ORC Model

SORCE handles the conversion of heat into electricity in the ORC module according to the structure of the classical Rankine cycle: isobaric heat addition, isentropic expansion, isobaric heat rejection, and isentropic pumping. Real gas properties of the working fluid are accessed from fundamental equations of state (EoS) within the internal libraries of EES (e.g. the reference fluid is R245fa, with an EoS derived from [91]). The initial process is treated as a 3-zone (superheated, vaporizing, and preheating) transfer of energy in counterflow plate heat exchangers from the HTF into the ORC working fluid with empirical heat transfer correlations developed for refrigerant [150]. The user selects both the working fluid and mass flow rate (roughly proportional to the desired power output) and establishes the ORC high temperature and degree of superheat, which (in conjunction with the ambient temperature identified in the Solar Resource module) determines the overall energy conversion potential within the finite heat transfer framework of the Curzon-Ahlborn modified Carnot efficiency [62].

Using the outlet temperature of the storage model as input, the ORC module first calculates the area of heat exchanger necessary for superheat, vaporization and preheating and then determines the heat consumption rate of the ORC and the final HTF output temperature. SORCE allows the user to select the expander unit from a list of HVAC compressor models (from the Copeland ZR family); the fixed volume ratio and displacement of the compressor determines the extractable power and RPMs of the machine. Depending on the specific volume ratio of the working fluid and the operating temperature regime, two stages of expansion may be indicated. The module calculates the thermal state of the working fluid bracketing each process in the Rankine cycle, determines the required area of recuperator (used for recovery of superheated expander exhaust in cogeneration or

recycling to the ORC) and air condenser for heat rejection, and imputes the parasitic loads from the condenser fans and from the HTF and working fluid pumps using a combination of regressions (from manufacturers data) and head calculations using empirical pump isentropic efficiencies from [96].

Note that dry cooling is currently specified in SORCE as water may be scarce in remote environments where a Solar ORC is suitable. As such, commercial HVAC air condensers are integrated into both the reference system and SORCE model [130]. A subroutine calculates the pressure drop in the vapor manifolds as a function of length and pipe diameter. In addition to providing these practical metrics (heat exchanger areas, manifold diameters, expander-generator ratings, etc.) for sizing and selection of system components, figures of merit are derived including ORC cycle efficiency, net power output, and daily and annual energy production.

4.4.5 Economic Modeling

The cost of the Solar ORC is developed from summation of a set of equations relating the costs of individual components to a relevant physical parameter, e.g. focal line length or heat exchanger area. These equations represent the components forming the largest fraction of systems costs and are either regressions or linear relationships derived from a bill of materials from the reference system (under construction in southern Africa) or data from manufacturer quotations. Most system components (compressors, reflective sheeting, structural steel, heat exchangers, etc.) are globally standardized products with a cost function reflecting underlying commodity prices (steel, copper, etc.), and it is assumed that these costs will not vary significantly from one location to another. This assumption breaks down as a function of distance from the global supply chain, which will incur additional and difficult to model logistics costs. The labor fraction of the system materials costs is a user defined variable, as labor costs are expected to be highly site-specific (the value for the reference system is about 0.25).

4.5 Cost and Performance Outputs for Selected SORCE Configurations

Steady state application of SORCE (i.e. no thermal storage) indicates specific costs (a 15 year Levelized Cost of Electricity (LCOE)) for the $3kW_e$ reference system of under \$0.25/kWh, which compares favorably with PV systems. Comparison of SORCE results for the reference system in selected locations, in 3, 5, and 10 kWe configurations, is shown in Fig. 4-5.

In this comparison of power rating configurations across geographic locations, it is possible to see the effect of both insolation variance and system scale on LCOE. As expected, an increase in either insolation or scale of power output corresponds to a decrease in specific costs. Other figures of merit (footprint, efficiency, etc.) can be compared across locations, and the physical characteristics of the systems themselves (collector geometries and materials, ORC operating conditions, etc.) can be manipulated in the model to achieve the desired simulation of planned or existing solar ORC systems. In general, results from SORCE indicate that the solar ORC approach can be cost competitive with diesel-fuel based generation and with photovoltaics in areas of high direct normal irradiance (DNI). Although lower sunlight to electricity conversion efficiencies (about 5%) necessitate greater land requirements in comparison with PV, this may not be a constraint in remote areas. The benefit of cogeneration implicit in solar thermal power may also promote Solar ORC technology as an approach to distributed generation. The current default role of recuperated heat in SORCE is recycling

Power Output	Focal Line Length [m]	Collector Area [m2]	HTF Flow rate [gpm]	R245fa Flow rate [kg/s]	Expander Inlet T [C]
3kWe	30	75	6	0.155	132
5kWe	60	150	10	0.31	132
10kWe	120	300	18	0.58	132

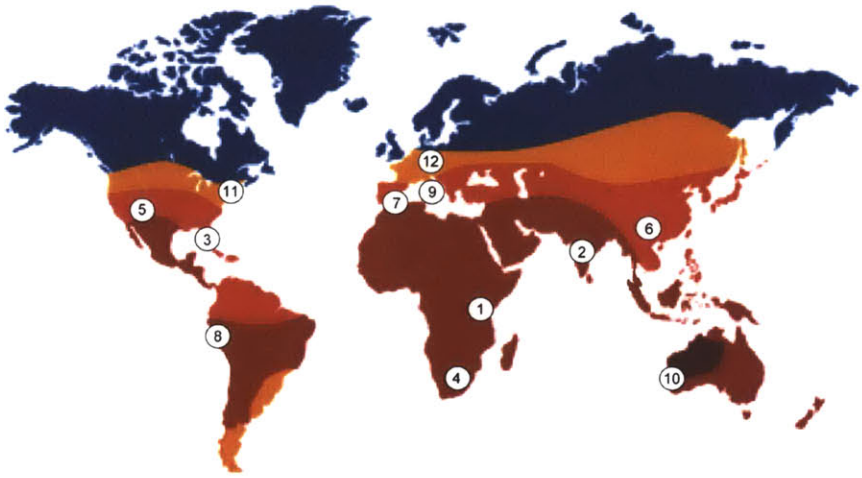

15-year LCOE of 3-10 kWe-scale Solar ORC [$/kWh]

	Location	3kWe	5kWe	10kWe	Lat	Long	Elevation [km]	Time zone
1	Nairobi, Kenya	0.21	0.13	0.11	-1.28	56.73	1.69	UTC+3
2	Bangalore, India	0.19	0.14	0.12	13.042	77.395	0.84	UTC+5.5
3	St. Pete, USA	0.24	0.16	0.13	27.77	82.64	0	UTC-4
4	Berea, Lesotho	0.21	0.17	0.14	-29.21	27.86	1.5	UTC+2
5	Pheonix, USA	0.27	0.17	0.14	3.45	-112.08	0.333	UTC-7
6	Kunming, China	0.31	0.18	0.15	25.037	102.72	1.9	UTC+8
7	Almeria, Spain	0.3	0.18	0.15	36.84	2.467	0.102	UTC+1
8	Lima, Peru	0.34	0.2	0.16	-12.04	-77.02	0.355	UTC-5
9	Rome, Italy	0.43	0.24	0.18	42.016	12.135	0.121	UTC+2
10	Perth, Australia	0.56	0.27	0.2	-31.96	115.86	0	UTC+8
11	Boston, USA	0.61	0.37	0.26	42.35	-71.06	0	UTC-4
12	Nuremburg, Germany	not viable	1.97	0.63	49.45	11.074	0.605	UTC+2

Competitive with Solar PV
Competitive with Diesel Power Generation
Not economically viable

Figure 4-5: Levelized electricity cost for selected size configurations across geographically variable meteorological conditions.

within the ORC, but this heat quantity could alternately be delivered to domestic hot water, heating, or absorption cooling end uses (see Chapter 2).

4.6 Model Component Validation Examples

Verification of the results of the global model is pending, awaiting completion of the reference system in southern Africa as well as the test facility at Eckerd college in St. Petersburg FL; however, many aspects of SORCE have been experimentally tested at the module and component level.

4.6.1 Fluid Machinery Experimental Validation

In particular, the model is very sensitive to parameters used for fluid machinery isentropic efficiency. In developing a low cost, small scale ORC the lack of suitable purpose built equipment necessitated the adaptation of available components from existing applications. In this case the thermo-mechanical characteristic of the machinery is not known. Our approach involved benchmarking candidate machines on test rigs to develop type curves and parameterize the model. The default model parameters are thus derived from the best results of component testing at an experimental ORC facility installed at MIT (Figs. 4-6 and 4-7, also described in [119]). Temperature measurements are taken using type T thermocouples ($\pm$ 0.8°C accuracy) inserted into probes at the flow stream centerline. Flow measurement is with Blancett Model 1100 turbine flow meters ($\pm$ 1% accuracy) and pressure measurement is with Honeywell 13mm Series temperature compensated isolated sensors ($\pm$ 0.1% full scale) 0-500 psig on the high pressure side and 0-300 psig on the low pressure side. Power is measured with an Acuvim II three phase power meter with 100:1 current transducers (IEC 62053-22 Class 0.2s accuracy $\pm$ 0.2%). Manually switchable resistive loads are used to vary the output of the generators, which are self–excited through the use of delta-wired capacitors according to the specifications of [135]. Data acquisition is via an Iotech Personal DAQ/55 with temperature compensation for thermocouple inputs. Working fluid pumps were tested on a separate rig described in [96], and the most efficient (81% isentropic) pump candidate (Fig. 4-8 from [96]) (a plunger type) was incorporated into the ORC design.

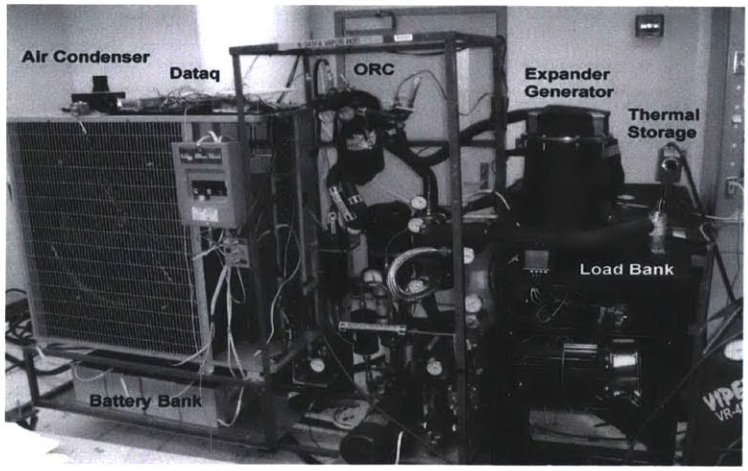

Figure 4-6: MIT ORC test rig 2010 with major components labelled. A piping and instrumentation diagram for the test rig is shown in Fig. 4-7

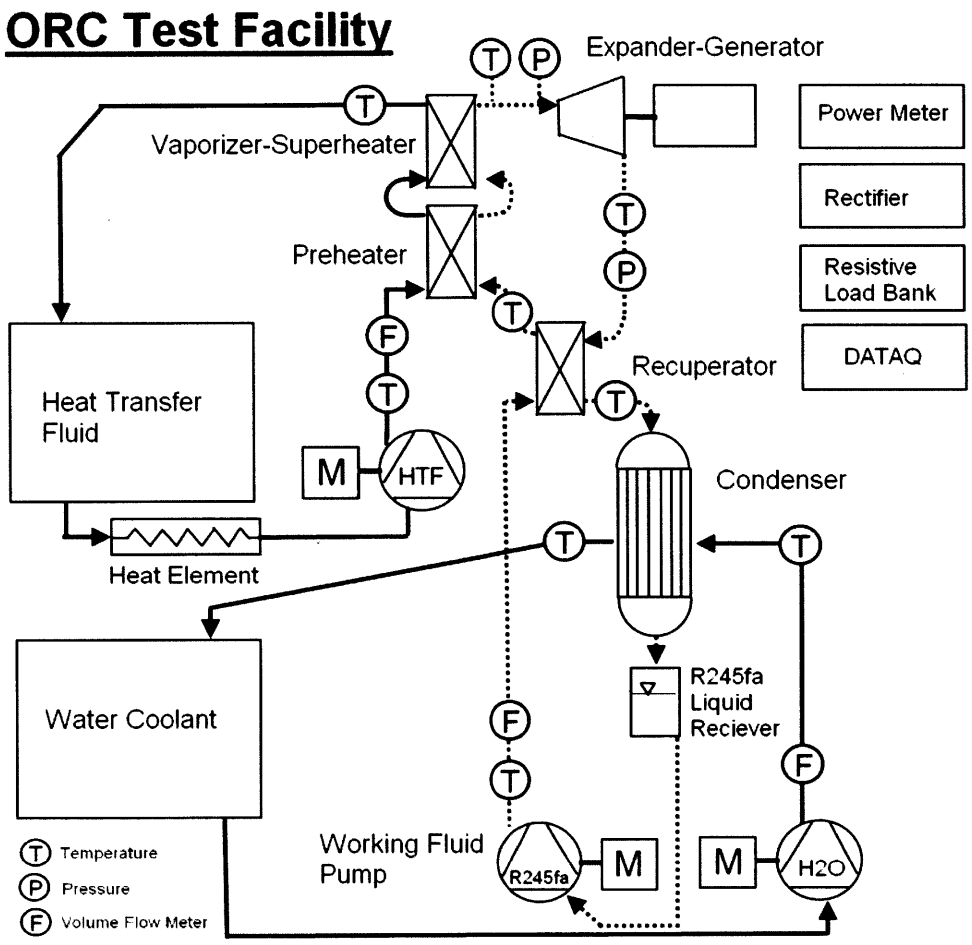

Figure 4-7: Piping and Instrumentation Diagram for ORC test facility at MIT in 2010. The HTF pump used is a Shuflo NG11Y–PH, and the working fluid pump is a Hypro 07302 plunger type. Pump drives are LEESON 1750 RPM 1.5hp NEMA 56 0–180VDC speed controlled motors. Heat exchangers for the recuperator, preheater and vaporizor–superheater are ITT compact brazed plate, and the condenser is an ITT shell-and tube with the working fluid in the shell and H_2O coolant in the tubes. Dotted lines indicate the ORC working fluid circuit, solid lines indicate heat transfer fluid circuits.

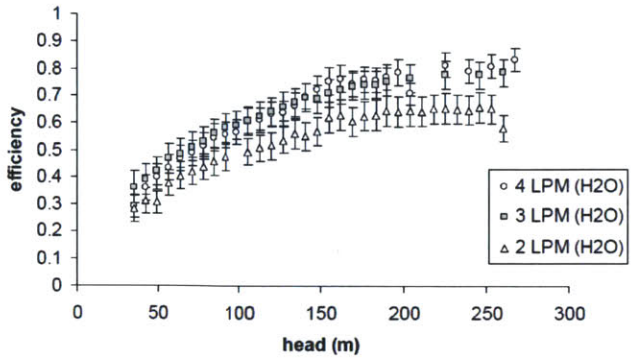

Figure 4-8: Isentropic efficiency as a function of head (in meters of H_2O) and flow rate (Liters per minute of water) for ORC working fluid pump (plunger-type) from [96]

The most significant fluid machine in the ORC is the expander, in our case a scroll compressor (Fig. 4-9) modified to work in reverse as an expander. The modifications include:

1. Separate the hermetic unit into re-sealable halves (using welded flanges)
2. Remove check valves and bypass valves
3. Optimize pressure port and support sealing piston with springs
4. Re-port the pressure vessel
5. Re-seal the unit

To demonstrate the practicality of repurposing HVAC equipment for an ORC expander application we tested various examples of the ZR family of scroll compressor manufactured by Copeland. The displacement in expander mode and motor nameplate rating were derived from catalogue datasheets and are tabulated in Table A.1 in Appendix A. Scroll compressors are coupled with an induction motor which can be used as the generator, meaning that the isentropic efficiency is imputed after factoring the generator efficiency (see section 4.6.2). The machine's capacity for compressor work (in a traditional refrigeration role) is large compared to its capacity for expander work with R245fa at the temperatures found in a solar ORC. This means the motor is oversized in comparison with the expander generator requirements, and part load operation tends to result in lowered mechanical to electrical conversion efficiency (see Fig. 4-17). Replacement of the motor with a capacity matched unit was not pursued in this study. The generator in a hermetic expander operates in the stream of superheated working fluid exhausted from the expander (typically 70-85°C), as opposed to e.g. a motor working at ambient temperature, but with limited convective heat transfer. In this study the relationship between generator operating temperature and efficiency was not quantified, but we note that it is likely to be influential.

For a dataset of n=122 stable operating points (measurements listed in Table A.2) the power output from the expanders is linearly correlated to the mass flow of the cycle (Fig. 4-10) as expected. The instrinsic volume ratio of the expanders (about 2.8) also dictates an efficiency curve with shoulders due to over and under expansion losses (Fig. 4-11).

One object of benchmarking scroll expanders is to derive a semi-empirical isentropic efficiency coefficient for use in the sizing and prediction SORCE model. For the same dataset, an isentropic

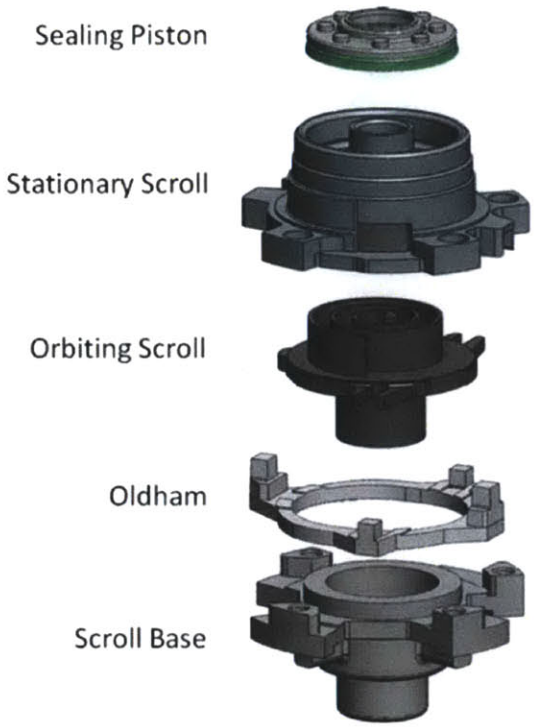

Figure 4-9: Exploded view of the working parts of a scroll compressor, from [65]

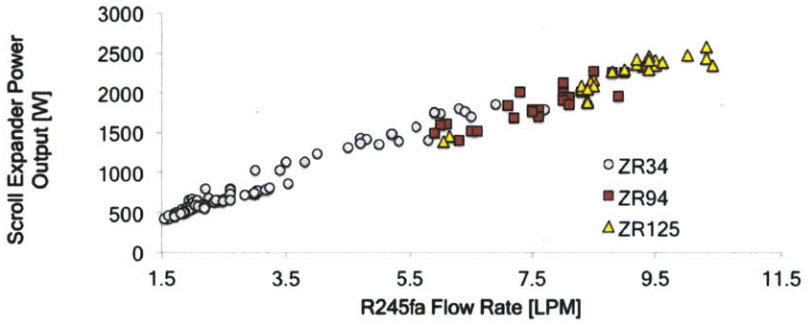

Figure 4-10: Measured power output and volumetric flow rate for three tested ZR scroll expanders. Error bars are small, and obscured by the data symbols.

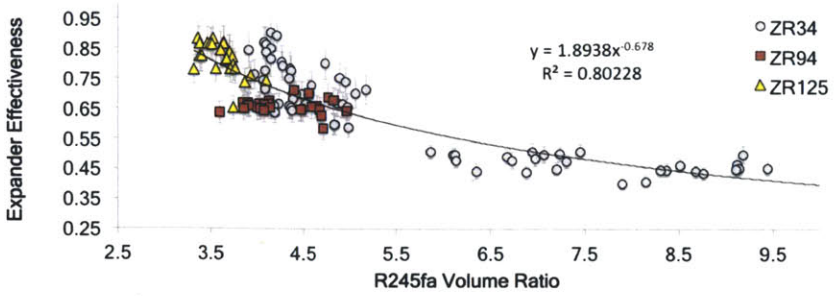

Figure 4-11: Expander effectiveness (accounting for generator losses) and working fluid specific volume ratio imposed on the expander between the suction and discharge ports (i.e. due to the interaction of the working fluid flow rate, the heat added prior to the expander, the expander displacement, RPM and volumetric efficiency, and the condensing pressure). The intrinsic ratio of the compressors is about 2.8, and the expected decrease in efficiency with volume ratio due to underexpansion losses is observed. The best fit is a power curve $R^2 = 0.80$

efficiency of 81% was calculated by estimating the generator efficiency from Fig. 4-17 and minimizing the variance between predicted and observed power output (R^2 = 96) of two individually tested hermetic expanders based on ZR34 and ZR125 compressors shown in Fig. 4-12.

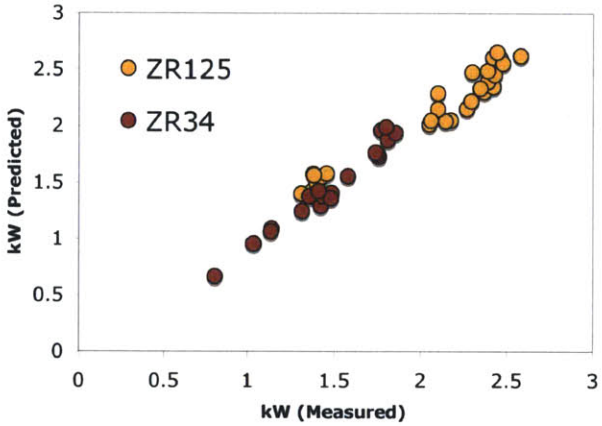

Figure 4-12: Power output as predicted by SORCE and measured on the ORC test rig. An empirical isentropic efficiency coefficient of 0.815 for the Copeland ZR series was found by minimization of the variance (R^2=0.96) between predicted and measured power under various operating regimes. The coefficient includes the generator derating function of Fig. 4-17.

These expanders were then tested in two stage configuration with the ZR34 operating between the high pressure vaporizer exhaust and the ZR125 operating between the ZR34 and the recuperator/condenser. Measured and modeled results are shown in Fig. 4-13.

At part load conditions the model overpredicts measured performance, but at close to full load (the cycle is targeted to produce 3-4kW$_e$) the relative error closes to within 10% (Fig. 4-14). We conclude that operation of a two stage scroll expansion is relatively more sensitive to part load inefficiencies than a single stage expansion, but a two stage configuration can better exploit a 100°C

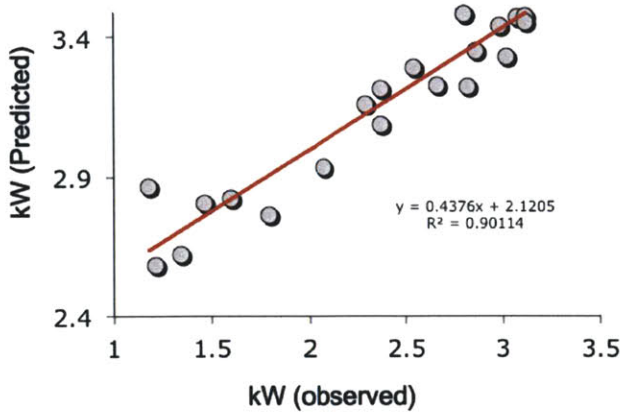

Figure 4-13: Power output as predicted by SORCE and measured on the ORC test rig for 2-stage series expansion using hermetic expanders.

temperature differential in a solar ORC using HVAC machines.

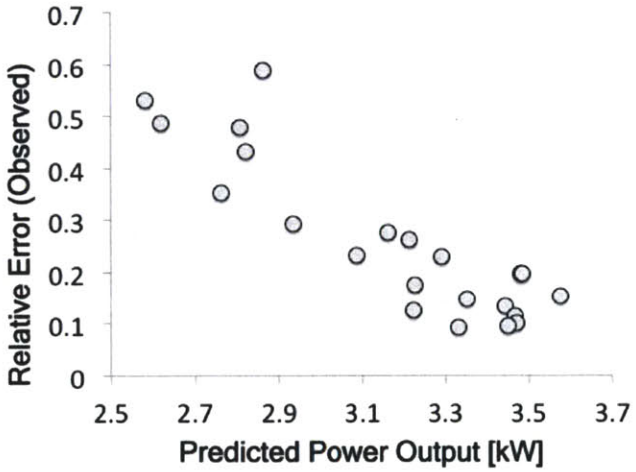

Figure 4-14: Relative error in observed power output compared to predicted power output. Error is minimized at full loading of the expander-generators.

Results of initial testing of the second stage (ZR144) of a 3kW$_e$ ORC built in partnership with the Government of Lesotho's Appropriate Technology Services and STG International (photo in Fig. 4-15) is shown in FIg. 4-16. The design thermal input is 40kW$_t$ at 150°C, and model and observed results converge above 30 kW$_t$. The electrical output of the expanders is routed through a 3 phase variac transformer, a rectifier, and DC to DC converters. Note that the top scroll expander stage was bypassed in this test, and full power thermal operation was not achieved due to time constraints during two days of on-sun testing. Tabulated sensor data for this test is available in Appendix A.

Figure 4-15: 3kW$_e$ ORC built in Lesotho in partnership with ATS and STG.

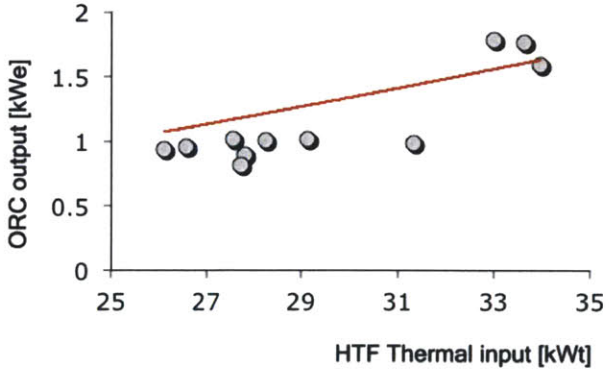

Figure 4-16: Second stage (ZR144) ORC electrical output as a function of HTF thermal input. Red line indicates SORCE predictions. $R^2 = 0.43$

4.6.2 Generator Efficiency

Induction generator performance for a representative (2.2 kW Leeson 3ϕ) machine has been characterized using a dynamometer facility at MIT's Laboratory for Electromagnetic and Electronic Systems (Fig. 4-17). The leading power factor for generator excitation was supplied with delta connected capacitors (50-67.5 μF) sized according to the method described in [135].

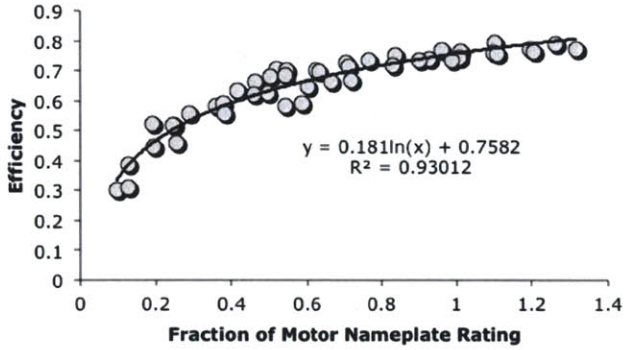

Figure 4-17: Leeson 2.2kW Induction machine mechanical to electrical efficiency as a generator, normalized as a function of motor nameplate power.

At full load the induction generator can reach 80% mechanical to electrical conversion efficiency. At below 30% full load the efficiency drops steeply, according to a function where the best fit to the data is logarithmic (Fig. 4-17).

4.6.3 Validation of Parabolic Trough Solar Collector Module

The 1-D parabolic trough solar collector model developed by has been validated for high temperature collectors using data from the SEGS plants and NREL [59]. In our application we modify this model to reflect the parameters of medium temperature, smaller aperture collectors having an air-filled rather than evacuated annulus in the HCE (i.e. the thermal resistance circuit is modified to include convection in the annulus in addition to radiation). To validate the collector submodule for our equipment an experimental campaign was carried out on medium temperature parabolic trough collectors.

Experimental Parameters

The solar collectors tested are NEP 1200 (Fig. 4-18), arranged in an East/West axis (zenith tracking) orientation using 8 modules in 4 rows for 230.4 m^2 total collector aperture. The geographic location is Almeria, Spain (latitude 37°5'35.39"N longitude 2°21'16.66"W). The Heat Transfer Fluid (HTF) is Therminol 55. Further specification of the collector apparatus is available in [113]. Inlet and outlet HTF temperature measurements are obtained by PT 100 (RTD) sensors (BS1904 class A $\pm$0.15°C), and these measurements, along with the volume flow rate [m^3 hr^{-1}], Direct Normal Irradiance (DNI) [W m^2], ambient temperature [°C], and windspeed [m s^{-1}] are digitally acquired by previously established online measurement systems at Plataforma Solar de Almeria (PSA) in Spain [10].

Figure 4-18: NEP solar collector field at Plataforma Solar de Almeria, Spain

Experimental Methods

To avoid uncertainties related to potential flow imbalance between the parralleled rows, a single row (2 x 28.8m^2 modules = 57.6m^2) was tested. The object of the experiments is to obtain steady state measurements across a range of operating conditions and compare these results to the 1-D model of the energy balance between optical and thermal components of the collectors.

The following conditions are varied:

1. The Heat Transfer Fluid (HTF) temperature (100-170°C in 25°C increments)
2. The HTF flow rate (1-3m^3 hr^{-1} in 0.25 m3/hr increments)
3. DNI (850-937 W m^{-2} natural solar variation)
4. The effect of dust on the collectors is evaluated by testing them before and after cleaning.

Experimental Results

A total of 51 on-sun steady-state working points are measured from Sept 6-8th 2011 prior to cleaning the troughs. The measured and modeled data are tabulated in A.3 in Appendix A.

Parameterized 1-D Parabolic Trough Model

The NREL Forristal model was adapted to specifications of the NEP 1200 solar collector and implemented in Engineering Equation Solver (EES). The respective geometries and material properties of the parabolic optics and heat collection element (HCE) are specified within the NEP EES model. The geometries and reflective coefficient of the optics are derived from the equipment specification document [113], including a 0.89 reflective coefficient for the reflector and dimensions for the air annulus HCE glass envelope and steel absorber pipe. The absorber selective coating is black chrome. Temperature dependencies of Therminol 55 properties (heat capacity, density, and viscosity) are derived from best-fit curves using tabulated data from the manufacturer Solutia [136]. The

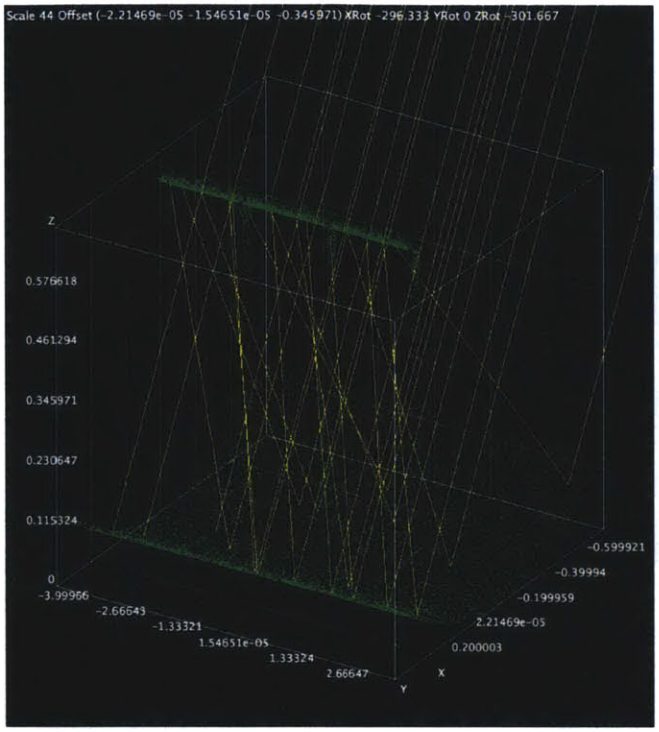

Figure 4-19: Raytracing plot of a section of NEP 1200 module rendered with SolTrace [152]

incidence angle θ is calculated based on dynamic earth-sun position equations from PSA, NREL and Duffie and Beckman [53]. A logarithmic incidence angle modifier (IAM) equation tailored to the NEP 1200 was developed using a ray-tracing program (Fig. 4-19) and measured dimensions of the HCE support bracket. The program ray intercepts are listed in Table A.5 in Appendix A. Superposed onto the regular cosθ losses, this approach approximates (slightly underestimates) the (proprietary) manufacturer supplied IAM graph [113].

$$IAM = 1 - 0.2114 \cdot e^{(-0.041 \cdot (90 - \theta))} \tag{4.5}$$

The EES model converges to a 1-D energy balance in a single node, accounting for optical and thermal losses (convection, conduction and radiation). The ΔT of the HTF as a result of thermal input is calculated for each node, where the resulting temperature of each node is passed through as the input temperature of the following node. The program uses 15 nodes, which in the case of the NEP 1200 loop examined results in a node length of 3.2 meters.

Model and Experimental Performance of Solar Collectors

The observed outlet temperature varies from 130-206°C and the ΔT for the collector ranged from 12-33°C during the experiments. Power output for the collector is calculated using the measured flow rates (converted from volumetric to mass flow using the density curve), temperatures, and the inlet and outlet heat capacities from the best fit curve. This method produces problematic results for flow rates below 1.5 $m^3\ hr^{-1}$: using the known area and the measured direct normal irradiance (DNI), thermal efficiency of the collectors exceed 100%. Assuming the methodology and physical property data are accurate, this indicates that one of the measured quantities is incorrect, e.g. temperature readings, DNI, or more likely the flow measurement. Temperature readings are corrob-

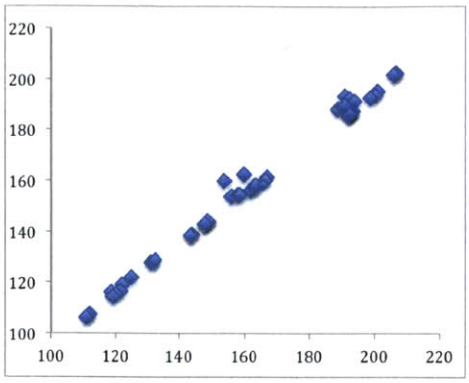

Figure 4-20: NEP 1200 array outlet temperature PT100 (y-axis) and row outlet PT100 (x-axis) in degrees Celsius. Since only one row of the array is being used, the measurements are redundant and consistent.

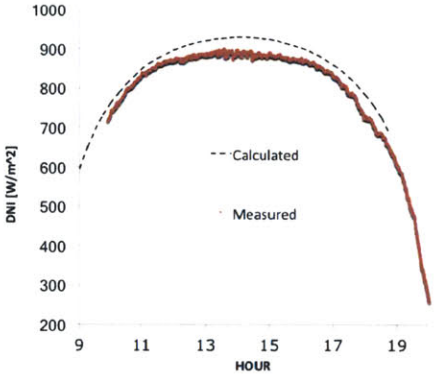

Figure 4-21: Predicted (the solar constant reduced by a calculated air mass via the incidence angle) and observed (online pyrheliometer) direct normal irradiance at Plataforma Solar de Almeria on 9/6/11

orated by sensor redundancy, as the row outlet temperature reading is virtually identical with the array outlet temperature reading (Fig. 4-20).

Faulty DNI measurement is unlikely given multiple calibrated cross-referenced pyrheliometers in use at PSA. In addition the DNI measurement tracks strongly with DNI prediction based on the solar constant, geoposition, and time of day, which also serves to validate the solar resource submodule of SORCE (Fig. 4-21).

This implicates error in flow measurement. It seems likely that the off-design low flow regime employed in the experiments in order to isolate a single row could be beneath the accuracy threshold for the flow sensor, or that absolute error negatively correlates to flow rate. Model and predicted results are more tightly correlated at flows above $1.5 m^3\ hr^{-1}$. To address this discrepancy our approach is to develop a flow rate correction to force overall energy conservation. This modification implies that the flow rate below $1.5 m^3\ hr^{-1}$ is actually lower than indicated by measurement. Using a 3rd order polynomial flow modification equation (Eq. 4.6) to compensate, the 1-D model can closely predict (R^2=99) the outlet temperature of the NEP 1200 (Fig. 4-22).

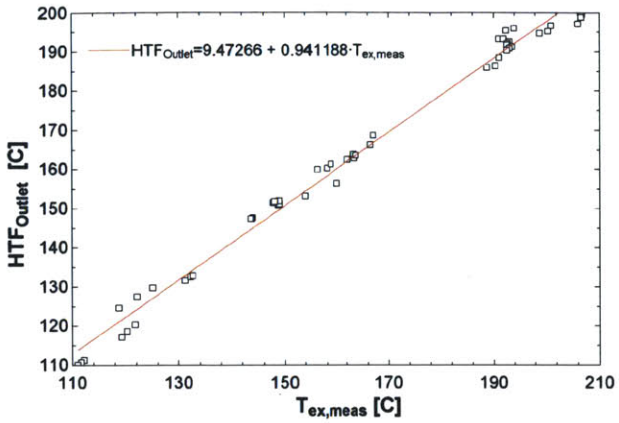

Figure 4-22: SORCE model predicted (y-axis) and the measured (x-axis) HTF outlet temperature for the 57.6 m^2 NEP solar parabolic trough row for the data tabulated in Appendix A

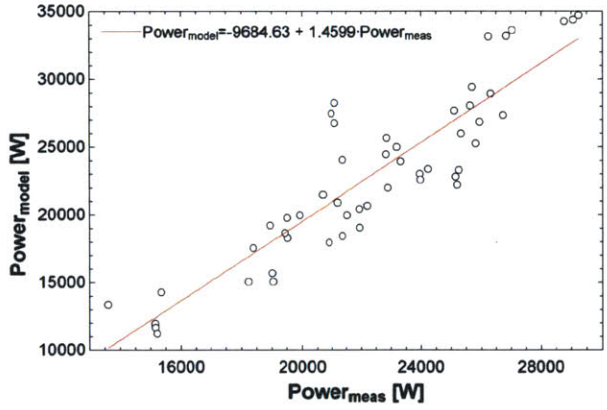

Figure 4-23: SORCE model predicted (y-axis) and measured (x-axis) thermal power (Watts) for the 57.6 m^2 NEP solar parabolic trough row for the data tabulated in Appendix A

$$Flow_{factor} = \frac{1}{-0.475 \cdot v_{dot}^3 + 3.5227 \cdot v_{dot}^2 - 8.5822 \cdot v_{dot} + 7.9} \tag{4.6}$$

Because the temperature difference is multiplied by the heat capacity (enthalpy change) and flow rate (Eq. 4.7), small differences in predicted and measured temperature lead to larger discrepancies between predicted and measured power output, where the correlation is lower at R^2=0.80 (Fig. 4-23).

$$\dot{Q} = \dot{m} \cdot c_p \cdot \Delta T \tag{4.7}$$

Overall the average predicted efficiency of the NEP 1200 using the tuned 1-D model is 62.6% (STDEV=4.2%) while the average observed efficiency is 62.5% (STDEV=5.6%). These are both within the range of values specified by the manufacturer (35-65% depending on operating and ambient temperature conditions).

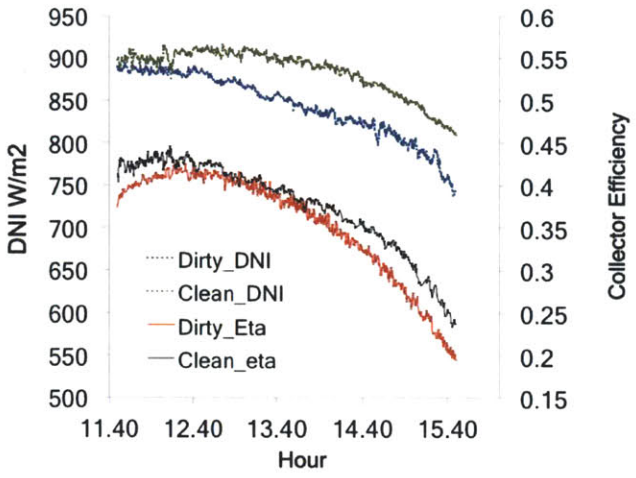

Figure 4-24: Time series of measured collector efficiency before and after washing the mirrors of the NEP 1200 collectors at PSA Spain, on September 13 and 14 2011.

4.6.4 Dirt and Optical Efficiency

Washing reflectors is an innate part of maintaining a CSP system. The tradeoff between frequency of washing mirrors, weather conditions (dust etc.), and the optical efficiency of the system is subject to an engineering cost benefit analysis. Provided the cost of maintenance is known, the relevant empirical data is the degradation of optics due to particulate build up. To examine this effect we measured the output of the NEP collectors on consecutive days, washing the mirrors between tests. The collectors had not been washed for several months prior to the experiment, so they had accumulated at least half a year's worth of particulates. The inlet temperature and flow rate for both experimental runs was fixed at 168°C and 2.5 m^3 $hour^{-1}$. Ambient conditions differed on the two days: the average windspeed was 5.4 m s^{-1} for the "dirty" run and 5.6 m s^{-1} for the "clean" run and the average ambient temperature was 26.6 °C and 27.2 °C respectively. These parameters will have had an opposing influence on the collector efficiency which was not quantified for this "quick and dirty" experiment. The collector efficiency was 0.355 on the "dirty" run and 0.377 on the "clean" run, amounting to a "dirt" coefficient of 0.94. As a first approximation, the cost of losing 6% of output over 6-months can be compared to the cost of a cleaning to devise an appropriate maintenance schedule, although it is not clear whether the degradation is linear over time or related to specific weather events.

Chapter 5

Semi-dynamical Modeling with SORCE: the Key Role of Thermal Storage

The foregoing sections have dealt with SORCE as a steady state model, i.e. average insolation conditions are established, an operating temperature regime is determined, and the program converges on an optimal cycle based on the averaged parameters. In practice, insolation and ambient temperature vary predictably with time of day and season and unpredictably with windspeed and weather conditions. A solar ORC optimized for an average set of conditions will fail to fully exploit the exergy under some conditions and fail to operate at all under others. Finally, the thermal storage component by definition retains information from the time domain which is not easily collapsed into a steady state model. A realistic solar ORC must both choose the parameters of operation and maintain the cycle within acceptable limits via a control system. To optimize such a control system, a semi-dynamical model in discrete time steps is proposed.

5.0.5 Overview of SORCE semi-D

A semi-dynamical (semi-D) version of SORCE was created based on consecutive runs of steady-state (SS) SORCE where the output of one run becomes the input of the following run and a control architecture is implemented along the lines of a basic state machine. This is achieved using a wrapper procedure that sequentially calls the individual modules of SORCE with boolean decisions to determine the state of the system.

Instead of operating with a single steady state insolation, SORCE semi-D creates an average 24-hour insolation profile using maximum and minimum temperature, assuming that the minimum temperature occurs at dawn and the maximum temperature occurs at 0.75 of the time from sunrise to sunset (i.e., a standard temperature lag [47]). Sinusoidal curves are fit to these maximum and minimum temperatures and the 24-hour solar period (Fig. 5-1).

SORCE can thus simulate operation at any point during the day based on the insolation and temperature curves. The thermal characteristic of the system is built sequentially from the insolation, the heat capacity of the storage component, and the extraction of thermal energy via the ORC. The logic diagram for SORCE semi-D is shown in Fig. 5-2.

By default, SORCE semi-D runs until a specified amount of time has elapsed. In this case, however, the goal is to achieve convergence of the tank temperature profile, and the amount of time required for this to occur is unknown *a priori*. Instead, SORCE semi-D is run for an arbitrary length of time with the endpoint adjusted in subsequent runs until convergence is achieved. Importantly, the timestep of the semi-dynamical model is determined by the assumptions driving the storage

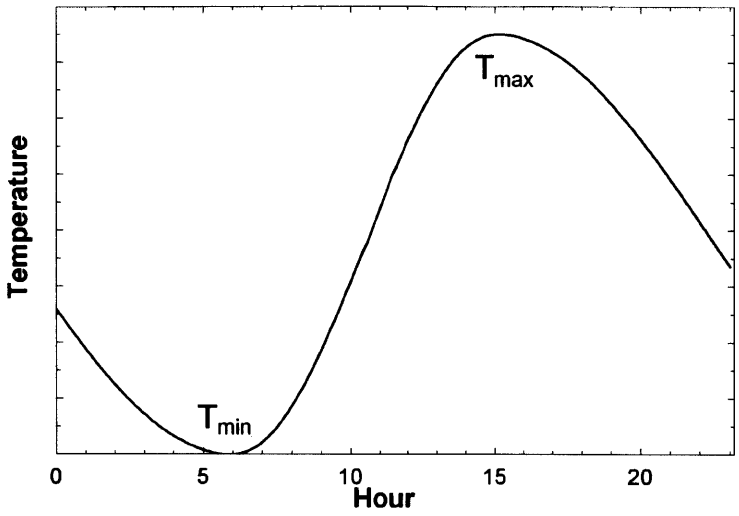

Figure 5-1: Generalized 2-sinusoid diurnal temperature profile based on mean maximum and minimum temperatures for an arbitrary location

module, i.e. lumped thermal parameters, no axial diffusion, infinite particle conductivity and NTU and plug flow equilibration of the fluid in the control volume. These are influenced primarily by the tank dimensions (chosen on the basis of thermal storage requirements) and HTF flow rate, which is optimized according to the collector requirements. The thermal profile in the tank is established from startup, i.e. the tank is at thermal equilibrium with the ambient temperature on the first day of operation, and the model is run until the temperature at each node converges to the operational profile. Convergence is mechanistically determined based on the average daily insolation and the control scheme. This thermal profile established after convergence balances the energy for the "average" day, enabling extrapolation to annual or multiyear outputs and overcoming the challenges identified in Chapter 3.

SORCE semi-D was parameterized for the reference system described in Chapter 4. The model generates a time series for relevant system parameters and storage tank node temperatures (Fig. 5-3), with convergence reached by the fourth day for a nominal $3kW_e$ system (Fig. 5-4). In general, for this and other systems that could be modeled using SORCE, the time to convergence is expected to track closely on the thermal mass and thermal power of the collectors.

5.0.6 Optimization using SORCE Semi-D

SORCE semi-D can also effectively model a solar ORC under varying insolation conditions, either using the solar module to create daily insolation and temperature profiles or by inputing heliometer and weather station measurements. This would likely produce insight into the interaction between control schemes and transient phenomenon such as, e.g., clouds temporarily obscuring the sun or extended periods of low insolation. It can also serve as the basis for online optimization of cycle parameters to best exploit the available thermal resource, for example modulating the HTF and working fluid flows or changing the temperature thresholds of the cycle to maximize power output.

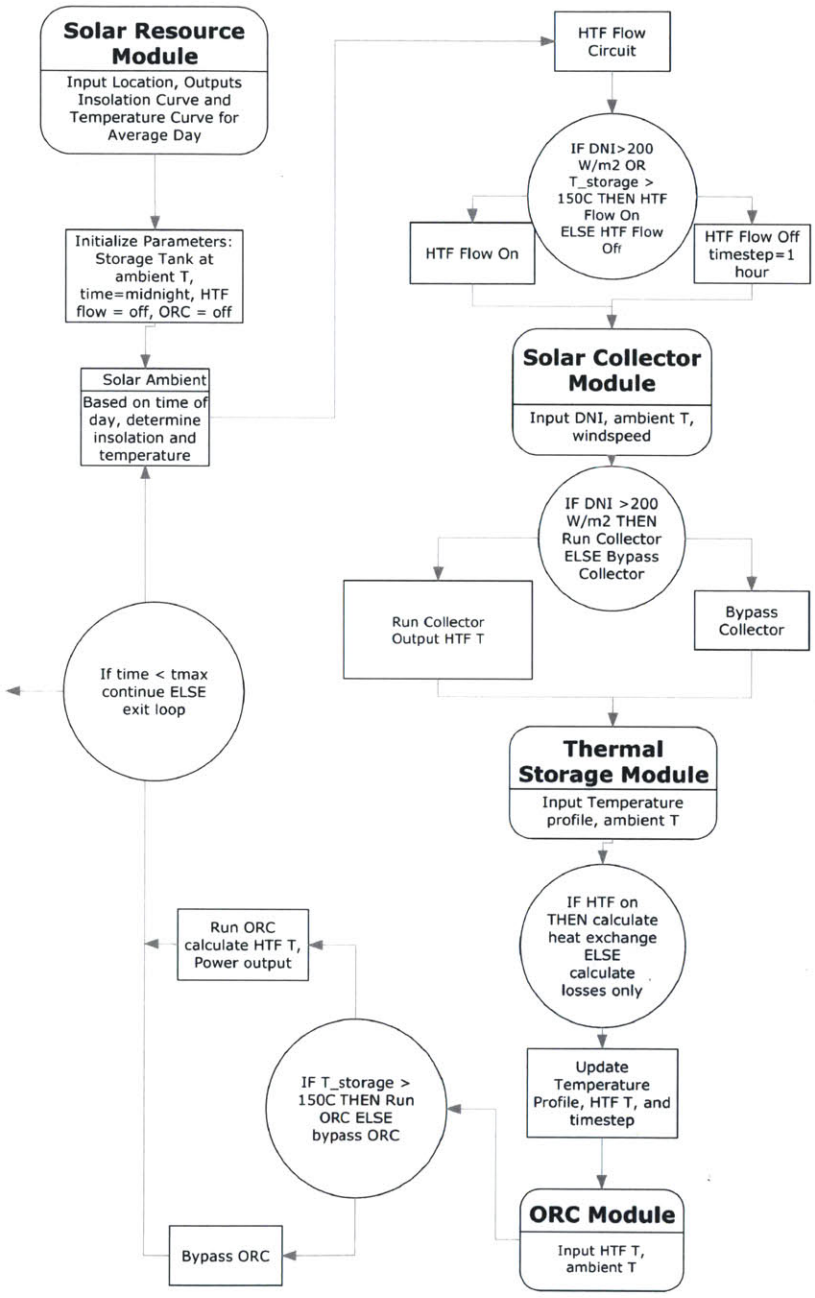

Figure 5-2: State logic decision diagram for SORCE semi-D corresponding to a simple control method for the solar ORC

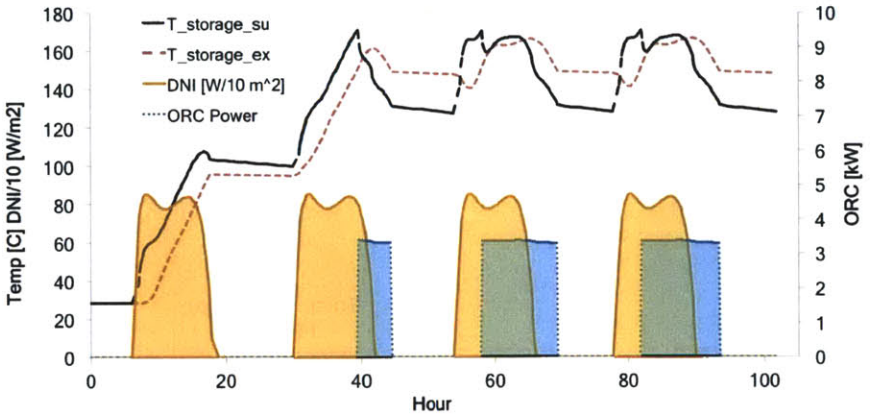

Figure 5-3: SORCE semi-D generated time series of inlet and outlet temperatures for the storage tank, the solar insolation on an E-W tracking surface, and the power output of the ORC for the reference system described in Chapter 4. Stable operation is achieved after 4 days.

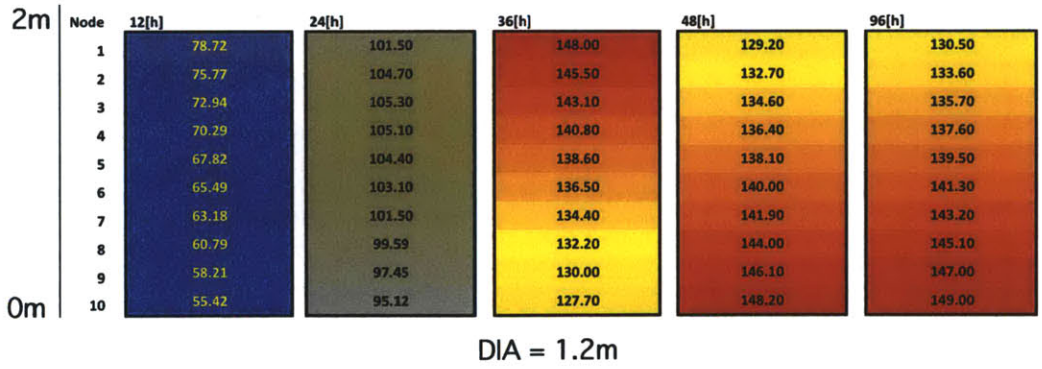

Figure 5-4: SORCE semi-D generated thermal profile of node temperatures in the storage tank after startup and reaching convergence by the fourth day, for the reference system described in Chapter 4.

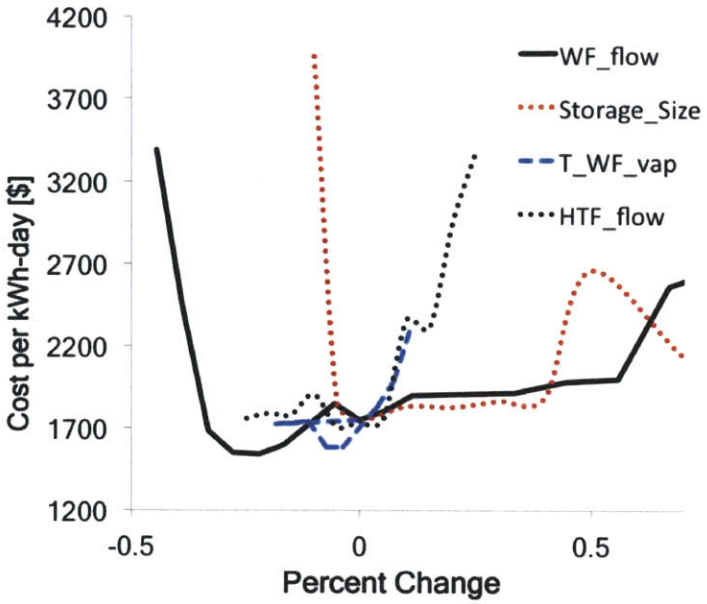

Figure 5-5: Sensitivity of Solar ORC system cost kWh^{-1} day^{-1} to percent change in operational parameters

Effect of Design Parameters on Performance and Cost

As an equipment sizing and performance prediction tool, SORCE semi-D can identify the optimal balance in system design between thermal and battery storage and engine capacity. The specification for energy output during the day in kWh_e and kWh_t (discussed in Chapter 2) will stipulate the array size for a parabolic trough collector module, within a range determined by the collector efficiency (see Chapter 3 and Section 5.0.6). The optimal ORC size is determined by examining the tradeoff between economies of scale for the engine and the cost of redistributing energy in the time domain either prior to the engine (sensible thermal storage) or after conversion to electricity (batteries). For the reference system of Chapter 4, these tradeoffs are illustrated by a sensitivity analysis (Fig. 5-5). From this analysis we can observe that each design parameter has a viable operational range outside of which the system loses effectiveness. In general, we can state that:

1. If the storage capacity is too small, thermal instability and ORC mismatch with the solar resource causes losses

2. If the storage capacity is too large, thermal inertia creates instabilities, and unnecessary thermal losses and system costs are incurred

3. All other things being equal, at high working fluid flow rates the proposed ORC is oversized compared to the solar resource.

4. At low HTF flow rates, pump work is lower, and average HTF temperature in the collector is lower, whereas at higher flow rates the heat transfer is promoted but parasitic losses increase.

Notably, the design space is non-monotonic for some parameters, and interactions between parameters result in a non-linear optimization problem. To determine optimal storage tank size, fluid flow rates, and evaporating temperature, we perform an optimization using the Max/Min genetic

Table 5.1: Design parameters for minimizing the specific cost of electricity production from a Solar ORC

Specific Cost \$ kWh^{-1} day^{-1}	DIA	$\dot{m}_{WF}$	$T_{WF,exp,su}$	$\dot{v}_{HTF}$	$Width_{UD}$
1169	2.5	0.15	130	30	2

algorithm function in EES, based on the method implemented by [42]. The optimal configuration for a Solar ORC meeting the reference specifications based on this technique is shown in Table 5.1.

Effect of Operation Parameters on Control Methods

The solar resource fluctuates with the sun's position, but there are limitations to following these fluctuations with the power cycle. This justifies use of thermal buffering along with the matching of the ORC power block to obtainable energy input levels. Within these constraints, however, it is still desirable to identify the optimal strategy for use of available solar resources.

The opportunity for varying the vaporizing temperature of the cycle to follow the solar input is limited by the choice of working fluid and the expander geometry: an optimal ORC will operate slightly below the critical temperature of its working fluid [124], and the fixed volume ratio of the expander precludes taking full advantage of a variable cycle specific volume ratio. It does not seem practical to address the former constraint, which is thermophysical, but a mechanical solution may be found to ease the latter. To examine the value of a relatively flat efficiency-power curve, we compare the output of a variable ratio system with a fixed capacity ORC in Figure 5-6. The control algorithm used is the maintenance of the temperature pinch in vaporizer at 15°C, which leads to a bimodal ORC operating period due to rapid drawdown of the storage tank charge. As an operating strategy the gains are modest at 0.5%, but this is expected since the reference cycle is optimized for the average day. This configuration may prove more advantageous when considering the wider seasonal variation in insolation and temperature at a site. Another possible strategy involves time shifting energy production towards the cooler evening to reduce the bottoming temperature of the cycle. This involves careful consideration of the shape of the load curve, the diurnal temperature curve, the financial tradeoff of potential extra investment in battery capacity. This is a potentially fruitful area for further inquiry well within the capabilities of SORCE.

As can be seen from the sensitivity analysis in Fig. 5-5, varying the HTF flow rate predictably affects the overall system performance via the heat transfer coefficient in the collector, the ΔT, and the pinch in the ORC 3-zone heat exchanger, in addition to controlling the pump parasitic load. Varying the working fluid flow rate correspondingly controls the power throughput of the ORC, the pinch in the heat exchangers, and the RPM and efficiency of the expander-generator. As described in Chapter 7, the expander efficiency is reduced at low RPMs due to leakages through the scroll wraps, and at high RPMs the effects of friction dominate, resulting in a typical performance curve such as the one derived in Appendix C. These effects are superimposed on the generator efficiency curve (Fig. 4-17), which is nonlinear at low power outputs and asymptotes to a maximum efficiency at higher outputs (up to a maximum output dictated by the materials limitations, i.e., winding insulation).

5.1 Summary

This chapter introduced the important aspects of dynamic behavior in a Solar ORC, including insolation change and thermal inertia, that require a control strategy to manage the timing and extent

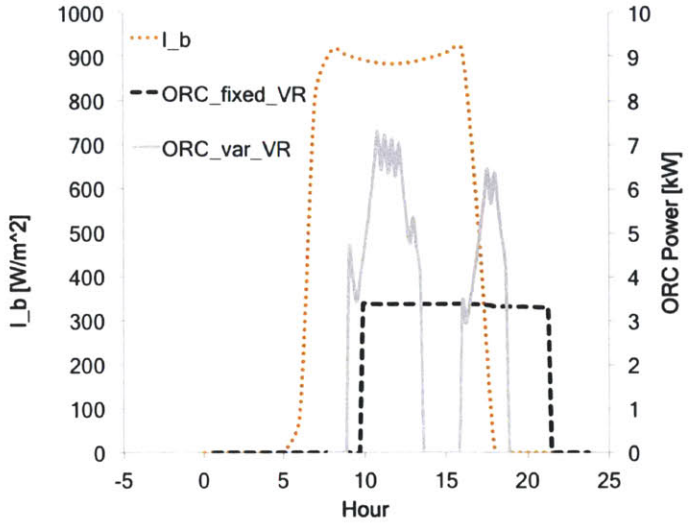

Figure 5-6: Operation of ORC with a constant vaporizer pinch control strategy leads to a bimodal production curve. This strategy can exploit meteorological variance but requires a variable VR expander.

of energy transfers. In particular, quantification of the thermal history of the storage tank is an important step towards approximating a benchmark for extrapolation to annual timescales or beyond. The effects of storing and releasing energy include setting constraints on the minimum ORC power block capacity and optimization opportunities such as matching resource availability over natural temperature variations. To handle this type of investigation a semi-dynamic version of SORCE, working on a timestep dictated by the node equilibrium of the storage component, was introduced. This model successfully predicts thermal startup behavior to (1) track storage history and (2) test macro level control strategies operating through temperature thresholds and flow adjustments.

Chapter 6

A Theoretical and Experimental Approach to Optimized Medium Temperature Hybrid Solar PV-Thermal Collectors using a Small Scale Organic Rankine Cycle

6.1 Abstract

An experimental hybrid concentrating solar photovoltaic (PV) system with thermal power cogeneration capability is proposed for small-scale power plants serving remote areas. This concept is evolves a traditional linear concentrating PV absorber, optimized for use at medium range thermal collector temperatures (200°C), whereby the heat transfer fluid (HTF) used for temperature control of the cells is cooled through additional power generation by an Organic Rankine Cycle (ORC). The conceptual approach is described and an engineering design analysis is performed to investigate the tradeoffs amongst cost, efficiency and operating temperature regimes to find an optimum configuration for kilowatt-scale plants. An open source variation of the multi-physics Solar Organic Rankine Cycle Economic model (SORCE), called PV-SORCE, is developed to facilitate the calculations for performance prediction and equipment

6.2 Hybrid PV–Thermal Concept

The hybridization of photovoltaic cells with thermal power generation leverages the principle of exergy to maximize the conversion efficiency for sunlight impinging on a collector. The traditional formulation of theoretical limits for photovoltaics assumes that all energy lost in the semiconductor junction is unrecoverable. In fact, the heat generated as a byproduct of photovoltaic inefficiencies can be converted to electricity if it has sufficient exergy (which is a function of temperature). From this perspective, the total theoretical limit for the conversion of sunlight to electricity should include both the photonic–bandgap conversion limit and the Carnot limit of the resulting phonons in the fluid flowing through the absorber target. This exergy can be exploited by any heat engine (a thermoelectric (Peltier-Seebeck), Rankine or Stirling engine), effectively increasing the theoretical limits of sunlight to electricity conversion efficiency [146]. Due to cost and scale considerations

described in Chapter 2 we limit this investigation to the domain of medium temperature collectors and organic Rankine cycle (ORC) heat engines.

There has already been substantial research on each subsystem individually: presentation of the theoretical and practical aspects of CSP technologies [104, 122], CPV [141], and organic Rankine cycles [124, 80, 144]. To date, however, there has been no attempt to integrate these approaches. The proposed approach could be expressed as the synthesis of two experimental studies conducted in Europe and Australia: the CSP-ORC platform of [77, 78] and the CPV combined heat and power system (CHAPS) investigated by [48]. The unification of these approaches entails specific physical and engineering challenges which we explore in the following sections.

In short, there are three major trends that must be counterbalanced. First, in practice, the temperature coefficients of most solar cell devices are negative, e.g. the efficiency of crystalline silicon solar cells decrease with temperature at a rate of the order of 0.1-0.4% per degree K [21, 55]. (At increased temperatures the dark saturation current of the PV cell increases leading to a decrease in open circuit voltage while the bandgap of the photovoltaic material also decreases [].) For silicon the latter can lead to an increase in photocurrent because a larger portion of the solar spectrum is available for forming electron-hole pairs, however in general the former effect is dominant and the efficiency of PV cells decrease with temperature [112]. Second, the effectiveness of a Thermal Heat Collection element (HCE) also decreases with temperature due to the convective and radiative thermal losses [59]. Third, and in direct contrast to the first two points, the Carnot efficiency increases monotonically with temperature. Hybridization of a PV-HCE-CSP system thus requires a compromise between the optimum operating temperature of either concentrating PV (CPV) or concentrating solar (thermal) power (CSP). In the following sections we define the design space and explore the optimization of parameters for hybrid CPVT (T signifying *thermal*).

6.2.1 Optical Considerations

Similar optical concentrators using point or line focus are developed in both photovoltaic and thermal power generation systems. In CPV systems the concentrating collector is employed to reduced costs (optics are usually inexpensive compared with semiconductors on an areal basis [97, 21]). A design optimum for CPV tends to feature high concentration ratios and active cooling to maintain cell temperatures at acceptable levels [140, 100]. In thermal CSP systems, typically employing a Rankine cycle, the concentrator instead serves to create a high temperature thermal reservoir from which potential the cycle extracts work [53]. In this study we consider line focus, parabolic optics of the form:

$$y = \frac{x^2}{4 \cdot p} \tag{6.1}$$

where p is the focal point of the optics in 2-D.

Combining the two approaches should offer cost advantages due to the shared optical and thermal infrastructure (with the heat engine replacing the cooling loop for the CPV cells). The output of the superposed CPV and CSP systems is additive, i.e. photons not involved in creating electron-hole pairs are thermally absorbed (thermalization) and thus available to contribute to a high temperature thermal reservoir. Note however that the addition of PV cells to the surface of a thermal absorber target may sacrifice some thermal efficiency if the optical properties of the PV cell (absorbtivity and emissivity) are inferior to the original solar selective coating (black chrome, Solec Hi/Sorb II, Cermet, etc. which are high absorbance in the visible and low emissivity in the infrared [99]). In this study black chrome, a composite of metallic chrome and the dialectric Cr_2O_3 [107], is used as the basis for comparison with silicon wafer optical properties (Fig. 6-1).

The main challenge in hybridizing PV and Carnot devices is thus optimizing for cost across the opposing trends of efficiency vs. temperature. Secondary obstacles for linear CPV, described by [48], include inhomogeneous solar flux and the temperature gradients at the PV-HCE boundary, both of which contribute to poorly matched I-V characteristics of individual cells. In this paper we examine the limitations of a PV-HCE comparing triple junction amorphous (a-Si), detailed in Figure 6-2, and monocrystalline silicon (c-Si) cells shown in Figure 6-3.

6.2.2 PV Device Characteristics

In practice most concentrating PV systems use specialized photovoltaic cells adapted to high concentration (high efficiency multi-junction cells with close metallization spacing, differential doping under contacts to reduce series resistance, thermal conductivity of rear contact for heat rejection, etc.) [79]. In this paper we explore the potential of four types of non-specialized (1 sun) solar cells in a hybrid thermal concentrator application up to 50 suns. The main advantage, assuming the cells remain functional, is cost and availability, although other factors are potentially beneficial. Amorphous silicon PV cells are particularly suited to high temperature applications due to their material properties, including the reversible Staebler-Wronski effect. This effect involves the light-induced degradation over time through increased defect density, which has a strong influence on the electronic transport properties. Over time the Staebler-Wronski effect reaches saturation at a lower sunlight to electricity conversion efficiency, but it can be reversed by thermal annealing of the cell at 150°C for a few minutes[84]. The annealing effect of high temperatures thus diminishes the temperature degradation of a-Si as compared to c-Si.

Whereas a-Si cells generally exhibit a lower overall efficiency compared to c-Si cells, the higher indirect bandgap range of amorphous silicon (up to 1.8eV, decreasing at higher temperatures) captures a greater portion of the 1.2eV-centered solar spectrum. Thin film a-Si on a stainless steel substrate also has the advantage of being readily conformable and thus more easily bonded thermally to standard absorber geometry for linear parabolic optics.

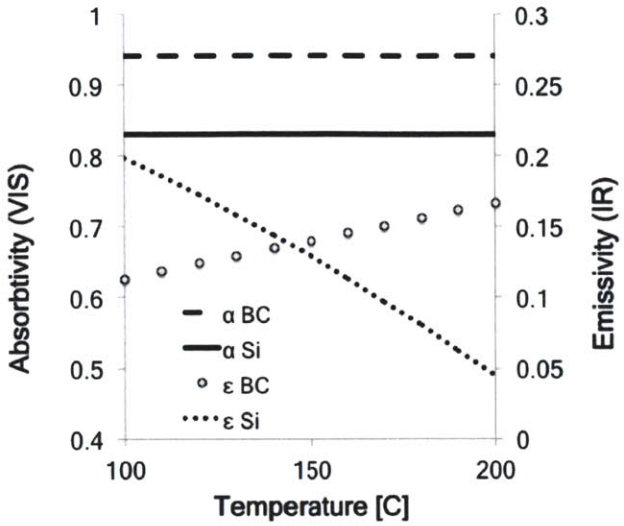

Figure 6-1: Lumped spectrum absorptivity and emissivity for Black Chrome and Silicon

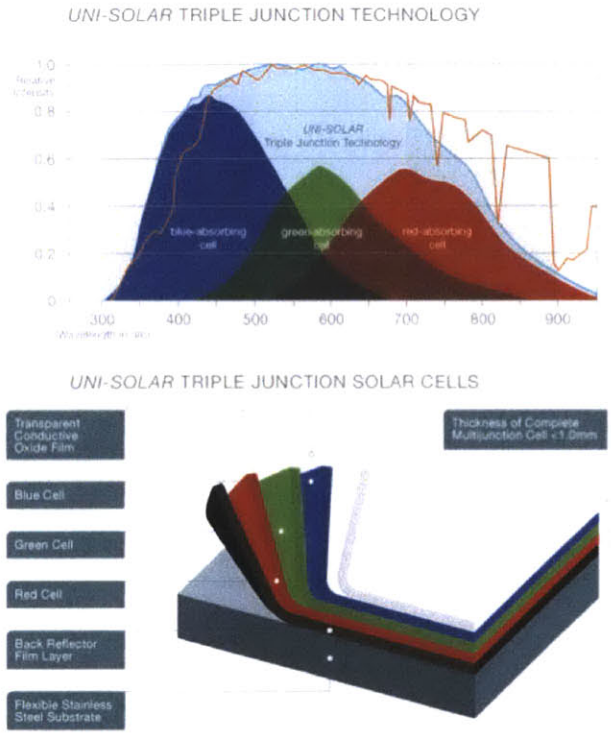

Figure 6-2: a-Si Triple Junction solar cell. Multiple band gaps facilitate photon absorption across a wider region of the solar spectrum. [158]

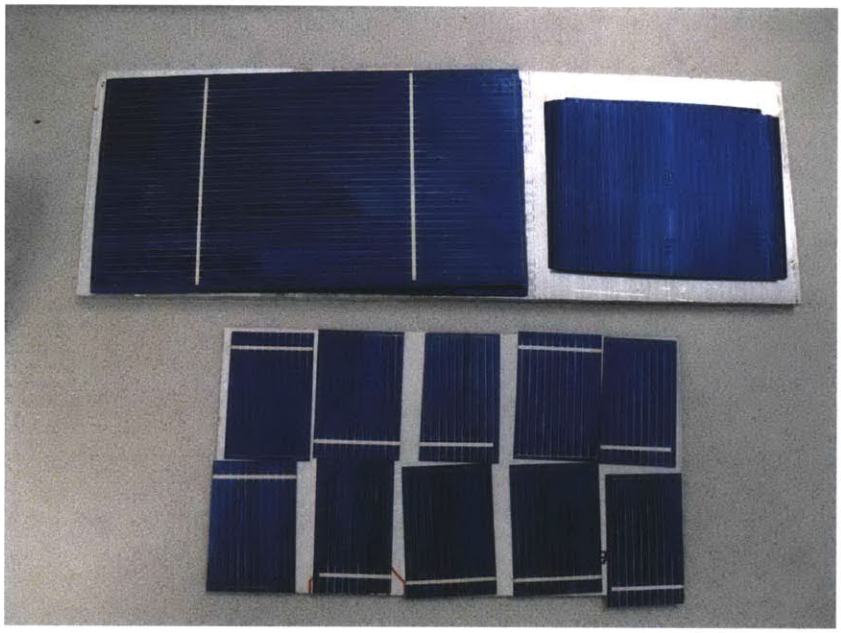

Figure 6-3: crystalline silicon solar cells manufactured by Evergreen solar (14% efficiency, 70% Fill Factor). Laser cutting the cells to fit onto the thermal stage in Fig. 6-6 reduced the Fill Factor by 10%.

6.2.3 PV-SORCE Multi-Physics and Economic Modeling

To facilitate study of this system we developed a Photovoltaic Solar Organic Rankine Cycle Economic (PV-SORCE) model combining semi-empirical multi-physics computation modules for solar resource and site environmental parameter characterization along with optical, solar cell, thermal and electromechanical performance prediction of hybrid PVT collectors and ORC systems. This model builds on a prior solar thermal organic rankine cycle model (SORCE) described in [128, 117] and elsewhere in this thesis, and integrates the seven parameter PV cell model of [49]. It also provides technical specifications and costs of standard system equipment.

Aside from the principal material and construction costs, numerous physical considerations affect the trade-off in engineering designs for CSP and PV systems; a non-exhaustive list would include optical properties of collectors and absorbers, heat transfer coefficients of thermal and working fluids, and fluid machinery isentropic efficiencies, as well as I-V curve characteristics and fill factor, shunt and series resistances, defects in solar cells and temperature coefficients.

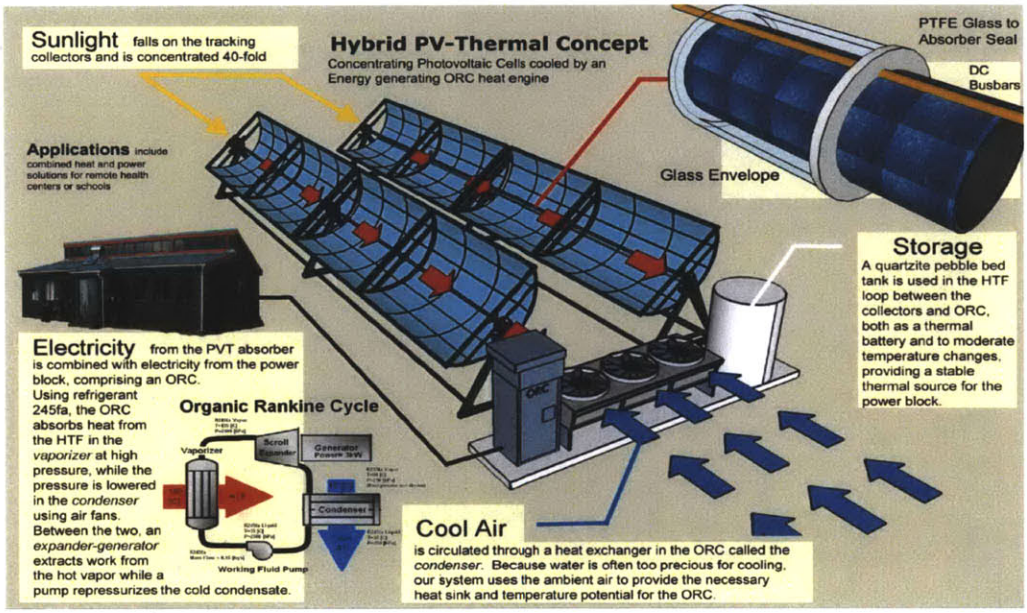

Figure 6-4: Schematic diagram of Solar PV-Thermal Hybrid System using a PV-HCE and ORC

Complex effects, such as potential damage to solar cells arising from the temperatures and flux intensity at the concentrator target, e.g. thermal degradation of polymer substrates, thermal stresses from differential expansion, and high currents in busbars, are not modeled. The diode model (Fig. 6-5) was adopted due to its computational efficiency but required modification to correct for inaccuracies in the simplifying assumptions. These include, e.g. the assumption that material parameters are insensitive to changes in bias or illumination and that minority-carrier concentrations at the edges of the space-charge region are independent of illumination [41]. The characteristic I-V relationship of the equivalent circuit takes the form of

$$I = I_L - I_D - I_{sh} = I_L - I_o \cdot (EXP(\frac{V + IR_s}{a}) - 1) - \frac{V + IR_s}{R_{sh}} \tag{6.2}$$

where I_L is the photocurrent, I_o is the diode reverse saturation current, a is a modified ideality factor (see Eq. 6.3) and R_s and R_{sh} are the series and shunt resistances [53]. Here series resistance is

assumed to be independent of temperature and illumination while shunt resistance varies inversely with illumination. While these assumptions are acceptable within the range of temperatures and illuminations encountered in normal PV operation, they fail to accurately predict performance at the high temperatures and illuminations under investigation here.

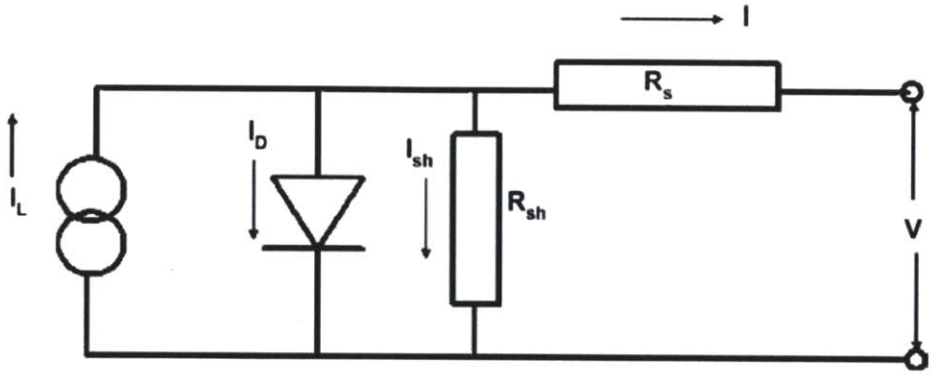

Figure 6-5: Equivalent circuit diode model of a solar cell [49]

6.3 Empirical Cell Characterization

6.3.1 Methods and Equipment

To characterize and correct for non-linear aspects of the diode model, an experimental benchmarking campaign measured output voltage and current while varying both illumination and temperature of a-Si and c-Si cells. Illumination was provided with a 1600W Oriel full spectrum Solar Simulator in diverging beam mode (unfiltered, beam uniformity $\pm$ 5%, light ripple $<$1%). The reference spectral output of the simulator is provided in Figure B-1. To achieve variable irradiance levels a flat response 33.5% opening Aluminum mesh filter was interposed between the cell and the simulator. The filter spectra is provided in Figure B-2. The experimental apparatus (Fig. 6-6) consists of a variable temperature hot plate stage made from aluminum and electrically isolated with a non-electrically conductive high thermal conductance epoxy (Timtronics TIM-813 HTC) incorporating a surface embedded type K thermocouple ($\pm$0.1°C accuracy). The temperature readout device is a digital multimeter (DMM). The cells are mounted on the stage with a silicone based thermal grease ($1.8 \cdot 10^{-3}$ Cal./Sec./cm/°C). Cell current and voltage measurements were recorded using an Amprobe Solar-600 four-wire I-V curve tracer (Accuracy $\pm$1% of V_{open} and I_{short}). During the experiments the temperature is ramped from ambient (approximately 40°C under illumination) to up to 200°C, with measurements taken at thermal equilibrium points. The illumination is held at either 4.75 kW m^{-2} at 3.5 inches or 1.6 kW m^{-2} at 3.5 inches with the Al filter.

6.3.2 PV Cell Parameters

Characteristics of the solar cells (V_{open} [V], I_{short} [A], V_{maxp} [V], I_{maxp} [A], P_{max} [W], η_cell R_{shunt} and R_{series} and Fill Factor) and their variation with temperature and illumination are listed in Table B.1. The c-Si cell dimensions are 26x44mm (lasercut from a larger wafer with a loss of 10% of FF) and the a-Si is 39x93mm (mechanically sheared, FF difference not measured). The

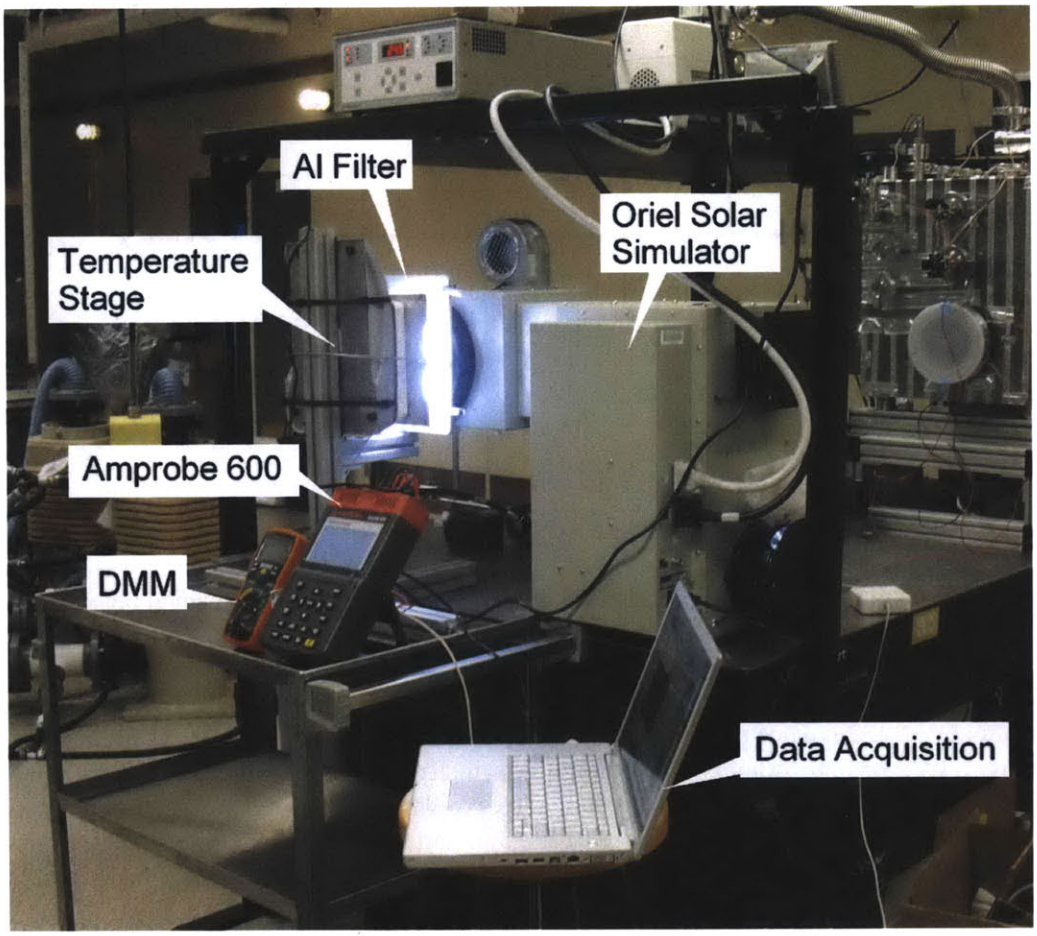

Figure 6-6: Experimental setup for benchmarking solar cell performance at varying temperature and illumination (lab space courtesy of the Wang Laboratory)

effects of increasing illumination and temperature on I-V characteristics are illustrated in Figure 6-7.

Contrary to the assumptions of the 5 parameter diode model, we observe that the shunt and series resistances are in fact a function of both temperature and illumination (Figure 6-8), and we can exploit these data to derive best fit curves for the 5 parameters of the model incorporating the concentration factor *X* (Table 6.1), with temperature effects accounted for in the *a* term and via the usual temperature dependent terms of the diode equations, e.g. the bandgap [49]:

$$a = \frac{N_s n_I k T_c}{q} \tag{6.3}$$

$$\frac{E_g}{E_{g,Tref}} = 1 - 0.0002677(T - T_{ref}) \tag{6.4}$$

where N_s is the number of cells in series, n_I is the ideality factor, q is the electron charge ($1.381 \cdot 10E-19$ coulomb) and k is Boltzmann's constant. The object of this modification is to provide a rapid and reliable method for prediction of cell performance at high insolation and temperature, as compared to a more physically realistic but computationally intensive model, such as PC1D [46]. The approach captures the behavior of PV cells under high injection conditions (i.e. photogenerated carrier densities are large compared to the doping density) without contending with the complexity of, for example, effects on transport and recombination in the electric fields generated by concentration induced carrier density gradients [112]. For our purposes, the semi-empirical diode approach is valid insofar as relevant outcomes can be simulated for engineering design. It should be noted that due to simulator limitations the empirical concentration factor (X) was limited to 4.75, so extrapolation of model results to higher X must still be verified through further benchmarking of the parameterization.

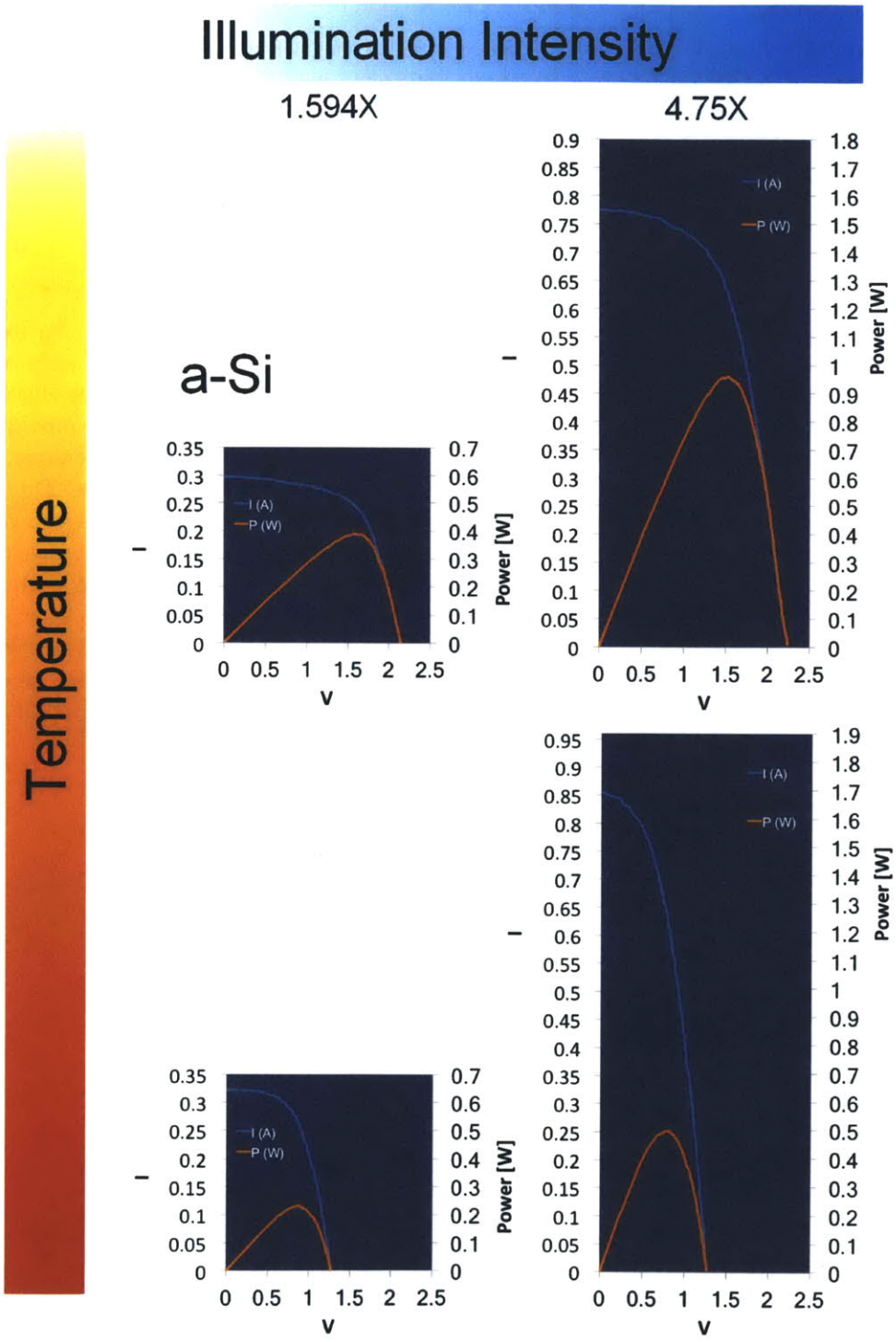

Figure 6-7: Current and Voltage characteristics of a triple junction a-Si cell heated from 40 to 155°C under 1.594X and 4.75X simulated solar spectrum

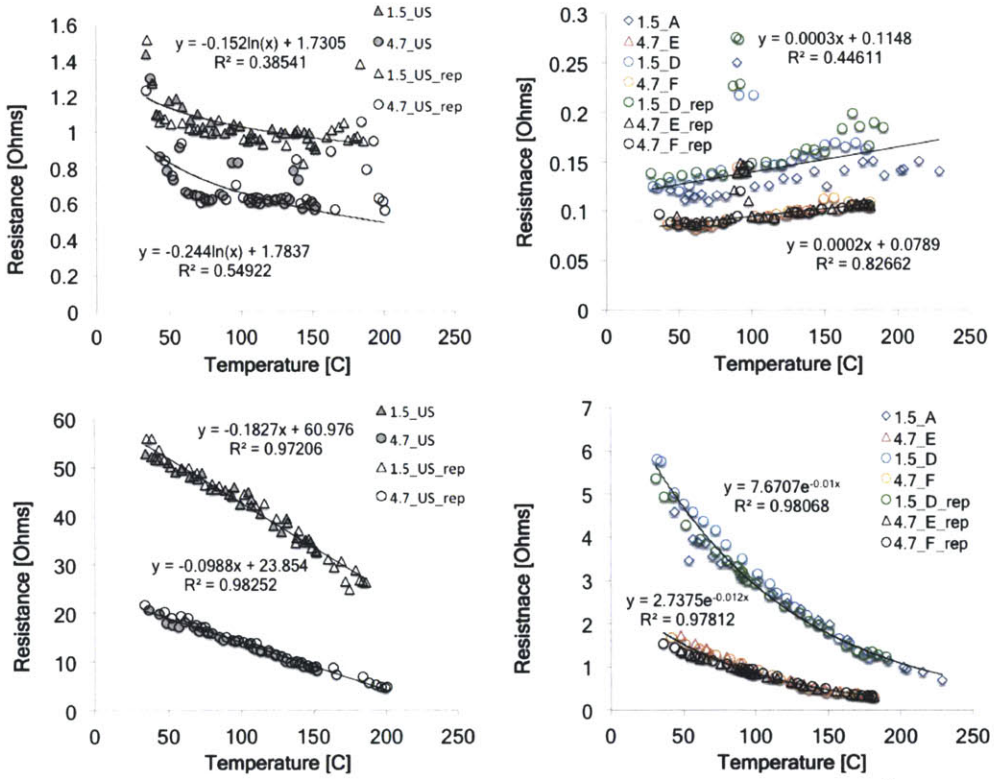

Figure 6-8: Empirical series and shunt resistances for two illumination levels using Unisolar a-Si (Left) and Evergreen c-Si cells (Right)

Table 6.1: 5-Parameter Diode Model Variable Illumination modification

Cell type	Empirical best fit curves to diode model	Goodness of fit
Unisolar a-Si	$R_{sh_{ref}} = 72.7553468 \cdot X^{-1.56052795}$	R^2=0.99
	$R_{s_{ref}} = 1.88468568 \cdot X^{-0.813707431}$	R^2=0.99
	$I_{o_{ref}} = 1.00994065E-14 \cdot X^{0.5074742}$	R^2=0.99
	$I_{L_{ref}} = 0.196988027 \cdot X^{0.97978355}$	R^2=0.99
	$a_{ref} = 0.0658977188 \cdot exp(-0.00938515413 \cdot X)$	R^2=0.99
Evergreen c-Si	$I_{L_{ref}} = 0.731404078 - 0.000140392708 \cdot X + 8.18141688E-07 \cdot X^2$	R^2=0.99
	$I_{o_{ref}} = 4.18934736E-11 - 1.36752359E-11 \cdot X + 6.51541844E-12 \cdot X^2 - 3.73388529E-13 \cdot X^3 + 1.64697845E-14 \cdot X^4$	R^2=1
	$a_{ref} = 0.0233094347 + 0.000270726125 \cdot X - 8.97577317E-07 \cdot X^2$	R^2=1
	$R_{sh} = 11.9116449 + 0.188876311 \cdot X - 0.000139004581 \cdot X^2 + 0.0000509150878 \cdot X^3$	R^2=1
	$R_s = 0.123090107 - 0.000798687027 \cdot X + 0.00000436959487 \cdot X^2 - 1.17955160E-08 \cdot X^3$	R^2=1

Table 6.2: Cost and specifications for the investigated a-Si and c-Si PV cells

Manufacturer	**Panel**	**Retail April 2012** $	**Power** W	**Area** m^2	$/W	$/$m^2$
Uni-Solar	PVL-136	210	129	1.85	1.63	113.51
Evergreen	ES-H-250	589	210	1.28	2.80	461.96

6.4 Semi-Empirical Diode Model

The implementation of the diode model follows [49] and [53], with the parameters of Table 6.1 and is attached as part of the SORCE code in Appendix CODEdix. In SORCE, the PV cell is interposed at the absorber envelope such that the energy converted to electrons is subtracted from the energy balance at that node, and the optical characteristics of the cell are used instead of the absorber selective coating. Using the modified 5-Parameter diode model, we can reproduce the experimental data from Table B.1 with high coefficients of determination (Fig. 6-9) while retaining the computational efficiency needed for integration with the modules of the SORCE program. With this tool we can explore the design space for CPVT and test hypotheses about particular features of the proposed systems.

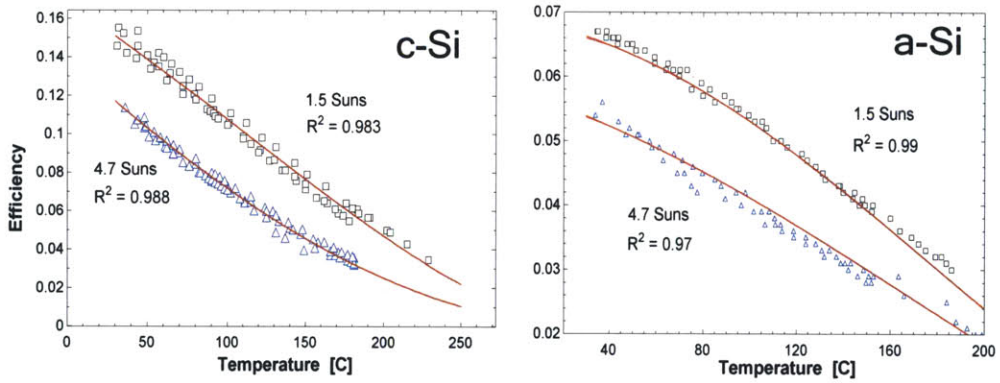

Figure 6-9: Goodness of fit between the semi-empirical diode model (red line) and experimental results for tested c-Si and a-SI cells

Typical medium temperature linear concentrators in use for CSP systems have a concentration ratio of 25–40 x [108, 113]. One straightforward approach to developing a CPVT system would be to adapt a PV-HCE for use in place of the traditional HCE used in such collectors. We can use PV-SORCE to determine which type of common 1-sun cell, if any, would be suitable, first by generating a type curve relating cell temperature to x for a-Si and c-Si (Figure 6-10). These graphs demonstrate the relatively flat response of a-Si to elevated temperatures, and indicate that the use of c-Si cells is problematic for all but the lowest concentration factors and temperatures. In light of this, and considering that the cost of c-Si cells is around four times the cost of a-Si cells on an areal basis (Table 6.2), a-Si cells are used for our investigation of CPVT.

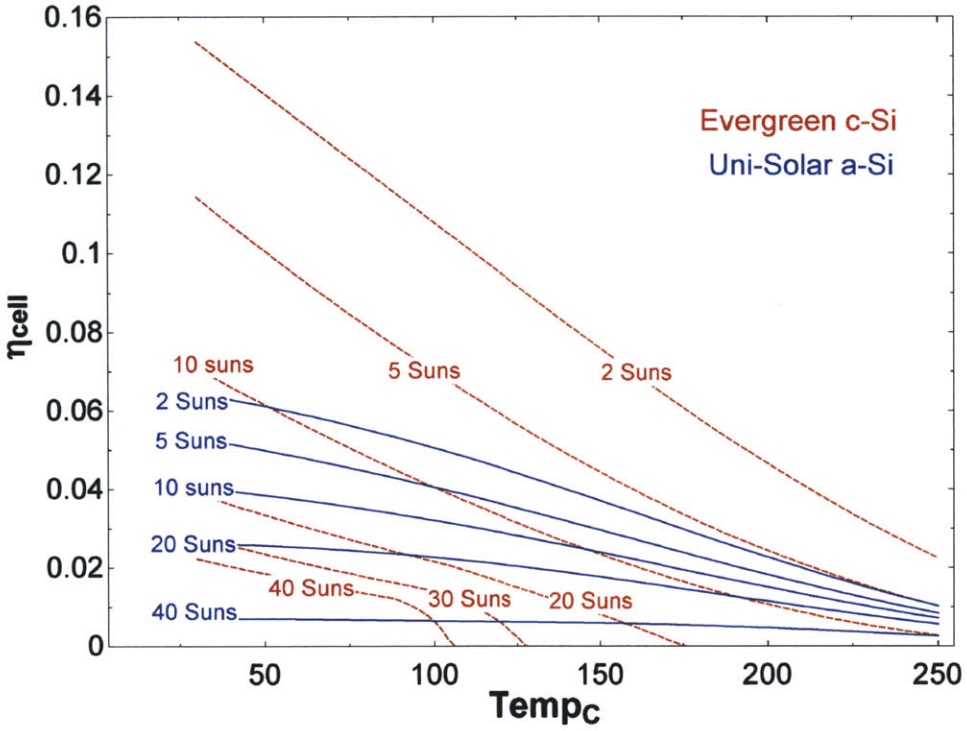

Figure 6-10: Semi-empirical diode model prediction of concentration factor and temperature effects on cell efficiency

Table 6.3: Boundary Conditions for optimizing CPVT against CSP alone

Parameter	**Lower**	**Upper**	**Units**
$T_{HTF-col-su}$	30	150	[C]
$v_{dot}{}_{H}TF$	30	50	[LPM]
$Width_{UD}$	1	4.5	[m]
CPV or CSP use	CSP On	CPV On	

6.5 PV-SORCE Optimization

The main parameters available for optimization of a CPVT collector design are its concentration factor ('x factor') and average operating temperature. As mentioned in section 6.2.1, the optical properties of silicon will necessarily impact the thermal properties of the absorber, which vary with x factor. Figure 6-11 illustrates these tradeoffs for hybrid system components at selected x factors. As expected, the efficiency of any target receiving concentrated sunlight decreases with temperature. A CSP absorber will operate at higher efficiency with a higher concentration factor due to a smaller effective surface area for heat loss. Within the investigated temperature range the reverse is true for a CPV absorber, which loses efficiency at higher concentration due to increased R_s losses and the non-linear effects mentioned in section 6.3.2. For the specific costs ($\$\cdot W^{-1}$) of the CPVT configuration, the influence works the other way, with lower costs at higher concentrations due to the reduced cell area dominating the efficiency losses (this decoupling of cost and efficiency is an important concept for the interpreting the optimization analyses that follow). The tradeoffs between global system efficiency, temperature, and x are illustrated in Figure 6-12.

PV-SORCE can address the topic of optimizing the hybrid design within constraints favoring either CSP or CPV relatively using the built in Max/Min genetic search algorithm functionality of the EES numerical simulation environment (following [42]). We establish the optimization boundary conditions (Table 6.3) and specify the objective function to maximize, initially global CPVT system efficiency. The design parameters are normalized to an irradiance of 100kW by varying the collector length in proportion to its width, and the ORC is modeled as a Curzon-Albhorn engine operating at the temperature of the CSP or CPV absorber. Concentration factor is varied by setting the width of the collector aperture and the HCE temperature (and cycle saturation temperature) is varied by setting the HTF supply temperature to the collector. The option for CPV or CSP is the final degree of freedom.

Whereas one might posit the optimal CPV system to favor lower temperatures and lower concentration factors, using the ORC as a "free" active cooling unit, the results of genetic optimization point to the central role of the heat engine. In both CPV-CSP and CSP scenarios, the algorithm finds a strong correlation of efficiency with increased operating temperature (Figure 6-13) and neither approach demonstrates a relative advantage.

Efficiency, however, is not the objective function for this study; the goal is to minimize specific costs of the CPV. In this case, the areal extent of cells at the absorber target is taken as fixed, and the areal cost (from Table 6.2) is evaluated over the output of the cells as a function of temperature and x (Fig. 6-14).

Uni-Solar cells outperform the Evergreen cells, especially at higher temperatures and concentrations. For operation at 50 °C, Evergreen cells reach an optimum below 10x, with higher concentrations leading to a exponential increase in specific costs related to temperature degradation. Uni-Solar cells, by contrast, reach an optimum at 30x, with a gradual increase in specific costs with temperature. Whereas temperature introduces localized defects and increases recombination losses

Table 6.4: Results of an optimization of parameters for minimization of specific costs [$ / kWh-day] for both CSP only and CPV-CSP hybridization

	Area [m2]	System Cost [$]	ORC kWh/day	PV kWh/day	$\dot{m}$ WF kg/s	$\dot{v}$ HTF LPM	$T_{exp,su}$ [C]	X	$ / kWh-day
Micro–CSP	68	29331	26		0.1	30	125	24.5	1123
PV–CSP	66	30665	23	2.6	0.11	30	126	25.5	1172

	Collector [$]	Power Block [$]	Storage [$]
Micro-CSP	8160	15458	1796
PV-CSP	7920	16924	1796

in c-Si cells, in amorphous silicon the density of of light-induced defects (the Staebler-Wronski effect [137]) can be reduced through annealing at temperatures greater than 150 °C. In a-Si cells, photoconductivity is positively correlated with temperature, and at high temperatures it can be correlated with illumination intensity [137]. These phenomenon can explain the relative suitability of a-Si as compared with c-Si in medium x CPV applications.

Concentration may negatively affect efficiency, however, given fixed cell costs, insofar as increased x (accounting for heat gain) increases net power production it will tend to reduce specific costs. As described above, the preferred cell type for a CPV-CSP application is not necessarily related to performance under standard conditions, rather, the ideal cell will have the highest output-to-areal cost ratio within the specified temperature envelope of operation. In general, for a CPV system with a given cell type, the optimal x factor will be set to the point where gains in power output are compensated by the incremental cost of optics for an increase in x, maximizing the specific cost function:

$$Cost_{spec} = \frac{A_{abs} \cdot Cost_{area,PV} + A_{abs} \cdot x \cdot Cost_{area,optics}\ [\$]}{Power(x,T)\ [W]} \tag{6.5}$$

For a linear concentrator with a monotonic temperature gradient, this function may be maximized with unique cell/optical architectures piecewise in sections along the absorber. A combination of cell types and/or x-factors may deployed in series, although in practice varying optical geometry introduces complexity and may not be a cost effective approach. Finally, the hybridization of CPV with a heat engine will likely lead to an incentive in the future to raise PV cell performances at higher temperatures to better exploit the efficiencies of the engine. At the limit, the PV-HCE could revert to a standard HCE mode beyond the compensation point found from Eq. 6.5, to provide the final temperature gain for the heat engine. In the present example, given an ORC vaporizing at 135 °C, this point is not reached and the entire absorber could be cost-effectively used in PV-HCE mode.

The tradeoffs between the efficiency of CSP only and CPV systems were examined using genetic optimization in Fig. 6-12. A similar optimization is performed to maximize the overall objective function of specific costs [$/W] for the design specifications identified in Chapter 2 (i.e. 25kWh$_e$ day^{-1}), with the results shown in Table 6.4. Despite a slight overall improvement in conversion efficiency, in comparison to CSP only systems the hybrid CPV-CSP system proposed here does not offer an improvement in cost efficiency and does not appear to justify the additional complexity.

6.6 Future Work

Based on optimization results in section 6.5, it seems productive to further benchmark a physical system using a PV-HCE with triple junction a-SI cells. A convenient prototype test section should

be conformable to an existing medium temperature parabolic trough, should include embedded thermocouple sensors, and requires an adequate DC bus for drawing away the current. Combinations of multiple cells in series or parallel will ultimately be necessary, and this aspect is likely to prove challenging due to temperature gradient and illumination irregularity-induced I-V curve mismatch.

Newly available low-cost integrated circuits may make the solutions to this problem both convenient and economical. The challenge lies in the optimum extraction of energy from a PV circuit, which should ideally be biased at voltages where power is maximized. Currently, many DC-DC converters (typically one unit per PV system) can employ an "observe and perturb" algorithm to briefly impose a bias across the array terminals for the purpose of locating the operating point where V*I is at a maximum, in a process known as Maximum Power Point Tracking (MPPT). The single optimum current value is then imposed through all PV devices wired in series. However, if one or more devices in series is shaded, damaged, or exposed to differential temperatures, that device will limit the current of all devices in series, and the available maximum power will deteriorate. This problem is common to all modules and large arrays, but is particularly pertinent to building integrated PV systems in urban areas where partial shading is frequent. It is also an instrinsic feature in cases where solar concentration is employed with linear collectors.

Solar array converters have recently been displaced by DC-DC converter/inverters that operate at the module level within the solar array [134]. The logical next step from module-level MPPT systems, and perhaps a necessary step for concentrated systems, is an individual cell-level MPPT system, where the fullest benefits of the approach can be realized. While this may not be justified for traditional one sun PV systems, such systems would have maximum impact in concentrating systems where the number of individual cells is fewer and the power output per cell is greater.

Systems that accomplish this do not currently exist, but could be developed with a dedicated effort. Existing systems would be cost prohibitive and oversized for the power levels of a single cell in a CPV absorber; they are also inappropriate in their designed voltage ranges. One potentially cost effective approach is to incorporate a new type of switched-mode MPPT integrated circuit (IC), originally developed for cell phone battery chargers, into the insulating glass envelope of the solar absorber in proximity to the PV target. This ameliorates the temperature and distance issues by localizing the MPPT unit while thermally buffering it. Newly available (2010) IC chips (e.g., SPV1040 by STMicroelectronics) with embedded MPPT feature a 100 kHz fixed frequency PWM step-up (or boost) converter and operate a 120 mω N-channel MOSFET power switch and a 140 mω P-channel MOSFET synchronous rectifier at appropriate voltages (0.3-5.2V) and current levels (1A) for single solar cell operation. Manufacturer application notes promote use of SPV1040 outputs in series and/or parallel, however optimization of the PV cell interconnections in this varied-insolation application will require careful characterization of the system and optimization. We anticipate that a dedicated control system will be necessary to integrate an array of SPV1040-based circuits with single CPV-cell inputs and combined DC outputs to a common DC bus (for use with downstream battery or inverter components).

The physical design must balance the difficulties of operating circuitry at high temperatures (given temperature limitations for even military-grade electronics of approximately 150°C) against the losses involved in conducting DC power at very low voltages over long distances. Overcoming this challenge would require modeling the thermal regime in detail using a 2-D variant of the SORCE linear absorber model; a physical design can then be approached with results from the optical and heat transfer outputs of the model. A preliminary effort to gain experience with mounting and operating a CPV test section on SopoNova collectors is pictured in Figure 6-15.

6.7 Summary

In this chapter we studied the hypothesis that synergies may exist between CPV and medium temperature CSP systems. To test this proposition, we extended the simple 5-parameter diode model for PV cells for use with concentrator optics by way of empirical illumination-dependent terms. With this modification, agreement between modeled and experimental results of a temperature sweep at 1.594 and 4.75 suns is good ($> R^2 = 0.97$). We cautiously extrapolate the modified model for use at x factors up to 45 and incorporate it into a PV-SORCE model capable of interrogating the physical and economic tradeoffs of a hybrid PV-Solar ORC system. The specific cost advantages of triple junction a-Si over c-Si cells are noted, and attributed to the more gradual temperature degradation of the amorphous device due to annealing properties, and a-Si is selected for further consideration in a PV–HCE. To guide the conceptual design, we employ a genetic optimization method to maximize or minimize objective criteria such as global efficiency or specific costs by varying important design parameters. The dynamic of interaction between the PV and thermal absorber attributes is explored and type curves are generated for PV cell and absorber efficiencies at varying T and x.

Within the temperature regime and optical parameters explored, there is no obvious local maximum for efficiency favoring either CPV-CSP or CSP alone, nor does their hybridization push the envelope for efficiency further than what could be achieved independently by an optimized CSP system or a low-concentrating CPV system. This result is sensitive to the optical and photovoltaic properties of the cell, and even a slight improvement in these (as can be expected from future advances in PV technology) would tilt the balance in favor of CPV-CSP hybridization.

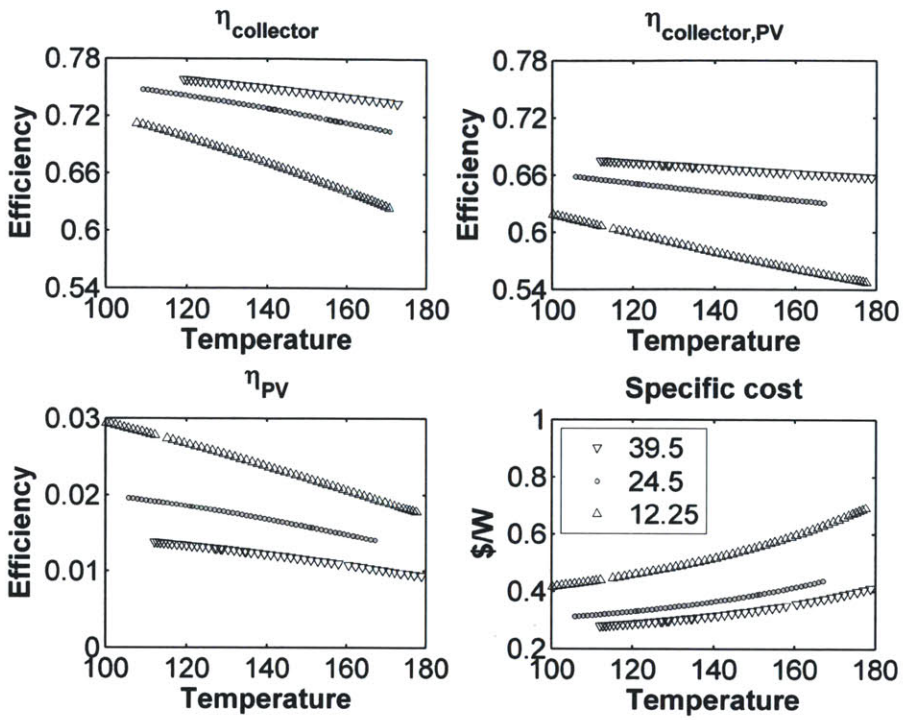

Figure 6-11: Variation of absorber effectiveness and PV efficiency with temperature at three concentration ratios: 12.25, 24.5, and 39.5.

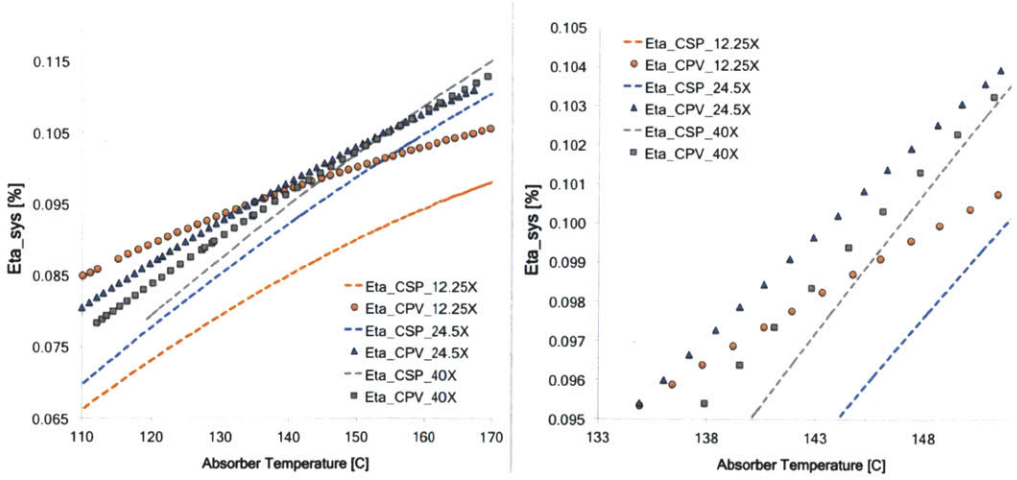

Figure 6-12: Variation of system efficiency for CPV and CSP configurations with temperature ([°C])

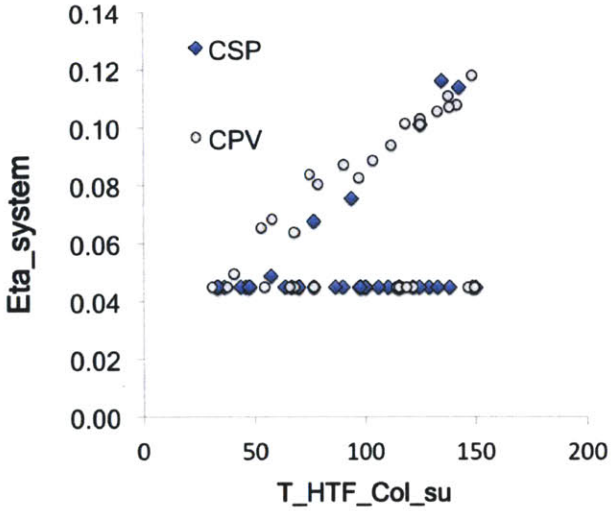

Figure 6-13: Result of a genetic search of the design parameter space to maximize the efficiencies of CPV and CSP

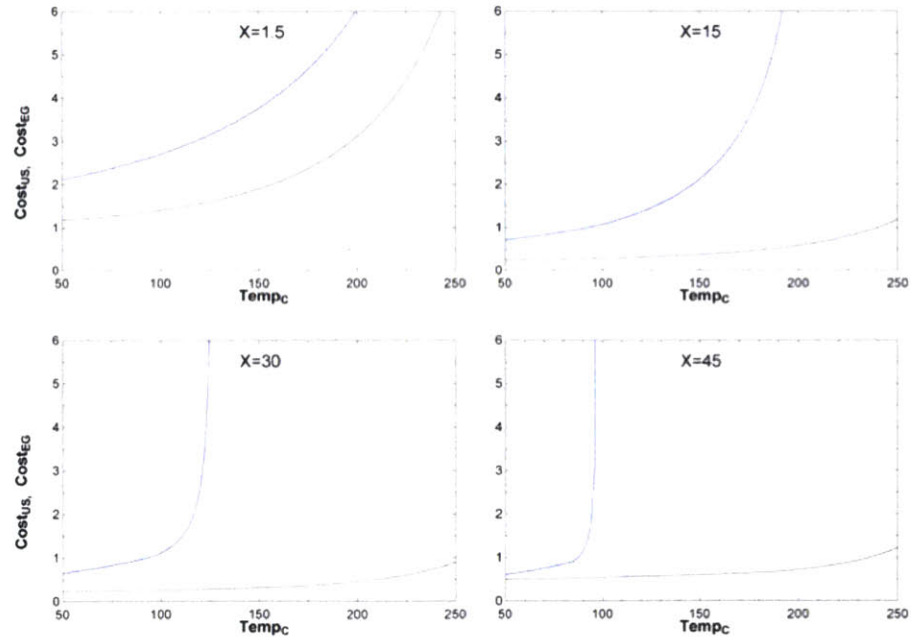

Figure 6-14: Comparison of the specific costs in $ per Watt for Evergreen c-Si cells (blue line) and Uni-Solar a-Si cells (black line) across a temperature gradient and at concentration ratios of 1.5 to 45. Uni-Solar cells outperform the Evergreen cells, especially at higher temperatures and concentrations, with an optimum for Evergreen cells at 5x and Uni-Solar at 30x.

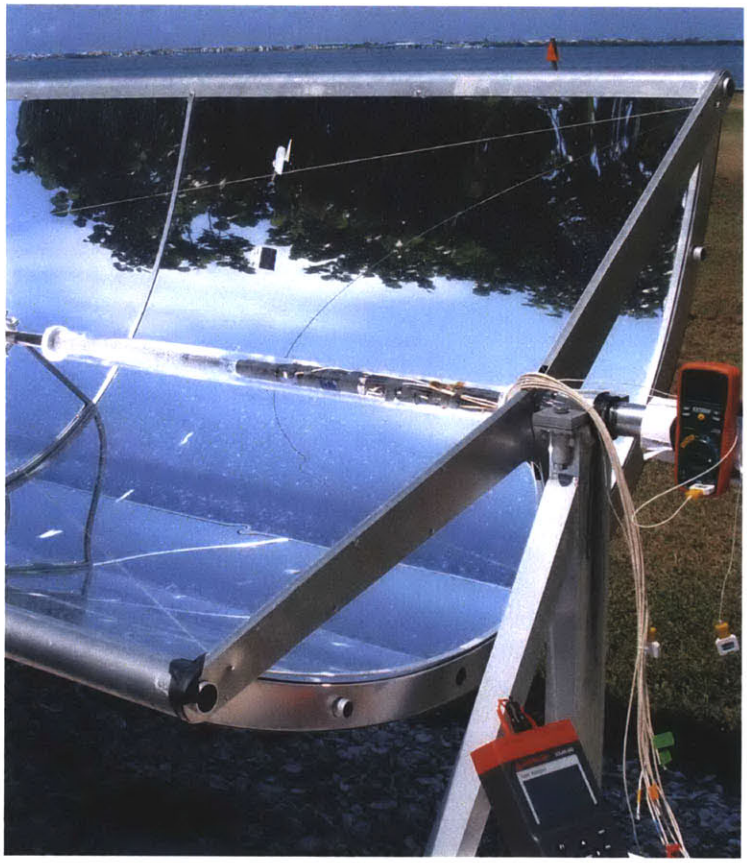

Figure 6-15: Experimental CPV absorber test section in the thermal loop of a SopoNova collector at Eckerd College

Chapter 7

Geometric Design of Scroll Expanders Optimized for Small Organic Rankine Cycles

The information in this chapter is taken directly from a submission to the ASME Journal of Engineering for Gas Turbines and Power (JEGTP), Organic Rankine Cycle (ORC 2011) Special Issue with coauthors A.V. Mueller and H.F. Hemond. It is reprinted here as submitted with additional information on thermo-mechanical model validation and prototype expander development supplied in Appendix C.

Abstract

Background: The application of organic Rankine cycles (ORC) for small scale power generation is inhibited by a lack of suitable expansion devices. Thermodynamic and mechanistic considerations suggest that scroll machines are advantageous in kilowatt–scale ORC equipment, but a method of independently selecting a geometric design optimized for high–volume–ratio ORC scroll expanders is needed. **Method of Approach**: The generalized 8–dimensional planar curve framework of Gravesen et. al., previously developed for scroll compressors, is applied to the expansion scroll, and its useful domain limits are defined. The set of workable scroll geometries is 1) established using a generate–and–test algorithm with inclusion based on theoretical viability and engineering criteria, and 2) the corresponding parameter space is related to thermodynamically relevant metrics through an analytic ranking quantity f_c ('compactness factor') equal to the volume ratio divided by the normalized scroll diameter. **Results**: This method for selecting optimal scroll geometry is described and demonstrated using, as an example, a 3kWe ORC specification. Workable scroll geometry identification is achieved at a rate greater than 3 s^{-1} with standard desktop computing, whereas the originally undefined 8-D parameter space yields an arbitrarily low success rate for determining valid scroll mating pairs. **Conclusions**: The rapid, computationally efficient generation and selection of complex, validated scroll geometries ranked by physically meaningful properties is demonstrated. This procedure represents an essential preliminary qualification for intensive modeling and prototyping efforts necessary to generate new high performance scroll expander designs for kilowatt scale ORC systems.

Keywords: scroll expander design, planar curves, volume ratio, kilowatt–scale organic Rankine cycle

7.1 Background

The Organic Rankine Cycle (ORC) is an established technology for power generation from low temperature (< 300°C) thermal sources (e.g., geothermal, solar, and industrial). ORC applications are generally more economical as the scale of thermal resource or potential load increases, however, as a result of rising energy costs and pressing environmental considerations, the minimum size for a commercially viable ORC unit is presently decreasing into the range of 1–10 kilowatts electrical output.

Whereas large ORC systems can use industrial turbomachinery similar to that widely used in common fossil–fuel–fired thermal power plants, the main challenge to developing ORC equipment in the range of 1–100kW is in the selection of a suitable expander, given the absence of commercially available turbines at this scale. Further, positive-displacement expanders may have certain advantages over small turbines, including lower rotational speeds, proportionally less windage loss, and potentially lower cost due to the availability of machines which can be adapted from HVAC applications, e.g., reversed scroll compressors. The primary drawback of the latter approach is the low intrinsic volume ratio of commercially available scroll machines (typically ~3) which limits the cycle operational temperature range or forces acceptance of under–expansion losses.

Development of a scroll expander optimized for the larger volume ratios encountered in typical ORC applications (3–15 or higher, depending on the temperature and working fluid) would promote the viability of ORC power generation from smaller, distributed thermal resources. While several investigations of scroll expander models and validation experiments are described in the literature [148, 65, 155, 109, 81, 147], discussion of choice of scroll geometry, the single feature upon which all other properties depend, is generally limited to the case of circle involutes in low volume ratio compressor applications [63, 29]. In contrast, the present work explores the effect of varying the basic scroll geometry as a method for developing novel scroll machinery at the higher volume ratios needed for many ORC applications. The results demonstrate a computationally efficient process, based on thermodynamically relevant criteria, for converging on a set of near–optimal candidates for scroll geometry. Details of the algorithm, along with a specific case study, are described in this publication. The complete thermodynamic analysis of a particular scroll expander in an ORC application, such as performed by [93, 44], is beyond the scope of this paper.

7.2 Method of Approach

Development of our design tool was based on the mathematical scroll model described by Gravesen et al. [63], generalized for a wide range of scroll geometries and vectorized for implementation in Matlab. In the following sections we briefly review the planar curve mathematic framework used, discuss the importance of discovering domain limits within the framework, and relate the input parameters to relevant metrics for scroll expander design.

7.2.1 Equations defining scroll geometry

The geometry of the scroll, classically based on circle involutes, was more generally described by Gravesen et al. [63] where the parameterization simplifies to the circle involute as a special case, but cases with varying wall thicknesses can also be modeled. As presented in [63], the planar curves of the scroll wrap are defined by the intrinsic equation linking the arc length s_x to the tangent direction ϕ:

$$s_x = c_1 + c_2 \cdot \phi + c_3 \cdot \phi^2 + c_4 \cdot \phi^3 + c_5 \cdot \phi^4 \tag{7.1}$$

where $c_1..c_5$ are scalar coefficients. Based on this general fourth-order polynomial for s_x and the coordinate system used by Gravesen, Cartesian coordinates for the initial scroll wall, x, can be found analytically, as shown in 7.2.

$$x = (\alpha \cdot sin(\phi) + \beta \cdot cos(phi), \beta \cdot cos(\phi) - \alpha \cdot cos(phi)) \tag{7.2}$$

Parameters α and β are related to the tangent direction, ϕ, and original scalar coefficients as follows:

$$\alpha = (c_1 - 6 \cdot c_3) + (2 \cdot c_2 - 24 \cdot c_4) \cdot \phi + (3 \cdot c_3) \cdot \phi^2 + (4 \cdot c_4) \cdot \phi^3 \tag{7.3}$$

$$\beta = (2 \cdot c_2 - 24 \cdot c_4) + (6 \cdot c_3) \cdot \phi + (12 \cdot c_4) \cdot \phi^2 \tag{7.4}$$

Equations for the mating curve, as well as opposite sides of these scroll walls, are found by reflection and symmetry following the method in [63]. This requires definition of two additional parameters: R, the orbital radius of the moving scroll, and d, a scalar length related to wall thickness. The range of ϕ over which these walls are considered is constrained by definition of N, the desired number of turns of the scroll spiral, such that $\phi_{max} - \phi_{min} = 2\pi \cdot N$. The N consecutive points of conjugacy between the moving scroll (orbiting at radius R) and the fixed scroll, found at $\{\phi_c, \phi_c + 2\pi, \phi_c + 4\pi, ...\}$ for some initial conjugacy angle ϕ_c, represent the terminal points of adjacent internal chambers ("pockets") within which working fluid expansion occurs (Fig. 7-1). For additional details on the determination of conjugacy points and calculation of pocket volumes see [63, 29].

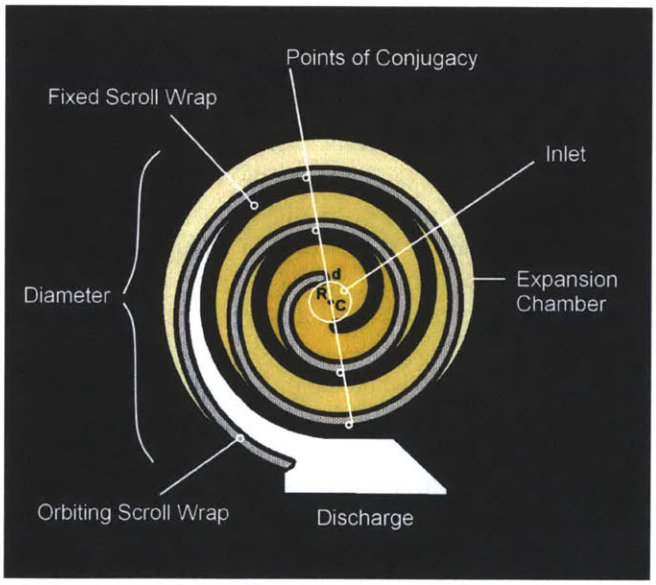

Figure 7-1: The expansion action of the scroll device works via a series of chambers defined by adjacent conjugate points. High pressure vapor enters at the inlet and expands against the orbiting scroll in an expanding chamber following the spiral. The orbit of radius R translates to rotation with a crank. The mating pairs of scroll curves are formed by reflection across the center point C, accounting for the wall thickness scalar d.

The scroll geometry parameter space is thus 8–dimensional, defined by $c_1..c_5$, d, R and N. While the relationship of these parameters to the scroll wall x is analytically derived in [63], the valid domains of these parameters and their effects on important scroll characteristics are not. This

Table 7.1: Viability constraints and parameter domains for the planar curve scroll geometry framework

Viability Constraints	
D_{max}	$D_{max} < 100{\cdot}ln(V_{in})$
R_{norm} **(after normalization)**	$R_{norm} > 2mm$
Wall thickness	$2mm < wall\ thickness < 100mm$
Parameter Domains (with envelopes)	
N	$3 < N < 12$
R	$(2.4241{\cdot}N - 16.1332) < R < 60$
d	$0.5{\cdot}R < d < 30$
c_1	$c_1 = 0$
c_2	$-4 < c_2 < 4$
c_3	$1.0145{\cdot}N - 8.8014 < c_3 < -0.40411{\cdot}N + 18.0718$
	$0.083725{\cdot}d - 4.8712 < c_3 < 0.54374{\cdot}d + 0.63304$
c_4	$-0.058902{\cdot}c_3 - 0.016956 < c_4 < -0.083835{\cdot}c_3 + 1.1011$
c_5	$-0.016401{\cdot}c_4 - 0.0013445 < c_5$
	$c_5 < min(0.02, 0.38923{\cdot}e^{(-0.64318{\cdot}N)} + 0.0014341)$

work addresses this limitation by systematically exploring the parameter domains and relating the eight–dimensional space to relevant design metrics.

7.2.2 Parameter domain definition

Because the parameter space for mating scroll pairs based on the intrinsic equation is infinite, realistic simulation of scrolls to meet physical specifications is greatly aided by knowledge of the parameter domains as they relate to viable examples. To discover envelopes of 'viability islands' within the parameter space and assign relationships to relevant criteria, we employ a generate–and–test algorithm for expanding the parameter domains from an initial set that includes known viable scroll geometries, i.e. the archetypal cases of [63] (circle involute and two examples with increasing wall thicknesses), followed by identification of parameterizations producing unworkable scroll designs.

Scroll designs are unworkable in cases where, e.g, the intrinsic equation produces a non–monotonically increasing spiral that crosses itself or its mating curve, violating the conjugacy between orbiting and fixed scrolls upon which the action of the machine depends; these cases are immediately discarded upon identification. To further improve the quality of resulting scrolls, however, we also include three other criteria of relevance to scroll engineering with which to evaluate potential scroll geometries: wall thickness (for mass and mechanical strength), scroll diameter (form factor, with size limited to D_{max} calculated as a function of V_{in}), and orbital radius R (i.e., the throw of the crank arm for power takeoff). The designer must choose an acceptable range for these values based on material constraints, conformation within the ORC, the mode of power transmission, and potentially on considerations related to leakage, lubrication, etc.; reasonable default values for a kilowatt–scale scroll expander are given in Table 7.1.

Creation of a distribution of useful scrolls proceeds as follows: random values for each parameter are generated from within the defined domains, a scroll is generated based on these parameters, the scroll size is normalized to match the specified inlet volume V_{in}, and finally the geometry is tested against the above criteria for viability and engineering utility (Fig. 7-2). This is repeated until a sufficiently large number of scrolls has been obtained (e.g., 10,000–20,000). At this point,

Table 7.2: Computer system hardware and software configuration

Workstation	
Operating System:	Windows Enterprise 64-bit
Processor:	Intel i7 LGA1366 2.67GHz
RAM:	6 GB
Programming Environment	Matlab R2011b 32-bit
Computation Time	4.3 scrolls·s^{-}1 ($\sigma = 0.23 scrolls{\cdot}s^{-1}$)

the distribution of each parameter is examined to determine whether the range capable of producing a valid scroll has been circumscribed; if no such 'envelope' is detected, the domains are expanded, generating a new scroll distribution, until this condition is met. Examples of the identification envelope relationships are shown in Fig. 7-3. Constraining the infinite domains of the 8–D parameter space for viable scrolls thus limits unproductive simulation effort, and represents a computationally efficient means for selection of optimal scroll geometry.

Because the domain envelopes are expected to be interdependent functions of each other, we characterize them in a hierarchy corresponding to the order of operations in the search algorithm (Table 7.1) and related to their relative independence in determining the outcome of the scroll geometry. The result of this process is a stable valid–scroll identification success rate of approximately 0.02 (valid scrolls per random parameter set generated), or greater than 3 scrolls s^{-1} using the computiational resources described in Table 7.2 and discussed further below. This success rate is a significant improvement over the case of arbitrary domain limits, where the success rate is very low; implementation of envelope identification provided approximately an order of magnitude improvement relative to searching arbitrarily within identified valid domains.

Domains for N, R_{max} and d_{max} are arbitrary and are chosen based on the experience of the researchers to include a reasonable search space. Values of N higher than 12 are possible, but achieving necessary mechanical tolerances presents an engineering challenge as N increases. Valid scroll geometries can also be found for arbitrarily high values of R and d, with the result simply scaled down during normalization. In practice, however, the uniqueness of scroll geometries is sufficiently captured at some finite domain limit for R and d. Finally, c_1 is set to zero because it has no effect on the output other than to locate the curve geometry within the coordinate system.

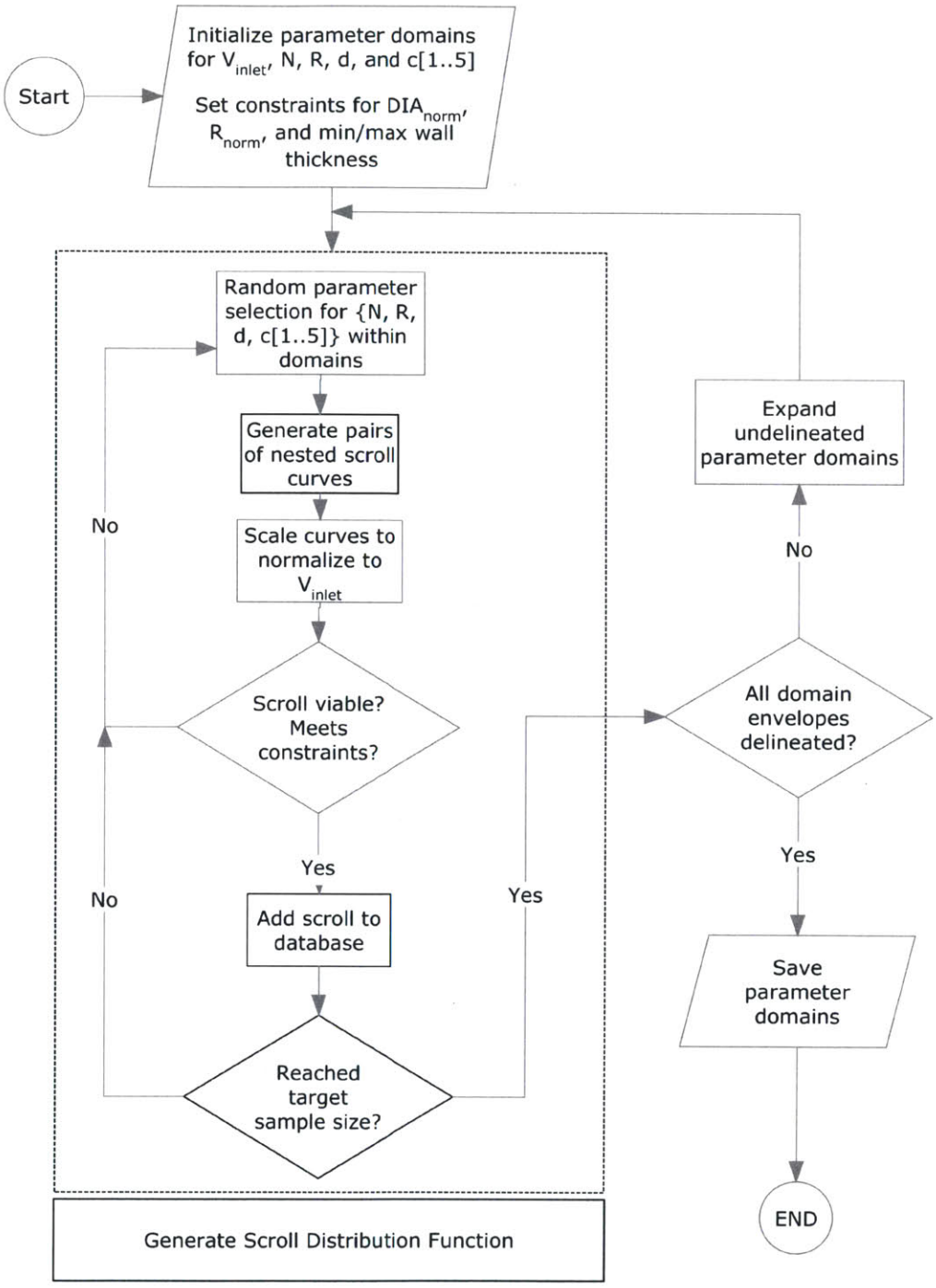

Figure 7-2: Flow diagram for design to development method.

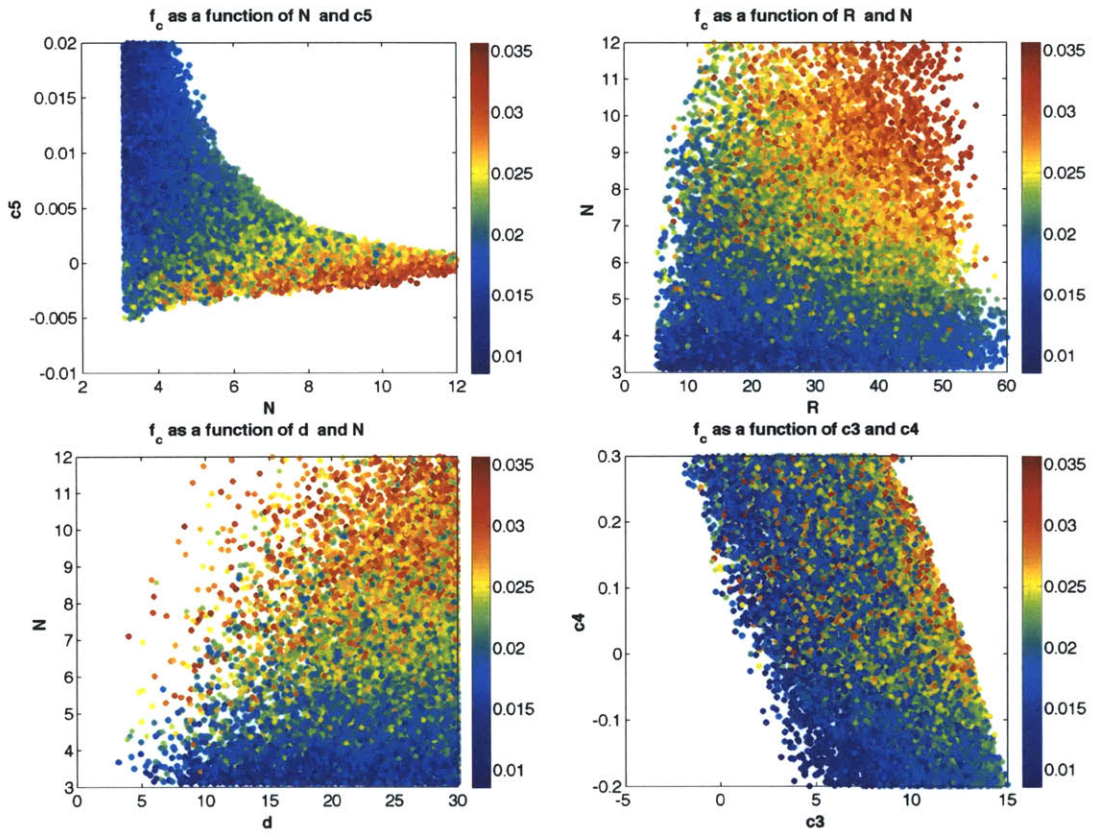

Figure 7-3: Four example scroll distributions are plotted from within the 8–D planar curve parameter space. The color bar represents the value of the proposed 'compactness factor' (volume ratio divided by normalized diameter), and gradients within the domains reveal the relationships of input parameters to this metric. White space indicates non-viability or practical constraint violation. The delineation of these domain envelopes through the algorithm of Fig. 7-2 forms the basis for the equations in Table 7.1. The resulting avoidance of non-productive parameter combinations conserves computation effort and accelerates selection of optimal scroll geometries.

7.2.3 Optimization of scroll geometry

Once a viable set of scrolls has been established with the previous method, optimization is possible over a range of criteria. Ideally, candidates should be chosen for further exploration using a mechanistic and thermodynamic model based on R_v or other geometric data. Gravesen suggested the leakage factor as a possible figure of merit to prioritize further investigation [63] but provided analytic treatment of only tangential leakage, whereas Chen identifies radial leakage as the dominant mode [44]. Within Graveson's generalized framework, radial leakage, which is dependent in large part on arc length, is problematic to compute because the arc length, s_x corresponding to the scaled version of x, cannot be derived analytically. To avoid this difficulty, as well as to simplify the ranking process, an alternative figure of merit – the compactness factor – is proposed.

7.2.4 Rapid selection based on compactness factor

In this study we have essentially normalized tangential leakage by normalizing scroll height, z, using a relationship we derived empirically from measurements of ZR-type scroll compressors ($N = 5$, $R^2 = 0.97$) manufactured by Copeland:

$$z = 7 \cdot V_{in}^{0.58} \tag{7.5}$$

where z is the scroll wrap height in mm and V_{in} is in units of cm^3. This leaves radial leakage, axial friction, and heat loss from the unit as the main relevant physical criteria to inform optimal scroll selection. Analytical calculation of these quantities is both difficult to achieve, as noted above for the case of radial leakage, and computationally expensive given that sufficiently dense coverage of the viable domain may include tens of thousands of potential scroll geometries. We instead propose that radial leakage, axial friction, and heat loss may be captured to a first approximation by aspects of the geometry distilled into a 'compactness factor' (f_c) as a function of the volume ratio R_v and the normalized scroll diameter:

$$f_c = R_v / D_{norm} \tag{7.6}$$

where f_c has units of 1/L. For the assumption of a constant leakage gap height, f_c will be inversely proportional to the radial leakage path as a function of (s_x) for any given R_v. Similarly, by conserving area and volume for a given R_v, fc intrinsically captures an important scale coefficient for both axial friction losses and heat transfer between the scroll and its surroundings. Thus, searching for maximal fc enables rapid, computationally inexpensive selection of a subset of viable scroll geometries that are likely to be close to optimal when evaluating mechanistic and thermodynamic features in an intensive model such as described by [147, 63], including, e.g., refinements for the suction wrap profiles [29] and tradeoffs between tangential and radial leakage as a function of varying z and the normalization factor.

7.3 Results

To illustrate the method proposed above, we provide the following case study wherein we consider the design of an expander for a 3kWe ORC having the characteristics defined in Table 7.3. The nominal expander isentropic efficiency combines assumed values for expander mechanical efficiency (0.8) and small induction generator efficiency (0.82) derived from test bench results using expander-generators based on reversed hermetic scroll compressors and separately tested induction machines [Orosz, unpublished data].

Table 7.3: Design specifications for a 3kW ORC using R245fa.

	Specification	**Units**
Output	3	kWe
$T_{exp,su}$	120	°C
T_{cd}	40	°C
Superheat	5	°C
Rotational speed	3000	RPM
Expander effectiveness	0.66	–
R_v	8.5	–
V_in	24.5	cc/rev
m_{dot}	0.123	kg/s

The data of Table 7.3 show ORC parameters that bear on the expander design, namely the targeted power output [kW], the working fluid temperature differential the rotational speed, and the working fluid (suggested by the ΔT) [125]. Pinch conditions of the heat exchangers may be considered using, e.g., the epsilon-NTU or LMTD method to arrive at actual working fluid conditions, including any superheat, from knowledge of thermal source temperatures [39].

From this data the desired volume ratio, RV, of the expander can be inferred from the working fluid properties assuming 95% volumetric efficiency (reasonable for scrolls) [148, 155, 67] and using an imputed isentropic efficiency from, e.g., [65, 155], which may be inclusive of downstream losses from a generator. These characteristics define the initial volume displacement (V_{in}) of the expansion pockets formed by the scroll wraps as follows:

$$V_{in} = (6{\cdot}10^7){\cdot}\frac{Power{\cdot}v_{in}(T_{su}, P_{su})}{RPM{\cdot}\epsilon_{exp}{\cdot}(h_{su}(T_{su}, P_{su}) - h_{ex}(T_{ex} - P_{ex}))}[cm^3{\cdot}rev^{-1}] \tag{7.7}$$

where $Power$ is in kilowatts. The initial pocket area $A = V_{in}/2z$ because two pockets form and discharge per cycle of the orbiting scroll. Using the wrap height z calculated with Eq. 7.6, initial pocket area can in turn be described as a function of V_{inlet}:

$$A = 71.4{\cdot}V_{in}^{0.42} \tag{7.8}$$

where A is in units of mm^2 and V_{inlet} is in units of cm^3. The search domain is thus set from these criteria-V_{in} relationships and the specified viability constraints from Table 7.1.

The optimization algorithm then proceeds according to Fig. 7-4. Scrolls are simulated, normalized to V_{in}, and checked for viability, with the resulting valid scrolls sub-selected for appropriate values of R_v and ranked based on f_c. Optimal results can be displayed for visual comparison; the scroll identified in this case as optimal is shown in Fig. 7-5. Total computation time to produce this result, along with 137 other potentially useful geometries in the appropriate range of R_v, was approximately 40 minutes using the workstation detailed above viable scroll dataset population of $n = 10,000$. Interestingly, the results with high compactness factor tend not to be true circle involutes. This raises the possibility that unexploited potential for scroll geometry optimization exists that could increase the performance of scroll devices in a variety of applications.

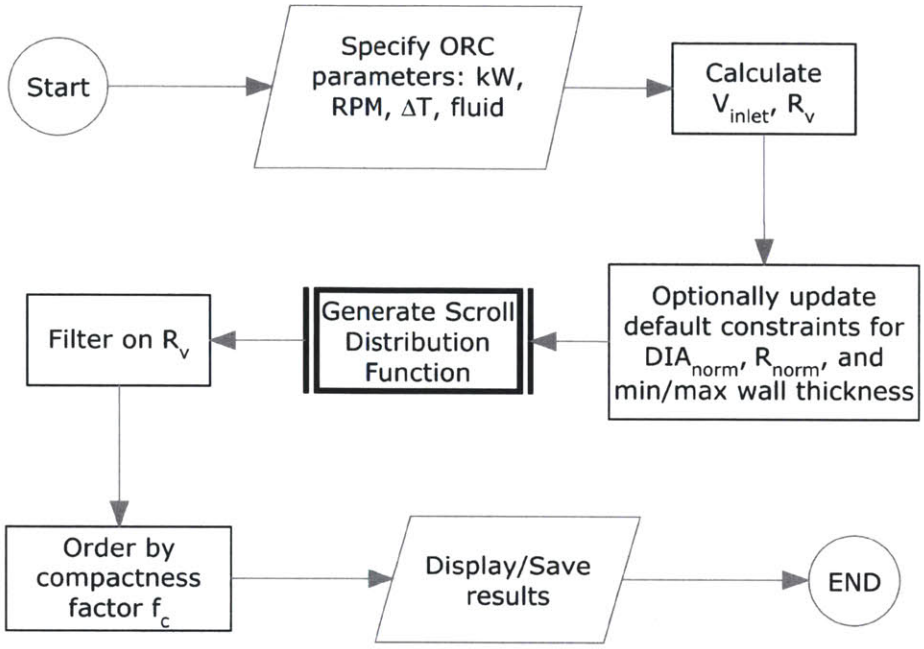

Figure 7-4: Flow diagram for use of design tool in an actual ORC application.

7.4 Conclusions

The generalized scroll geometry framework of Gravesen [63] was employed to develop a design tool for ORC scroll expanders using an algorithm based on the generate-and-test selection process. Computational efficiency is optimized by identifying key domain boundaries within the 8–dimensional parameter space and implementing physically relevant constraints. The success rate for identifying valid scrolls by this method was approximately 2%, enabling computation of valid scroll geometries for a given design specification in <1 hour using standard desktop computing available in 2012. A figure of merit from analytic geometric data, the 'compactness factor' f_c, is proposed as a proxy for identifying scrolls with advantageous properties regarding leakage, friction and heat losses. The procedures are combined into a design tool and its use is demonstrated through selection of an optimal scroll geometry for an example ORC specification. This method provides a rapid and physically meaningful basis for selecting scroll geometries for subsequent, more computationally intensive mechanistic and thermodynamic modeling. The results of this method should promote improved outcomes with detailed expander models and ultimately support the development of high performance scroll expanders in kilowatt–scale ORC systems.

Acknowledgements

This work was supported by the William E. Leonhard Professorship; the MIT Energy Initiative Seed Fund [award number 015728-020]; and the United States Environmental Protection Agency through a P3 Phase II [award number SU 83436701] (This work does not necessarily reflect the views of the Agency and no official endorsement should be inferred).

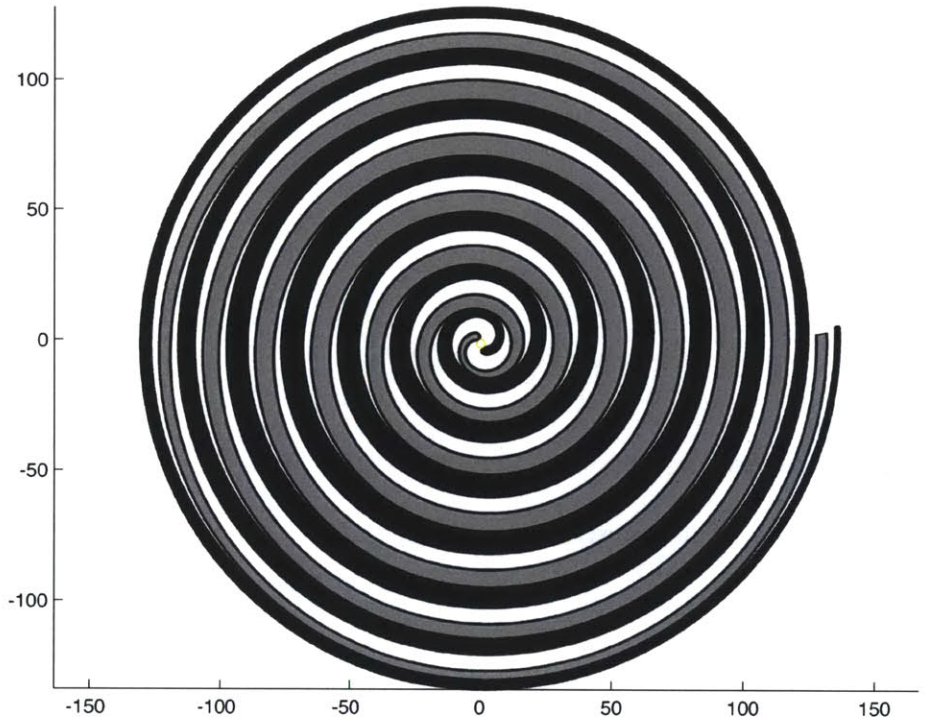

Figure 7-5: A high 'compactness factor' design for a non-circle involute scroll proposed for an ORC case study based on a $R_v = 8.5$. Planar curve parameters chosen are: $c_1 = 0$, $c_2 = -0.44$, $c_3 = 3.8$, $c_4 = 0.3$, $c_5 = -0.0027$, $N = 7.25$, $R = 28.8$, $d = 25.8$. The scaling factor to normalize to $V_{in} = 24.5$ cm^3 is 3.1.

Nomenclature

A	area (m^2)
c	coefficient (–)
D	diameter (mm)
d	wall thickness offset (mm)
f_c	compactness factor (mm^{-1})
h	specific enthalpy ($J \cdot kg^{-1} \cdot K^{-1}$)
m_dot	mass flow rate ($kg \cdot s^{-1}$)
n	scroll sample set size
N	number of wraps
P	pressure
R	radius (mm)
R	ratio (–)
RPM	revolutions per minute (RPM)
T	temperature (°C)
v	specific volume ($m^3 \cdot kg^{-1}$)
V	volume (cm^3)
z	height (mm)

Greek symbols

ϕ	tangent direction
ϵ	effectiveness

Subscripts and superscripts

c	compactness
cd	condenser
ex	exhaust
exp	expander
in	inlet
norm	normalized
su	supply
v	volume

Chapter 8

Conclusion

In this thesis the design space for μ-CSP and PV-thermal hybridization was explored. Using SORCE, we examined some of the main tradeoffs between design parameters (concentration factor, storage and engine size, operating setpoints) by performing optimization searches against the objective criteria of cost and performance for a specified application in remote power generation for health clinics. Some of the practical aspects of selecting equipment and configuring the mechanical systems were highlighted, and experimental data were presented from test solar ORC installations. In over five years of development, much was learned about parabolic trough solar collectors and the working characteristics of an ORC assembled from off-the-shelf components, as well as best practices for deploying systems in remote areas in Africa with local partners, materials and supply chains. This tacit knowledge is an important, if less well documented, aspect of this work.

ORC operation presents many technical challenges, from managing a hermetic system to avoiding pump cavitation and the design of appropriate power management systems. In particular, we found that HVAC scrolls, being optimized for their cooling applications, are not particularly well suited to the volume ratios of a solar ORC operating from a thermal resource at greater than 100°C. Our interim solution is to use two in series, and this is practical if unwieldy. Despite their drawbacks, hermetic HVAC scrolls are nonetheless surprisingly effective expanders, and provide a good benchmark for the high isentropic efficiencies (80%) that are achievable and essential to a viable cycle. Future work through collaboration with the University of Liége will expand upon the scroll geometric modeling described in this thesis, and the prototype development effort based on this work should yield further insight into the potential for adapting the scroll expander format for optimal solar ORC conditions.

The preliminary results of semi-dynamic modeling with SORCE indicate the importance of considering thermal and power generation aspects in the time domain, and field work researching load curves at sites in Lesotho provides some basis for understanding the time-variance of power delivery needs. For performance prediction and cost-sizing, this work is adequate, but for control strategy optimization future work should create a fully dynamic model that handles short duration transients in the solar, thermal and load operating regimes including the thermal loads described in Chapter 2. This aspect will be particularly important if e.g., μ-CSP systems are hybridized with other energy resources (fossil fuels, wind, hydro, PV etc.), especially if the thermal storage component interacts with these sources.

Regarding the hybridization of photovoltaic-thermal systems using medium concentration (<50x), medium-temperature (<200°C) linear optics, preliminary results indicate few cost advantages, but these are highly sensitive to the performance parameters of the investigated cells. Cells having similar thermal characteristics to the triple junction a-Si cell but slightly higher efficiency could make

a hybrid system practical and cost effective. Further investigation of cells with properties meeting the specifications of this application is recommended. If these challenges are met, an integrated circuit individual cell maximum power point tracking approach may be able to surmount the additional challenges of adding the outputs of concentrator PV cells working against temperature and illumination gradients.

Appendix A

Supplementary Materials for Chapter 4

This appendix contains additional tables and as referenced from Chapter 4, including experimental and modeled results.

Table A.1: Specifications of Copeland Scroll Compressors for use as Expanders

Model	**Displacement** [cc/rev]	**Motor Power** [kW]
ZR18	8.5	1.1
ZR22	10.2	1.4
ZR26	12	1.6
ZR34	15.4	2.1
ZR47	21.4	2.9
ZR54	24.4	3.4
ZR57	25.7	3.5
ZR61	27.5	3.8
ZR68	31	4.2
ZR72	32.7	4.5
ZR81	35.9	5
ZR94	42.3	5.8
ZR125	55.7	7.8
ZR144	64.3	9.7

Table A.2: ZR 34, ZR94 and ZR125 scroll expander data from MIT test rig

Motor Power	P_{expsu}	P_{expex}	R245fa Flow	Power	T_{expsu}	T_{expex}	T_{ppsu}	Hz	Ohms	$\eta_{combined}$	r_p	Superheat	r_v	η_{Igen}	η_{exp}
[kW]	[psig]	[psig]	[LPM]	[W]	[C]	[C]	[C]					[C]			
2.1	125.18	30.67	1.94	656	127.14	100.80	23.01	51.46	100.00	0.49	4.08	43.62	3.85	0.55	0.89
2.1	118.7	28.7	1.99	670	125.5	101.2	28.3	50.4	71	0.48	4.14	44.17	3.92	0.55	0.88
2.1	114.1	28.5	2.00	629	125.7	102.5	28.0	52.9	100	0.46	4.00	45.95	3.81	0.54	0.86
2.1	110.0	27.2	1.81	544	126.8	103.4	29.5	48.9	71	0.44	4.05	48.43	3.84	0.51	0.85
2.1	116.6	28.6	2.07	653	125.6	101.8	28.2	51.5	83	0.46	4.08	44.97	3.87	0.55	0.84
2.1	100.48	25.48	1.61	426	122.46	93.73	22.86	47.57	71.00	0.3895	3.94	47.63	3.69	0.47	0.83
2.1	112.2	27.8	1.91	562	127.0	103.5	29.9	49.1	71	0.43	4.03	47.90	3.83	0.52	0.83
2.1	95.3	22.4	1.53	418	130.9	98.8	26.4	50.2	125	0.37	4.26	58.14	3.95	0.47	0.80
2.1	98.8	23.0	1.72	500	130.1	103.1	26.4	48.4	71	0.40	4.29	55.95	4.04	0.50	0.79
2.1	97	20.45	1.6	463	118.2	90.75	25.3	47.9	100	0.3829	4.743	44.72	4.45	0.48	0.79
2.1	120.4	28.7	2.25	679	125.5	100.6	28.4	49.5	63	0.43	4.19	43.51	3.97	0.55	0.78
2.1	82.94	19.01	1.70	462	118.77	95.90	23.10	52.51	83.00	0.37	4.36	51.14	4.14	0.48	0.77
2.1	114.8	26.6	1.96	568	129.9	105.2	27.5	46.8	42	0.40	4.32	49.87	4.09	0.52	0.76
2.1	117.6	29.3	2.18	603	127.3	103.5	30.1	49.6	71	0.41	4.02	46.24	3.81	0.53	0.76
2.1	110.3	28.2	2.21	590	126.1	103.6	27.8	54.6	125	0.40	3.91	47.62	3.72	0.53	0.75
2.1	122.3	26	2	556	114.5	91.1	27.75	45.85	63	0.384	4.702	31.94	4.47	0.52	0.74
2.1	108.2	25.1	1.93	529	129.8	105.6	27.1	46.6	42	0.38	4.31	52.13	4.09	0.51	0.74
2.1	122.1	30.6	2.37	641	129.5	105.5	30.6	49.9	71	0.40	3.99	47.01	3.79	0.54	0.73
2.1	100.5	20.55	1.85	516	114.3	89.25	24.25	47.3	83	0.367	4.888	39.43	4.62	0.50	0.73
2.1	113.15	24.62	2.04	591	128.46	98.28	21.63	46.18	63.00	0.38	4.60	49.00	4.29	0.53	0.72
2.1	122.2	30.5	2.47	641	127.7	103.6	30.2	50.1	71	0.38	4.00	45.13	3.80	0.54	0.70
2.1	90.51	17.47	1.70	472	119.53	93.33	22.96	45.00	83.00	0.34	5.18	48.66	4.88	0.49	0.70
2.1	111.60	24.27	2.09	583	128.59	97.54	21.31	47.02	71.00	0.36	4.60	49.67	4.28	0.53	0.69
2.1	123.6	28.7	2.33	628	130.1	104.9	28.0	47.1	42	0.37	4.31	47.08	4.08	0.54	0.69
2.1	88.69	17.53	1.70	446	118.91	93.74	22.38	45.27	100.00	0.33	5.06	48.80	4.77	0.48	0.69
2.1	124.45	28.13	2.38	662	127.72	99.88	22.77	47.07	63.00	0.38	4.42	44.44	4.16	0.55	0.69
2.1	122.62	28.02	2.37	652	127.95	99.95	22.62	48.01	71.00	0.38	4.38	45.27	4.11	0.55	0.69
2.1	129.6	30.2	2.51	664	130.2	104.6	28.7	47.3	42	0.37	4.29	45.29	4.06	0.55	0.67
2.1	99.05	19.75	1.88	507	128.76	92.85	20.47	45.22	63.00	0.33	5.02	54.48	4.60	0.50	0.66
2.1	109.61	23.98	2.18	573	128.68	96.78	20.95	48.08	83.00	0.34	4.57	50.47	4.25	0.52	0.66
2.1	136.3	33.2	3.02	775	125.3	99.6	30.7	49.7	56	0.38	4.10	38.31	3.88	0.58	0.66
2.1	130.4	33.2	3.00	740	125.2	101.2	30.0	52.9	83	0.37	3.93	40.07	3.73	0.57	0.66
2.1	97.76	19.00	1.85	502	128.82	88.30	20.39	45.81	71.00	0.33	5.15	55.04	4.66	0.50	0.66
2.1	132.8	33.2	3.03	757	125.3	100.6	30.2	51.6	71	0.37	4.00	39.38	3.79	0.57	0.65
2.1	134.8	33.2	3.04	767	125.4	100.2	30.5	50.5	63	0.37	4.06	38.90	3.85	0.58	0.65
2.1	120.41	27.93	2.49	639	128.21	100.00	22.42	49.15	83.00	0.35	4.31	46.27	4.05	0.54	0.65
2.1	96.21	18.18	1.80	485	128.78	82.52	20.43	46.56	83.00	0.32	5.29	55.61	4.72	0.49	0.65
2.1	136.24	32.47	2.96	737	118.72	93.94	24.69	49.15	71.00	0.37	4.20	31.73	3.98	0.57	0.65
2.1	138.08	32.22	2.99	747	117.48	92.18	25.02	48.11	63.00	0.37	4.29	29.93	4.06	0.57	0.64
2.1	107.12	23.45	2.19	555	128.83	95.27	20.50	49.43	100.00	0.33	4.57	51.52	4.22	0.52	0.64
2.1	136.6	32.0	2.83	718	130.4	104.4	29.3	47.5	42	0.36	4.27	43.31	4.04	0.56	0.63
2.1	152.6	38.1	3.53	858	122.9	96.9	33.5	49.6	50	0.38	4.01	31.08	3.79	0.60	0.63
2.1	138.96	29.65	3.22	805	118.93	90.07	28.87	48.78	63.00	0.35	4.69	31.11	4.40	0.58	0.59
2.1	140.84	30.35	3.17	786	120.94	95.07	27.25	49.55	83.00	0.34	4.64	32.56	4.39	0.58	0.59
2.1	143.24	30.01	3.23	807	120.64	93.89	28.14	48.20	71.00	0.34	4.77	31.55	4.51	0.59	0.58
2.1	271.1	48.7	6	1740	143.9	88.5	34.3	59.1		0.3643	5.567	25.48	4.92	0.72	0.50
2.1	232	36.4	5.2	1480	124.2	95.2	30	56.3		0.3492	6.374	13.43	6.04	0.69	0.50
2.1	149.8	20.6	2.6	805	156.1	104	21.5	51.5		0.293	7.272	65.12	6.46	0.58	0.50
2.1	228	34.6	4.7	1436	139.4	106.1	28	55.9		0.341	6.59	29.46	6.18	0.69	0.49
2.1	279.4	50.4	6.3	1810	146.2	103.3	35.3	59.5		0.361	5.544	26.27	5.08	0.73	0.49
2.1	282.7	53.5	6.9	1855	138.6	102.8	36.6	60.2		0.3629	5.284	18.07	4.93	0.74	0.49
2.1	157.4	21.6	2.6	780	155.8	107.3	21.4	48.4		0.2848	7.287	62.69	6.54	0.58	0.49
2.1	136	12.6	2.2	800	154.8	64.8	17.5	51.4		0.2864	10.79	67.88	8.61	0.58	0.49
2.1	214.7	33	4	1234	154.3	111.3	23.6	53.8		0.3219	6.506	47.21	5.94	0.66	0.49
2.1	195.4	28.1	3.4	1032	155.4	109.3	21.4	51.4		0.3006	6.954	52.68	6.29	0.63	0.48

Continued...

Motor Power	$P_{exp_{su}}$	$P_{exp_{ex}}$	R245fa Flow	Power	$T_{exp_{su}}$	$T_{exp_{ex}}$	$T_{pp_{su}}$	Hz	Ohms	$\eta_{combined}$	r_p	Superheat	r_v	η_{lgen}	η_{exp}
2.1	284.9	56.5	7.7	1800	129.6	95.6	39.2	59.6		0.3447	5.042	8.679	4.73	0.73	0.47
2.1	142	19.7	2.6	736	156.4	98	21.9	55.4		0.2681	7.208	67.68	6.29	0.57	0.47
2.1	228.8	37.3	5.8	1410	115	82	35.1	55.8		0.3227	6.134	4.895	5.75	0.69	0.47
2.1	221.8	27	4.8	1423	126.4	85.4	35.8	53.1		0.3175	8.215	17.77	7.54	0.69	0.46
2.1	225.8	29.5	5.2	1485	126	84.2	37.3	56.3		0.3191	7.654	16.52	7.01	0.70	0.46
2.1	201.9	23.9	4.5	1314	125.9	85.1	31.2	58.5		0.3015	8.448	21.68	7.74	0.67	0.45
2.1	169	16.9	3	1033	157.2	94.6	17.9	54.8		0.2818	10	61	8.65	0.63	0.45
2.1	231	33.8	4.7	1370	151.4	111	25.3	54.9		0.3034	6.834	40.84	6.29	0.68	0.45
2.1	182.1	20.1	3.5	1137	148.5	102	19.4	56.2		0.2878	9.06	48.98	8.18	0.65	0.44
2.1	244.2	32.1	5.6	1580	132.2	85.1	38.4	57.4		0.3126	7.607	18.95	6.87	0.71	0.44
2.1	256.5	34	5.9	1754	141.8	98.6	40	59		0.3207	7.544	26.14	6.91	0.73	0.44
2.1	135	18.9	2.6	654	156.3	83.6	22.9	57.9		0.2391	7.143	69.69	5.99	0.55	0.44
2.1	263.2	33.7	5.9	1758	142	98.9	39.8	56.3		0.3171	7.81	25.06	7.16	0.73	0.44
2.1	228.4	34.9	5.3	1400	144.8	100.8	40.1	67		0.297	6.544	34.78	5.96	0.68	0.43
2.1	214.1	26.9	5	1355	125.7	85.3	34.2	59		0.2927	7.959	18.74	7.31	0.68	0.43
2.1	172.7	16.9	3.8	1133	124.5	97.3	24.3	56.3		0.2749	10.22	27.34	9.70	0.65	0.43
2.1	256.5	33.6	6.4	1772	143.8	92.3	39.3	59.5		0.2939	7.634	28.14	6.83	0.73	0.40
2.1	249.6	34.4	6.5	1703	142.3	99.4	39.9	63.2	timestep	0.2861	7.256	27.98	6.64	0.72	0.40
5.8	150.3	36.4	6.5	1525	121.7	101.1	40.9	46.8	15401	0.3616	4.129	30.57	3.97	0.52	0.70
5.8	167.2	38.2	7.1	1850	128.8	97.5	42.2	45	1997	0.3814	4.377	33.07	4.09	0.55	0.69
5.8	150.9	32.4	6.1	1612	133	102.3	37.7	44	1427	0.3579	4.657	41.7	4.36	0.53	0.68
5.8	152.1	31.8	6	1600	135.9	101.6	36.5	43.5	1220	0.3508	4.783	44.27	4.43	0.53	0.67
5.8	189.4	47.4	8	2000	143.4	111.5	44.6	47.8	1901	0.3766	3.996	42.1	3.74	0.57	0.67
5.8	204	50.7	8	2128	155.1	99.3	38.5	48.1	14650	0.3804	4.024	50.4	3.54	0.58	0.66
5.8	213.4	53.8	8.5	2280	156.1	107	38.7	48.5	14741	0.3885	3.967	49.3	3.55	0.59	0.66
5.8	196.7	50.1	8.3	2020	145.1	109.5	46.7	48.4	2320	0.3725	3.926	42.08	3.64	0.57	0.66
5.8	187.1	46.8	8	1950	142.5	110.2	44.5	48.2	2172	0.3676	3.998	41.76	3.73	0.56	0.66
5.8	190	48.3	8.1	1950	143.8	112.5	45.4	47.7	1803	0.367	3.934	42.36	3.69	0.56	0.65
5.8	215.2	55.7	8.8	2260	154.2	113.9	40.4	48.5	14837	0.3836	3.864	47	3.54	0.59	0.65
5.8	187.5	48.6	7.6	1800	147.7	111.8	39.7	48	1390	0.356	3.858	46.86	3.57	0.55	0.65
5.8	203.7	48.6	9	2264	135.7	117.6	45.6	48.5	15071	0.3822	4.191	31.06	4.07	0.59	0.65
5.8	176.2	40.1	7.2	1695	128.9	96.1	43.1	45	2189	0.3466	4.394	30.85	4.09	0.54	0.65
5.8	188.7	47.1	8	1912	143	110.7	44.6	47.9	2034	0.3597	4.006	41.87	3.74	0.56	0.65
5.8	184.3	46.3	7.5	1800	147.8	109.8	38.6	49.3	1290	0.351	3.981	47.74	3.66	0.55	0.64
5.8	220.6	57	9.3	2325	150.7	117.5	41.7	48.8	14942	0.3802	3.87	42.33	3.62	0.59	0.64
5.8	188.4	49.7	7.6	1708	147.6	113.3	41.4	47.3	1519	0.3438	3.791	46.54	3.52	0.54	0.64
5.8	165.8	38.5	7.5	1764	129.9	98.9	42.2	45	1800	0.3462	4.306	34.53	4.03	0.54	0.64
5.8	152.6	34	6.6	1520	127.3	100.3	39.7	43.7	1680	0.328	4.488	35.52	4.24	0.52	0.64
5.8	192.9	49.3	8.1	1862	144.1	114	43.5	47.4	1645	0.3506	3.913	41.97	3.68	0.55	0.63
5.8	143.1	28.9	5.9	1500	135.6	100.3	35.6	43	1078	0.3252	4.952	46.55	4.58	0.51	0.63
5.8	212.2	59.3	8.9	1970	155.2	115.2	46.5	48.3	2490	0.3533	3.578	48.66	3.28	0.56	0.63
5.8	177.7	36.2	7.3	2010	142.2	85.6	32.1	48.7	14484	0.3509	4.909	43.77	4.29	0.57	0.62
5.8	139.2	28.9	6.3	1410	137.5	96.6	35.4	45	958	0.2885	4.817	49.61	4.38	0.50	0.57
7.8	189.2	54.6	8.8	2270	128	87.6	48.8	45	2080	0.4649	3.465	26.75	3.16	0.53	0.87
7.8	201.5	60.1	9.2	2370	133.2	89	49	45.2	2198	0.4716	3.353	29.07	3.03	0.54	0.87
7.8	180.5	50.6	8.5	2175	124.8	85.9	46.9	44.4	1803	0.4514	3.567	25.67	3.26	0.53	0.86
7.8	204.3	61.2	9.5	2390	133.5	91.5	51.5	45.4	2554	0.4654	3.338	28.73	3.03	0.54	0.86
7.8	201.3	60.1	9.5	2348	129.2	91.3	50.6	45.2	2401	0.4625	3.349	25.11	3.08	0.54	0.86
7.8	178.9	50.2	8.45	2145	124.7	86.1	47.4	44.3	1886	0.4482	3.564	25.97	3.26	0.52	0.85
7.8	203.4	59.8	9.5	2423	130.7	91.2	48.8	45.3	2307	0.467	3.401	26.13	3.11	0.55	0.85
7.8	191.1	54.9	9	2295	128.9	86.8	48.2	45	2003	0.4562	3.481	27.2	3.16	0.54	0.85
7.8	136.8	37.6	6.15	1459	130.3	95.15	32.5	49.06	5419	0.3774	3.638	43.09	3.35	0.45	0.83
7.8	171.3	47.1	8.3	2050	123.8	85.8	45.8	44	1680	0.4264	3.637	27	3.33	0.52	0.83
7.8	180.5	51.1	8.3	2100	136.6	110.8	47.9	45	15392	0.4297	3.532	37.47	3.35	0.52	0.83
7.8	206.2	62.6	9.4	2300	141	105.3	43.3	45	14947	0.4361	3.294	35.8	3.05	0.54	0.81
7.8	191.5	57	8.5	2100	145	109	43.8	45	15274	0.4225	3.36	43.2	3.11	0.52	0.81
7.8	171.6	46.6	8.4	2060	124.1	84.6	45.1	44.7	1499	0.4183	3.682	27.22	3.36	0.52	0.81
7.8	202.8	56.8	9.2	2430	143	108	45.4	45	15123	0.4384	3.57	38.57	3.31	0.55	0.80
7.8	135.6	36.35	6.05	1393	130.8	93.55	30.6	50.33	9682	0.3571	3.729	44.02	3.42	0.45	0.80

Continued...

Motor Power	$\mathbf{P}_{expsu}$	$\mathbf{P}_{expex}$	**R245fa Flow**	**Power**	$\mathbf{T}_{expsu}$	$\mathbf{T}_{expex}$	$\mathbf{T}_{ppsu}$	**Hz**	**Ohms**	$\eta_{combined}$	$\mathbf{r}_p$	**Superheat**	$\mathbf{r}_v$	η_{Igen}	η_{exp}
7.8	164.2	44.9	8.4	1913	120.1	84.6	44.4	45.7	1307	0.3939	3.657	25.16	3.37	0.50	0.78
7.8	213.3	59.9	9.4	2465	150.4	107.1	43	45.4	11934	0.4246	3.561	43.62	3.24	0.55	0.77
7.8	209.2	58.5	9.6	2391	138.6	103.2	43.3	45	14822	0.4202	3.576	32.73	3.31	0.54	0.77
7.8	165.5	45.1	8.4	1885	120.5	84.9	44.3	45.7	1213	0.3868	3.67	25.21	3.38	0.50	0.77
7.8	205.3	58.5	9.4	2420	149.1	91.5	41	47.8	11731	0.4197	3.509	44.1	3.06	0.55	0.77
7.8	212.2	57	10	2478	135.9	102.1	45.3	45	14689	0.4127	3.723	29.36	3.47	0.55	0.75
7.8	214	55.7	10.3	2581	134.8	102.5	45.4	45.1	14558	0.4101	3.842	27.86	3.59	0.56	0.73
7.8	210.7	57.6	10.3	2445	135.5	103.2	43.2	45.7	14405	0.399	3.658	29.29	3.42	0.55	0.73
7.8	241.9	63.9	10.4	2350	161.8	111.4	53	45.1	866	0.3483	3.786	49.01	3.39	0.54	0.64

Table A.3: **Experimental data from nepsolar field at PSA, Spain**

Month	**Day**	**Hour**	$\mathbf{v}_dot, su$	$\mathbf{T}_su$	**Wind2m**	$\mathbf{T}_local$	**DNI**	$\mathbf{T}_ex$	$\mathbf{Col}_\eta$	**Power**	Δ**T**
			[m^3/hour]	[C]	[m/s]	[C]	[W/m^2]	[C]		W	[C]
Sep	6	11.37	1.00	102.30	3.89	26.44	851.00	153.90	0.58	13595	51.59
Sep	6	11.48	1.00	102.20	4.32	27.07	859.90	160.00	0.62	15341	57.76
Sep	6	12.02	1.50	102.80	3.33	27.55	869.60	131.10	0.62	18934	28.34
Sep	6	12.07	1.50	103.20	3.10	27.56	875.20	132.20	0.62	19491	28.99
Sep	6	12.10	1.50	103.00	3.40	27.44	874.00	132.70	0.63	19908	29.69
Sep	6	12.78	1.00	98.79	3.31	28.24	882.70	191.00	0.61	25318	92.22
Sep	6	12.85	1.00	97.88	3.53	28.52	886.00	192.40	0.61	25936	94.49
Sep	6	12.90	1.00	97.31	4.04	28.15	886.10	193.90	0.62	26725	96.62
Sep	6	15.35	2.00	100.40	5.22	29.88	879.90	118.70	0.49	21084	18.27
Sep	6	15.42	2.00	104.00	3.95	29.96	877.50	122.10	0.50	20963	18.07
Sep	6	15.48	2.00	107.00	3.91	29.86	876.90	125.00	0.52	21083	18.03
Sep	6	15.80	2.50	104.10	4.37	30.13	873.90	121.70	0.70	25249	17.59
Sep	6	15.85	2.50	102.70	4.33	30.02	872.90	120.20	0.71	25134	17.54
Sep	6	15.90	2.50	101.60	5.08	29.64	870.30	119.20	0.73	25185	17.63
Sep	6	16.08	3.01	99.21	4.23	30.02	868.20	112.20	0.69	22194	12.95
Sep	6	16.12	3.00	98.70	4.15	30.35	871.00	111.60	0.69	21933	12.89
Sep	6	16.17	3.00	98.31	4.84	30.15	870.00	110.90	0.69	21519	12.63
Sep	7	11.85	1.00	122.00	1.91	30.66	880.70	188.70	0.62	18374	66.7
Sep	7	11.95	1.01	121.20	2.44	30.81	881.30	190.30	0.64	19507	69.12
Sep	7	12.00	1.00	120.50	2.60	30.98	882.00	191.00	0.62	19429	70.53
Sep	7	12.45	1.50	125.40	1.82	30.79	894.60	156.10	0.57	21354	30.71
Sep	7	12.50	1.50	125.20	2.79	30.75	894.90	158.00	0.60	22827	32.75
Sep	7	12.55	1.50	125.50	2.35	30.68	893.30	158.70	0.60	23176	33.21
Sep	7	12.78	2.00	127.80	2.76	31.76	900.50	148.80	0.60	25629	21.03
Sep	7	12.85	2.00	127.30	2.79	31.87	902.30	148.90	0.60	26302	21.63
Sep	7	12.88	2.00	127.70	2.63	31.87	906.10	148.90	0.58	25700	21.18
Sep	7	14.42	2.50	128.70	3.72	32.99	904.30	147.90	0.56	28759	19.18
Sep	7	14.47	2.51	128.60	3.92	32.75	907.30	147.90	0.57	29055	19.32
Sep	7	14.50	2.50	128.60	0.84	32.44	905.20	148.10	0.57	29226	19.48
Sep	7	14.68	3.00	129.00	2.37	32.76	885.10	144.00	0.55	27024	14.97
Sep	7	14.73	3.00	128.90	3.97	32.92	880.30	143.80	0.55	26832	14.92
Sep	7	14.80	3.00	129.00	2.01	32.73	879.70	143.60	0.55	26236	14.55
Sep	7	15.53	2.99	154.80	5.11	32.98	868.90	167.10	0.57	22845	12.27
Sep	7	15.58	2.99	152.60	3.43	32.86	868.80	166.50	0.66	25805	13.87
Sep	7	15.72	2.99	149.40	2.76	32.85	871.90	162.00	0.63	23308	12.62
Sep	7	15.88	2.50	148.50	4.13	32.79	866.70	163.40	0.66	22885	14.86
Sep	7	15.93	2.50	149.80	3.28	32.85	864.70	163.20	0.61	20662	13.4
Sep	7	15.98	2.50	149.90	4.06	33.08	862.50	163.70	0.64	21190	13.75
Sep	8	15.53	3.01	179.00	3.92	34.57	935.80	191.90	0.58	25098	12.87
Sep	8	15.87	2.50	177.90	3.19	34.33	925.10	193.00	0.65	24221	15.09
Sep	8	15.92	2.50	177.70	4.89	34.51	935.40	192.60	0.65	23947	14.93
Sep	8	15.97	2.50	177.60	4.16	34.32	936.90	192.50	0.66	23967	14.94
Sep	8	16.30	2.00	176.60	3.84	34.49	921.30	193.50	0.69	21946	16.87
Sep	8	16.35	2.01	176.70	3.60	34.31	913.90	193.00	0.69	21350	16.32
Sep	8	16.40	2.00	176.40	4.58	34.40	914.90	192.50	0.69	20876	16.11
Sep	8	16.63	1.50	175.50	4.22	34.66	906.10	201.00	0.68	19006	25.48
Sep	8	16.67	1.50	175.00	4.54	34.58	892.20	200.40	0.71	19036	25.38
Sep	8	16.72	1.50	174.50	3.40	34.21	904.40	198.80	0.68	18213	24.3
Sep	8	17.00	1.20	172.30	3.09	34.12	872.00	206.70	0.66	15141	34.4
Sep	8	17.03	1.20	172.00	4.50	33.92	875.70	206.60	0.67	15157	34.58
Sep	8	17.10	1.20	171.30	3.23	33.75	873.90	206.00	0.69	15202	34.71

Table A.4: **SORCE model results for predicting data of tabletable:NEP**

Month	**Day**	**Hour**	**Col$_\eta$**	**Optics** [kW]	**Conduction** [kW]	**Convection** [kW]	**Radiation** [kW]	**Power$_{in}$** [W]	**Power$_{out}$** [W]	**HTF$_{Outlet}$** [C]	**DELTA$_T$** [C]	**THETA** [degrees]	**AIM**	**IAM**	**Power$_{model}$** [W]
Sep	6	11.37	45.46	8.058	0.01944	3.069	0.7784	24572	11170	153.1	50.8	59.92	0.5013	0.9524	13373
Sep	6	11.48	45.88	8.51	0.02041	3.199	0.7723	25983	11922	156.3	54.08	58.36	0.5246	0.953	14296
Sep	6	12.02	50.31	10.67	0.015	2.638	0.7564	32285	16243	131.6	28.77	49.87	0.6446	0.9486	19231
Sep	6	12.07	50.49	10.92	0.01483	2.648	0.7813	33072	16697	132.6	29.41	49	0.656	0.9491	19784
Sep	6	12.1	50.52	11.01	0.01529	2.697	0.7612	33374	16860	132.8	29.79	48.48	0.6629	0.9494	19977
Sep	6	12.78	51.18	12.41	0.02366	4.248	1.092	41654	21319	193.2	94.43	34.99	0.8193	0.9948	25994
Sep	6	12.85	51.69	12.47	0.02436	4.363	1.085	42594	22017	195.4	97.5	33.42	0.8346	1	26861
Sep	6	12.9	51.98	12.48	0.02552	4.5	1.038	43150	22428	196	98.67	32.28	0.8454	1	27363
Sep	6	15.35	56.13	12.39	0.01559	2.887	0.6901	42745	23995	124.7	24.29	32.5	0.8434	1	28265
Sep	6	15.42	55.5	12.35	0.01482	2.823	0.7579	41860	23231	127.5	23.5	34.09	0.8282	0.999	27462
Sep	6	15.48	54.86	12.33	0.01519	2.853	0.766	41161	22583	129.7	22.75	35.42	0.8149	0.9927	26772
Sep	6	15.8	53.03	11.95	0.01412	2.571	0.6878	37345	19803	120.4	16.28	42.11	0.7419	0.9637	23320
Sep	6	15.85	52.84	11.83	0.01379	2.514	0.6802	36719	19402	118.7	15.95	43.09	0.7303	0.9604	22808
Sep	6	15.9	52.57	11.68	0.01427	2.522	0.6408	36027	18938	117.2	15.6	44.05	0.7187	0.9575	22231
Sep	6	16.08	52.26	11.14	0.01245	2.273	0.6458	33852	17691	111.3	12.07	47.4	0.6769	0.9506	20670
Sep	6	16.12	52.22	11.05	0.01222	2.237	0.6464	33497	17492	110.7	12.01	48.11	0.6677	0.9498	20424
Sep	6	16.17	52.04	10.86	0.01272	2.257	0.6145	32881	17112	110	11.73	48.99	0.6562	0.9491	19969
Sep	7	11.85	46.08	10.25	0.01909	3.411	1.227	31015	14290	185.9	63.94	52.31	0.6114	0.949	17556
Sep	7	11.95	46.28	10.64	0.02055	3.602	1.137	32182	14892	186.3	65.13	50.66	0.634	0.9485	18292
Sep	7	12	46.3	10.84	0.02117	3.697	1.128	32785	15179	188.4	67.93	49.81	0.6453	0.9487	18656
Sep	7	12.45	51.29	12.29	0.01585	3.018	1.134	38587	19792	159.8	34.42	41.51	0.7488	0.9658	24053
Sep	7	12.5	51.38	12.37	0.01806	3.286	0.9899	39191	20138	160.2	35.02	40.51	0.7603	0.9697	24475
Sep	7	12.55	51.78	12.42	0.01731	3.228	1.057	39709	20562	161.2	35.73	39.49	0.7717	0.974	25008
Sep	7	12.78	54.25	12.67	0.01674	3.183	0.9798	42700	23166	150.8	22.97	34.59	0.8232	0.9966	28062
Sep	7	12.85	54.83	12.71	0.01679	3.214	0.9839	43574	23893	151	23.73	33.03	0.8384	1	28939
Sep	7	12.88	55.08	12.76	0.01663	3.215	1.011	44093	24287	151.9	24.16	32.35	0.8448	1	29434
Sep	7	14.42	54.88	15.56	0.01824	3.512	0.9344	51505	28266	151.4	22.75	8.578	0.9888	0.9889	34267
Sep	7	14.47	55.1	15.4	0.01857	3.547	0.9172	51472	28361	151.4	22.76	9.963	0.9849	0.993	34379
Sep	7	14.5	55.93	15.22	0.01175	2.603	1.519	51218	28647	151.6	23.05	10.79	0.9823	0.996	34729
Sep	7	14.68	56.59	13.9	0.01549	3.176	1.062	49083	27778	147.5	18.54	15.69	0.9628	1	33614
Sep	7	14.73	56.62	13.57	0.01801	3.428	0.8917	48484	27449	147.3	18.39	17.02	0.9562	1	33211
Sep	7	14.8	57.15	13.24	0.01472	3.063	1.116	47948	27404	147.3	18.3	18.87	0.9463	1	33158
Sep	7	15.53	51.51	12.2	0.02388	3.959	0.887	40302	20758	168.6	13.77	36.37	0.8053	0.9882	25683
Sep	7	15.58	51.51	12.17	0.02078	3.649	0.9964	39737	20469	166.2	13.59	37.43	0.7941	0.9832	25273
Sep	7	15.72	50.83	12.07	0.01883	3.378	1.038	38283	19460	162.4	12.96	40.33	0.7623	0.9704	23950
Sep	7	15.88	49.36	11.7	0.02127	3.548	0.8975	36218	17877	162.8	14.3	43.49	0.7255	0.9592	21997
Sep	7	15.93	49.07	11.56	0.02003	3.438	0.9707	35560	17450	163.7	13.93	44.44	0.714	0.9565	21493
Sep	7	15.98	48.64	11.4	0.02127	3.522	0.9015	34896	16974	163.5	13.57	45.38	0.7024	0.9542	20905
Sep	8	15.53	50.4	13.14	0.02651	4.631	1.147	43485	21915	193.2	14.17	36.22	0.8067	0.9889	27693
Sep	8	15.87	47.61	12.54	0.02478	4.332	1.2	38895	18519	192.5	14.58	43.12	0.7299	0.9603	23383
Sep	8	15.92	47.09	12.56	0.02805	4.606	1.029	38711	18228	192.1	14.36	44.07	0.7185	0.9575	23010
Sep	8	15.97	46.91	12.44	0.02671	4.481	1.083	38155	17897	191.7	14.09	45.01	0.707	0.9551	22588
Sep	8	16.3	45	11.09	0.02591	4.293	1.09	33529	15089	191.3	14.67	50.81	0.6318	0.9485	19032
Sep	8	16.35	44.73	10.8	0.02537	4.226	1.109	32668	14614	190.8	14.12	51.64	0.6206	0.9487	18431
Sep	8	16.4	44.36	10.61	0.02716	4.354	1.014	32114	14246	190.3	13.89	52.45	0.6094	0.949	17961
Sep	8	16.63	42.61	9.574	0.02729	4.38	1.061	29160	12425	196.7	21.15	56.03	0.5587	0.9518	15700
Sep	8	16.67	42.21	9.273	0.02767	4.369	1.022	28267	11932	195.2	20.21	56.63	0.55	0.9523	15065
Sep	8	16.72	42.48	9.207	0.02535	4.168	1.125	28093	11934	194.7	20.18	57.36	0.5393	0.9527	15061
Sep	8	17	39.26	7.95	0.02516	4.118	1.168	24133	9475	199.7	27.41	61.28	0.4805	0.9503	11972
Sep	8	17.03	38.64	7.898	0.02807	4.353	1.017	23925	9244	198.9	26.87	61.68	0.4743	0.9493	11675
Sep	8	17.1	38.44	7.695	0.02518	4.071	1.127	23159	8903	197.2	25.9	62.61	0.4601	0.9462	11233

Time	Date	P_{low}	HTF_{sup}	Vap_{exp}	HTF_{exp}	Pre_{sup}	$RecupH_{sup}$	exp_{exp}	P_{high}	P_{mid}	HTF_{flow}	WF_{flow}
		psig	C	C	C	C	C	C	psig	psig	LPM	LPM
6:27:29 PM	1/25	43.70	112.01	106.97	94.04	60.81	31.06	77.72	119.24	122.85	28.26	7.26
6:28:29 PM	1/25	42.29	109.93	106.04	94.85	61.04	31.23	79.29	121.24	125.49	30.93	7.25
6:29:30 PM	1/25	41.66	107.70	102.06	94.38	61.09	31.26	79.72	121.09	125.34	33.09	7.27
9:41:29 PM	1/25	27.52	117.80	111.79	93.40	39.86	25.22	42.16	92.25	90.01	22.44	5.69
9:43:03 PM	1/25	38.11	115.36	113.65	95.34	50.32	25.24	62.46	128.54	127.61	27.19	5.66
9:44:20 PM	1/25	39.33	111.98	110.19	95.50	53.74	25.07	66.66	129.28	128.24	30.75	5.71
9:45:30 PM	1/25	39.64	109.26	105.77	94.49	55.22	25.07	69.64	127.84	126.64	33.54	5.75
9:46:39 PM	1/25	39.42	106.74	97.89	93.90	55.94	25.41	72.34	127.42	126.35	34.68	5.81
9:47:37 PM	1/25	39.20	105.14	93.98	92.65	55.39	24.90	70.76	124.60	123.42	35.33	5.81
7:15:30 PM	1/27	41.09	96.38	88.49	85.09	55.92	27.55	71.35	111.39	109.91	36.75	6.35
7:16:30 PM	1/27	41.29	95.72	87.27	84.27	55.60	27.55	70.17	108.86	107.29	36.68	6.35

Time	VDC	ADC	VAC	AAC	Power Factor	ORC Power	Ohms	NOTES	HTF_{in}	$epsilon_{exp}$	$epsilon_{gen}$	RPM	Model Power
	V	A	V/ph	A/ph		kW			kW				
6:27:29 PM	394.00	4.05	120	1.80	0.80	1.60	167	ATS Test - Resistive Load	33.95	0.64	0.54	5491	1.558
6:28:29 PM	343.00	5.15	115	3.00	0.80	1.77	100	ATS Test - Resistive Load	33.64	0.70	0.55	5354	1.614
6:29:30 PM	320.00	5.57	100	3.00	0.70	1.78	83	ATS Test - Resistive Load	32.99	0.72	0.55	5277	1.595
9:41:29 PM	71.20	13.90	110	4.00	0.14	0.99		ATS Test - Battery Load	31.33	0.55	0.47	5883	1.561
9:43:03 PM	71.20	14.30	93	5.20	0.93	1.02		ATS Test - Battery Load	29.12	0.58	0.48	4037	1.258
9:44:20 PM	71.10	14.10	126	3.10	0.90	1.00		ATS Test - Battery Load	28.27	0.58	0.47	3983	1.179
9:45:30 PM	72.30	14.10	50	5.50	0.90	1.02		ATS Test - Battery Load	27.57	0.60	0.48	3981	1.166
9:46:39 PM	69.60	13.75	106	6.10	0.91	0.96		ATS Test - Battery Load	26.56	0.59	0.47	3882	1.147
9:47:37 PM	71.00	13.20	54	5.70	0.93	0.94		ATS Test - Battery Load	26.12	0.59	0.47	3908	1.102
7:15:30 PM	140.00	6.40				0.90		Pilot Test - Battery Load	27.83	0.52	0.46	4761	1.078
7:16:30 PM	135.00	6.00				0.81		Pilot Test - Battery Load	27.75	0.49	0.45	4864	1.213

Table A.5: Raytrace output from Soltrace program for opticial interception of NEP 1200 collector at varying incidence angles

Mirror hits	**Absorber hits**	**Percent**	**Theta**
9725	9862	1.01	90.0
9704	9793	1.00	76.0
9722	9757	1.00	63.4
9760	9717	0.99	53.1
9731	9581	0.98	45.0
9721	9518	0.97	38.7
9735	9456	0.97	33.7
9736	9422	0.96	29.7
9717	9366	0.96	26.6
9703	8945	0.92	18.4
9651	7662	0.79	14.0

Appendix B

CPV Experimental Data

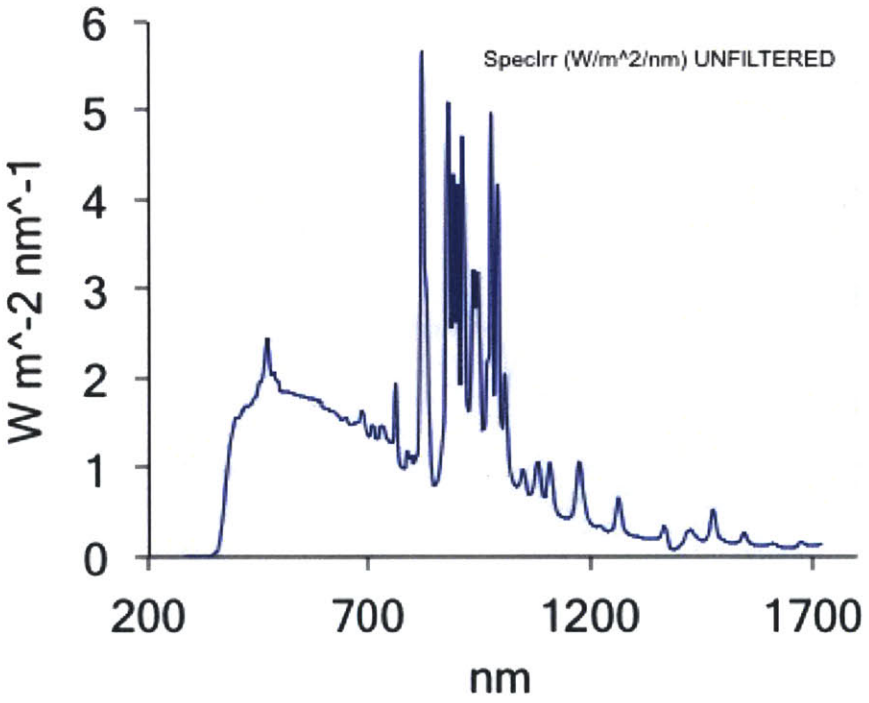

Figure B-1: Spectral output of the Oriel Solar Simulator used in PV Cell benchmarking

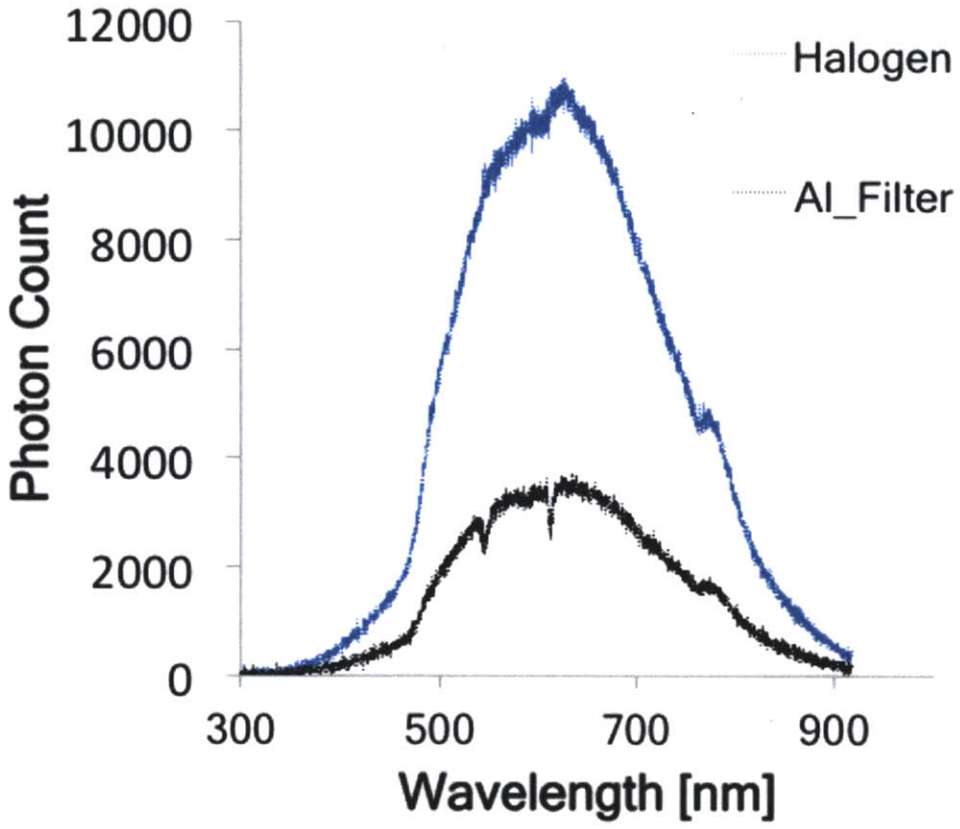

Figure B-2: Neutral filtering of a halogen lamp simulated solar spectrum with a 33.5% open Aluminum mesh

Table B.1: Measured PV cell parameters under variable illumination and temperature

Vopen (V)	Ishort (A)	Vmaxp (V)	Imaxp (A)	Pmax (W)	T [C]	W/m2	Filter	W	Efficiency	FF	Rsh	Rs
1.5_{EG_A}												
0.565	0.742	0.426	0.658	0.28	44	4745	0.336	1.824	0.154	0.668	4.58	0.12
0.508	0.79	0.366	0.685	0.25	54	4745	0.336	1.824	0.137	0.623	3.45	0.11
0.529	0.762	0.39	0.666	0.259	57	4745	0.336	1.824	0.142	0.643	3.96	0.12
0.523	0.762	0.387	0.66	0.255	60	4745	0.336	1.824	0.140	0.640	3.87	0.11
0.514	0.771	0.379	0.657	0.249	65	4745	0.336	1.824	0.137	0.628	3.87	0.12
0.503	0.771	0.359	0.673	0.241	70	4745	0.336	1.824	0.132	0.621	3.55	0.11
0.493	0.77	0.359	0.652	0.234	76	4745	0.336	1.824	0.128	0.616	3.39	0.12
0.485	0.776	0.349	0.651	0.227	82	4745	0.336	1.824	0.124	0.603	3.39	0.11
0.47	0.778	0.331	0.654	0.216	90	4745	0.336	1.824	0.118	0.591	3.07	0.25
0.442	0.783	0.313	0.647	0.202	102	4745	0.336	1.824	0.111	0.584	2.99	0.13
0.428	0.783	0.298	0.648	0.193	112	4745	0.336	1.824	0.106	0.576	2.69	0.13
0.409	0.791	0.279	0.643	0.179	122	4745	0.336	1.824	0.098	0.553	2.48	0.13
0.395	0.791	0.262	0.649	0.17	131	4745	0.336	1.824	0.093	0.544	2.33	0.13
0.373	0.792	0.247	0.628	0.155	143	4745	0.336	1.824	0.085	0.525	2.06	0.14
0.358	0.796	0.246	0.589	0.144	151	4745	0.336	1.824	0.079	0.505	1.97	0.13
0.34	0.794	0.218	0.614	0.133	163	4745	0.336	1.824	0.073	0.493	1.63	0.14
0.315	0.794	0.198	0.593	0.117	176	4745	0.336	1.824	0.064	0.468	1.35	0.15
0.305	0.795	0.191	0.583	0.111	183	4745	0.336	1.824	0.061	0.458	1.26	0.15
0.293	0.795	0.188	0.551	0.103	191	4745	0.336	1.824	0.056	0.442	1.14	0.14
0.273	0.796	0.182	0.504	0.091	202	4745	0.336	1.824	0.050	0.419	0.99	0.14
0.272	0.802	0.18	0.497	0.089	204	4745	0.336	1.824	0.049	0.408	0.94	0.14
0.256	0.801	0.175	0.449	0.078	215	4745	0.336	1.824	0.043	0.380	0.88	0.15
0.227	0.79	0.121	0.521	0.063	229	4745	0.336	1.824	0.035	0.351	0.69	0.14
1.5_{EG_D}												
0.575	0.725	0.427	0.662	0.283	32	4745	0.336	1.824	0.155	0.679	5.81	0.13
0.567	0.728	0.425	0.655	0.278	35	4745	0.336	1.824	0.152	0.673	5.75	0.12
0.55	0.734	0.409	0.651	0.266	44	4745	0.336	1.824	0.146	0.659	5.03	0.13
0.537	0.738	0.393	0.654	0.257	50	4745	0.336	1.824	0.141	0.648	4.77	0.12
0.523	0.734	0.368	0.67	0.246	57	4745	0.336	1.824	0.135	0.641	4.58	0.13
0.516	0.736	0.374	0.643	0.24	64	4745	0.336	1.824	0.132	0.632	4.38	0.13
0.501	0.738	0.357	0.64	0.228	72	4745	0.336	1.824	0.125	0.617	4.16	0.14
0.49	0.745	0.35	0.631	0.22	79	4745	0.336	1.824	0.121	0.603	3.83	0.14
0.468	0.745	0.318	0.645	0.205	91	4745	0.336	1.824	0.112	0.588	3.51	0.22
0.443	0.752	0.311	0.622	0.193	101	4745	0.336	1.824	0.106	0.579	3.14	0.22
0.425	0.751	0.289	0.626	0.18	110	4745	0.336	1.824	0.099	0.564	2.91	0.15
0.413	0.753	0.285	0.608	0.173	115	4745	0.336	1.824	0.095	0.556	2.71	0.15
0.405	0.756	0.276	0.605	0.167	121	4745	0.336	1.824	0.092	0.545	2.58	0.15
0.391	0.758	0.255	0.616	0.157	127	4745	0.336	1.824	0.086	0.530	2.39	0.15
0.377	0.759	0.255	0.582	0.148	135	4745	0.336	1.824	0.081	0.517	2.19	0.16
0.364	0.763	0.233	0.595	0.138	144	4745	0.336	1.824	0.076	0.497	1.97	0.16

Continued...

Vopen (V)	Ishort (A)	Vmaxp (V)	Imaxp (A)	Pmax (W)	T [C]	W/m2	Filter	W	Efficiency	FF	Rsh	Rs
0.352	0.761	0.226	0.578	0.13	150	4745	0.336	1.824	0.071	0.485	1.80	0.17
0.339	0.767	0.219	0.557	0.122	157	4745	0.336	1.824	0.067	0.469	1.66	0.17
0.329	0.761	0.208	0.563	0.117	164	4745	0.336	1.824	0.064	0.467	1.52	0.17
0.314	0.762	0.194	0.554	0.107	171	4745	0.336	1.824	0.059	0.447	1.35	0.17
0.303	0.759	0.184	0.546	0.1	178	4745	0.336	1.824	0.055	0.435	1.21	0.16
$1.5_{EG_{Drep}}$												
0.583	0.68	0.435	0.612	0.266	31	4745	0.336	1.824	0.146	0.671	5.37	0.14
0.567	0.693	0.41	0.633	0.259	37	4745	0.336	1.824	0.142	0.659	4.94	0.13
0.557	0.696	0.403	0.631	0.254	43	4745	0.336	1.824	0.139	0.655	4.94	0.13
0.539	0.709	0.392	0.623	0.244	52	4745	0.336	1.824	0.134	0.638	4.28	0.14
0.521	0.716	0.374	0.625	0.233	62	4745	0.336	1.824	0.128	0.625	3.96	0.14
0.502	0.719	0.351	0.628	0.22	72	4745	0.336	1.824	0.121	0.610	3.67	0.14
0.491	0.728	0.346	0.621	0.215	80	4745	0.336	1.824	0.118	0.601	3.46	0.14
0.475	0.726	0.325	0.634	0.206	87	4745	0.336	1.824	0.113	0.597	3.31	0.23
0.473	0.73	0.331	0.618	0.204	89	4745	0.336	1.824	0.112	0.591	3.18	0.28
0.468	0.728	0.323	0.626	0.202	91	4745	0.336	1.824	0.111	0.593	3.21	0.27
0.465	0.732	0.32	0.624	0.199	92	4745	0.336	1.824	0.109	0.585	3.07	0.23
0.453	0.735	0.315	0.627	0.197	94	4745	0.336	1.824	0.108	0.592	3.00	0.14
0.445	0.734	0.32	0.597	0.191	100	4745	0.336	1.824	0.105	0.585	2.92	0.15
0.425	0.737	0.29	0.614	0.178	110	4745	0.336	1.824	0.098	0.568	2.63	0.15
0.406	0.742	0.276	0.599	0.165	120	4745	0.336	1.824	0.090	0.548	2.40	0.15
0.396	0.742	0.265	0.599	0.158	130	4745	0.336	1.824	0.087	0.538	2.24	0.16
0.382	0.748	0.254	0.583	0.148	137	4745	0.336	1.824	0.081	0.518	2.05	0.16
0.374	0.747	0.251	0.568	0.142	143	4745	0.336	1.824	0.078	0.508	1.97	0.16
0.363	0.747	0.232	0.583	0.135	150	4745	0.336	1.824	0.074	0.498	1.82	0.16
0.338	0.755	0.208	0.573	0.119	162	4745	0.336	1.824	0.065	0.466	1.49	0.18
0.326	0.749	0.201	0.554	0.111	169	4745	0.336	1.824	0.061	0.455	1.36	0.20
0.316	0.752	0.2	0.527	0.105	174	4745	0.336	1.824	0.058	0.442	1.28	0.19
0.321	0.749	0.208	0.539	0.112	180	4745	0.336	1.824	0.061	0.466	1.35	0.17
4.7_{EG_E}												
7 0.585	1.898	0.367	1.607	0.589	48	4745	1	5.428	0.109	0.530	1.72	0.09
0.54	1.92	0.332	1.6	0.531	58	4745	1	5.428	0.098	0.512	1.53	0.09
0.528	1.923	0.33	1.551	0.512	66	4745	1	5.428	0.094	0.504	1.42	0.09
0.516	1.924	0.33	1.488	0.491	69	4745	1	5.428	0.090	0.495	1.31	0.09
0.499	1.922	0.309	1.486	0.459	80	4745	1	5.428	0.085	0.479	1.24	0.09
0.48	1.927	0.298	1.426	0.425	90	4745	1	5.428	0.078	0.459	1.09	0.14
0.46	1.922	0.278	1.422	0.395	100	4745	1	5.428	0.073	0.447	0.95	0.09
0.43	1.916	0.262	1.354	0.354	111	4745	1	5.428	0.065	0.430	0.75	0.10
0.419	1.913	0.253	1.326	0.335	124	4745	1	5.428	0.062	0.418	0.70	0.10
0.394	1.897	0.226	1.315	0.297	133	4745	1	5.428	0.055	0.397	0.59	0.10
0.38	1.891	0.221	1.26	0.278	140	4745	1	5.428	0.051	0.387	0.52	0.10
0.368	1.872	0.213	1.223	0.26	147	4745	1	5.428	0.048	0.377	0.48	0.10
0.35	1.855	0.209	1.137	0.237	158	4745	1	5.428	0.044	0.365	0.42	0.10

Continued...

Vopen (V)	Ishort (A)	Vmaxp (V)	Imaxp (A)	Pmax (W)	T [C]	W/m2	Filter	W	Efficiency	FF	Rsh	Rs
0.329	1.813	0.188	1.111	0.209	171	4745	1	5.428	0.039	0.350	0.38	0.11
0.317	1.824	0.182	1.07	0.194	181	4745	1	5.428	0.036	0.336	0.34	0.10
4.7_{EG_F}												
0.581	1.81	0.376	1.52	0.571	42	4745	1	5.428	0.105	0.543	1.68	0.09
0.552	1.824	0.364	1.471	0.535	51	4745	1	5.428	0.099	0.531	1.53	0.09
0.535	1.833	0.347	1.466	0.508	61	4745	1	5.428	0.094	0.518	1.42	0.08
0.521	1.841	0.339	1.436	0.487	66	4745	1	5.428	0.090	0.508	1.36	0.08
0.508	1.845	0.325	1.426	0.463	72	4745	1	5.428	0.085	0.494	1.27	0.08
0.493	1.845	0.305	1.426	0.435	82	4745	1	5.428	0.080	0.478	1.18	0.09
0.478	1.854	0.299	1.372	0.41	90	4745	1	5.428	0.076	0.463	1.10	0.14
0.449	1.844	0.279	1.352	0.377	102	4745	1	5.428	0.069	0.455	0.93	0.09
0.433	1.841	0.259	1.35	0.349	111	4745	1	5.428	0.064	0.438	0.80	0.09
0.418	1.84	0.247	1.324	0.327	117	4745	1	5.428	0.060	0.425	0.72	0.10
0.405	1.834	0.237	1.296	0.307	125	4745	1	5.428	0.057	0.413	0.64	0.10
0.377	1.813	0.224	1.185	0.265	131	4745	1	5.428	0.049	0.388	0.52	0.10
0.364	1.798	0.21	1.187	0.249	137	4745	1	5.428	0.046	0.380	0.47	0.10
0.339	1.773	0.194	1.111	0.215	149	4745	1	5.428	0.040	0.358	0.40	0.11
0.347	1.768	0.202	1.096	0.221	156	4745	1	5.428	0.041	0.360	0.41	0.11
0.327	1.736	0.185	1.088	0.201	166	4745	1	5.428	0.037	0.354	0.37	0.11
0.323	1.727	0.188	1.071	0.201	169	4745	1	5.428	0.037	0.360	0.38	0.10
0.305	1.678	0.183	0.95	0.174	181	4745	1	5.428	0.032	0.340	0.33	0.11
4.7_{EG_Erep}												
0.579	1.821	0.373	1.506	0.561	48	4745	1	5.428	0.103	0.532	1.38	0.10
0.549	1.835	0.352	1.492	0.525	55	4745	1	5.428	0.097	0.521	1.25	0.09
0.534	1.842	0.345	1.461	0.504	62	4745	1	5.428	0.093	0.512	1.18	0.09
0.524	1.856	0.34	1.435	0.488	66	4745	1	5.428	0.090	0.502	1.17	0.09
0.504	1.866	0.316	1.43	0.452	76	4745	1	5.428	0.083	0.481	1.07	0.09
0.494	1.864	0.307	1.416	0.434	83	4745	1	5.428	0.080	0.471	1.00	0.09
0.489	1.863	0.301	1.416	0.426	86	4745	1	5.428	0.078	0.468	0.96	0.09
0.485	1.869	0.292	1.433	0.418	88	4745	1	5.428	0.077	0.461	0.96	0.12
0.482	1.868	0.292	1.419	0.414	90	4745	1	5.428	0.076	0.460	0.91	0.14
0.478	1.864	0.293	1.391	0.407	92	4745	1	5.428	0.075	0.457	0.91	0.15
0.475	1.873	0.281	1.436	0.403	94	4745	1	5.428	0.074	0.453	0.91	0.15
0.47	1.865	0.29	1.367	0.396	96	4745	1	5.428	0.073	0.452	0.86	0.14
0.465	1.871	0.286	1.36	0.388	98	4745	1	5.428	0.071	0.446	0.83	0.11
0.459	1.869	0.281	1.371	0.385	100	4745	1	5.428	0.071	0.449	0.83	0.09
0.441	1.871	0.271	1.335	0.361	108	4745	1	5.428	0.067	0.438	0.76	0.09
0.434	1.87	0.269	1.309	0.352	115	4745	1	5.428	0.065	0.434	0.74	0.09
0.418	1.867	0.255	1.282	0.326	125	4745	1	5.428	0.060	0.418	0.63	0.10
0.397	1.858	0.238	1.251	0.297	133	4745	1	5.428	0.055	0.403	0.55	0.10
0.382	1.852	0.224	1.222	0.273	142	4745	1	5.428	0.050	0.386	0.49	0.10
0.361	1.828	0.202	1.219	0.246	155	4745	1	5.428	0.045	0.373	0.43	0.10
0.335	1.792	0.189	1.123	0.212	166	4745	1	5.428	0.039	0.353	0.37	0.10

Continued...

Vopen (V)	Ishort (A)	Vmaxp (V)	Imaxp (A)	Pmax (W)	T [C]	W/m2	Filter	W	Efficiency	FF	Rsh	Rs
0.321	1.778	0.183	1.067	0.195	172	4745	1	5.428	0.036	0.342	0.35	0.11
0.313	1.74	0.179	1.044	0.186	177	4745	1	5.428	0.034	0.342	0.33	0.11
$4.7_{EG_F rep}$												
0.608	1.839	0.4	1.545	0.618	36	4745	1	5.428	0.114	0.553	1.53	0.10
0.577	1.866	0.375	1.555	0.583	44	4745	1	5.428	0.107	0.541	1.44	0.09
0.565	1.86	0.371	1.525	0.565	49	4745	1	5.428	0.104	0.538	1.33	0.09
0.553	1.868	0.367	1.494	0.548	54	4745	1	5.428	0.101	0.530	1.29	0.09
0.543	1.873	0.359	1.486	0.533	58	4745	1	5.428	0.098	0.524	1.24	0.09
0.538	1.878	0.346	1.514	0.524	62	4745	1	5.428	0.097	0.519	1.24	0.09
0.526	1.877	0.333	1.502	0.5	70	4745	1	5.428	0.092	0.506	1.14	0.09
0.511	1.882	0.326	1.455	0.474	80	4745	1	5.428	0.087	0.493	1.06	0.09
0.487	1.889	0.294	1.474	0.433	90	4745	1	5.428	0.080	0.471	0.98	0.09
0.485	1.889	0.297	1.448	0.43	92	4745	1	5.428	0.079	0.469	0.94	0.12
0.482	1.891	0.289	1.462	0.422	95	4745	1	5.428	0.078	0.463	0.95	0.14
0.474	1.897	0.285	1.442	0.411	98	4745	1	5.428	0.076	0.457	0.94	0.15
0.453	1.885	0.288	1.357	0.39	105	4745	1	5.428	0.072	0.457	0.86	0.09
0.439	1.9	0.271	1.355	0.367	115	4745	1	5.428	0.068	0.440	0.79	0.09
0.413	1.882	0.254	1.28	0.325	129	4745	1	5.428	0.060	0.418	0.62	0.10
0.405	1.877	0.248	1.264	0.313	131	4745	1	5.428	0.058	0.412	0.57	0.10
0.393	1.883	0.227	1.293	0.293	139	4745	1	5.428	0.054	0.396	0.54	0.10
0.378	1.876	0.224	1.226	0.274	148	4745	1	5.428	0.050	0.386	0.49	0.10
0.353	1.843	0.2	1.191	0.238	162	4745	1	5.428	0.044	0.366	0.41	0.10
0.341	1.815	0.192	1.162	0.223	168	4745	1	5.428	0.041	0.360	0.37	0.11
0.332	1.795	0.187	1.125	0.21	173	4745	1	5.428	0.039	0.352	0.34	0.11
0.326	1.782	0.19	1.069	0.203	177	4745	1	5.428	0.037	0.349	0.34	0.11
0.321	1.778	0.183	1.078	0.197	180	4745	1	5.428	0.036	0.345	0.33	0.11
1.5_{US_B}												
2.155	0.297	1.593	0.244	0.389	34.6	4745	0.336	5.783	0.067	0.608	52.80	1.43
2.107	0.299	1.546	0.249	0.385	38.7	4745	0.336	5.783	0.067	0.611	52.14	1.29
2.081	0.299	1.559	0.245	0.382	41.2	4745	0.336	5.783	0.066	0.614	52.13	1.10
2.055	0.299	1.547	0.245	0.379	43.7	4745	0.336	5.783	0.066	0.617	51.63	1.10
2.031	0.3	1.522	0.246	0.375	49.8	4745	0.336	5.783	0.065	0.615	50.91	1.17
2.004	0.302	1.489	0.249	0.371	55	4745	0.336	5.783	0.064	0.613	49.09	1.19
1.972	0.303	1.471	0.248	0.365	59.2	4745	0.336	5.783	0.063	0.611	49.45	1.14
1.917	0.305	1.415	0.254	0.36	64.9	4745	0.336	5.783	0.062	0.616	48.10	1.07
1.878	0.306	1.423	0.248	0.354	70	4745	0.336	5.783	0.061	0.616	47.65	1.10
1.854	0.308	1.376	0.254	0.35	73	4745	0.336	5.783	0.061	0.613	48.87	1.03
1.805	0.308	1.316	0.258	0.34	79.2	4745	0.336	5.783	0.059	0.612	45.61	1.06
1.777	0.308	1.347	0.248	0.334	82.7	4745	0.336	5.783	0.058	0.610	45.51	1.01
1.735	0.31	1.308	0.25	0.327	89	4745	0.336	5.783	0.057	0.608	45.43	0.99
1.713	0.311	1.251	0.257	0.321	92	4745	0.336	5.783	0.056	0.603	44.59	1.02
1.69	0.309	1.222	0.26	0.317	95.2	4745	0.336	5.783	0.055	0.607	45.94	1.04
1.658	0.312	1.198	0.26	0.312	99.4	4745	0.336	5.783	0.054	0.603	42.50	1.04

Continued...

Vopen (V)	Ishort (A)	Vmaxp (V)	Imaxp (A)	Pmax (W)	T [C]	W/m2	Filter	W	Efficiency	FF	Rsh	Rs
1.608	0.312	1.149	0.266	0.306	105.2	4745	0.336	5.783	0.053	0.610	44.93	0.95
1.589	0.314	1.13	0.266	0.301	107	4745	0.336	5.783	0.052	0.603	42.12	1.00
1.543	0.316	1.086	0.268	0.291	113.3	4745	0.336	5.783	0.050	0.597	40.45	0.96
1.483	0.318	1.056	0.26	0.275	122.3	4745	0.336	5.783	0.048	0.583	38.02	1.02
1.447	0.319	1.001	0.266	0.266	128.2	4745	0.336	5.783	0.046	0.576	36.75	1.00
1.424	0.317	0.988	0.264	0.261	131.2	4745	0.336	5.783	0.045	0.578	39.50	1.00
1.382	0.32	0.941	0.267	0.251	138.6	4745	0.336	5.783	0.043	0.568	35.42	1.00
1.331	0.32	0.908	0.267	0.242	144.7	4745	0.336	5.783	0.042	0.568	35.09	1.00
1.308	0.32	0.897	0.265	0.237	148.1	4745	0.336	5.783	0.041	0.566	34.61	0.99
1.272	0.322	0.855	0.27	0.231	152.5	4745	0.336	5.783	0.040	0.564	32.66	0.90
1.5_{USBrep}												
2.147	0.296	1.576	0.246	0.388	35	4745	0.336	5.783	0.067	0.611	55.94	1.51
2.093	0.298	1.555	0.246	0.383	38.5	4745	0.336	5.783	0.066	0.614	56.05	1.27
2.05	0.3	1.522	0.25	0.381	41.6	4745	0.336	5.783	0.066	0.620	51.60	1.10
2.031	0.299	1.513	0.249	0.377	43.4	4745	0.336	5.783	0.065	0.621	53.59	1.06
2.005	0.302	1.471	0.253	0.373	47.4	4745	0.336	5.783	0.065	0.616	51.63	1.07
1.976	0.302	1.453	0.254	0.369	51.3	4745	0.336	5.783	0.064	0.618	50.11	1.05
1.911	0.304	1.441	0.25	0.36	59.3	4745	0.336	5.783	0.062	0.620	50.02	1.05
1.88	0.303	1.364	0.26	0.355	64.1	4745	0.336	5.783	0.061	0.623	49.97	1.02
1.854	0.305	1.376	0.254	0.35	67.1	4745	0.336	5.783	0.061	0.619	48.29	1.01
1.834	0.305	1.36	0.254	0.345	69.7	4745	0.336	5.783	0.060	0.617	48.87	1.02
1.793	0.305	1.295	0.26	0.337	75	4745	0.336	5.783	0.058	0.616	46.30	1.00
1.772	0.306	1.255	0.263	0.331	79.8	4745	0.336	5.783	0.057	0.610	46.65	0.99
1.741	0.307	1.263	0.258	0.326	84.8	4745	0.336	5.783	0.056	0.610	46.14	1.07
1.688	0.309	1.215	0.26	0.316	94.1	4745	0.336	5.783	0.055	0.606	44.16	1.01
1.612	0.31	1.152	0.265	0.305	102	4745	0.336	5.783	0.053	0.610	44.51	0.96
1.574	0.312	1.138	0.262	0.298	107.1	4745	0.336	5.783	0.052	0.607	43.48	0.97
1.546	0.313	1.093	0.267	0.292	110	4745	0.336	5.783	0.050	0.603	42.10	0.97
1.513	0.313	1.089	0.261	0.284	116	4745	0.336	5.783	0.049	0.600	42.53	0.93
1.468	0.316	1.061	0.257	0.272	124.6	4745	0.336	5.783	0.047	0.586	39.47	0.97
1.406	0.317	0.973	0.264	0.256	132.3	4745	0.336	5.783	0.044	0.574	38.60	0.93
1.367	0.32	0.911	0.273	0.248	138	4745	0.336	5.783	0.043	0.567	34.50	1.00
1.34	0.318	0.922	0.265	0.244	139.9	4745	0.336	5.783	0.042	0.573	37.07	1.01
1.304	0.319	0.88	0.27	0.237	144	4745	0.336	5.783	0.041	0.570	34.69	0.83
1.294	0.319	0.872	0.268	0.234	146.8	4745	0.336	5.783	0.040	0.567	35.37	0.97
1.275	0.32	0.858	0.269	0.23	149.1	4745	0.336	5.783	0.040	0.564	33.52	0.93
1.264	0.321	0.849	0.267	0.227	152	4745	0.336	5.783	0.039	0.559	32.81	0.92
4.7_{USB}												
2.27	0.775	1.521	0.63	0.959	37	4745	1	17.210	0.056	0.545	20.65	1.30
2.101	0.785	1.417	0.644	0.912	43.8	4745	1	17.210	0.053	0.553	19.76	0.87
2.053	0.796	1.387	0.647	0.897	48.5	4745	1	17.210	0.052	0.549	17.98	0.79
2.01	0.797	1.381	0.637	0.88	52.6	4745	1	17.210	0.051	0.549	17.47	0.74
1.958	0.805	1.377	0.628	0.865	57.2	4745	1	17.210	0.050	0.549	17.12	0.92

Continued...

Vopen (V)	Ishort (A)	Vmaxp (V)	Imaxp (A)	Pmax (W)	T [C]	W/m2	Filter	W	Efficiency	FF	Rsh	Rs
1.909	0.806	1.306	0.65	0.849	61.2	4745	1	17.210	0.049	0.552	18.14	0.67
1.852	0.815	1.229	0.668	0.821	67.5	4745	1	17.210	0.048	0.544	17.06	0.65
1.819	0.817	1.214	0.664	0.806	71.2	4745	1	17.210	0.047	0.542	16.37	0.64
1.792	0.815	1.191	0.663	0.79	75.6	4745	1	17.210	0.046	0.541	16.22	0.61
1.76	0.815	1.14	0.679	0.774	79.6	4745	1	17.210	0.045	0.540	15.79	0.62
1.72	0.822	1.166	0.647	0.754	85	4745	1	17.210	0.044	0.533	14.99	0.65
1.693	0.822	1.083	0.679	0.736	87.6	4745	1	17.210	0.043	0.529	14.47	0.64
1.659	0.827	1.086	0.661	0.718	94.1	4745	1	17.210	0.042	0.523	14.39	0.83
1.659	0.827	1.086	0.661	0.718	98	4745	1	17.210	0.042	0.523	14.39	0.83
1.583	0.832	1.064	0.632	0.673	105	4745	1	17.210	0.039	0.511	13.49	0.62
1.57	0.828	1.056	0.629	0.665	108.2	4745	1	17.210	0.039	0.512	12.85	0.63
1.548	0.831	1.03	0.631	0.65	110.6	4745	1	17.210	0.038	0.505	12.57	0.63
1.533	0.834	0.955	0.673	0.643	113.2	4745	1	17.210	0.037	0.503	12.42	0.62
1.495	0.833	0.938	0.661	0.62	118.8	4745	1	17.210	0.036	0.498	11.85	0.62
1.463	0.838	0.904	0.665	0.601	124	4745	1	17.210	0.035	0.490	11.20	0.62
1.431	0.841	0.875	0.667	0.583	128.2	4745	1	17.210	0.034	0.484	10.99	0.63
1.415	0.843	0.887	0.646	0.573	130.8	4745	1	17.210	0.033	0.480	10.13	0.60
1.394	0.844	0.857	0.658	0.564	134	4745	1	17.210	0.033	0.479	9.75	0.62
1.367	0.846	0.838	0.654	0.548	137	4745	1	17.210	0.032	0.474	9.86	0.78
1.348	0.847	0.82	0.655	0.537	140.6	4745	1	17.210	0.031	0.470	9.56	0.73
1.327	0.848	0.824	0.645	0.531	143	4745	1	17.210	0.031	0.472	9.06	0.57
4.7_{USBrep}												
2.252	0.743	1.531	0.604	0.925	34	4745	1	17.210	0.054	0.553	21.64	1.23
2.07	0.76	1.381	0.638	0.882	47	4745	1	17.210	0.051	0.561	20.34	0.84
2.026	0.767	1.373	0.634	0.871	51.9	4745	1	17.210	0.051	0.561	18.97	0.75
1.95	0.773	1.35	0.624	0.842	58.1	4745	1	17.210	0.049	0.559	19.45	0.94
1.886	0.778	1.268	0.643	0.816	63	4745	1	17.210	0.047	0.556	18.97	0.66
1.81	0.779	1.229	0.633	0.778	69	4745	1	17.210	0.045	0.552	17.50	0.64
1.783	0.778	1.191	0.643	0.766	72	4745	1	17.210	0.045	0.552	17.12	0.61
1.744	0.781	1.13	0.656	0.741	75	4745	1	17.210	0.043	0.544	17.05	0.62
1.726	0.786	1.135	0.644	0.731	77.4	4745	1	17.210	0.042	0.539	15.92	0.62
1.677	0.791	1.1	0.638	0.702	89.5	4745	1	17.210	0.041	0.529	14.96	0.62
1.639	0.794	1.099	0.619	0.681	96.3	4745	1	17.210	0.040	0.523	14.15	0.70
1.595	0.796	1.059	0.626	0.663	101.7	4745	1	17.210	0.039	0.522	14.05	0.63
1.564	0.796	1.063	0.605	0.643	106.5	4745	1	17.210	0.037	0.516	13.73	0.61
1.564	0.796	1.063	0.605	0.643	110.9	4745	1	17.210	0.037	0.516	13.73	0.61
1.507	0.804	0.952	0.643	0.612	113.8	4745	1	17.210	0.036	0.505	12.17	0.60
1.483	0.809	0.948	0.631	0.598	118.9	4745	1	17.210	0.035	0.498	12.29	0.61
1.458	0.808	0.923	0.63	0.582	124	4745	1	17.210	0.034	0.494	11.45	0.62
1.41	0.816	0.895	0.62	0.555	131.8	4745	1	17.210	0.032	0.482	10.57	0.63
1.366	0.817	0.834	0.637	0.531	138.8	4745	1	17.210	0.031	0.476	10.04	0.85
1.337	0.821	0.831	0.624	0.518	142	4745	1	17.210	0.030	0.472	9.89	0.60
1.31	0.82	0.828	0.612	0.506	146	4745	1	17.210	0.029	0.471	9.25	0.62

Continued...

Vopen (V)	Ishort (A)	Vmaxp (V)	Imaxp (A)	Pmax (W)	T [C]	W/m2	Filter	W	Efficiency	FF	Rsh	Rs
1.281	0.822	0.792	0.619	0.49	149.6	4745	1	17.210	0.028	0.465	8.69	0.61
1.262	0.828	0.768	0.629	0.483	151.8	4745	1	17.210	0.028	0.462	8.92	0.57
1.273	0.833	0.765	0.555	0.425	184	4745	1	17.210	0.025	0.401	6.81	1.05
1.148	0.843	0.626	0.612	0.383	188	4745	1	17.210	0.022	0.396	5.73	0.79
1.08	0.843	0.627	0.579	0.363	192.7	4745	1	17.210	0.021	0.399	5.26	0.95
1.5_{USA}												
2.17	0.283	1.464	0.218	0.32	27	4745	0.336	5.720	0.056	0.521	45.21	1.89
2.076	0.268	1.438	0.214	0.308	31	4745	0.336	5.720	0.054	0.554	57.04	1.56
2.014	0.269	1.412	0.213	0.301	36	4745	0.336	5.720	0.053	0.556	59.28	1.47
1.972	0.275	1.376	0.22	0.303	41	4745	0.336	5.720	0.053	0.559	57.17	1.42
1.939	0.284	1.378	0.219	0.302	45	4745	0.336	5.720	0.053	0.548	49.55	2.03
1.894	0.288	1.36	0.217	0.295	51	4745	0.336	5.720	0.052	0.541	47.00	1.32
1.862	0.295	1.27	0.226	0.287	56	4745	0.336	5.720	0.050	0.522	38.49	1.34
1.846	0.295	1.284	0.22	0.282	60	4745	0.336	5.720	0.049	0.518	38.81	1.44
1.823	0.296	1.252	0.221	0.277	65	4745	0.336	5.720	0.048	0.513	36.22	1.45
1.797	0.297	1.214	0.221	0.269	70	4745	0.336	5.720	0.047	0.504	33.22	1.44
1.774	0.297	1.178	0.222	0.261	75	4745	0.336	5.720	0.046	0.495	29.53	1.47
1.742	0.299	1.179	0.211	0.249	79	4745	0.336	5.720	0.044	0.478	24.60	1.52
1.715	0.299	1.158	0.207	0.24	84	4745	0.336	5.720	0.042	0.468	21.05	1.51
1.682	0.298	1.143	0.205	0.234	89	4745	0.336	5.720	0.041	0.467	20.47	1.51
1.616	0.297	1.104	0.202	0.223	95	4745	0.336	5.720	0.039	0.465	17.83	1.44
1.585	0.296	1.068	0.203	0.217	100	4745	0.336	5.720	0.038	0.463	16.25	1.44
1.546	0.293	1.06	0.197	0.209	105	4745	0.336	5.720	0.037	0.461	17.20	1.50
1.504	0.29	1.066	0.187	0.2	111	4745	0.336	5.720	0.035	0.459	15.82	1.42
1.466	0.289	0.949	0.202	0.192	117	4745	0.336	5.720	0.034	0.453	15.16	1.39
1.431	0.285	0.944	0.197	0.186	122	4745	0.336	5.720	0.033	0.456	15.45	1.40
1.393	0.284	0.934	0.193	0.18	126	4745	0.336	5.720	0.031	0.455	14.79	1.33
1.373	0.283	0.9	0.196	0.176	129	4745	0.336	5.720	0.031	0.453	14.60	1.40
1.346	0.281	0.885	0.193	0.171	134	4745	0.336	5.720	0.030	0.452	14.73	1.82
1.304	0.279	0.859	0.191	0.164	140	4745	0.336	5.720	0.029	0.451	14.63	1.35
1.263	0.276	0.84	0.186	0.156	146	4745	0.336	5.720	0.027	0.448	13.41	1.38
1.25	0.274	0.812	0.188	0.152	149	4745	0.336	5.720	0.027	0.444	14.37	1.38
4.7_{USA}												
1.425	0.578	0.839	0.378	0.317	148	4745	1	17.025	0.019	0.385	6.59	1.90
1.546	0.582	0.912	0.396	0.361	127	4745	1	17.025	0.021	0.401	7.07	1.66
1.252	0.535	0.761	0.371	0.282	132	4745	1	17.025	0.017	0.421	8.71	1.00
2.145	0.619	1.355	0.425	0.575	44	4745	1	17.025	0.034	0.433	2.96	1.63
2.033	0.551	1.371	0.385	0.528	52	4745	1	17.025	0.031	0.471	14.01	1.42
1.947	0.552	1.27	0.398	0.505	57	4745	1	17.025	0.030	0.470	13.35	1.42
1.873	0.554	1.234	0.395	0.488	61	4745	1	17.025	0.029	0.470	13.34	1.26
1.782	0.553	1.186	0.39	0.463	66	4745	1	17.025	0.027	0.470	12.61	1.15
1.737	0.554	1.133	0.398	0.451	69	4745	1	17.025	0.026	0.469	12.29	1.10
1.701	0.556	1.119	0.392	0.439	74	4745	1	17.025	0.026	0.464	11.16	1.06

Continued...

Vopen (V)	Ishort (A)	Vmaxp (V)	Imaxp (A)	Pmax (W)	T [C]	W/m2	Filter	W	Efficiency	FF	Rsh	Rs
1.662	0.553	1.058	0.405	0.429	78	4745	1	17.025	0.025	0.467	11.10	1.35
1.638	0.553	1.057	0.398	0.421	83	4745	1	17.025	0.025	0.465	11.04	1.07
1.596	0.557	1.061	0.386	0.409	88	4745	1	17.025	0.024	0.460	10.14	1.05
1.572	0.552	1.051	0.379	0.398	94	4745	1	17.025	0.023	0.459	10.81	1.04
1.528	0.554	0.979	0.391	0.383	98	4745	1	17.025	0.022	0.452	10.31	1.03
1.5	0.552	0.926	0.405	0.375	102	4745	1	17.025	0.022	0.453	10.31	1.01
1.47	0.555	0.942	0.388	0.365	105	4745	1	17.025	0.021	0.447	9.68	0.99
1.441	0.555	0.889	0.399	0.355	111	4745	1	17.025	0.021	0.444	9.70	1.04
1.394	0.552	0.865	0.39	0.337	120	4745	1	17.025	0.020	0.438	9.66	1.05
1.361	0.557	0.869	0.375	0.326	125	4745	1	17.025	0.019	0.430	8.80	1.34
1.324	0.553	0.835	0.379	0.316	131	4745	1	17.025	0.019	0.432	8.86	1.02
1.289	0.553	0.772	0.394	0.304	135	4745	1	17.025	0.018	0.426	8.14	1.00
1.26	0.55	0.765	0.385	0.294	141	4745	1	17.025	0.017	0.424	8.23	1.01
1.225	0.547	0.777	0.361	0.28	145	4745	1	17.025	0.016	0.418	7.99	0.97
1.195	0.546	0.757	0.357	0.27	149	4745	1	17.025	0.016	0.414	7.39	0.94
1.173	0.548	0.684	0.383	0.262	153	4745	1	17.025	0.015	0.408	7.19	0.93
1.5_{USArep}												
2.115	0.242	1.462	0.174	0.254	35	4745	0.336	5.720	0.044	0.496	31.57	2.49
2.038	0.24	1.465	0.17	0.249	38	4745	0.336	5.720	0.044	0.509	33.25	2.15
2.002	0.24	1.423	0.173	0.246	40	4745	0.336	5.720	0.043	0.512	33.16	1.85
1.978	0.241	1.453	0.169	0.245	42	4745	0.336	5.720	0.043	0.514	33.07	1.87
1.955	0.242	1.414	0.172	0.244	43	4745	0.336	5.720	0.043	0.516	33.09	2.33
1.932	0.243	1.383	0.175	0.242	50	4745	0.336	5.720	0.042	0.515	33.02	2.04
1.89	0.241	1.383	0.17	0.236	58	4745	0.336	5.720	0.041	0.518	32.66	1.89
1.842	0.242	1.364	0.168	0.229	65	4745	0.336	5.720	0.040	0.514	31.46	1.88
1.806	0.243	1.26	0.178	0.225	72	4745	0.336	5.720	0.039	0.513	30.92	1.85
1.729	0.243	1.231	0.175	0.215	81	4745	0.336	5.720	0.038	0.512	30.01	1.73
1.694	0.243	1.208	0.175	0.211	84	4745	0.336	5.720	0.037	0.513	28.56	1.69
1.668	0.243	1.175	0.176	0.207	88	4745	0.336	5.720	0.036	0.511	28.03	1.68
1.591	0.241	1.083	0.18	0.195	100	4745	0.336	5.720	0.034	0.509	26.77	1.66
1.563	0.241	1.077	0.176	0.19	104	4745	0.336	5.720	0.033	0.504	25.37	1.68
1.494	0.24	1.062	0.168	0.178	114	4745	0.336	5.720	0.031	0.496	24.48	1.64
1.438	0.238	0.95	0.178	0.169	121	4745	0.336	5.720	0.030	0.494	24.36	1.61
1.391	0.239	0.928	0.175	0.162	129	4745	0.336	5.720	0.028	0.487	24.42	1.56
1.364	0.241	0.93	0.17	0.158	135	4745	0.336	5.720	0.028	0.481	22.06	2.29
1.327	0.243	0.902	0.172	0.155	139	4745	0.336	5.720	0.027	0.481	21.73	1.59
1.271	0.246	0.86	0.17	0.146	149	4745	0.336	5.720	0.026	0.467	18.88	1.53
1.242	0.244	0.815	0.174	0.141	155	4745	0.336	5.720	0.025	0.465	19.12	1.66
1.202	0.24	0.789	0.168	0.133	162	4745	0.336	5.720	0.023	0.461	18.01	1.62
4.7_{USArep}												
2.206	0.567	1.392	0.401	0.558	33	4745	1	17.025	0.033	0.446	11.56	1.84
2.053	0.55	1.337	0.385	0.515	42	4745	1	17.025	0.030	0.456	11.96	1.61
1.95	0.534	1.252	0.395	0.495	49	4745	1	17.025	0.029	0.475	15.49	1.49

Continued...

Vopen (V)	Ishort (A)	Vmaxp (V)	Imaxp (A)	Pmax (W)	T [C]	W/m2	Filter	W	Efficiency	FF	Rsh	Rs
1.848	0.537	1.202	0.393	0.473	53	4745	1	17.025	0.028	0.477	14.48	1.18
1.763	0.539	1.145	0.395	0.453	62	4745	1	17.025	0.027	0.477	13.87	1.11
1.731	0.543	1.105	0.402	0.444	66	4745	1	17.025	0.026	0.472	12.72	1.13
1.686	0.542	1.102	0.394	0.434	71	4745	1	17.025	0.025	0.475	12.89	1.08
1.658	0.541	1.073	0.397	0.425	74	4745	1	17.025	0.025	0.474	12.81	1.37
1.602	0.547	1.051	0.39	0.41	81	4745	1	17.025	0.024	0.468	11.49	0.99
1.588	0.547	1.056	0.383	0.404	85	4745	1	17.025	0.024	0.465	11.08	1.04
1.546	0.544	0.977	0.399	0.39	91	4745	1	17.025	0.023	0.464	11.40	1.01
1.51	0.552	0.963	0.394	0.379	98	4745	1	17.025	0.022	0.455	10.52	0.99
1.483	0.555	0.928	0.4	0.371	102	4745	1	17.025	0.022	0.451	10.00	1.01
1.451	0.559	0.902	0.402	0.363	109	4745	1	17.025	0.021	0.448	9.50	0.98
1.413	0.559	0.864	0.402	0.347	115	4745	1	17.025	0.020	0.439	9.01	0.98
1.38	0.561	0.875	0.385	0.337	119	4745	1	17.025	0.020	0.435	8.93	1.15
1.343	0.559	0.835	0.388	0.323	127	4745	1	17.025	0.019	0.430	8.33	0.99
1.312	0.556	0.789	0.397	0.313	132	4745	1	17.025	0.018	0.429	8.30	0.98
1.28	0.551	0.788	0.382	0.301	138	4745	1	17.025	0.018	0.427	8.20	1.01
1.235	0.543	0.768	0.369	0.283	145	4745	1	17.025	0.017	0.422	8.19	1.02
1.202	0.539	0.763	0.356	0.271	149	4745	1	17.025	0.016	0.418	7.99	0.96
1.175	0.537	0.763	0.34	0.259	152	4745	1	17.025	0.015	0.410	7.77	0.94

Appendix C

Validation of Scroll Geometry Selection Method and Development of a Scroll Expander for Micro-CSP with Organic Rankine Cycle

Bertrand Dechesne[1] and Matthew Orosz[2] and Harold Hemond[2]
[1]University of Liege. Rue des Eglantines 31, 4801 Stembert, Belgium
[2]Massachusetts Institute of Technology, Parsons Laboratory 15 Vassar St. 48-216, Cambridge, MA, USA

C.1 Introduction

The application of micro-CSP systems of a few kilowatts is limited by the lack of suitable expansion devices for thermodynamic cycles. While scroll compressors have been adapted to work as expanders in Organic Rankine Cycles, they require compounding or superposition to accommodate the large expansion ratios encountered in solar ORC systems with over 100°C. In this paper we describe a method for developing a high volume ratio scroll expander optimized for kilowatts scale micro-CSP, including detailed design of a working prototype for a 3kWe solar ORC.

C.2 Solar ORC Specifications

To test the advantages of an application-specific expander optimization, we propose a solar ORC cycle coupled with 75m^2 parabolic trough array using R245fa as the working fluid and generating 3kWe net output. The cycle operates at 150°C HCE output, with 135°C vaporizing temperature, (5°C superheat) and 35°C condensing temperature in the cycle. The mass flow of R245fa is 0.15 kg·s^{-1}.

C.3 Geometric Selection

Using the 8-dimensional planar curve framework geometric framework of Graveson et. al. [63] a set of viable scroll geometries for the cycle intrinsic volume ratio was identified with a computationally

efficient method developed by Orosz et. al. [118], where the optimal geometry is selected on the basis of compactness factor (volume ratio/diameter). In this study we validate the compactness factor figure of merit using specific thermo-mechanical criteria for the ORC expander.

C.4 Scroll Expander Design

C.4.1 Review Criteria

To confirm that compactness factor is representative of the thermodynamic performances of the scroll expander, we develop a deterministic model based on [118, 37] to calculate the isentropic efficiency for different geometries. This Thermodynamic model takes into account the following losses:

- Pressure drop at the inlet port taking including the throttling due to the orbiting scroll motion.
- Radial and flank leakages: radial leakages are modeled using a frictional flow between the scroll wrap and plate and flank leakages is treated as nozzle flow.
- Pressure drop at the outlet of the exhaust chamber.
- Axial friction losses between the two scrolls are assumed to be lubricated friction.

According to [92], the hydrodynamic friction force is equal to

(C.1)

where V is the velocity, μ the dynamic viscosity, A_{scroll} the area of the scroll and t the oil film thickness. We used POE oil for our application and the variation of the oil viscosity with the temperature has been taken into account.

Assuming a tangential and radial gap of five microns, Figure C-1 (right) shows the variation of the isentropic efficiency with the compactness factor. We conclude that the compactness factor is indeed a rapid and effective metric for ranking optimal scroll geometries, and the optimal geometry for the experimental ORC is shown in Figure C-2.

C.4.2 Machine Speed Characteristics

The thermodynamic model facilitates determination of the optimal rotation speed. Figure C-1 (left) shows the variation of the isentropic efficiency with respect to the RPM. At low speed leakages proportionally impact efficiency whereas at high speed frictional losses dominate. We note that the largest pressure differences between two adjacent pockets occur at the center of the scroll, i.e. at the beginning of the expansion process. Therefore one approach to decrease the leakage losses is to decrease the flank and radial gap while increasing the thickness of the scroll at this location, as the frictional flow rate depends on the length of the leakage path.

C.5 Prototype Development

After selecting geometry (Figure C-2 (left), a 3D CAD model (Figure C-2 (right) for machining the prototype is developed. The materials used are P20 steel for the expander stator and rotor. Testing of the prototype is being undertaken at the MIT ORC test facility and on-sun testing will be completed at the 3kWe micro-CSP test facility at Eckerd College in St. Petersburg, FL. Modeled and experimental results will be compared, and adaptations to future applications will be specified.

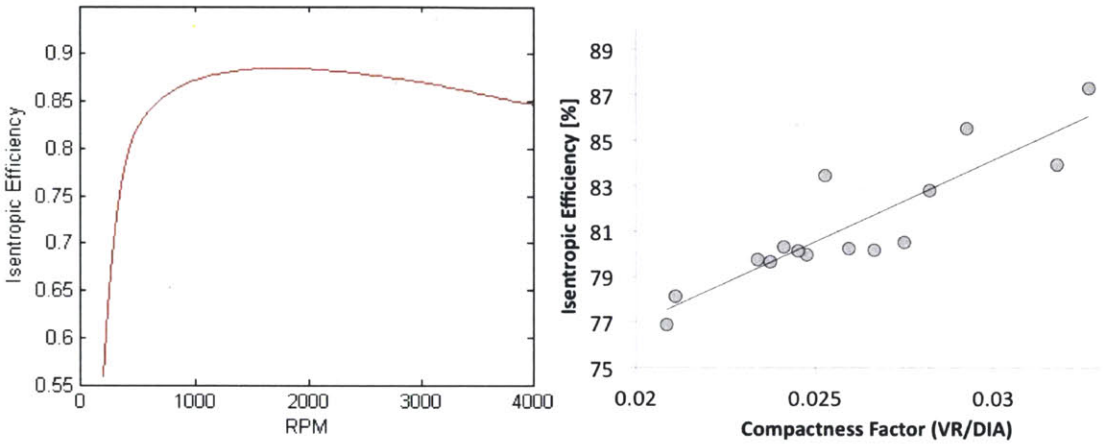

Figure C-1: Modeled variation of isentropic efficiency for a scroll expander with RPM (left), and modeled variation of isentropic efficiency between varying scroll expander geometries with the compactness factor (right)

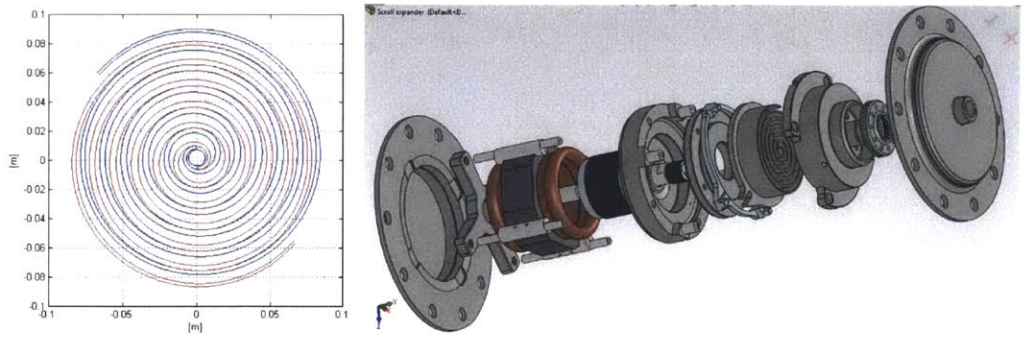

Figure C-2: Selected geometry for a scroll expander of volume ratio 8.5 maximizing the compactness factor (left), and an exploded view of a CAD model for a prototype scroll expander (right)

Appendix D

SORCE Code

SORCE2_timestep_dyn_paperrun_NEP4

Equations

CONSTANT imax#=15
CONSTANT Node#=10
CONSTANT hmax#=700

*

SORCE V2.0

Revised December 2011, March 2012 MSO
Energy balance on fluid and solids in a control volume From Duffie&Beckman, Allen K Thesis and McMahan Thesis

Simplifying assumptions:
Lumped thermal parameters
no axial thermal diffusion
Infinite particle conductivity (no temperature gradients in particles)
timestep = plug flow fluid moving through control volume dx in 1 timestep
infinite NTU - equilibration of fluid and particle temperatures in each node

*

SORCE proceeds by sequentially finding the energy flow from sunlight to collector to storage to ORC and back to the collector through the loop described in WRAPPER

procedure $WRAPPER(\epsilon_{pump}, \epsilon_{drive}, alt, lat, long, \delta_{TGMT}, Track\$, GlazingIntact\$, Shadowing_{UD}, TrackingError_{UD}, GeomEffects_{UD}, Reflectivity,$

$Dirt_{factor,UD}, HCEtype\$, L_{HCE}, L_{aperture}, Width_{UD}, D_{2,UD}, D_{3,UD}, D_{4,UD}, D_{5,UD}, SelectiveCoating\$, T_{WF,exp,su}, SH, Pinch_{cond}, TopScroll\$, BotScroll\$, WF\$, fluid\$, \dot{m}_{WF},$

$\dot{v}_{HTF}, DIA, Height : \eta_{ORC}, \eta_{sys}, \eta_{solar}, Cost_{cond}, Cost_{HCE}, Cost_{track}, Cost_{exp1}, Cost_{exp2}, Cost_{mat}, Cost_{col}, Cost_{PB}, Cost_{Storage}, ORC$

$_{kWh}, Col_{kWh}, Solar_{kWh}, Storage_{kWh}, Area_{aperture}, P_{ORC,max})$

Initialize problematic arrays

SOLAR RESOURCE

call $SOLARRESOURCE(alt, lat, long, \delta_{TGMT}, Track\$: I_b, \Theta_{Ave}, T_{Local}, Wind2m, I_{Hour,0..23}, \Theta_{hour,0..23}, Hour_{0..23}, risesecond, setsecond,$
$Seconds2_{0..12}, I_{Hour2,0..12}, Clouds, Tmax, Tmin)$

call $CURVEFIT1D\left(\text{'Poly6'}, Seconds2_{0..12}, I_{Hour2.0..12} : a_{1..7}, RMS, Bias, R^2, a_{stderr,1..7}\right)$ (D.1)

Initialize variables

$$Start_{int} = 0 \quad \text{(D.2)}$$

$$\text{end}_{int} = 0 \quad \text{(D.3)}$$

$$P_{ORC,max} = 0 \tag{D.4}$$

$$Q_{cond} = 0 \tag{D.5}$$

$$RPM_1 = 0 \tag{D.6}$$

$$RPM_2 = 0 \tag{D.7}$$

$$\dot{v}_1 = 0 \tag{D.8}$$

$$\dot{v}_2 = 0 \tag{D.9}$$

$$ORC_{count} = 0 \tag{D.10}$$

$$ORC_{kWh} = 0 \tag{D.11}$$

$$Solar_{kWh} = 0 \tag{D.12}$$

$$Storage_{kWh} = 0 \tag{D.13}$$

$$Col_{kWh} = 0 \tag{D.14}$$

$$Lost_{kWh} = 0 \tag{D.15}$$

$$E_{HTF,pump} = 0 \tag{D.16}$$

$$\theta = \theta_{Ave} \tag{D.17}$$

$$T_{amb} = T_{Local} \tag{D.18}$$

$flow = 0$ is HTF flowing? 0=no 1=yes. start from rest (D.19)

$\dot{m}_{HTF} = 0$ initialize m_{dot} so storage timestep can be calculated (D.20)

$timestep = 3600$ seconds - initialize timestep to one hour for system at rest (D.21)

$seconds_1 = 0$ initialize time (D.22)

$$T_{HTF,Col,su} = T_{amb} \tag{D.23}$$

$$T_{HTF,Col,ex} = T_{amb} \tag{D.24}$$

END SOLAR RESOURCE

Initialize temperature in storage tank

$$i = 1 \tag{D.25}$$

$$imax = Node\# \tag{D.26}$$

repeat (D.27)

$$T_{sin,i} = T_{amb} \tag{D.28}$$

$$i := i + 1 \tag{D.29}$$

until $i > imax$ (D.30)

WRAPPER LOOP

$$h = 1 \tag{D.31}$$

$$hmax = hmax\# \tag{D.32}$$

repeat (D.33)

set boundaries to Integrate outputs on 4rth day - convergence is observed by then

If($seconds_h > 345599$) then (D.34)

If($Seconds_h < 350000$) then (D.35)

$Start_{int} := h$ (D.36)

endif (D.37)

If($Seconds_h < 432000$) then (D.38)

end $_{int} := h$ (D.39)

endif (D.40)

endif (D.41)

SOLAR - AMBIENT

Set beam radiation equal to the irradiance distribution calculated in the solar module

First establish the time of day in seconds

If($seconds_h > 86400$) then factor the timestep down to get the time of day (D.42)

$$factor = \text{Floor}\left(\frac{seconds_h}{86400}\right) \tag{D.43}$$

$$daysecond = seconds_h - factor \cdot 86400 \tag{D.44}$$

else (D.45)

$daysecond = seconds_h$ timestep is the time of day during the first day (D.46)

endif (D.47)

derive I_b from 6th order polynomial if time of day is between sunrise and sunset

If($daysecond > risesecond$) then (D.48)

If($daysecond < setsecond$) then (D.49)

$N = 7$ (D.50)

$$I_b = \left(a_1 + \text{Sum}\left(a_j \cdot daysecond^{j-1},\ \text{j} = 2,\ N\right)\right) \cdot (1 - clouds)$$ 6th order polynomial for beam irradiance in W/m2 diminished by cloud cover (D.51)

$I_{timestep,h} = I_b$ (D.52)

else nighttime (D.53)

$I_b = 0$ (D.54)

$I_{timestep,h} = 0$ (D.55)

endif (D.56)

else nighttime (D.57)

$$I_b = 0 \tag{D.58}$$

$$I_{timestep,h} = 0 \tag{D.59}$$

endif (D.60)

set ambient temperature to the sinusoidal temperature distribution calculated from Tmax and Tmin

call $AMBIENT(Tmax,\ Tmin,\ risesecond,\ setsecond,\ daysecond : Temp)$ (D.61)

$$T_{amb} = Temp \tag{D.62}$$

END SOLAR

FLOW - CIRCUIT

If $\left(I_{b<200}\right)$ then Fluid is only flowing if sun is shining above 200W/m2 or storage tank has temperature to run ORC (D.63)

If $\left(T_{sin,Node\#<150}\right)$ then (D.64)

$Flow = 0$ is HTF flowing? 1=yes 0=no (D.65)

$\dot{m}_{HTF} = 0$ (D.66)

$timestep = 3600$ (D.67)

else (D.68)

$Flow = 1$ If tank temperature is above threshold (D.69)

$T_{HTF,Col,ex} := T_{HTF,Col,su}$ short circuit collector (D.70)

endif (D.71)

else (D.72)

$Flow = 1$ If sun is shining (D.73)

endif (D.74)

If$(seconds_h > 345599)$ then (D.75)

If$(seconds_h < 432000)$ then (D.76)

HTF Pump - this uses the assumption that 10x the height of the tank is a reasonable proxy for the differential head required to recirculate the fluid
a more detailed calculation would calculate the friction head in the fluid circuit

$$Work_{HTF,pump} = \frac{\frac{\dot{m}_{HTF} \cdot g\# \cdot Height \cdot 10}{1000}}{\left(\epsilon_{pump} \cdot \epsilon_{drive}\right)}\ [\text{kW}] \tag{D.77}$$

$$E_{HTF,pump} := E_{HTF,pump} + Work_{HTF,pump} \cdot timestep/3600 \tag{D.78}$$

endif (D.79)

endif (D.80)

END FLOW-CIRCUIT

COLLECTOR

$$\text{If}\left(I_{b<200}\right) \text{ then} \qquad \text{bypass collectors if irradiance is less than 200W/m2} \tag{D.81}$$

$$\text{If}(seconds_h > 345599) \text{ then} \tag{D.82}$$

$$\text{If}(seconds_h < 432000) \text{ then} \tag{D.83}$$

$$P_{solar,h} = 0 \tag{D.84}$$

$$\text{endif} \tag{D.85}$$

$$\text{endif} \tag{D.86}$$

$$T_{HTF,Col,ex} := T_{HTF,Col,su} \qquad \text{short circuit collector} \tag{D.87}$$

$$\text{else} \tag{D.88}$$

$$\text{call } COLLECTOR I_b, Wind2m, T_{amb}, \Theta, fluid\$, \dot{v}_{HTF}, GlazingIntact\$, Shadowing_{UD}, TrackingError_{UD}, GeomEffects_{UD}, Reflectivity, Dirt_{factor,UD}, HCEtype\$, L_{HCE},$$

$$L_{aperture}, T_{HTF,Col,su}, Width_{UD}, D_{2,UD}, D_{3,UD}, D_{4,UD}, D_{5,UD}, SelectiveCoating\$: \dot{m}_{HTF}, T_{HTF,Col,ex}, Col_\eta, E_{col}, Width, Cost_{col})$$

$$\text{If}(seconds_h > 345599) \text{ then} \tag{D.89}$$

$$\text{If}(seconds_h < 432000) \text{ then} \tag{D.90}$$

$$Solar_{kWh} := Solar_{kWh} + (I_b \cdot timestep/3600000) \cdot L_{Aperture} \cdot Width \tag{D.91}$$

$$P_{solar,h} = E_{col} \text{ [kW]} \tag{D.92}$$

$$\text{endif} \tag{D.93}$$

$$\text{endif} \tag{D.94}$$

$$\text{endif} \tag{D.95}$$

END COLLECTOR

STORAGE

$$\text{call } STORAGE\left(flow, fluid\$, \dot{m}_{HTF}, T_{HTF,col,ex}, T_{amb}, DIA, Height, T_{sin,1..Node\#} : T_{HTF,Storage,ex}, T_{sop,1..Node\#}, E_{Storage}, L_{Storage}, P_{Storage}, timestep\right) \tag{D.96}$$

record data only on 4rth day

$$\text{If}(seconds_h > 345599) \text{ then} \tag{D.97}$$

$$\text{If}(seconds_h < 432000) \text{ then} \tag{D.98}$$

$$P_{stored,h} = P_{Storage} \tag{D.99}$$

$$E_{stored,h} = E_{Storage} \tag{D.100}$$

$$Storage_{kWh} := Storage_{kWh} + E_{stored,h} \tag{D.101}$$

$$E_{lost,h} = L_{Storage} \tag{D.102}$$

$$Lost_{kWh} := Lost_{kWh} + E_{lost,h} \tag{D.103}$$

$$P_{lost,h} = L_{Storage} \cdot 3600/timestep \tag{D.104}$$

endif (D.105)

endif (D.106)

T profile in storage tank becomes input profile for next iteration

$$i = 1 \tag{D.107}$$

$$imax = Node\# \tag{D.108}$$

repeat (D.109)

$T_{tank,h,\mathrm{i}} = T_{sop,i}$ stores array of tank temperatures (D.110)

$$T_{sin,i} = T_{sop,i} \tag{D.111}$$

$$i := i + 1 \tag{D.112}$$

until $i > imax$ (D.113)

END STORAGE

ORC

$$\text{If}\left(T_{sin,Node\#>150}\right) \text{ then} \qquad \text{ORC ON} \tag{D.114}$$

call $ORC(TopScroll\$, BotScroll\$, WF\$, fluid\$, T_{WF,exp,su}, SH, \dot{m}_{WF}, T_{amb}, Pinch_{cond}, T_{HTF,Storage,ex}, \dot{m}_{HTF} : T_{HTF,ORC,ex}, A_{vap}, A_{pre}, A_{SH}, A_{recup}, P_{exp1}, P_{exp2},$

$Work_{WF,pump,s}, Work_{ORC,fans}, vol_{flow,WF}, Q_{condenser}, Thermal_{Power,HTF,ORC}, RPM_{exp1}, RPM_{exp2}, Pinch_{vap}, \dot{v}_{exp1}, \dot{v}_{exp2})$

record outputs only on 4rth day

$$\text{If}(seconds_h > 345599) \text{ then} \tag{D.115}$$

$$\text{If}(seconds_h < 432000) \text{ then} \tag{D.116}$$

$ORC_{count} := ORC_{count} + 1$ counter used to derive average RPMs of expanders in cost functions (D.117)

Define ORC outputs

$$WF_{mdot,h} = \dot{m}_{WF} \tag{D.118}$$

$$Pinch_{HTF,h} = Pinch_{vap} \tag{D.119}$$

$$E_{HTF,ORC,h} := Thermal_{Power,HTF,ORC} \cdot timestep/3600 \tag{D.120}$$

$$P_{HTF,ORC,h} = Thermal_{Power,HTF,ORC} \tag{D.121}$$

Max RPMs and $\dot{v}$ and Q_{cond} for cost/sizing

$$\text{If}\left(RPM_{1<RPM,exp1}\right) \text{ then} \tag{D.122}$$

$$RPM_1 = RPM_{exp1} \tag{D.123}$$

$$\dot{v}_1 = \dot{v}_{exp1} \tag{D.124}$$

$$Q_{cond} = Q_{condenser} \tag{D.125}$$

endif (D.126)

If$\left(RPM_{2<RPM,exp2}\right)$ then (D.127)

$$RPM_2 = RPM_{exp2} \tag{D.128}$$

$$\dot{v}_2 = \dot{v}_{exp2} \tag{D.129}$$

endif (D.130)

Power out and cycle efficiency

$$Work_{WF,pump} = \frac{Work_{WF,pump,s}}{\epsilon_{drive} \cdot \epsilon_{pump}} \tag{D.131}$$

$$P_{ORC,net,h} = \left(P_{exp1} + P_{exp2}\right) - \left(Work_{WF,pump} + Work_{ORC,fans}\right) \tag{D.132}$$

Power max for cost/sizing

If$\left(P_{ORC,max<P,ORC,net,h}\right)$ then (D.133)

$$P_{ORC,max} = P_{ORC,net,h} \tag{D.134}$$

endif (D.135)

$$E_{ORC,net,h} = P_{ORC,net,h} \cdot timestep/3600 \tag{D.136}$$

$ORC_{kWh} := ORC_{kWh} + E_{ORC,net,h}$ ORC 4rth day energy out (D.137)

$$\eta_{ORC,h} = \frac{P_{ORC,net,h}}{P_{HTF,ORC,h}} \tag{D.138}$$

Circulating HT Fluid energy balance between timesteps ORC ON

If$\left(I_{h<200}\right)$ then change in fluid energy is between tank and ORC (D.139)

$$T_{HTF,ave} = \frac{T_{HTF,ORC,ex} + T_{HTF,Col,ex}}{2} \tag{D.140}$$

call $prop_{htf}\left(fluid\$,\ T_{HTF,ave} : \mu_1,\ \rho_{HTF},\ Cp_{HTF},\ k_1\right)$ (D.141)

$$P_{HTF,h} = \frac{\dot{m}_{HTF} \cdot Cp_{HTF} \cdot \left(T_{HTF,ORC,ex} - T_{HTF,Col,ex}\right)}{1000} \tag{D.142}$$

$$E_{HTF,h} = \dot{m}_{HTF} \cdot Cp_{HTF} \cdot \left(T_{HTF,ORC,ex} - T_{HTF,Col,ex}\right) \cdot timestep/3600 \tag{D.143}$$

else change in fluid energy is between ORC and collector (D.144)

$$T_{HTF,ave} = \frac{T_{HTF,ORC,ex} + T_{HTF,col,su}}{2} \tag{D.145}$$

$$\text{call } prop_{htf}\left(fluid\$,\ T_{HTF,ave} : \mu_1,\ \rho_{HTF},\ Cp_{HTF},\ k_1\right) \tag{D.146}$$

$$P_{HTF,h} = \frac{\dot{m}_{HTF} \cdot Cp_{HTF} \cdot \left(T_{HTF,ORC,ex} - T_{HTF,Col,su}\right)}{1000} \tag{D.147}$$

$$E_{HTF,h} = \dot{m}_{HTF} \cdot Cp_{HTF} \cdot \left(T_{HTF,ORC,ex} - T_{HTF,Col,su}\right) \cdot timestep/3600 \tag{D.148}$$

endif (D.149)

endif (D.150)

endif (D.151)

$T_{HTF,col,su} := T_{HTF,ORC,ex}$ Set Collector input to ORC output (D.152)

else change in fluid energy is between tank and collector (D.153)

record data only on 4rth day

$$\text{If}(seconds_h > 345599) \text{ then} \tag{D.154}$$

$$\text{If}(seconds_h < 432000) \text{ then} \tag{D.155}$$

$$T_{HTF,ave} = \frac{T_{sin,Node\#} + T_{HTF,col,su}}{2} \tag{D.156}$$

$$\text{call } prop_{htf}\left(fluid\$,\ T_{HTF,ave} : \mu_1,\ \rho_{HTF},\ Cp_{HTF},\ k_1\right) \tag{D.157}$$

$$P_{HTF,h} = \frac{\dot{m}_{HTF} \cdot Cp_{HTF} \cdot \left(T_{sin,Node\#} - T_{HTF,Col,su}\right)}{1000} \tag{D.158}$$

$$E_{HTF,h} = \dot{m}_{HTF} \cdot Cp_{HTF} \cdot \left(T_{sin,Node\#} - T_{HTF,Col,su}\right) \cdot timestep/3600 \tag{D.159}$$

$$E_{HTF,ORC,h} = 0 \tag{D.160}$$

$$P_{HTF,ORC,h} = 0 \tag{D.161}$$

$$E_{ORC,net,h} = 0 \tag{D.162}$$

$$P_{ORC,net,h} = 0 \tag{D.163}$$

endif (D.164)

endif (D.165)

$T_{HTF,Col,su} := T_{sin,Node\#}$ Set Collector input to storage tank output (D.166)

endif (D.167)

END ORC

record data only on 4rth day

$$\text{If}(seconds_h > 345599) \text{ then} \tag{D.168}$$

$$\text{If}(seconds_h < 432000) \text{ then} \tag{D.169}$$

$$\text{If}\left(I_{b<200}\right)\ \text{then} \tag{D.170}$$

$$E_{solar,h} = 0 \tag{D.171}$$

$$\text{else} \tag{D.172}$$

$$E_{solar,h} = E_{col} \cdot \frac{timestep}{3600\ [\text{kWh}]} \qquad \text{Collector energy is determined after timestep has been determined in STORAGE} \tag{D.173}$$

$$Col_{kWh} := Col_{kWh} + E_{solar,h} \tag{D.174}$$

$$\text{endif} \tag{D.175}$$

$$\text{endif} \tag{D.176}$$

$$\text{endif} \tag{D.177}$$

$$seconds_{h+1} := seconds_h + timestep \tag{D.178}$$

$$h := h + 1 \tag{D.179}$$

$$Until h > hmax \tag{D.180}$$

END OF WRAPPER LOOP

Collector Tracker Drives - Assume this is negligible - e.g. on a 75m2 system 2kW is used for 3 seconds every 2 minutes. This is about 50 W

$$Area_{aperture} = Width \cdot L_{Aperture} \tag{D.181}$$

$$W_{tracker} = 0.05 \cdot \frac{75}{\left(Area_{aperture}\right)\ [\text{kW}]} \tag{D.182}$$

SYSTEM EFFICIENCIES

$$\eta_{ORC} = ORC_{kWh}/Col_{kWh} \tag{D.183}$$

$$\eta_{sys} = \frac{ORC_{kWh} - E_{HTF,pump} - W_{Tracker}}{Solar_{kWh}} \tag{D.184}$$

$$\eta_{Solar} = Col_{kWh}/Solar_{kWh} \tag{D.185}$$

COST FUNCTIONS AND PARASITIC LOSSES

Absorbers/Heat Collection Elements - cost as a function of line length
Reference is 60.3mm galv pipe from Macsteel at $21/m + 80mmOD DURAN tube from Schott at $48/m

$$Cost_{HCE} = 69 \cdot L_{Aperture} \tag{D.186}$$

Tracker sytems - drives and sensors - cost as a function of aperture area
Sensors are Level Developments inclinometers at $112/apiece and Drives are Leeson 3/4hp 24VDC motors at $388/apiece covering 18.75 m2 plus $50 supporting material

$$Cost_{track} = 30 \cdot Width \cdot L_{Aperture} \tag{D.187}$$

Power Block STG ORC Design

Expanders - cost as a function of inlet volume flow rate (Regression based on Emerson catalog)

call $SCALE(RPM_1,\ RPM_2 : Scale1,\ Scale2)$ If the system size exceeds the catalog of compressors here,costs are extrapolated to running machines in parallel (D.188)

$$Cost_{exp1} = 221.2 + 305372 \cdot \dot{v}_1 \cdot Scale1 \quad \$ \tag{D.189}$$

$$Cost_{exp2} = 221.2 + 305372 \cdot \dot{v}_2 \cdot Scale2 \quad \$ \tag{D.190}$$

Brazed Plate Heat Exchangers - cost as a function of heat exchange area (From Tchanche et al. ECOS 2010)

$$Cost_{hx} = 388 + 480 \cdot \left(A_{prc} + A_{SH} + A_{vap} + A_{recup}\right) \cdot 1.27 \quad \text{1.27 Converts Euro to USD in July 2010} \tag{D.191}$$

Air Condenser - cost as function of heat rejected (assuming 3/8 tubing 4 rows 14 fpi)

unit cost/kW cooling is $78 based on DCNE catalog and quotation 2007

$$Cost_{Cond} = 78 \cdot Q_{cond} \quad \$ \tag{D.192}$$

Pumps and drives - cost is relatively stable over the range of a few kilowatts
Reference pump for WF is Hypro Plunger, 4gpm $510 (McMasterCarr)
Reference pump for HTF is Hypro Gear NG11V-PH, $588 (Grainger)
Reference Drives are LEESON 1hp 24VDC NEMA56C motors $400

$$Start = Start_{int} + 1 \tag{D.193}$$

$$Stop = \text{end}_{\ int} - 1 \tag{D.194}$$

$$Cost_{WFpump} = 510 \cdot P_{ORC,max} \quad \text{values are normalized to a 3.2kW ORC} \tag{D.195}$$

$$Cost_{HTFpump} = 588 \cdot P_{ORC,max} \quad \$ \tag{D.196}$$

$$Cost_{drives} = 400 \cdot 2 \cdot P_{ORC,max} \quad \$ \tag{D.197}$$

Electronics - cost is relatively stable over the range of a few kilowatts
PIC Microcontroller, components, wiring, rectifiers

$$Cost_{elec} = 1000 \cdot P_{ORC,max} \quad \$ \tag{D.198}$$

Balance of system - sensors, fluid manifolds, batteries, structure, insulation etc.

$$Cost_{bos} = 3000 \cdot P_{ORC,max} \quad \$ \tag{D.199}$$

$$Cost_{PB} = Cost_{bos} + Cost_{drives} + Cost_{HTFpump} + Cost_{WFpump} + Cost_{cond} + Cost_{hx} + Cost_{exp1} + Cost_{exp2} + Cost_{elec} \tag{D.200}$$

Based on steel envelope and quartzite filler

$$Fillerspeccost = 0.09\ [\$/\text{kg}] \tag{D.201}$$

$$HTFspeccost = 0.06\ [\$/\mathrm{kg}] \tag{D.202}$$

$$Insulationspeccost = 8\ \left[\$/\mathrm{m}^2\right] \tag{D.203}$$

$$SA = 2 \cdot \pi \cdot (DIA/2)^2 + 2 \cdot \pi \cdot (DIA/2) \cdot Height \qquad \text{Surface Area of Tank} \tag{D.204}$$

$$Vol_{Tank} = Height \cdot \pi \cdot (DIA/2)^2 \tag{D.205}$$

$$Porosity = 0.3 \tag{D.206}$$

$$Vol_{HTF,storage} = vol_{tank} \cdot Porosity \tag{D.207}$$

$$Vol_{mat} = vol_{tank} \cdot (1 - Porosity) \tag{D.208}$$

$$Tankcost = \left(4 \cdot 10^{-12}\right) \cdot vol_{tank}^2 + 250 \cdot vol_{tank} + 5 \cdot 10^{-12} \tag{D.209}$$

$$Cost_{storage} = Fillerspeccost \cdot Vol_{mat} \cdot 1000 + HTFspeccost \cdot Vol_{HTF,storage} \cdot 1000 + Tankcost + Insulationspeccost \cdot SA \tag{D.210}$$

$$Cost_{mat} = Cost_{storage} + Cost_{PB} + Cost_{col} + Cost_{HCE} + Cost_{Track} \tag{D.211}$$

$$Cost_{kWh,day} = Cost_{mat}/ORC_{kWh} \tag{D.212}$$

END COST FUNCTIONS

$$\text{end} \qquad \text{PROCEDURE WRAPPER} \tag{D.213}$$

$$\text{procedure}\ SOLARDATASHIFT\left(sethour,\ risehour,\ I_{Hour,0..23},\ Seconds_{0..23} : Seconds2_{0..12},\ I_{Hour2,0..12}\right) \tag{D.214}$$

Get poly fit for insolation

$$f = 0 \tag{D.215}$$

$$\text{end}\ point = 12 \tag{D.216}$$

$$\text{repeat} \tag{D.217}$$

$$Seconds2_f = Seconds_{risehour+f} \tag{D.218}$$

$$I_{Hour2,f} = I_{Hour,risehour+f} \tag{D.219}$$

$$f := f + 1 \tag{D.220}$$

$$\text{until}\ \ (f > endpoint) \tag{D.221}$$

$$\text{end} \tag{D.222}$$

***PROCEDURE $SOLAR$ RESOURCE ***

$$\text{procedure}\ SOLAR\left(Track\$,\ lat,\ long,\ \delta_{TGMT},\ alt,\ zen : I_{AVE},\ Elevation,\ I_{Hour,0..23},\ \Theta_{hour,0..23},\ Hour_{0..23},\ kWh_{day},\ \Theta_{Ave},\ seconds_{0..23},\ risesecond,\ setsecond,\ Seconds2_{0..12},\ I_{Hour2,0..12}\right) \tag{D.223}$$

$$n = 0 \tag{D.224}$$

$$\text{repeat} \tag{D.225}$$

$$n := n + 1 \tag{D.226}$$

$$AMO = \left(1 + 0.033 \cdot \mathbf{Cos}\left(\frac{360 \cdot (n-2)}{365}\right)\right) \cdot 1356 \tag{D.227}$$

$$\mathbf{If}(zen > 90) \text{ then} \tag{D.228}$$

$$Zen = 90 \tag{D.229}$$

$$\text{endif} \tag{D.230}$$

$$AM = \frac{1}{\mathbf{Cos}(zen) + 0.50572 \cdot (96.07995 - zen)^{-1.36364}} \tag{D.231}$$

$$B = (360/365) \cdot (n - 81) \tag{D.232}$$

$$EOT = 229.2 \cdot (0.000075 + 0.001868 \cdot \mathbf{Cos}(B) - 0.032077 \cdot \sin(B) - 0.014615 \cdot \mathbf{Cos}(2 \cdot B) - 0.04089 \cdot \sin(2 \cdot B)) \tag{D.233}$$

$$LSTM = 15 \cdot \Delta_{TGMT} \tag{D.234}$$

$$TC = 4 \cdot (LSTM - long) + EOT \tag{D.235}$$

$$\Delta = (180/\pi) \cdot (0.006918 - 0.399912 \cdot \mathbf{Cos}(B) + 0.070257 \cdot \sin(B) - 0.006758 \cdot \mathbf{Cos}(2 \cdot B) + 0.000907 \cdot \sin(2 \cdot B) - 0.002697 \cdot \mathbf{Cos}(3 \cdot B) + 0.00148 \cdot \sin(3 \cdot B)) \tag{D.236}$$

$$sunrise = 12 - (1/15) \cdot \arccos\left(-\sin(lat) \cdot \frac{\sin(\Delta)}{COS(lat) \cdot COS(\Delta)}\right) - TC/60 \tag{D.237}$$

$$sunset = 12 + (1/15) \cdot \arccos\left(-\sin(lat) \cdot \frac{\sin(\Delta)}{COS(lat) \cdot COS(\Delta)}\right) - TC/60 \tag{D.238}$$

$$StartHour = \mathbf{Ceil}(sunrise + .75) \tag{D.239}$$

$$\text{end } Hour = \mathbf{Floor}(sunset - .75) \tag{D.240}$$

$$h = -1 \tag{D.241}$$

$$hmax = 23 \tag{D.242}$$

$$\text{repeat} \tag{D.243}$$

$$h := h + 1 \tag{D.244}$$

$$LT = h \tag{D.245}$$

$$LST = LT + TC/60 \tag{D.246}$$

$$HRA = 15 \cdot (LST - 12) \tag{D.247}$$

$$Elevation = \arcsin(SIN(\Delta) \cdot SIN(lat) + \mathbf{Cos}(\Delta) \cdot \mathbf{Cos}(lat) \cdot \mathbf{Cos}(HRA)) \tag{D.248}$$

Determine incidence angle for tracking mode

$$\text{If}(Track\$ = \text{'E-W'}) \text{ then} \tag{D.249}$$

Incidence Angle on E-W Tracking surface

$$\Theta = \arccos\left(\left((\sin(lat) \cdot \sin(\Delta) + COS(lat) \cdot COS(\Delta) \cdot COS(HRA))^2 + COS(\Delta) \cdot COS(\Delta) \cdot \sin(HRA) \cdot \sin(HRA)\right)^{0.5}\right) \tag{D.250}$$

else (D.251)

If($Track\$ = $ 'N-S') then (D.252)

Incidence Angle on N-S Tracking surface

$$\Theta = \arccos\left(\left(\left(1 - \left(COS\left(\Delta\right)^2\right) \cdot \left(\sin\left(HRA\right)^2\right)\right)\right)^{0.5}\right) \quad \text{(D.253)}$$

else (D.254)

If($Track\$ = $ 'two-axis') then (D.255)

$\Theta = 0$ (D.256)

endif (D.257)

endif (D.258)

endif (D.259)

$$I_d = AMO \cdot \left((1 - 0.14 \cdot alt) \cdot 0.7^{AM^{0.678}} + 0.14 \cdot alt\right) \quad \text{(D.260)}$$

If($h < StartHour$) then (D.261)

$I_b = 0$ (D.262)

$\Theta_{h,h} = 0$ (D.263)

else (D.264)

If($h > EndHour$) then (D.265)

$I_b = 0$ (D.266)

$\Theta_{h,h} = 0$ (D.267)

else (D.268)

$I_b = I_d \cdot \mathrm{Cos}(\Theta)$ (D.269)

$\Theta_{h,h} = THETA$ (D.270)

endif (D.271)

endif (D.272)

$I2_h = I_b$ (D.273)

$solar_{aves,n,\mathrm{h:}} = I2_h$ (D.274)

$\Theta_{aves,n,\mathrm{h:}} = \Theta_{h,h}$ (D.275)

$Hours_n = \text{end } Hour - StartHour$ (D.276)

$Until\,(h = hmax)$ (D.277)

$$daily_{\Theta,ave,n} := \frac{\mathrm{Sum}\left(\Theta_{h,4..22}\right)}{(Hours_n)} \quad \text{(D.278)}$$

$$daily_{aves,n} := \frac{\text{Sum}(I2_{4..22})}{Hours_n} \tag{D.279}$$

$$Until\,(n > 365) \tag{D.280}$$

Create an average day solar insolation hourly distribution with average angle of incidence

$$j = 0 \tag{D.281}$$

$$jmax = 23 \tag{D.282}$$

repeat (D.283)

$$Hour_j = j \tag{D.284}$$

$$Temp = 0 \tag{D.285}$$

$$Temp1 = 0 \tag{D.286}$$

$$i = 1 \tag{D.287}$$

repeat (D.288)

$$Temp = Temp + solar_{aves,i,j} \tag{D.289}$$

$$Temp1 = Temp1 + \Theta_{aves,i,j} \tag{D.290}$$

$$i = i + 1 \tag{D.291}$$

until $(i > 365)$ (D.292)

Average Hourly Beam radiation Outputs on tracking surface

$$I_{Hour,j} = Temp/365 \qquad \text{Average Hour Insolation} \tag{D.293}$$

$$\Theta_{Hour,j} = Temp1/365 \tag{D.294}$$

$$j = j + 1 \tag{D.295}$$

until $(j > jmax)$ (D.296)

Average Day Outputs for beam radiation on a tracking surface

$$I_{AVE} = \frac{\text{Sum}\left(daily_{aves,1..365}\right)}{365} \tag{D.297}$$

$$\Theta_{ave} = \frac{\text{Sum}\left(daily_{\Theta,ave,1..365}\right)}{365} \tag{D.298}$$

$$kWh_{day} = \frac{\text{Sum}\left(I_{Hour,0..23}\right)}{1000} \tag{D.299}$$

generate polynomial fit from I_{Hour} distribution

find the start and end of of the insolation curve

$$risehour = 0 \tag{D.300}$$

$$k = 0 \tag{D.301}$$

$$kmax = 12 \tag{D.302}$$

repeat (D.303)

$$k := k + 1 \tag{D.304}$$

$$\text{If}\left(I_{Hour,k>200}\right) \text{ then} \tag{D.305}$$

$$risehour = k - 1 \tag{D.306}$$

$$kmax := k \tag{D.307}$$

endif (D.308)

$$\text{until } (k = kmax) \tag{D.309}$$

$$sethour = 0 \tag{D.310}$$

$$s = 20 \tag{D.311}$$

$$smin = 12 \tag{D.312}$$

repeat (D.313)

$$s := s - 1 \tag{D.314}$$

$$\text{If}\left(I_{Hour,s>200}\right) \text{ then} \tag{D.315}$$

$$sethour = s + 1 \tag{D.316}$$

$$smin := s \tag{D.317}$$

endif (D.318)

$$\text{until } (s = smin) \tag{D.319}$$

convert time domain into seconds

$$p = 0 \tag{D.320}$$

$$pmax = 23 \tag{D.321}$$

repeat (D.322)

$$Seconds_p = Hour_p \cdot 3600 \tag{D.323}$$

$$p := p + 1 \tag{D.324}$$

$$\text{until } (p > pmax) \tag{D.325}$$

$$\text{call } SOLARDATASHIFT\left(sethour,\ risehour,\ I_{Hour,0..23},\ Seconds_{0..23} : Seconds2_{0..12},\ I_{Hour2,0..12}\right) \tag{D.326}$$

$$setsecond = Seconds_{sethour} \tag{D.327}$$

$$risesecond = Seconds_{rischour} \tag{D.328}$$

end (D.329)

bookmark SOLAR

SUBPROGRAM*SOLAR RESOURCE *

$$SUBPROGRAM SOLAR RESOURCE(alt,\ lat,\ long,\ \delta_{TGMT},\ Track\$: I_b,\ \Theta_{Ave},\ T_{Local},\ Wind2m,\ I_{Hour,0..23},\ \Theta_{hour,0..23},\ Hour_{0..23},\ risesecond,\ setsecond,\ Seconds2_{0..12},\ I_{Hour2.0..12},\ Clouds,\ Tmax,\ Tmin)$$

CALL Solar Calculation Procedure

$$\text{call } SOLAR\Big(Track\$,\ lat,\ long,\ \delta_{TGMT},\ alt,\ zen : I_{AVE},\ Elevation,\ I_{Hour,0..23},\ \Theta_{hour,0..23},\ Hour_{0..23},\ kWh_{day},\ \Theta_{Ave},\ seconds_{0..23},\ risesecond,\ setsecond,\ Seconds2_{0..12},\ I_{Hour2.0..12}\Big) \tag{D.330}$$

$$zen = ABS\,(90 - ABS\,(Elevation)) \tag{D.331}$$

Local atmospheric pressure correction

$$P_{local} = 760 \cdot \exp\left(-g\# \cdot 0.0289 \cdot \frac{alt \cdot 1000}{8.31 \cdot (T_{local} + 273)}\right) \quad \text{Torr} \tag{D.332}$$

Local average Temperature and windspeed

$$T_{local} = \text{Interpolate2d}\Big(\text{'Climate'},\ Latitude,\ Longitude,\ T_{amb,ave},\ Latitude = Lat,\ Longitude = Long,\ 8\Big)\ [\text{C}] \tag{D.333}$$

$$Clouds = \text{Interpolate2d('Climate'},\ Latitude,\ Longitude,\ Cloud,\ Latitude = Lat,\ Longitude = Long,\ 8) \quad \text{Cloud data from NASA meteorology database online} \tag{D.334}$$

$$Wind10m = \text{Interpolate2d('Climate'},\ Latitude,\ Longitude,\ Wind,\ Latitude = Lat,\ Longitude = Long)\ [\text{m/s}] \tag{D.335}$$

$$Wind2m = Wind10m \cdot (2/10)^{0.08} \tag{D.336}$$

$$Wind_{Local} = Wind2m \cdot \left|2.23693629\ \frac{\text{mph}}{\text{m/s}}\right| \tag{D.337}$$

$$I_b = I_{AVE} \cdot (1 - Clouds) \tag{D.338}$$

$$TMin = \text{Interpolate2dm('MinTemp'},\ Long,\ Lat) \tag{D.339}$$

$$TMax = \text{Interpolate2dm('MaxTemp'},\ Long,\ Lat) \tag{D.340}$$

$$\text{end} \quad \text{SUBPROGRAM SOLAR RESOURCE} \tag{D.341}$$

Creates diurnal temperature distribution as a two-part sinusoidal function of Tmax and Tmin

$$\text{procedure } AMBIENT(Tmax,\ Tmin,\ risesecond,\ setsecond,\ daysecond : Temp) \tag{D.342}$$

$$A = \frac{Tmax - Tmin}{2} \quad \text{adjusts amplitude of sinusoid} \tag{D.343}$$

$$B = Tmin + A \quad \text{adjusts curve so minimum of sinusoid at Tmin} \tag{D.344}$$

$$maxsecond = 0.75 \cdot (setsecond - risesecond) + risesecond \quad \text{expected time for max temperature} \tag{D.345}$$

$$\text{If}(daysecond > risesecond)\ \text{then} \tag{D.346}$$

$$\text{If}(daysecond < maxsecond)\ \text{then} \quad \text{during heat up of day} \tag{D.347}$$

$$\phi = \frac{\pi}{maxsecond - risesecond} \tag{D.348}$$

$$xoffset = 3 \cdot \pi/2 - \phi \cdot risesecond \tag{D.349}$$

else after max temperature, cooling down (D.350)

$$\phi = \frac{\pi}{86400 - maxsecond + risesecond} \tag{D.351}$$

$$xoffset = \pi/2 - \phi \cdot maxsecond \tag{D.352}$$

endif (D.353)

else before sunrise (D.354)

$$\phi = \frac{\pi}{86400 - maxsecond + risesecond} \tag{D.355}$$

$$xoffset = 3 \cdot \pi/2 - \phi \cdot risesecond \tag{D.356}$$

endif (D.357)

$$Temp = A \cdot \sin(\phi \cdot daysecond + xoffset) + B \tag{D.358}$$

end PROCEDURE AMBIENT (D.359)

procedure $prop_{htf}(fluid\$,\ T : \mu,\ \rho,\ cp,\ k)$ (D.360)

These relationships are valid only for MEG

If $fluid\$ =$ 'glycol' then (D.361)

$$\mu = -0.00197505085 + 0.450245894/T - \frac{1.01338701}{T^2} \qquad \textbf{T is in °C !} \tag{D.362}$$

$$\rho = 1148.28275 - 0.675538335 \cdot T - 0.000198964867 \cdot T^2 \tag{D.363}$$

$$Cp = 2329.09926 + 4.81933829 \cdot T \tag{D.364}$$

$$k = 0.304902525 - 0.000771015939 \cdot T \tag{D.365}$$

endif (D.366)

These relationships are valid only for Therminol 55

If $fluid\$ =$ 'Therminol 55' then (D.367)

$$CP = 1000 \cdot (1.8362895 + 0.00353262314 \cdot T)\ [\mathrm{J/kg \cdot K}] \tag{D.368}$$

$$\rho = 885.151113 - 0.646315736 \cdot T - 0.000207666379 \cdot T^2\ \left[\mathrm{kg/m^3}\right] \tag{D.369}$$

$$\mu = 18.983 \cdot (T)^{-1.915}\ [\mathrm{Pa \cdot s}] \tag{D.370}$$

$$k = -0.0001 \cdot T + 0.1308\ [\mathrm{W/m \cdot K}] \qquad \textbf{T is in °C !} \tag{D.371}$$

endif (D.372)

end prof_{htf} (D.373)

PROCEDURES*SOLAR THERMAL COLLECTORS *

PROCEDURE Pq_{12conv} : Convective heat transfer rate from the HTF to the inside of the receiver tube

$$\text{procedure } Pq_{12conv}(fluid\$,\ D_h,\ D_2,\ T_{1ave},\ v_{1ave},\ T_2 : q_{12conv},\ Cp_1) \tag{D.374}$$

Thermophysical properties for HTF

$$\text{call } prop_{htf}(fluid\$,\ T_{1ave} : \mu_1,\ \rho_1,\ cp_1,\ k_1) \tag{D.375}$$

$$\text{call } prop_{htf}(fluid\$,\ T_2 : \mu_2,\ \rho_2,\ cp_2,\ k_2) \tag{D.376}$$

$$Re_{D2} := ABS\left(\frac{(\rho_1 \cdot D_h \cdot v_{1ave})}{(\mu_1)}\right) \tag{D.377}$$

$$Pr_2 := ABS\,(Cp_2 \cdot \mu_2/k_2) \tag{D.378}$$

$$Pr_1 := ABS\,(Cp_1 \cdot \mu_1/k_1) \tag{D.379}$$

$$\text{If}(Pr_2 < 0)\ \text{then} \tag{D.380}$$

$$Pr_2 := 1 \tag{D.381}$$

$$\text{endif} \tag{D.382}$$

Warning statements if Nusselt Number correlation is used out of recommended range

$$\text{If}(Pr_1 \leq 0.5) or\,(2000 \leq Pr_1)\ \text{then}\ \ \text{call Warning('The result may not be accurate, since 0.5 ¡ Pr\_1 ¡ 2000 does not hold. See PROCEDURE Pq\_12conv. Pr\_1 = XXXA1' ,}\ Pr_1) \tag{D.383}$$

$$\text{If}(Pr_2 \leq 0.5) or\,(2000 \leq Pr_2)\ \text{then}\ \ \text{call Warning('The result may not be accurate, since 0.5 ¡ Pr\_2 ¡ 2000 does not hold. See PROCEDURE Pq\_12conv. Pr\_2 = XXXA1' ,}\ Pr_2) \tag{D.384}$$

$$\text{If}(Re_{D2} \leq (2300)) or\left(5 \cdot 10^6 \leq Re_{D2}\right)\ \text{then}\ \ \text{call Warning}\left(\text{'The result may not be accurate, since 2300 ¡ Re\_D2 ¡ (5 * 10\^6) does not hold. See PROCEDURE Pq\_12conv. Re\_D2 =XXXA1' ,}\ Re_{D2}\right) \tag{D.385}$$

Turbulent/transitional flow Nusselt Number correlation (modified Gnielinski correlation)

$$f_2 := (1.82 \cdot \log 10(Re_{D2}) - 1.64)^{-2} \tag{D.386}$$

$$Nu\#_{D2} := (f_2/8) \cdot (Re_{D2} - 1000) \cdot \frac{Pr_1}{\left(1 + 12.7 \cdot (f_2/8)^{0.5} \cdot \left(Pr_1^{0.6667} - 1\right)\right)} \cdot (Pr_1/Pr_2)^{0.11} \tag{D.387}$$

$$h_1 := Nu\#_{D2} \cdot \frac{k_1}{D_h\ \left[\mathrm{W/m^2 \cdot K}\right]} \tag{D.388}$$

$$q_{12conv} := h_1 \cdot D_2 \cdot \pi \cdot (T_2 - T_{1ave})\ [\mathrm{W/m}] \tag{D.389}$$

$$\text{end} \tag{D.390}$$

FUNCTION fq_{34conv} : Convective heat transfer rate between the absorber outer surface and the glazing inner surface

$$\text{function } fq_{34conv}(D_3,\ D_4,\ P_6,\ v_6,\ T_{amb},\ T_3,\ T_4) \tag{D.391}$$

$$T_{36} := \frac{(T_3 + T_{amb})}{2\ [\mathrm{C}]} \tag{D.392}$$

$$T_{34} := \frac{(T_3 + T_4)}{2\ [\mathrm{C}]} \tag{D.393}$$

$$\text{If}(T_{34<0})\ \text{then} \tag{D.394}$$

$$T_{34} = 50 \tag{D.395}$$

$$\text{endif} \tag{D.396}$$

Thermophysical Properties for gas in annulus space

$$\mu_{34} := \mu\,(AIR,\ \mathrm{T} = T_{34})\ [\mathrm{kg/m \cdot s}] \tag{D.397}$$

$$Cp_{34} := \mathrm{c_p}\,(AIR,\ \mathrm{T} = T_{34})\ [\mathrm{kJ/kg \cdot K}] \tag{D.398}$$

$$Cv_{34} := \mathrm{c_v}\,(AIR,\ \mathrm{T} = T_{34})\ [\mathrm{kJ/kg \cdot K}] \tag{D.399}$$

$$k_{34} := \mathrm{k}\,(AIR,\ \mathrm{T} = T_{34})\ [\mathrm{W/m \cdot K}] \tag{D.400}$$

$$\rho_{34} := \rho\,(AIR,\ \mathrm{T} = T_{34},\ \mathrm{P} = P_6)\ \left[\mathrm{kg/m^3}\right] \tag{D.401}$$

$$\text{If}\left(Cp_{34<0.001}\right)\ \text{then} \tag{D.402}$$

$$Cp_{34} = 1 \tag{D.403}$$

$$\text{endif} \tag{D.404}$$

$$\text{If}(\rho_{34<0.001})\ \text{then} \tag{D.405}$$

$$\rho_{34} = 1 \tag{D.406}$$

$$\text{endif} \tag{D.407}$$

Modified Raithby and Hollands correlation for natural convection in an annular space between horizontal cylinders

$$\alpha_{34} := \frac{k_{34}}{\left(Cp_{34} \cdot \rho_{34} \cdot \left|1000\ \frac{\mathrm{J}}{\mathrm{kJ}}\right|\right)\ \left[\mathrm{m^2/s}\right]} \tag{D.408}$$

$$\text{If}(\alpha_{34} < 0.001)\ \text{then} \tag{D.409}$$

$$\alpha_{34} = 1 \tag{D.410}$$

$$\text{endif} \tag{D.411}$$

$$\nu_{34} := \frac{\mu_{34}}{\rho_{34}\ \left[\mathrm{m^2/s}\right]} \tag{D.412}$$

$$\beta_{34} := \frac{1}{(T_{34} + 273.15)\ [1/\mathrm{K}]} \tag{D.413}$$

$$Ra_{D3} := g\# \cdot \beta_{34} \cdot ABS\,(T_3 - T_4) \cdot \frac{(D_3)^3}{(\alpha_{34} \cdot \nu_{34})} \tag{D.414}$$

$$Ra_{D4} := g\# \cdot \beta_{34} \cdot ABS\left(T_3 - T_4\right) \cdot \frac{(D_4)^3}{(\alpha_{34} \cdot \nu_{34})} \tag{D.415}$$

$$Pr_{34} := \nu_{34}/\alpha_{34} \tag{D.416}$$

$$DelT_{34} = T_3 - T_4 \tag{D.417}$$

$$\text{If}(DelT_{34<0.01}) \text{ then} \tag{D.418}$$

$$DelT_{34} = 1 \tag{D.419}$$

$$\text{endif} \tag{D.420}$$

$$Natq_{34conv} := 2.425 \cdot k_{34} \cdot (DelT_{34}) \cdot \frac{ABS\left(Pr_{34} \cdot \frac{Ra_{D3}}{0.861+Pr_{34}}\right)^{0.25}}{\left(1 + (D_3/D_4)^{0.6}\right)^{1.25}} \text{ [W/m]} \tag{D.421}$$

Free-molecular heat transfer for an annular space between horizontal cylinders

$$P := P_6 \cdot \left| 7.50061505 \frac{\text{mmHg}}{\text{kPa}} \right| \text{ [mmHg]} \tag{D.422}$$

$$C1 := 2.331 \cdot 10^{-20} \left[\text{mmHg} \cdot \text{cm}^3/\text{K}\right] \tag{D.423}$$

$$\delta := 3.53 \cdot 10^{-8} \text{ [cm]} \tag{D.424}$$

$$\lambda := C1 \cdot \frac{(T_{34} + 273.15)}{\left(P \cdot \delta^2\right) \text{ [cm]}} \tag{D.425}$$

$$\gamma := Cp_{34}/Cv_{34} \tag{D.426}$$

$$a := 1 \tag{D.427}$$

$$b := (2 - a) \cdot \frac{(9 \cdot \gamma - 5)}{(2 \cdot a \cdot (\gamma + 1))} \tag{D.428}$$

$$h_{34} := \frac{k_{34}}{(D_3/2 \cdot \ln(D_4/D_3) + b \cdot \lambda \cdot (D_3/D_4 + 1)) \left[\text{W/m}^2 \cdot \text{K}\right]} \tag{D.429}$$

$$Kineticq_{34conv} := D_3 \cdot \pi \cdot h_{34} \cdot (T_3 - T_4) \text{ [W/m]} \tag{D.430}$$

Following compares free molecular heat transfer with natural convection heat transfer and uses the largest value for heat transfer in annulus

$$\text{If}(Kineticq_{34conv} > Natq_{34conv}) \text{ then} \tag{D.431}$$

$$fq_{34conv} := Kineticq_{34conv} \text{ [W/m]} \tag{D.432}$$

Warning statement if free molecular correlation is used out of range

$$\text{If}\left(Ra_{D4} < 10^7\right) \text{ then call Warning}\left(\text{'The result may not be accurate, since (D\_4 / (D\_4 - D\_3))}\hat{4} \text{ ¡ Ra\_D4 ¡ } 10\hat{7} \text{ does not hold. See Function fq\_34conv. Ra\_D4 = XXXA1'}, Ra_{D4}\right) \tag{D.433}$$

$$\text{else} \tag{D.434}$$

$$fq_{34conv} := Natq_{34conv} \ [\mathrm{W/m}] \tag{D.435}$$

endif (D.436)

end (D.437)

FUNCTION fq_{34rad} : Radiation heat transfer rate between the absorber surface and glazing inner surface

$$\text{function } fq_{34rad}\left(D_3,\ D_4,\ T_7,\ \epsilon_4,\ T_3,\ T_4,\ i,\ \epsilon_{3,1..imax\#}\right) \tag{D.438}$$

$$fq_{34rad} := \pi \cdot D_3 \cdot sigma\# \cdot \frac{\left((T_3 + 273.15)^4 - (T_4 + 273.15)^4\right)}{\left(\frac{1}{\epsilon_{3,i}} + D_3/D_4 \cdot (1/\epsilon_4 - 1)\right)} \ [\mathrm{W/m}] \tag{D.439}$$

end (D.440)

FUNCTION fq_{56conv} : Convective heat transfer rate between the glazing outer surface and the ambient air

$$\text{function } fq_{56conv}(D_5,\ P_6,\ v_6,\ T_5,\ T_{amb}) \tag{D.441}$$

$$T_{56} := \frac{(T_5 + T_{amb})}{2 \ [\mathrm{C}]} \tag{D.442}$$

$$\text{If}(T_{5<0}) \text{ then} \tag{D.443}$$

$$T_5 = 50 \tag{D.444}$$

endif (D.445)

$$\text{If}(T_{56<0}) \text{ then} \tag{D.446}$$

$$T_{56} = 50 \tag{D.447}$$

endif (D.448)

Thermophysical Properties for air

$$\mu_5 := \mu\,(Air,\ \mathrm{T} = T_5) \ [\mathrm{kg/m \cdot s}] \tag{D.449}$$

$$\mu_6 := \mu\,(Air,\ \mathrm{T} = T_{amb}) \ [\mathrm{kg/m \cdot s}] \tag{D.450}$$

$$\mu_{56} := \mu\,(Air,\ \mathrm{T} = T_{56}) \ [\mathrm{kg/m \cdot s}] \tag{D.451}$$

$$k_5 := \mathrm{k}\,(Air,\ \mathrm{T} = T_5) \ [\mathrm{W/m \cdot K}] \tag{D.452}$$

$$k_6 := \mathrm{k}\,(Air,\ \mathrm{T} = T_{amb}) \ [\mathrm{W/m \cdot K}] \tag{D.453}$$

$$k_{56} := \mathrm{k}\,(Air,\ \mathrm{T} = T_{56}) \ [\mathrm{W/m \cdot K}] \tag{D.454}$$

$$Cp_5 := \mathrm{c_p}\,(Air,\ \mathrm{T} = T_5) \ [\mathrm{kJ/kg \cdot K}] \tag{D.455}$$

$$Cp_6 := \mathrm{c_p}\,(Air,\ \mathrm{T} = T_{amb}) \ [\mathrm{kJ/kg \cdot K}] \tag{D.456}$$

$$Cp_{56} := \mathrm{c_p}\,(AIR,\ \mathrm{T} = T_{56}) \ [\mathrm{kJ/kg \cdot K}] \tag{D.457}$$

$$\rho_5 := \rho\,(Air,\ \mathrm{T} = T_5,\ \mathrm{P} = P_6)\ \left[\mathrm{kg/m^3}\right] \tag{D.458}$$

$$\rho_6 := \rho\,(Air,\ \mathrm{T} = T_{amb},\ \mathrm{P} = P_6)\ \left[\mathrm{kg/m^3}\right] \tag{D.459}$$

$$\rho_{56} := \rho\,(Air,\ \mathrm{T} = T_{56},\ \mathrm{P} = P_6)\ \left[\mathrm{kg/m^3}\right] \tag{D.460}$$

$$\mathrm{If}(v_6 \le 0.1)\ \text{then} \tag{D.461}$$

Coefficients for Churchill and Chu natural convection correlation

$$\nu_{56} := \frac{\mu_{56}}{\rho_{56}\ \left[\mathrm{m^2/s}\right]} \tag{D.462}$$

$$\alpha_{56} := \frac{k_{56}}{\left(Cp_{56}\cdot\rho_{56}\cdot\left|1000\ \frac{\mathrm{J}}{\mathrm{kJ}}\right|\right)\ \left[\mathrm{m^2/s}\right]} \tag{D.463}$$

$$\beta_{56} := \frac{1}{(T_{56}+273.15)\ [1/\mathrm{K}]} \tag{D.464}$$

$$Ra_{D5} := g\# \cdot \beta_{56} \cdot ABS\,(T_5 - T_{amb}) \cdot \frac{(D_5)^3}{(\alpha_{56}\cdot\nu_{56})} \tag{D.465}$$

Warning Statement if following Nusselt Number correlation is used out of range

$$\mathrm{If}\left(Ra_{D5} \le 10^{-5}\right) or\ \left(Ra_{D5} \ge 10^{12}\right)\ \text{then}\ \ \text{call Warning}\left(\text{'The result may not be accurate, since 10(-5) ¡ Ra\_D5 ¡ 10}\hat{1}2\text{ does not hold. See Function fq\_56conv. Ra\_D5 = XXXA1'},\ Ra_{D5}\right) \tag{D.466}$$

Churchill and Chu correlation for natural convection for a horizontal cylinder

$$Pr_{56} := \nu_{56}/\alpha_{56} \tag{D.467}$$

$$N\bar{u}\# := \left(0.60 + \frac{\left(0.387\cdot Ra_{D5}^{0.1667}\right)}{\left(1+(0.559/Pr_{56})^{0.5625}\right)^{0.2963}}\right)^2 \tag{D.468}$$

$$h_6 := N\bar{u}\# \cdot \frac{k_{56}}{D_5\ \left[\mathrm{W/m^2\cdot K}\right]} \tag{D.469}$$

$$fq_{56conv} := h_6 \cdot \pi \cdot D_5 \cdot (T_5 - T_{amb})\ [\mathrm{W/m}] \tag{D.470}$$

$$\text{else} \tag{D.471}$$

Coefficients for Zhukauskas's correlation

$$\alpha_5 := \frac{k_5}{\left(Cp_5\cdot\rho_5\cdot\left|1000\ \frac{\mathrm{J}}{\mathrm{kJ}}\right|\right)\ \left[\mathrm{m^2/s}\right]} \tag{D.472}$$

$$\alpha_6 := \frac{k_6}{\left(Cp_6\cdot\rho_6\cdot\left|1000\ \frac{\mathrm{J}}{\mathrm{kJ}}\right|\right)\ \left[\mathrm{m^2/s}\right]} \tag{D.473}$$

$$\nu_5 := \frac{\mu_5}{\rho_5 \left[\mathrm{m}^2/\mathrm{s}\right]} \tag{D.474}$$

$$\nu_6 := \frac{\mu_6}{\rho_6 \left[\mathrm{m}^2/\mathrm{s}\right]} \tag{D.475}$$

$$Pr_5 := \nu_5/\alpha_5 \tag{D.476}$$

$$Pr_6 := \nu_6/\alpha_6 \tag{D.477}$$

$$Re_{D5} := v_6 \cdot D_5 \cdot \rho_6/\mu_6 \tag{D.478}$$

Warning Statement if following Nusselt Number coorelation is used out of range

$$\text{If}(Pr_6 \leq 0.7) or\ (Pr_6 \geq 500)\ \text{ then }\ \text{call Warning}(\text{'The result may not be accurate, since 0.7 ¡ Pr\_6 ¡ 500 does not hold. See Function fq\_56conv. Pr\_6 = XXXA1'}\ ,\ Pr_6) \tag{D.479}$$

$$\text{If}(Re_{D5} \leq 1) or \left(Re_{D5} \geq 10^6\right)\ \text{ then }\ \text{call Warning}\left(\text{'The result may not be accurate, since 1 ¡ Re\_D5 ¡ 10\^{}6 does not hold. See Function fq\_56conv. Re\_D5 = XXXA1 '}\ ,\ Re_{D5}\right) \tag{D.480}$$

Zhukauskas's correlation for forced convection over a Longitude horizontal cylinder

$$\text{If}(Pr_6 \leq 10)\ \text{ then} \tag{D.481}$$

$$n := 0.37 \tag{D.482}$$

$$\text{else} \tag{D.483}$$

$$n := 0.36 \tag{D.484}$$

$$\text{endif} \tag{D.485}$$

$$\text{If}(Re_{D5} < 40)\ \text{ then} \tag{D.486}$$

$$C := 0.75 \tag{D.487}$$

$$m := 0.4 \tag{D.488}$$

$$\text{else} \tag{D.489}$$

$$\text{If}(40 \leq Re_{D5}) and \left(Re_{D5} < 10^3\right)\ \text{ then} \tag{D.490}$$

$$C := 0.51 \tag{D.491}$$

$$m := 0.5 \tag{D.492}$$

$$\text{else} \tag{D.493}$$

$$\text{If}\left(10^3 \leq Re_{D5}\right) and \left(Re_{D5} < 2 \cdot 10^5\right)\ \text{ then} \tag{D.494}$$

$$C := 0.26 \tag{D.495}$$

$$m := 0.6 \tag{D.496}$$

$$\text{else} \tag{D.497}$$

$$\text{If}\left(2 \cdot 10^5 \leq Re_{D5}\right) and \left(Re_{D5} < 10^6\right)\ \text{ then} \tag{D.498}$$

$$C := 0.076 \tag{D.499}$$

$$m := 0.7 \tag{D.500}$$

endif (D.501)

endif (D.502)

endif (D.503)

$$\text{If}\left(Re_{D5<0}\right) \text{ then} \tag{D.504}$$

$$ReD5 = 2000 \tag{D.505}$$

endif (D.506)

$$\text{If}(Pr_{6<0}) \text{ then} \tag{D.507}$$

$$Pr_6 = 1 \tag{D.508}$$

endif (D.509)

$$\text{If}(Pr_{5<0}) \text{ then} \tag{D.510}$$

$$Pr_5 = 1 \tag{D.511}$$

endif (D.512)

$$Nu\#_6 := C \cdot Re_{D5}^{m} \cdot Pr_6^{n} \cdot (Pr_6/Pr_5)^{0.25} \tag{D.513}$$

$$h_6 := Nu\#_6 \cdot \frac{k_6}{D_5 \ \left[\mathrm{W/m^2 \cdot K}\right]} \tag{D.514}$$

$$fq_{56conv} := h_6 \cdot \pi \cdot D_5 \cdot (T_5 - T_{amb}) \ [\mathrm{W/m}] \tag{D.515}$$

endif (D.516)

endif (D.517)

end (D.518)

FUNCTION fq_{57rad} : Radiation heat transfer rate between the glazing outer surface and the sky

$$\text{function } fq_{57rad}(\epsilon_5, D_5, T_5, T_7) \tag{D.519}$$

radiative heat transfer for a small convex object in a large cavity

$$fq_{57rad} := \epsilon_5 \cdot \pi \cdot D_5 \cdot sigma\# \cdot \left((T_5 + 273.15)^4 - (T_7 + 273.15)^4\right) \ [\mathrm{W/m}] \tag{D.520}$$

end (D.521)

FUNCTION $fq_{5SolAbs}$: Solar flux on glazing

$$\text{function } fq_{5SolAbs}(\alpha_{env}, OptEff_{env} : q_i) \tag{D.522}$$

solar absorption is estimated with an optical efficiency term

$$fq_{5SolAbs} := q_i \cdot OptEff_{env} \cdot \alpha_{env} \ [\mathrm{W/m}] \tag{D.523}$$

end (D.524)

PROCEDURE Pq_{45cond} : One dimensional energy equation about inside surface of glazing

$$\text{procedure } Pq_{45cond}(q_{34conv},\ q_{34rad} : q_{45cond}) \tag{D.525}$$

for radial conduction the energy balance is used

$$q_{45cond} := q_{34conv} + q_{34rad} \ [\mathrm{W/m}] \tag{D.526}$$

end (D.527)

PROCEDURE Pq_{56conv} : One dimensional energy equation about outside surface of glazing

$$\text{procedure } Pq_{56conv}(q_{45cond},\ q_{5SolAbs},\ q_{57rad} : q_{56conv}) \tag{D.528}$$

For convective heat transfer from the envelope, the energy balance is used

$$q_{56conv} := q_{45cond} + q_{5SolAbs} - q_{57rad} \ [\mathrm{W/m}] \tag{D.529}$$

end (D.530)

FUNCTION fETA_{Col} : Collector efficiency

$$\text{function } fETA_{Col}\left(q_{heat,gain},\ q_i\right) \tag{D.531}$$

If heat is leaving the HTF, then the collector efficiency is set to zero

$$\text{If}\left(\left(q_{heat,gain}/q_i\right) \le 0.001\right) \text{ then} \tag{D.532}$$

$$fETA_{Col} := 0 \tag{D.533}$$

else (D.534)

$$fETA_{Col} := q_{heat,gain}/q_i \tag{D.535}$$

endif (D.536)

end (D.537)

FUNCTION fk_{23}: Absorber conductance

$$\text{function } fk_{23}(T_2,\ T_3) \tag{D.538}$$

$$T_{23} := \frac{T_2 + T_3}{2 \ [\mathrm{C}]} \tag{D.539}$$

$$fk_{23} := 0.013 \cdot T_{23} + 15.2 \ [\mathrm{W/m \cdot K}] \tag{D.540}$$

end (D.541)

PROCEDURE pSelectiveCoatingProperties: Selective Coating Emissivity and Absorptance

$$\text{procedure } pSelectiveCoatingProperties\left(SelectiveCoating\$,\ imax\#,\ T_{3,1..imax\#} : \epsilon_{3,1..imax\#},\ \alpha_{abs},\ \tau_{envelope}\right) \tag{D.542}$$

Do-Loop to calculate emissivity for all the HCE increments, and to return optical properties for chosen selective coating type

$$j := 0 \tag{D.543}$$

repeat (D.544)

$$j := j + 1 \tag{D.545}$$

$$\text{If}(SelectiveCoating\$ = \text{'Black Chrome'})\ \text{then} \tag{D.546}$$

$$\tau_{envelope} := 0.935 \tag{D.547}$$

$$\alpha_{abs} := 0.94 \tag{D.548}$$

$$\epsilon_{3,j} := 0.0005333 \cdot \left(T_{3,j} + 273.15\right) - 0.0856 \tag{D.549}$$

$$\text{If}\left(\epsilon_{3,j} < 0.11\right)\ \text{then} \tag{D.550}$$

$$\epsilon_{3,j} := 0.11 \tag{D.551}$$

endif (D.552)

endif (D.553)

$$\text{If}(SelectiveCoating\$ = \text{'Solec Hi/Sorb-II'})\ \text{then} \tag{D.554}$$

$$\tau_{envelope} := 0.96 \tag{D.555}$$

$$\alpha_{abs} := 0.91 \tag{D.556}$$

$\epsilon_{3,j} := 0.39$ http://www.solarmirror.com/cgi-bin/faq.cgi?$recurse$=1&file=27 (D.557)

endif (D.558)

$$\text{If}(SelectiveCoating\$ = \text{'PV-Unisolar a-Si'})\ \text{then} \tag{D.559}$$

$$\tau_{envelope} := 0.96 \tag{D.560}$$

$$\alpha_{abs} := 0.83 \tag{D.561}$$

$$\epsilon_{3,j} := -3 \times 10^{-6} \cdot \left(T_{3,j} + 273.15\right)^2 + 0.001 \cdot \left(T_{3,j} + 273.15\right) + 0.2429 \tag{D.562}$$

endif (D.563)

$$\text{If}(SelectiveCoating\$ = \text{'PV-First Solar CdTe'})\ \text{then} \tag{D.564}$$

$$\tau_{envelope} := 0.96 \tag{D.565}$$

$$\alpha_{abs} := 0.87 \tag{D.566}$$

$\epsilon_{3,j} := 1$ R.U. Barz 1997 (D.567)

endif (D.568)

If($SelectiveCoating\$ = $ 'PV-Sanyo c-Si') then (D.569)

$\tau_{envelope} := 0.96$ (D.570)

$\alpha_{abs} := 0.83$ (D.571)

$\epsilon_{3,j} := -3 \times 10^{-6} \cdot \left(T_{3,j} + 273.15\right)^2 + 0.001 \cdot \left(T_{3,j} + 273.15\right) + 0.2429$ (D.572)

endif (D.573)

If($SelectiveCoating\$ = $ 'PV-SunPower c-Si') then (D.574)

$\tau_{envelope} := 0.96$ (D.575)

$\alpha_{abs} := 0.83$ (D.576)

$\epsilon_{3,j} := -3 \times 10^{-6} \cdot \left(T_{3,j} + 273.15\right)^2 + 0.001 \cdot \left(T_{3,j} + 273.15\right) + 0.2429$ (D.577)

endif (D.578)

If($SelectiveCoating\$ = $ 'PV-Global Solar CIGS') then (D.579)

$\tau_{envelope} := 0.96$ (D.580)

$\alpha_{abs} := 0.9$ (D.581)

$\epsilon_{3,j} := 0.18$ Kazunori Shimazaki 2007 (D.582)

endif (D.583)

If($SelectiveCoating\$ = $ 'Luz Cermet') then (D.584)

$\tau_{envelope} := 0.935$ (D.585)

$\alpha_{abs} := 0.92$ (D.586)

$\epsilon_{3,j} := 0.000327 \cdot \left(T_{3,j} + 273.15\right) - 0.065971$ (D.587)

If$\left(\epsilon_{3,j} < 0.05\right)$ then (D.588)

$\epsilon_{3,j} := 0.05$ (D.589)

endif (D.590)

endif (D.591)

If($SelectiveCoating\$ = $ 'Solel UVAC Cermet') then (SNL test a) from Forristall 2003 (D.592)

$\tau_{envelope} := 0.965$ (D.593)

$\alpha_{abs} := 0.96$ (D.594)

$\epsilon_{3,j} := 2.249 \cdot 10^{-7} \cdot \left(T_{3,j}\right)^2 + 1.039 \cdot 10^{-4} \cdot T_{3,j} + 5.599 \cdot 10^{-2}$ (D.595)

endif (D.596)

until $(j \geq (imax\#))$ (D.597)

end (D.598)

PROCEDURE pOpticalEfficiency: Optical Efficiencies based on HCE type

procedure $pOpticalEfficiency(A_{aperture},\ HCEtype\$,\ Dirt_{factor,UD},\ Reflectivity,\ \tau_{envelope},\ GlazingIntact\$,\ Shadowing_{UD},\ TrackingError_{UD},\ GeomEffects_{UD},\ Width_{UD},\ D_{2,UD},$

$D_{3,UD},\ D_{4,UD},\ D_{5,UD},\ \Theta : OptEff_{env},\ OptEff_{abs},\ D_2,\ D_3,\ D_4,\ D_5,\ Width,\ Cost_{col})$

If$(HCEtype\$ =$ 'UserDefined') then (D.599)

$Cost_{col} = 175 \cdot A_{aperture}$ Price, Journal of Solar Energy Engineering Copyright 2002 by ASME MAY 2002, Vol. 124 (D.600)

$Width := Width_{UD}$ (D.601)

$D_2 := D_{2,UD}$ (D.602)

$D_3 := D_{3,UD}$ (D.603)

$D_4 := D_{4,UD}$ (D.604)

$D_5 := D_{5,UD}$ (D.605)

$Shadowing := Shadowing_{UD}$ (D.606)

$TrackingError := TrackingError_{UD}$ (D.607)

$GeomEffects := GeomEffects_{UD}$ (D.608)

$\rho_{mirror,clean} := Reflectivity$ (D.609)

endif (D.610)

All the following optical properties should be modified as updated values are determined

If$(HCEtype\$ =$ 'LS-2') then (D.611)

$Cost_{col} = 175 \cdot A_{aperture}$ Price, Journal of Solar Energy Engineering Copyright 2002 by ASME MAY 2002, Vol. 124 (D.612)

Incident angle modifier from test data for SEGS LS-2 Receiver

$IAM = \text{Cos}(\Theta) + 0.000884 \cdot \Theta - 0.00005369 \cdot (\Theta)^2$ (D.613)

$Width = Width_{UD}$ (D.614)

$D_2 := D_{2,UD}$ (D.615)

$D_3 := D_{3,UD}$ (D.616)

$D_4 := D_{4,UD}$ (D.617)

$D_5 := D_{5,UD}$ (D.618)

$Shadowing := 0.974$ (D.619)

$$TrackingError := 0.994 \tag{D.620}$$

$$GeomEffects := 0.98 \tag{D.621}$$

$$\rho_{mirror,clean} := 0.935 \tag{D.622}$$

endif (D.623)

If($HCEtype\$ = $ 'LS-3')or $(HCEtype\$ = $ 'IST') then (D.624)

$Cost_{col} = 175 \cdot A_{aperture}$ Price, Journal of Solar Energy Engineering Copyright 2002 by ASME MAY 2002, Vol. 124 (D.625)

Incident angle modifier from test data for SEGS LS-2 Receiver

$$IAM = \text{Cos}(\Theta) + 0.000884 \cdot \Theta - 0.00005369 \cdot (\Theta)^2 \tag{D.626}$$

$$Width := Width_{UD} \tag{D.627}$$

$$D_2 := D_{2,UD} \tag{D.628}$$

$$D_3 := D_{3,UD} \tag{D.629}$$

$$D_4 := D_{4,UD} \tag{D.630}$$

$$D_5 := D_{5,UD} \tag{D.631}$$

$$Shadowing := 0.974 \tag{D.632}$$

$$TrackingError := 0.994 \tag{D.633}$$

$$GeomEffects := 0.98 \tag{D.634}$$

$$\rho_{mirror,clean} := 0.935 \tag{D.635}$$

endif (D.636)

If($HCEtype\$ = $ 'NEP1200') then (D.637)

$Cost_{col} = 120 \cdot A_{aperture}$ STG 2009 Design - cost as function of aperture area Cost is \$120/m^2 including structural steel, MIRO4, mounting hardware (D.638)

Percent losses due to shadowing by the absorber bracket - this is a best fit curve derived from data using SolTrace and the collector and bracket geometry of the NEP1200. θ is in degrees with 0 degrees = normal incidence angle to the E-W axis collector

$$Width := 1.2 \tag{D.639}$$

$$D_2 := 0.025 \tag{D.640}$$

$$D_3 := 0.028 \tag{D.641}$$

$$D_4 := 0.039 \tag{D.642}$$

$$D_5 := 0.045 \tag{D.643}$$

$$Shadowing := 1 - 0.2114 \cdot \exp\left(-0.041 \cdot (90 - \Theta)\right) \tag{D.644}$$

$$TrackingError := 1 \tag{D.645}$$

$$GeomEffects := 1 \tag{D.646}$$

$\rho_{mirror,clean} := 0.93$ From NEP-PSA-TenderSpec.pdf (D.647)

endif (D.648)

If($HCEtype\$ = $ 'SopoNova4') then (D.649)

$Cost_{col} = 150 \cdot A_{aperture}$ Target pricepoint for Sopogy based on conversation with Ben Morgenstern (D.650)

Incident angle modifier from test data for SEGS LS-2 Receiver

$$IAM = \text{Cos}(\Theta) + 0.000884 \cdot \Theta - 0.00005369 \cdot (\Theta)^2 \quad \text{(D.651)}$$

$Width := 1.486$ (D.652)

$D_2 := 0.02329$ (D.653)

$D_3 := 0.0254$ (D.654)

$D_4 := 0.051$ (D.655)

$D_5 := 0.055$ (D.656)

$Shadowing := 1$ Unknown (D.657)

$TrackingError := 1$ Unknown (D.658)

$GeomEffects := 1$ Unknown (D.659)

$\rho_{mirror,clean} := 0.93$ (D.660)

endif (D.661)

If($HCEtype\$ = $ 'STG_Pilot') then (D.662)

$Cost_{col} = 120 \cdot A_{aperture}$ STG 2009 Design - cost as function of aperture area Cost is \$120/m^2 including structural steel, MIRO4, mounting hardware (D.663)

$Width := 2.5$ (D.664)

$D_2 := 0.057$ (D.665)

$D_3 := 0.063$ (D.666)

$D_4 := 0.08$ (D.667)

$D_5 := 0.088$ (D.668)

$Shadowing := 1$ Unknown (D.669)

$TrackingError := 1$ Unknown (D.670)

$GeomEffects := .9$ Unknown (D.671)

$\rho_{mirror,clean} := 0.93$ (D.672)

endif (D.673)

$$OptEff_{env} := Shadowing \cdot TrackingError \cdot GeomEffects \cdot \rho_{mirror,clean} \cdot Dirt_{Factor,UD} \quad \text{(D.674)}$$

$$OptEff_{abs} := OptEff_{env} \cdot \tau_{Envelope} \quad \text{(D.675)}$$

end (D.676)

FUNCTION fq$_{cond,bracket}$: Heat loss estimate through HCE support bracket

function $fq_{cond,bracket}\left(L_{HCE},\ L_{aperture},\ T_{amb},\ P_6,\ v_6,\ \Delta L,\ T_3,\ i\right)$ (D.677)

call Warning('iteration number i=' , i) (D.678)

Need to update these values for NEP 1200

effective bracket perimeter for convection heat transfer

$$P_{brac} := 0.2032\ [\mathrm{m}] \tag{D.679}$$

effective bracket diameter (2 x 1in)

$$D_{brac} := 0.0508\ [\mathrm{m}] \tag{D.680}$$

minimum bracket cross-sectional area for conduction heat transfer

$$A_{cs,brac} := 0.00016129\ \left[\mathrm{m}^2\right] \tag{D.681}$$

conduction coefficient for carbon steel at 600 K

$$k_{brac} := 48\ [\mathrm{W/m \cdot K}] \tag{D.682}$$

effective bracket base temperature

$$T_{base} := T_3 - 10\ [\mathrm{C}]\ [\mathrm{C}] \tag{D.683}$$

estimate average bracket temperature

$$T_{brac} := \frac{(T_{base} + T_{amb})}{3\ [\mathrm{C}]} \tag{D.684}$$

estimate film temperature for support bracket

$$T_{brac6} := \frac{(T_{brac} + T_{amb})}{2\ [\mathrm{C}]} \tag{D.685}$$

convection coefficient with and without wind

If($v_6 \leq 0.1$) then (D.686)

$$\mu_{brac6} := \mu\left(AIR,\ \mathrm{T} = T_{brac6}\right)\ \left[\mathrm{N \cdot s/m^2}\right] \tag{D.687}$$

$$\rho_{brac6} := \rho\left(AIR,\ \mathrm{T} = T_{brac6},\ \mathrm{P} = P_6\right)\ \left[\mathrm{kg/m^3}\right] \tag{D.688}$$

$$Cp_{brac6} := \mathrm{c_p}\left(AIR,\ \mathrm{T} = T_{brac6}\right)\ [\mathrm{kJ/kg \cdot K}] \tag{D.689}$$

$$k_{brac6} := \mathrm{k}\left(AIR,\ \mathrm{T} = T_{brac6}\right)\ [\mathrm{W/m \cdot K}] \tag{D.690}$$

$$\nu_{brac6} := \frac{\mu_{brac6}}{\rho_{brac6}\ \left[\mathrm{m^2/s}\right]} \tag{D.691}$$

$$\alpha_{brac6} := \frac{k_{brac6}}{\left(Cp_{brac6} \cdot \rho_{brac6} \cdot \left|1000\ \frac{\mathrm{J}}{\mathrm{kJ}}\right|\right)\ \left[\mathrm{m^2/s}\right]} \tag{D.692}$$

$$\beta_{brac6} := \frac{1}{(T_{brac6} + 273.15)\ [1/\mathrm{K}]} \tag{D.693}$$

$$Ra_{Dbrac} := g\# \cdot \beta_{brac6} \cdot ABS\left(T_{brac} - T_{amb}\right) \cdot \frac{(D_{brac})^3}{(\alpha_{brac6} \cdot \nu_{brac6})} \tag{D.694}$$

Warning Statement if following Nusselt Number correlation is used out of recommended range

$$\text{If}\left(Ra_{Dbrac} \leq 10^{-5}\right) or \left(Ra_{Dbrac} \geq 10^{12}\right) \text{ then call Warning}\left(\text{'The result may not be accurate, since 10\^(-5) ¡ Ra\_Dbrac ¡ 10\^12 does not hold. See Function fq\_cond\_bracket. Ra\_Dbrac = XXXA1'}\ ,\ Ra_{Dbrac}\right) \tag{D.695}$$

Churchill and Chu correlation for natural convection from a Longitude isothermal horizontal cylinder

$$Pr_{brac6} := \nu_{brac6}/\alpha_{brac6} \tag{D.696}$$

$$N\bar{u}\# := \left(0.60 + \frac{\left(0.387 \cdot Ra_{Dbrac}^{0.1667}\right)}{\left(1 + (0.559/Pr_{brac6})^{0.5625}\right)^{0.2963}}\right)^2 \tag{D.697}$$

$$h_{brac6} := N\bar{u}\# \cdot \frac{k_{brac6}}{D_{brac}\ \left[\mathrm{W/m^2 \cdot K}\right]} \tag{D.698}$$

else (D.699)

Thermophysical Properties for air

$$\text{If}\left(T_{brac<0}\right) \text{ then} \tag{D.700}$$

$$T_{brac} = 25 \tag{D.701}$$

endif (D.702)

$$\mu_{brac} := \mu\left(AIR,\ \mathrm{T} = T_{brac}\right)\ \left[\mathrm{N \cdot s/m^2}\right] \tag{D.703}$$

$$\mu_6 := \mu\left(AIR,\ \mathrm{T} = T_{amb}\right)\ \left[\mathrm{N \cdot s/m^2}\right] \tag{D.704}$$

$$\rho_6 := \rho\left(AIR,\ \mathrm{T} = T_{amb},\ \mathrm{P} = P_6\right)\ \left[\mathrm{kg/m^3}\right] \tag{D.705}$$

$$\rho_{brac} := \rho\left(AIR,\ \mathrm{T} = T_{brac},\ \mathrm{P} = P_6\right)\ \left[\mathrm{kg/m^3}\right] \tag{D.706}$$

$$k_{brac} := \mathrm{k}\left(AIR,\ \mathrm{T} = T_{brac}\right)\ [\mathrm{W/m \cdot K}] \tag{D.707}$$

$$k_6 := \mathrm{k}\left(AIR,\ \mathrm{T} = T_{amb}\right)\ [\mathrm{W/m \cdot K}] \tag{D.708}$$

$$k_{brac6} := \mathrm{k}\left(AIR,\ \mathrm{T} = T_{brac6}\right)\ [\mathrm{W/m \cdot K}] \tag{D.709}$$

$$Cp_{brac} := \mathrm{c_p}\left(AIR,\ \mathrm{T} = T_{brac}\right)\ [\mathrm{kJ/kg \cdot K}] \tag{D.710}$$

$$Cp_6 := \mathrm{c_p}\left(AIR,\ \mathrm{T} = T_{amb}\right)\ [\mathrm{kJ/kg \cdot K}] \tag{D.711}$$

$$\nu_6 := \frac{\mu_6}{\rho_6\ \left[\mathrm{m^2/s}\right]} \tag{D.712}$$

$$\nu_{brac} := \frac{\mu_{brac}}{\rho_{brac}\ \left[\mathrm{m}^2/\mathrm{s}\right]} \tag{D.713}$$

$$\alpha_{brac} := \frac{k_{brac}}{\left(Cp_{brac}\cdot\rho_{brac}\cdot\left|1000\ \frac{\mathrm{J}}{\mathrm{kJ}}\right|\right)\ \left[\mathrm{m}^2/\mathrm{s}\right]} \tag{D.714}$$

$$\alpha_6 := \frac{k_6}{\left(Cp_6\cdot\rho_6\cdot\left|1000\ \frac{\mathrm{J}}{\mathrm{kJ}}\right|\right)\ \left[\mathrm{m}^2/\mathrm{s}\right]} \tag{D.715}$$

$$Re_{Dbrac} := v_6\cdot D_{brac}/\nu_6 \tag{D.716}$$

$$Pr_{brac} := \nu_{brac}/\alpha_{brac} \tag{D.717}$$

$$Pr_6 := \nu_6/\alpha_6 \tag{D.718}$$

Warning Statements if following Nusselt Correlation is used out of range

$$\text{If}(Re_{Dbrac}\le 1)or\left(Re_{Dbrac}\ge 10^6\right)\ \text{then}\ \ \text{call Warning}\left(\text{'The result may not be accurate, since 1 ¡ Re\_Dbrac ¡ 10\^6 does not hold. See Function fq\_cond\_bracket. Re\_Dbrac = XXXA1'},\ Re_{Dbrac}\right) \tag{D.719}$$

$$\text{If}(Pr_6\le 0.7)or\,(Pr_6\ge 500)\ \ \text{then}\ \ \text{call Warning}(\text{'The result may not be accurate, since 0.7 ¡ Pr\_6 ¡ 500 does not hold. See Function fq\_cond\_bracket. Pr\_6 = XXXA1'},\ Pr_6) \tag{D.720}$$

Coefficients for external forced convection Nusselt Number correlation (Zhukauskas's correlation)

$$\text{If}(Pr_6\le 10)\ \text{then} \tag{D.721}$$

$$n := 0.37 \tag{D.722}$$

$$\text{else} \tag{D.723}$$

$$n := 0.36 \tag{D.724}$$

$$\text{endif} \tag{D.725}$$

$$\text{If}(Re_{Dbrac}<40)\ \text{then} \tag{D.726}$$

$$C := 0.75 \tag{D.727}$$

$$m := 0.4 \tag{D.728}$$

$$\text{else} \tag{D.729}$$

$$\text{If}(40\le Re_{Dbrac})and\left(Re_{Dbrac<}10^3\right)\ \text{then} \tag{D.730}$$

$$C := 0.51 \tag{D.731}$$

$$m := 0.5 \tag{D.732}$$

$$\text{else} \tag{D.733}$$

$$\text{If}\left(10^3\le Re_{Dbrac}\right)and\left(Re_{Dbrac}<2\cdot 10^5\right)\ \text{then} \tag{D.734}$$

$$C := 0.26 \tag{D.735}$$

$$m := 0.6 \tag{D.736}$$

else (D.737)

$\text{If}\left(2 \cdot 10^5 \leq Re_{Dbrac}\right) and \left(Re_{Dbrac} < 10^6\right)$ then (D.738)

$C := 0.076$ (D.739)

$m := 0.7$ (D.740)

endif (D.741)

endif (D.742)

endif (D.743)

endif (D.744)

$\text{If}(Pr_{6<0})$ then (D.745)

$Pr_6 = 1$ (D.746)

endif (D.747)

$\text{If}\left(Pr_{brac<0}\right)$ then (D.748)

$Pr_{brac} = 1$ (D.749)

endif (D.750)

Zhukauskas's correlation for external forced convection flow normal to an isothermal cylinder

$$\bar{Nu\#} := C \cdot (Re_{Dbrac})^m \cdot (Pr_6)^n \cdot (Pr_6/Pr_{brac})^{0.25} \quad \text{(D.751)}$$

$$h_{brac6} := \bar{Nu\#} \cdot \frac{k_{brac6}}{D_{brac}\left[\mathrm{W/m^2 \cdot K}\right]} \quad \text{(D.752)}$$

$\text{If}\left(h_{brac6<0}\right)$ then (D.753)

$h_{brac6} = 1$ (D.754)

endif (D.755)

endif (D.756)

number of HCE support brackets for each HCE segment

$\text{If}(\Delta L \leq L_{HCE})$ then (D.757)

$$index_1 := \text{Round}\left(i \cdot \frac{\Delta L}{L_{HCE}}\right) \quad \text{(D.758)}$$

$index_2 := index_1 \cdot L_{HCE}$ (D.759)

$\text{If}(((i-1) \cdot \Delta L) \leq index_2) AND\, (index_2 \leq (i \cdot \Delta L))$ then (D.760)

$n := 1$ (D.761)

else (D.762)

$n := 0$ (D.763)

endif (D.764)

else (D.765)

$$n := \text{Round}\left(\frac{\Delta L}{L_{HCE}}\right) \quad \text{(D.766)}$$

endif (D.767)

If$(i = 1) OR (i = imax\#)$ then (D.768)

$n := n + 1$ (D.769)

endif (D.770)

$$fq_{cond,bracket} := n \cdot \left(\sqrt{h_{brac6} \cdot P_{brac} \cdot k_{brac} \cdot A_{cs,brac}}\right) \cdot (T_{base} - T_{amb}) \text{ [W]} \quad \text{(D.771)}$$

end (D.772)

FUNCTION fHeatLoss: Heat loss term for temperature out equation

function $fHeatLoss(q_{34rad}, q_{34conv}, q_{56conv}, q_{57rad})$ (D.773)

$fHeatLoss := q_{56conv} + q_{57rad}$ [W/m] (D.774)

end (D.775)

SUBPROGRAM*SOLAR THERMAL COLLECTORS *

$SUBPROGRAMCOLLECTOR(I_b, Wind2m, T_{amb}, \Theta, fluid\$, \dot{v}_{HTF}, GlazingIntact\$, Shadowing_{UD}, TrackingError_{UD}, GeomEffects_{UD}, Reflectivity, Dirt_{factor,UD}, HCEtype\$,$

$L_{HCE}, L_{aperture}, T_{HTF,Col,su}, Width_{UD}, D_{2,UD}, D_{3,UD}, D_{4,UD}, D_{5,UD}, SelectiveCoating\$: \dot{m}_{HTF}, T_{HTF,Col,ex}, Col_{\eta}, E_{col}, Width, Cost_{col})$

Constants and conversions

Glass envelope conductance

$$K_{45} = 1.04 \text{ [W/m·K]} \quad \text{(D.776)}$$

Absorber pipe inside surface equivalent roughness factor

$$e = 1.5 \times 10^{-6} \text{ [m]} \quad \text{(D.777)}$$

Optical properties

Glass envelope absorbtivity from Forristal pg. 36

$$\alpha_{env} = .04 \tag{D.778}$$

Inner and outer glass envelope surface emissivities (pyrex)

$$\epsilon_4 = 0.86 \tag{D.779}$$

$$\epsilon_5 = 0.86 \tag{D.780}$$

Heat collector element size

$$A_{aperture} = L_{aperture} \cdot Width \ \left[\mathrm{m}^2\right] \tag{D.781}$$

Ambient conditions

Effective sky temperature estimated as 8 C below ambient

$$T_7 = T_{amb} - 8 \ [\mathrm{C}] \ [\mathrm{C}] \tag{D.782}$$

Converts ambient pressure from Torr to kPa, ambient pressure is treated as a function of altitude and ambient temperature

$$P_6 = P_{Local} \cdot 0.13332237 \ [\mathrm{kPa}] \tag{D.783}$$

Incoming solar irradiance per aperture segment set by imax#

$$q_i = I_b \cdot \frac{A_{aperture}}{L_{aperture} \ [\mathrm{W/segment}]} \tag{D.784}$$

Indexes

Iteration stepsize along aperture length

$$\Delta L = \frac{L_{aperture}}{(imax\#) \ [\mathrm{m}]} \tag{D.785}$$

Hydraulic diameter

$$D_h = D_2 \ [\mathrm{m}] \qquad \text{Hydraulic diameter} \tag{D.786}$$

Heat transfer fluid flow rates

Calls function to calculate HTF cross-section flow area

$$A_{cs} = \pi \cdot (D_2/2)^2 \ \left[\mathrm{m}^2\right] \tag{D.787}$$

Calculates HTF velocity - converts volume flow rate from LPM to velocity in m/s

$$v_{1inlet} = \frac{\dot{v}_{HTF}}{(A_{cs} \cdot 60000) \ [\mathrm{m/s}]} \tag{D.788}$$

Mass flow rate (conserved)

$$\dot{m}_{HTF} = v_{1inlet} \cdot \rho_{1inlet} \cdot A_{cs} \text{ [kg/s]} \tag{D.789}$$

get density

$$\text{call } prop_{htf}(fluid\$,\ T_{1inlet} : muna,\ \rho_{1inlet},\ cpna,\ kna) \tag{D.790}$$

Calls procedure that determines optical properties

$$\text{call } pSelectiveCoatingProperties\Big(SelectiveCoating\$,\ imax\#,\ T_{3,1..imax\#} : \epsilon_{3,1..imax\#},\ \alpha_{abs},\ \tau_{envelope}\Big) \tag{D.791}$$

Calls procedure that determines optical efficiencies at the glass envelope and absorber and HCE geometries

$$\text{call } pOpticalEfficiency(A_{aperture},\ HCEtype\$,\ Dirt_{factor,UD},\ Reflectivity,\ \tau_{envelope},\ GlazingIntact\$,\ Shadowing_{UD},\ TrackingError_{UD},\ GeomEffects_{UD},\ Width_{UD},\ D_{2,UD},$$

$$D_{3,UD},\ D_{4,UD},\ D_{5,UD},\ \Theta : OptEff_{env},\ OptEff_{abs},\ D_2,\ D_3,\ D_4,\ D_5,\ Width,\ Cost_{col})$$

*
*
Do-loops for temperatures along aperture length
*
*

Do-Loop to set the inlet temperature and velocity of each increment to the previous increment's outlet temperature and velocity

$$T_{1in,1} = T_{1inlet} \text{ [C]} \tag{D.792}$$

$$v_{1in,1} = v_{1inlet} \text{ [m/s]} \tag{D.793}$$

$$\text{duplicate } i = 1,\ (imax\# - 1) \tag{D.794}$$

$$T_{1in,i+1} = T_{1out,i} \text{ [C]} \tag{D.795}$$

$$v_{1in,i+1} = v_{1out,i} \text{ [m/s]} \tag{D.796}$$

$$\text{end} \tag{D.797}$$

Do-Loop to conduct an energy balance on each increment that determines outlet temperature, heat loss, and efficiency

$$\text{duplicate } i = 1,\ imax\# \tag{D.798}$$

$$meter_i = (i) \cdot \Big(L_{aperture}/imax\#\Big) \tag{D.799}$$

$$v_{1ave,i} = \frac{v_{1in,i} + v_{1out,i}}{2 \text{ [m/s]}} \tag{D.800}$$

$$Re_{D2ave,i} = \rho_{1ave,i} \cdot v_{1ave,i} \cdot \frac{D_2}{\mu_{1ave,i}} \tag{D.801}$$

$$\text{call } prop_{htf}\left(fluid\$,\ T_{1out,i} : muna1_i,\ \rho_{1out,i},\ cpna1_i,\ kna1_i\right) \tag{D.802}$$

$$\text{call } prop_{htf}\left(fluid\$,\ T_{1ave,i} : \mu_{1ave,i},\ \rho_{1ave,i},\ cpna2_i,\ kna2_i\right) \tag{D.803}$$

friction factor, f, relation

$$f_i = (1.82 \cdot \log 10(2300) - 1.64)^{-2} \tag{D.804}$$

HTF velocities

Outlet velocity of each increment

$$v_{1out,i} = \frac{\dot{m}_{HTF}}{\left(\rho_{1out,i} \cdot A_{cs}\right)}\ [\text{m/s}] \tag{D.805}$$

Heat loss estimate through HCE support bracket

$$q_{cond,bracket,i} = fq_{cond,bracket}\left(L_{HCE},\ L_{aperture},\ T_{amb},\ P_6,\ v_6,\ \Delta L,\ T_{3,i},\ i\right)\ [\text{W}] \tag{D.806}$$

HTF temperatures

Outlet HTF temperature for each increment

$$HeatLoss_i = fHeatLoss\left(q_{34rad,i},\ q_{34conv,i},\ q_{56conv,i},\ q_{57rad,i}\right)\ [\text{W/m}] \tag{D.807}$$

$$T_{1out,i} = \frac{\left(\left(q_{5SolAbs} + q_{3SolAbs} \cdot \left(1 - \frac{-6\times10^{-5} \cdot T_{3,i} + 0.0649}{0.83}\right) - HeatLoss_i\right) \cdot \Delta L - q_{cond,bracket,i}\right)}{\left(\dot{m}_{HTF} \cdot Cp_{1ave,i}\right)} + \frac{\left(v_{1in,i}\right)^2 - \left(v_{1out,i}\right)^2}{2 * Cp_{1ave,i}} + T_{1in,i}\ [\text{C}] \tag{D.808}$$

Average HTF temperature for each increment

$$T_{1ave,i} = \frac{T_{1in,i} + T_{1out,i}}{2\ [\text{C}]} \tag{D.809}$$

$$\Delta P_i = \frac{\left(f_i \cdot \left(\frac{\Delta L}{D_2}\right) \cdot (\dot{m}_{HTF}/A_{cs})^2\right)}{\left(2 \cdot \rho_{1ave,i}\right)\ [\text{Pa}]} \tag{D.810}$$

Local efficiency of absorber

$$\epsilon_{local,i} = \frac{q_{12conv,i}}{I_b \cdot Width} \tag{D.811}$$

$q_{12conv,i}$ Convective heat transfer rate between the heat transfer fluid and absorber

$$\text{call } Pq_{12conv}\left(fluid\$,\ D_h,\ D_2,\ T_{1ave,i},\ v_{1ave,i},\ T_{2,i} : q_{12conv,i},\ Cp_{1ave,i}\right) \tag{D.812}$$

$q_{23cond,i}$ Conduction heat transfer rate through the absorber

Absorber conductance, temperature and material type dependent

$$k_{23,i} = fk_{23}\left(T_{2,i},\ T_{3,i}\right)\ [\mathrm{W/m \cdot K}] \tag{D.813}$$

$$q_{23cond,i} = 2 \cdot \pi \cdot k_{23,i} \cdot \frac{\left(T_{3,i} - T_{2,i}\right)}{\ln\left(D_3/D_2\right)\ [\mathrm{W/m}]} \tag{D.814}$$

$q_{34conv,i}$ Convective heat transfer rate between the absorber pipe and glazing

$$q_{34conv,i} = fq_{34conv}\left(D_3,\ D_4,\ P_6,\ v_6,\ T_{amb},\ T_{3,i},\ T_{4,i}\right)\ [\mathrm{W/m}] \tag{D.815}$$

$q_{34rad,i}$ Radiation heat transfer rate between the absorber surface and glazing inner surface

$$q_{34rad,i} = fq_{34rad}\left(D_3,\ D_4,\ T_7,\ \epsilon_4,\ T_{3,i},\ T_{4,i},\ i,\ \epsilon_{3,1..imax\#}\right)\ [\mathrm{W/m}] \tag{D.816}$$

$q_{45cond,i}$ Conduction heat transfer rate through the glass envelope

$$q_{45cond,i} = 2 \cdot \pi \cdot K_{45} \cdot \frac{\left(T_{4,i} - T_{5,i}\right)}{\ln\left(D_5/D_4\right)\ [\mathrm{W/m}]} \tag{D.817}$$

$q_{56conv,i}$ Convective heat transfer rate from the glazing to the atmosphere

$$q_{56conv,i} = fq_{56conv}\left(D_5,\ P_6,\ v_6,\ T_{5,i},\ T_{amb}\right)\ [\mathrm{W/m}] \tag{D.818}$$

$q_{57rad,i}$ Radiation heat transfer rate between the glazing outer surface and the sky

$$q_{57rad,i} = fq_{57rad}\left(\epsilon_5,\ D_5,\ T_{5,i},\ T_7\right)\ [\mathrm{W/m}] \tag{D.819}$$

One dimensional (Radial) model

$$\text{call}\ \ Pq_{45cond}\left(q_{34conv,i},\ q_{34rad,i} : q_{45cond,i}\right)\ [\mathrm{W/m}] \tag{D.820}$$

$$\text{call}\ \ Pq_{56conv}\left(q_{45cond,i},\ q_{5SolAbs},\ q_{57rad,i} : q_{56conv,i}\right)\ [\mathrm{W/m}] \tag{D.821}$$

$$q_{12conv,i} = q_{23cond,i}\ [\mathrm{W/m}] \tag{D.822}$$

$$q_{3SolAbs} \cdot \left(1 - \frac{-6 \times 10^{-5} \cdot T_{3,i} + 0.0649}{0.83}\right) - q_{23cond,i} - q_{34conv,i} - q_{34rad,i} - \frac{q_{cond,bracket,i}}{\Delta L} = 0\ [\mathrm{W/m}] \tag{D.823}$$

$$\text{end} \tag{D.824}$$

*

Outlet temperature set equal to the final increment outlet temperature

$$T_{1outlet} = T_{1out,imax\#}\ [\mathrm{C}] \tag{D.825}$$

$$v_{1outlet} = v_{1out,imax\#}\ [\mathrm{m/s}] \tag{D.826}$$

$$\Delta P_{total} = \text{Sum}\left(\Delta P_j,\ \text{j} = 1,\ imax\#\right)\ [\text{Pa}] \tag{D.827}$$

Average HTF Temperature

$$T_{ave} = \text{Average}\left(T_{1ave,1..imax\#}\right)\ [\text{C}] \tag{D.828}$$

Effective optical efficiency and optical loss

$$Reflection_{abs} = q_i \cdot (1 - OptEff_{abs} \cdot \alpha_{abs}) \tag{D.829}$$

$$Reflection_{abs,tot} = Reflection_{abs} \cdot L_{aperture} \tag{D.830}$$

$$\eta_{OptEff.env} = OptEff_{env} \cdot 100\ [\%] \tag{D.831}$$

$$q_{OptLoss} = q_i \cdot (1 - OptEff_{env})\ [\text{W/m}] \tag{D.832}$$

$$q_{OptLoss,tot} = q_{OptLoss} \cdot L_{aperture} \tag{D.833}$$

ETA_{Col} Collector efficiency

Total HTF convection heat gain equals summation of heat gain for each increment

$$q_{heat,gain} = \frac{\text{Sum}\left(\left(q_{12conv,j} \cdot \Delta L\right),\ \text{j} = 1,\ imax\#\right)}{L_{aperture}\ [\text{W/m}]} \tag{D.834}$$

$$E_{col} = q_{in,tot} \cdot \frac{Col_\eta}{100 \cdot 1000} \tag{D.835}$$

$$Col_\eta = fETA_{Col}\left(q_{heat,gain},\ q_i\right) \cdot 100\ [\%] \tag{D.836}$$

$$q_{in,tot} = q_i \cdot L_{aperture} \tag{D.837}$$

$q_{3SolAbs}$ Solar flux on absorber pipe

$$q_{3SolAbs} = q_i \cdot OptEff_{abs} \cdot \alpha_{abs}\ [\text{W/m}] \tag{D.838}$$

$q_{5SolAbs}$ Solar Flux on glazing Envelope

$$q_{5SolAbs} = fq_{5SolAbs}(\alpha_{env},\ OptEff_{env} : q_i)\ [\text{W/m}] \tag{D.839}$$

HCE heat losses

$$q_{cond,bracket,total} = \text{Sum}\left(q_{cond,bracket,j},\ \text{j} = 1,\ imax\#\right)\ [\text{W}] \tag{D.840}$$

$$q_{cond,bracket,L} = \frac{q_{cond,bracket,total}}{L_{aperture}\ [\text{W/m}]} \tag{D.841}$$

$$q_{HeatLoss,ApertureLength} = \frac{\text{Sum}\left(\left(HeatLoss_j \cdot \Delta L\right),\ \text{j} = 1,\ imax\#\right)}{L_{aperture}} + q_{cond,bracket,L}\ [\text{W/m}] \tag{D.842}$$

$$q_{HeatLoss,HCEarea} = \frac{q_{HeatLoss,ApertureLength}}{(\pi \cdot D_5)\ \left[\mathrm{W/m^2}\right]} \tag{D.843}$$

$$q_{HeatLoss,ColArea} = \frac{q_{HeatLoss,ApertureLength} \cdot L_{aperture}}{A_{aperture}\ \left[\mathrm{W/m^2}\right]} \tag{D.844}$$

$$q_{34rad,total} = \mathrm{Sum}\left(q_{34rad,j},\ \mathrm{j} = 1,\ imax\#\right) \cdot \Delta L\ [\mathrm{W}] \tag{D.845}$$

$$q_{34conv,total} = \mathrm{Sum}\left(q_{34conv,j},\ \mathrm{j} = 1,\ imax\#\right) \cdot \Delta L\ [\mathrm{W}] \tag{D.846}$$

$$q_{45cond,total} = \mathrm{Sum}\left(q_{45cond,j},\ \mathrm{j} = 1,\ imax\#\right) \cdot \Delta L\ [\mathrm{W}] \tag{D.847}$$

$$q_{57rad,total} = \mathrm{Sum}\left(q_{57rad,j},\ \mathrm{j} = 1,\ imax\#\right) \cdot \Delta L\ [\mathrm{W}] \tag{D.848}$$

$$q_{56conv,total} = \mathrm{Sum}\left(q_{56conv,j},\ \mathrm{j} = 1,\ imax\#\right) \cdot \Delta L\ [\mathrm{W}] \tag{D.849}$$

Solar Collector

$$Power_{in} = I_b \cdot Width \cdot L_{aperture} \tag{D.850}$$

$$Power_{out} = Col_\eta \cdot Power_{in}/100 \tag{D.851}$$

$$\Delta_T = T_{1outlet} - T_{1inlet} \tag{D.852}$$

$$Optics = \frac{q_{OptLoss,tot} + Reflection_{abs,tol}}{1000} \tag{D.853}$$

$$Convection = q_{56conv,total}/1000 \tag{D.854}$$

$$Radiation = q_{57rad,total}/1000 \tag{D.855}$$

$$Conduction = q_{cond,bracket,total}/1000 \tag{D.856}$$

$$Reflection = reflection_{abs,tot}/1000 \tag{D.857}$$

$$T_{1inlet} = T_{HTF,Col,su} \tag{D.858}$$

$$T_{HTF,Col,ex} = T_{1outlet} \tag{D.859}$$

Conservation of Energy

$$Residual_{Collector} = Power_{in}/1000 - (Power_{out}/1000 + Convection + Radiation + Conduction + Reflection) \tag{D.860}$$

Local atmospheric pressure correction

$$P_{local} = 760 \quad \text{Torr} \tag{D.861}$$

$$v_6 = Wind2m\ [\mathrm{m/s}] \tag{D.862}$$

end (D.863)

*

PROCEDURE HOUR - initializes bed temperature on first run, calculates losses and energy storage

and final tank node temperature when flow is on and when flow is off

*

```
procedure $HOUR\left(vol_{HTF.node}, flow, A_{end}, T_{amb}, R_{tot}, A_{dx}, Fluid\$, T_{HTF}, \dot{m}_{HTF}, timestep, m_s, Cp_s, T_{sin.1..Node\#} : T_{f.out}, E_{Storage}, L_{Storage}, P_{storage}, T_{sop.1..Node\#}\right)$    (D.864)
    $i = 1$    iterate over the nodes    (D.865)
    $imax = Node\#$    (D.866)
    repeat    (D.867)
        $T_{s,i} := T_{sin,i}$ [C]    set the solid temperature for run h to the solid temperature of run h-1    (D.868)
        $i := i + 1$    (D.869)
    until $(i > imax)$    (D.870)
    If$(flow = 1)$ then    (D.871)
        call $OPBEDCHARGE\left(A_{end}, T_{amb}, R_{tot}, A_{dx}, Fluid\$, T_{HTF}, \dot{m}_{HTF}, timestep, m_s, Cp_s, T_{s,1..Node\#} : T_{sop,1..Node\#}, T_{fop,1..Node\#}, Stored2_{1..Node\#}, StoragekW, StoragekWh, LosskWh\right)$    (D.872)
        $E_{Storage} = StoragekWh$    (D.873)
        $L_{Storage} = LosskWh$    (D.874)
        $P_{Storage} = StoragekW$    (D.875)
        $T_{f.out} := T_{sop.Node\#}$    (D.876)
    else    (D.877)
        call $STATICLOSS\left(vol_{HTF.node}, A_{end}, T_{amb}, R_{tot}, A_{dx}, Fluid\$, T_{HTF}, \dot{m}_{HTF}, timestep, m_s, Cp_s, T_{s,1..Node\#} : T_{sop,1..Node\#}, LosskWh\right)$    (D.878)
        $E_{Storage} = 0$    (D.879)
        $L_{Storage} = LosskWh$    (D.880)
        $P_{Storage} = 0$    (D.881)
        $T_{f.out} := T_{sop.Node\#}$    (D.882)
    endif    (D.883)
    $L_{Storage} = LosskWh$    (D.884)
end    (D.885)
```

%%

```
procedure $OPBEDCHARGE\left(A_{end}, T_{amb}, R_{tot}, A_{dx}, Fluid\$, T_{HTF}, \dot{m}_{HTF}, timestep, m_s, Cp_s, T_{s,1..Node\#} : T_{sop,1..Node\#}, T_{fop,1..Node\#}, Stored2_{1..Node\#}, StoragekW, StoragekWh, LosskWh\right)$    (D.886)
```

This procedure implements the Schumann equations via Hughes method described in Duffie and Beckman pg 391 and Mcmahan Thesis

with the timestep-control volume equalization and infinite NTU simplication

Initialize the array lost because its causing problems

$$i = 1 \tag{D.887}$$

$$imax = Node\# \tag{D.888}$$

repeat i counter (D.889)

$$T_{sop,i} = T_{s,i} \tag{D.890}$$

If$(i = 1)$ then (D.891)

$$Stored2_i = 0 \tag{D.892}$$

$$loss_i = 0 \tag{D.893}$$

First subtract losses from temperature of HTF

$$loss_1 = A_{end} \cdot \frac{T_{HTF} - T_{amb}}{R_{tot}\ [\mathrm{W}]}$$ losses off the top greater than out the sides of individual nodes (D.894)

call $prop_{htf}(fluid\$,\ T_{HTF} : \mu_1,\ \rho_1,\ Cp_{HTF},\ k_1)$ (D.895)

$$T_{local} = -\frac{loss_1}{\dot{M}_{HTF} \cdot Cp_{HTF}} + T_{HTF} \tag{D.896}$$

else i > 1 (D.897)

$$loss_i = A_{dx} \cdot \frac{T_{fop,i-1} - T_{amb}}{R_{tot}\ [\mathrm{W}]} \tag{D.898}$$

$$T_{HTF,cp} = T_{fop,i-1} \tag{D.899}$$

call $prop_{htf}\left(fluid\$,\ T_{HTF,cp} : \mu_1,\ \rho_1,\ Cp_{HTF},\ k_1\right)$ (D.900)

$$T_{local} = -\frac{loss_i}{\dot{M}_{HTF} \cdot Cp_{HTF}} + T_{fop,i-1} \tag{D.901}$$

endif IF(i = 1) (D.902)

Now find equilibrium HTF temperature after equilibrating temperature of node solid and HTF

call $prop_{htf}(fluid\$,\ T_{local} : \mu_1,\ \rho_1,\ Cp_{HTF2},\ k_1)$ (D.903)

$$T_{fop,i} = \frac{T_{local} \cdot \dot{m}_{HTF} \cdot Cp_{HTF2} \cdot timestep + T_{sop,i} \cdot m_s \cdot Cp_s}{\dot{m}_{HTF} \cdot Cp_{HTF2} \cdot timestep + m_s \cdot Cp_s} \tag{D.904}$$

$$Stored2_i = m_s \cdot Cp_s \cdot \left(T_{fop,i} - T_{sop,i}\right)\ [\mathrm{J}]$$ energy stored in solid at each node (D.905)

$$T_{sop,i} := T_{fop,i} \tag{D.906}$$

$$i := i + 1 \tag{D.907}$$

until $(i > imax)$ (D.908)

$$LosskWh = \frac{\text{Sum}\left(loss_{1..Node\#}\right) \cdot timestep/3600}{1000\ [\text{kWh}]} \tag{D.909}$$

$$Stored3 = \left(\frac{\text{Sum}\left(Stored2_{1..Node\#}\right)}{1000}\right)\ [\text{kJ}] \tag{D.910}$$

$$StoragekW = \frac{Stored3}{timestep\ [\text{kW}]} \tag{D.911}$$

$$StoragekWh = Stored3 \cdot 0.000277777778 \qquad \text{converts kJ to [kWh]} \tag{D.912}$$

$$T_{ave} = \frac{T_{HTF} + T_{fop.Node\#}}{2} \tag{D.913}$$

$$\text{call } prop_{htf}(fluid\$,\ T_{ave} : \mu_1,\ \rho_1,\ Cp_{HTF},\ k_1) \tag{D.914}$$

$$Sanity_{init} = \dot{m}_{HTF} \cdot Cp_{HTF} \cdot \frac{T_{HTF} - T_{fop.Node\#}}{1000\ [\text{kWh}]} \tag{D.915}$$

$$\text{end} \qquad \text{Procedure OPBedCharge} \tag{D.916}$$

$$\text{procedure } STATICLOSS\left(vol_{HTF,node},\ A_{end},\ T_{amb},\ R_{tot},\ A_{dx},\ Fluid\$,\ T_{HTF},\ \dot{m}_{HTF},\ timestep,\ m_s,\ Cp_s,\ T_{s,1..Node\#} : T_{sop,1..Node\#},\ LosskWh\right) \tag{D.917}$$

This procedure calculates the heat loss to the ambient for each storage node and updates the temperature profile - timestep is 1 hour

$$k = 1 \tag{D.918}$$

$$kmax := 60 \qquad 60 * 60 \text{ second timesteps} \tag{D.919}$$

$$\text{repeat} \tag{D.920}$$

$$i = 1 \tag{D.921}$$

$$imax = Node\# \tag{D.922}$$

$$\text{repeat} \tag{D.923}$$

$$\text{If}(i = 1)\ \text{then} \tag{D.924}$$

$$loss_i = 0 \tag{D.925}$$

losses off the top greater than out the sides of individual nodes

$$loss_1 = A_{end} \cdot \frac{T_{s,1} - T_{amb}}{R_{tot}\ [\text{W}]} \qquad \text{Temp of solid} \tag{D.926}$$

Equilibrate to new solid temp

$$T_{cp} := T_{s,1} \tag{D.927}$$

$$\text{call } prop_{htf}\left(fluid\$,\ T_{cp} : \mu_1,\ \rho_{HTF},\ Cp_{HTF},\ k_1\right) \tag{D.928}$$

$$m_{HTF,node} = vol_{HTF,node} \cdot \rho_{HTF} \tag{D.929}$$

$$T_{new} = -loss_1 \cdot \frac{60}{0.3 \cdot m_{HTF,node} \cdot Cp_{HTF} + 0.7 \cdot m_s \cdot Cp_s} + T_{s,1} \qquad \text{The 60 in this equation is for seconds} \tag{D.930}$$

$$T_{sop,1} = T_{new} \tag{D.931}$$

$$T_{s,1} = T_{new} \tag{D.932}$$

else (D.933)

$$loss_i = A_{dx} \cdot \frac{T_{s,i} - T_{amb}}{R_{tot}\ [\mathrm{W}]} \qquad \text{Temp of solid} \tag{D.934}$$

Equilibrate to new solid temp

$$T_{cp} := T_{s,i} \tag{D.935}$$

call $prop_{htf}\left(fluid\$,\ T_{cp} : \mu_1,\ \rho_{HTF},\ Cp_{HTF},\ k_1\right)$ (D.936)

$$m_{HTF,node} = vol_{HTF,node} \cdot \rho_{HTF} \tag{D.937}$$

$$T_{new} = -loss_i \cdot \frac{60}{0.3 \cdot m_{HTF,node} \cdot Cp_{HTF} + 0.7 \cdot m_s \cdot Cp_s} + T_{s,i} \tag{D.938}$$

$$T_{sop,i} = T_{new} \tag{D.939}$$

$$T_{s,i} = T_{new} \tag{D.940}$$

endif (D.941)

$$i := i + 1 \tag{D.942}$$

until $(i > imax)$ (D.943)

$$Lost_k := \frac{\mathrm{Sum}\left(loss_{1..Node\#}\right)}{60\ [\mathrm{Wh}]} \tag{D.944}$$

$$k := k + 1 \tag{D.945}$$

until $(k > 60)$ (D.946)

$$LosskWh := \frac{\mathrm{Sum}(Lost_{1..kmax})}{1000\ [\mathrm{kWh}]} \tag{D.947}$$

end Procedure STATICLOSS (D.948)

bookmark Storage

procedure $STORAGE\left(flow,\ fluid\$,\ \dot{m}_{HTF},\ T_{HTF,col,ex},\ T_{amb},\ DIA,\ Height,\ T_{sin,1..Node\#} : T_{HTF,Storage,ex},\ T_{sop,1..Node\#},\ E_{Storage},\ L_{Storage},\ P_{Storage},\ timestep\right)$ (D.949)

$$dx = Height/Node\# \qquad \text{height of each node} \tag{D.950}$$

Insulation value of storage unit (converting american to SI)

$$R_{tot} = 20 \cdot 0.1761\ \left[\mathrm{K \cdot m^2/W}\right] \tag{D.951}$$

Void space in quartzite matrix

$$Porosity = 0.3 \tag{D.952}$$

$$A_c = \pi \cdot (DIA/2)^2 \quad \text{Area of the tank top} \tag{D.953}$$

$$SA = 2 \cdot \pi \cdot (DIA/2)^2 + 2 \cdot \pi \cdot (DIA/2) \cdot Height \quad \text{Surface Area of Tank} \tag{D.954}$$

$$A_{dx} = 2 \cdot \pi \cdot (DIA/2) \cdot dx \quad \text{Surface area of any internal node} \tag{D.955}$$

$$A_{end} = A_{dx} + A_c \quad \text{Surface area of end node} \tag{D.956}$$

$$Vol_{Tank} = Height \cdot \pi \cdot (DIA/2)^2 \tag{D.957}$$

$$Vol_{HTF,storage} = vol_{tank} \cdot Porosity \tag{D.958}$$

Determine appropriate timestep from fluid and tank geometry in 1 node

$$T_{HTF} = T_{HTF,col.ex} \tag{D.959}$$

$$\text{call } prop_{htf}(fluid\$,\ T_{HTF} : \mu_1,\ \rho_{HTF},\ cp_1,\ k_1) \tag{D.960}$$

$$Vol_{HTF,node} = Vol_{HTF,storage}/Node\# \tag{D.961}$$

$$m_{HTF,node} = vol_{HTF,node} \cdot \rho_{HTF} \tag{D.962}$$

$$\text{If}(flow = 0)\ \text{then} \tag{D.963}$$

$$timestep = 3600 \quad \text{one hour timesteps when system is at rest} \tag{D.964}$$

$$\text{else} \tag{D.965}$$

$$timestep = m_{HTF,node}/\dot{m}_{HTF} \tag{D.966}$$

$$\text{endif} \tag{D.967}$$

Material properties of solid matrix (quartzite) from Allen Thesis

$$\rho_s = 2640\ \left[\text{kg/m}^3\right] \tag{D.968}$$

$$k_s = 6.35\ [\text{W/m} \cdot \text{K}] \tag{D.969}$$

$$Cp_s = 810\ [\text{J/kg} \cdot \text{K}] \tag{D.970}$$

Initialize the packed bed temperature

$$Bed_{init} = T_{amb}\ [\text{C}] \tag{D.971}$$

Mass of solid matrix in a node

$$Vol_{mat} = vol_{tank} \cdot (1 - Porosity) \tag{D.972}$$

$$m_s = vol_{mat} \cdot \frac{\rho_s}{Node\#\ [\text{kg}]} \tag{D.973}$$

Physical parameters

$$\text{call } HOUR\Big(vol_{HTF,node},\ flow,\ A_{end},\ T_{amb},\ R_{tot},\ A_{dx},\ Fluid\$,\ T_{HTF},\ \dot{m}_{HTF},\ timestep,\ m_s,\ Cp_s,\ T_{sin,1..Node\#} : T_{f,out},\ E_{Storage},\ L_{Storage},\ P_{storage},\ T_{sop,1..Node\#}\Big) \tag{D.974}$$

$$T_{HTF,Storage,ex} = T_{f,out} \tag{D.975}$$

$$\text{end} \qquad \text{PROCEDURE STORAGE} \tag{D.976}$$

$$\text{procedure } prop_{htf}(fluid\$,\ T : \mu,\ \rho,\ cp,\ k) \tag{D.977}$$

These relationships are valid only for MEG

$$\text{If } fluid\$ = \text{'glycol' then} \tag{D.978}$$

$$\mu = -0.00197505085 + 0.450245894/T - \frac{1.01338701}{T^2} \qquad \textbf{T is in °C !} \tag{D.979}$$

$$\rho = 1148.28275 - 0.675538335 \cdot T - 0.000198964867 \cdot T^2 \tag{D.980}$$

$$Cp = 2329.09926 + 4.81933829 \cdot T \ [\mathrm{J/kg \cdot K}] \tag{D.981}$$

$$k = 0.304902525 - 0.000771015939 \cdot T \tag{D.982}$$

$$\text{endif} \tag{D.983}$$

These relationships are valid only for Therminol 55

$$\text{If } fluid\$ = \text{'Therminol 55' then} \tag{D.984}$$

$$CP = 1000 \cdot (1.8362895 + 0.00353262314 \cdot T) \ [\mathrm{J/kg \cdot K}] \tag{D.985}$$

$$\rho = 885.151113 - 0.646315736 \cdot T - 0.000207666379 \cdot T^2 \ \left[\mathrm{kg/m^3}\right] \tag{D.986}$$

$$\mu = 18.983 \cdot (T)^{-1.915} \ [\mathrm{Pa \cdot s}] \tag{D.987}$$

$$k = -0.0001 \cdot T + 0.1308 \ [\mathrm{W/m \cdot K}] \qquad \textbf{T is in °C !} \tag{D.988}$$

$$\text{endif} \tag{D.989}$$

$$\text{end} \qquad \text{prof}_{htf} \tag{D.990}$$

Nusselt Number Correlations from Focke et al. quoted by Wang et. al. 2007 for Chevron Plate 45 Degree

$$\text{procedure } PREHEATER\Big(P_{WF,exp,su},\ T_{WF,PRE,su},\ T_{WF,PRE,ex},\ T_{HTF,PRE,ex},\ T_{HTF,PRE,su},\ v_{HTF},\ v_{WF},\ WF\$,\ Fluid\$,\ TS : h_c,\ h_h,\ Cp_{HTF},\ Cp_{WF}\Big) \tag{D.991}$$

Access fluid properties

$$D_h = 0.004 \tag{D.992}$$

$$L_{char} = D_h \qquad \text{characteristic length} \tag{D.993}$$

Thermophysical properties for HTF

$$\text{call } prop_{htf}\left(fluid\$,\ T_{HTF,PRE,su} : \mu_{1,htf},\ \rho_{1,htf},\ cp_{1,htf},\ k_{1,htf}\right) \tag{D.994}$$

$$\text{call } prop_{htf}\left(fluid\$,\ T_{HTF,PRE,ex} : \mu_{2,htf},\ \rho_{2,htf},\ cp_{2,htf},\ k_{2,htf}\right) \tag{D.995}$$

$$Re_{HTF} = ABS\left(\frac{\left(\rho_{1,HTF} \cdot D_h \cdot v_{HTF}\right)}{\left(\mu_{1,HTF}\right)}\right) \tag{D.996}$$

$$Pr_{2,HTF} = ABS\left(Cp_{2,HTF} \cdot \mu_{2,HTF}/k_{2,HTF}\right) \tag{D.997}$$

$$Pr_{1,HTF} = ABS\left(Cp_{1,HTF} \cdot \mu_{1,HTF}/k_{1,HTF}\right) \tag{D.998}$$

$$Pr_{HTF} = \text{Average}\left(Pr_{2,HTF},\ Pr_{1,HTF}\right) \tag{D.999}$$

$$k_{HTF} = \text{Average}\left(k_{2,HTF},\ k_{1,HTF}\right) \tag{D.1000}$$

$$Cp_{HTF} = \text{Average}\left(Cp_{1,HTF},\ Cp_{2,HTF}\right) \tag{D.1001}$$

Thermophysical properties for WF

$$\mu_{1,WF} = \mu\left(WF\$,\ \text{T} = T_{WF,PRE,su},\ \text{P} = P_{WF,exp,su}\right)\ [\text{kg/m}\cdot\text{s}] \tag{D.1002}$$

$$\mu_{2,WF} = \mu\left(WF\$,\ \text{T} = T_{WF,PRE,ex},\ \text{X} = 0\right)\ [\text{kg/m}\cdot\text{s}] \tag{D.1003}$$

$$Cp_{1,WF} = \text{c}_\text{p}\left(WF\$,\ \text{T} = T_{WF,PRE,su},\ \text{P} = P_{WF,exp,su}\right) \cdot \left|1000\ \frac{\text{J}}{\text{kJ}}\right|\ [\text{J/kg}\cdot\text{K}] \tag{D.1004}$$

$$Cp_{2,WF} = \text{c}_\text{p}\left(WF\$,\ \text{T} = T_{WF,PRE,ex},\ \text{X} = 0\right) \cdot \left|1000\ \frac{\text{J}}{\text{kJ}}\right|\ [\text{J/kg}\cdot\text{K}] \tag{D.1005}$$

$$k_{1,WF} = \text{k}\left(WF\$,\ \text{T} = T_{WF,PRE,su},\ \text{P} = P_{WF,exp,su}\right)\ [\text{W/m}\cdot\text{K}] \tag{D.1006}$$

$$k_{2,WF} = \text{k}\left(WF\$,\ \text{T} = T_{WF,PRE,ex},\ \text{X} = 0\right)\ [\text{W/m}\cdot\text{K}] \tag{D.1007}$$

$$\rho_{1,Wf} = \rho\left(WF\$,\ \text{T} = T_{WF,PRE,su},\ \text{P} = P_{WF,exp,su}\right)\ \left[\text{kg/m}^3\right] \tag{D.1008}$$

$$Re_{WF} = ABS\left(\left(\left(\rho_{1,WF} \cdot D_h \cdot \frac{v_{WF}}{\left(\mu_{1,WF}\right)}\right)\right)\right) \tag{D.1009}$$

$$Pr_{2,WF} = ABS\left(Cp_{2,WF} \cdot \mu_{2,WF}/k_{2,WF}\right) \tag{D.1010}$$

$$Pr_{1,WF} = ABS\left(Cp_{1,WF} \cdot \mu_{1,WF}/k_{1,WF}\right) \tag{D.1011}$$

$$Pr_{WF} = \text{Average}\left(Pr_{2,WF},\ Pr_{1,WF}\right) \tag{D.1012}$$

$$k_{WF} = \text{Average}\left(k_{2,WF},\ k_{1,WF}\right) \tag{D.1013}$$

$$Cp_{WF} = \text{Average}\left(Cp_{1,WF},\ Cp_{2,WF}\right) \tag{D.1014}$$

$$\text{If}\left(Re_{HTF<300}\right)\ \text{then} \tag{D.1015}$$

$$Nu\#_{HTF} = 1.67 \cdot \left(Re_{HTF}^{0.44}\right) \cdot Pr_{HTF}^{0.5} \tag{D.1016}$$

$$\text{else} \tag{D.1017}$$

$$\text{If}(Re_{HTF} < 2000)\ \text{then} \tag{D.1018}$$

$$Nu\#_{HTF} = 0.405 \cdot \left(Re_{HTF}^{0.7}\right) \cdot Pr_{HTF}^{0.5} \tag{D.1019}$$

$$\text{else} \tag{D.1020}$$

$$Nu\#_{HTF} = 0.84 \cdot \left(Re_{HTF}^{0.6}\right) \cdot Pr_{HTF}^{0.5} \tag{D.1021}$$

$$\text{endif} \tag{D.1022}$$

$$\text{endif} \tag{D.1023}$$

$$\text{If}\left(Re_{WF<300}\right)\ \text{then} \tag{D.1024}$$

$$Nu\#_{WF} = 1.67 \cdot \left(Re_{WF}^{0.44}\right) \cdot Pr_{WF}^{0.5} \tag{D.1025}$$

$$\text{else} \tag{D.1026}$$

$$\text{If}\left(Re_{WF<2000}\right)\ \text{then} \tag{D.1027}$$

$$Nu\#_{WF} = 0.405 \cdot \left(Re_{WF}^{0.7}\right) \cdot Pr_{WF}^{0.5} \tag{D.1028}$$

$$\text{else} \tag{D.1029}$$

$$Nu\#_{WF} = 0.84 \cdot \left(Re_{WF}^{0.6}\right) \cdot Pr_{WF}^{0.5} \tag{D.1030}$$

$$\text{endif} \tag{D.1031}$$

$$\text{endif} \tag{D.1032}$$

hot fluid convection coefficient
*

$$h_h = Nu\#_{HTF} \cdot k_{HTF}/L_{char} \tag{D.1033}$$

cold fluid convection coefficient
*

$$h_c = Nu\#_{WF} \cdot k_{WF}/L_{char} \tag{D.1034}$$

$$\text{end} \tag{D.1035}$$

procedure $VAPORIZER\left(\dot{M}_{WF},\ T_{WF,vap,su},\ T_{WF,vap,ex},\ T_{HTF,vap,ex},\ T_{HTF,vap,su},\ v_{HTF},\ WF\$,\ Fluid\$,\ TS : h_{c,vap},\ h_{h,vap},\ Cp_{HTF,vap},\ Cp_{WF,vap}\right)$ (D.1036)

Access fluid properties

$$D_{phe} = 0.004 \tag{D.1037}$$

$$L_{char} = D_{phe} \qquad \text{characteristic length} \tag{D.1038}$$

Thermophysical properties for HTF

$$\text{call } prop_{htf}\left(fluid\$,\ T_{HTF,vap,su} : \mu_{1,HTF},\ \rho_{1,HTF},\ Cp_{1,HTF},\ k_{1,htf}\right) \tag{D.1039}$$

$$\text{call } prop_{htf}\left(fluid\$,\ T_{HTF,vap,ex} : \mu_{2,HTF},\ \rho_{2,HTF},\ Cp_{2,HTF},\ k_{2,htf}\right) \tag{D.1040}$$

$$Re_{HTF} = ABS\left(\frac{\left(\rho_{1,HTF} \cdot D_{phe} \cdot v_{HTF}\right)}{\left(\mu_{1,HTF}\right)}\right) \tag{D.1041}$$

$$Pr_{2,HTF} = ABS\left(Cp_{2,HTF} \cdot \mu_{2,HTF} / k_{2,HTF}\right) \tag{D.1042}$$

$$Pr_{1,HTF} = ABS\left(Cp_{1,HTF} \cdot \mu_{1,HTF} / k_{1,HTF}\right) \tag{D.1043}$$

$$Pr_{HTF} = \text{Average}\left(Pr_{2,HTF},\ Pr_{1,HTF}\right) \tag{D.1044}$$

$$k_{HTF} = \text{Average}\left(k_{2,HTF},\ k_{1,HTF}\right) \tag{D.1045}$$

$$Cp_{HTF,vap} = \frac{\text{Average}\left(Cp_{1,HTF},\ Cp_{2,HTF}\right)}{1000} \qquad \text{convert J to kJ} \tag{D.1046}$$

Thermophysical properties for WF

$$\mu_{1,WF} = \mu\left(WF\$,\ \mathrm{T} = TS,\ \mathrm{x} = 0\right)\ [\mathrm{kg/m \cdot s}] \tag{D.1047}$$

$$Cp_{1,WF} = \mathrm{c_p}\left(WF\$,\ \mathrm{T} = TS,\ \mathrm{x} = 0\right) \cdot \left|1000\ \frac{\mathrm{J}}{\mathrm{kJ}}\right|\ [\mathrm{J/kg \cdot K}] \tag{D.1048}$$

$$Cp_{2,WF} = \mathrm{c_p}\left(WF\$,\ \mathrm{T} = TS,\ \mathrm{x} = 1\right) \cdot \left|1000\ \frac{\mathrm{J}}{\mathrm{kJ}}\right|\ [\mathrm{J/kg \cdot K}] \tag{D.1049}$$

$$k_{1,WF} = \mathrm{k}\left(WF\$,\ \mathrm{T} = TS,\ \mathrm{x} = 0\right)\ [\mathrm{W/m \cdot K}] \tag{D.1050}$$

$$k_{2,WF} = \mathrm{k}\left(WF\$,\ \mathrm{T} = TS,\ \mathrm{x} = 1\right)\ [\mathrm{W/m \cdot K}] \tag{D.1051}$$

$$\rho_{1,Wf} = \rho\left(WF\$,\ \mathrm{T} = T_{WF,vap,su},\ \mathrm{x} = 0\right)\ \left[\mathrm{kg/m^3}\right] \tag{D.1052}$$

$$\rho_{l,WF} := \rho\left(WF\$,\ \mathrm{T} = TS,\ \mathrm{x} = 0\right)\ \left[\mathrm{kg/m^3}\right] \tag{D.1053}$$

$$\rho_{g,WF} := \rho\left(WF\$,\ \mathrm{T} = 128,\ \mathrm{x} = 1\right)\ \left[\mathrm{kg/m^3}\right] \tag{D.1054}$$

$$Pr_{l,WF} = ABS\left(Cp_{1,WF} \cdot \mu_{1,WF}/k_{1,WF}\right) \tag{D.1055}$$

$$k_{WF} = \text{Average}\left(k_{2,WF},\ k_{1,WF}\right) \tag{D.1056}$$

$$Cp_{WF,vap} = \frac{Cp_{1,WF} + Cp_{2,WF}}{2} \tag{D.1057}$$

Nusselt Number Correlations quoted by Wang et. al. 2007
*

$$\text{If}\left(Re_{HTF<300}\right)\ \text{then} \tag{D.1058}$$

$$Nu\#_{HTF,vap} = 1.67 \cdot \left(Re_{HTF}^{0.44}\right) \cdot Pr_{HTF}^{0.5} \tag{D.1059}$$

$$\text{else} \tag{D.1060}$$

$$\text{If}(Re_{HTF} < 2000)\ \text{then} \tag{D.1061}$$

$$Nu\#_{HTF,vap} = 0.405 \cdot \left(Re_{HTF}^{0.7}\right) \cdot Pr_{HTF}^{0.5} \tag{D.1062}$$

$$\text{else} \tag{D.1063}$$

$$Nu\#_{HTF,vap} = 0.84 \cdot \left(Re_{HTF}^{0.6}\right) \cdot Pr_{HTF}^{0.5} \tag{D.1064}$$

$$\text{endif} \tag{D.1065}$$

$$\text{endif} \tag{D.1066}$$

Nusselt Number Correlations modified from Lin et al. quoted by Wang et. al. 2007 for r134a
q nucleate is from Cengel 2007
*

$$x_{ave} = 0.5 \tag{D.1067}$$

$$h_{fg} = 104000\ [\text{J/kg}] \tag{D.1068}$$

$$\sigma = 0.00000013 \tag{D.1069}$$

$$T_{app} = 10\ [\text{C}] \tag{D.1070}$$

$$C_{sf} = 0.015 \tag{D.1071}$$

$$q_{nuc} = \mu_{1,WF} \cdot h_{fg} \cdot \left(\left(\left(9.8 \cdot \frac{ABS\left(\rho_{l,WF} - \rho_{g,WF}\right)}{\sigma}\right)^{.5}\right) \cdot \left(Cp_{WF,vap} \cdot \frac{T_{app}}{C_{sf} \cdot h_{fg} \cdot PR_{l,WF}^{1.7}}\right)^{3}\right. \tag{D.1072}$$

$$G = \frac{\dot{M}_{WF}}{L_{char} \cdot 0.05} \tag{D.1073}$$

$$G_{eq} = G \cdot \left((1 - x_{ave}) + x_{ave} \cdot \left(\rho_{l,WF}/\rho_{g,WF}\right)^{0.5}\right) \tag{D.1074}$$

$$Re_{eq} = G_{eq} \cdot D_{phe}/\mu_{1,WF} \tag{D.1075}$$

$$Bo_{eq} = \frac{q_{nuc}}{G_{eq} \cdot h_{fg}} \tag{D.1076}$$

$$NU\#_{WF,vap} = 1.926 \cdot \left(Pr_{l,WF}^{0.333}\right) \cdot \left(Bo_{eq}^{0.3}\right) \cdot \left(Re_{eq}^{0.5}\right) \cdot \left((1 - x_{ave}) + x_{ave} \cdot \left(\rho_{l,WF}/\rho_{g,WF}\right)^{0.5}\right) \tag{D.1077}$$

hot fluid convection coefficient
*

$$h_{h,vap} = Nu\#_{HTF,vap} \cdot k_{HTF}/L_{char} \tag{D.1078}$$

cold fluid convection coefficient
*

$$h_{c,vap} = Nu\#_{WF,vap} \cdot k_{WF}/L_{char} \tag{D.1079}$$

end (D.1080)

bookmark HEATX

$$SUBPROGRAMHEATX\left(TS,\ T_{WF,recupH,ex},\ P_{WF,exp,su},\ T_{HTF,Storage,ex},\ \dot{m}_{HTF},\ \dot{m}_{WF},\ SH,\ WF\$,\ fluid\$: \dot{Q}_{pre},\ A_{pre},\ A_{vap},\ A_{SH},\ T_{HTF,PRE,ex},\ Pinch_{vap}\right) \tag{D.1081}$$

*
ORC PLATE HEAT EXCHANGER EQUATIONS NOTE: all HTF Fluid Cp calls are in J not kJ!!!!
*

$$T_{WF,PRE,su} = T_{WF,recupH,ex} \tag{D.1082}$$

Superheat - isobaric heat addition to the working fluid gas - Simple assumption that the energy for superheat will require an additional heat exchanger area proportional to the vaporizor
*

call $prop_{htf}\left(fluid\$,\ T_{HTF,Storage,ex} : \mu_{sh},\ \rho_{HTF},\ Cp_{HTF,SH,su},\ k_{sh}\right)$ (D.1083)

call $prop_{htf}\left(fluid\$,\ T_{HTF,vap,su} : \mu_x,\ \rho_{HTFx},\ Cp_{HTF,SH,ex},\ k_x\right)$ (D.1084)

$$Cp_{HTF,SH,ave} = \frac{Cp_{HTF,SH,su} + Cp_{HTF,SH,ex}}{2} \quad \text{average cp of HTF} \tag{D.1085}$$

$$T_{WF,SH} = TS + SH/2 \quad \text{midpoint of the temperature gain in superheat} \tag{D.1086}$$

$$Cp_{WF,SH} = \mathrm{c_P}\left(WF\$,\ \mathrm{T} = T_{WF,SH},\ \mathrm{P} = P_{WF,exp,su}\right) \quad \text{average heat capacity of workingfluid in superheater} \tag{D.1087}$$

$$\dot{Q}_{SH} = \dot{m}_{WF} \cdot Cp_{WF,SH} \cdot (SH)\ [\mathrm{kW}] \quad \text{power transferred in superheater} \tag{D.1088}$$

$$T_{HTF,vap,su} = T_{HTF,Storage,ex} - \frac{\dot{Q}_{SH}}{\dot{m}_{HTF} \cdot Cp_{HTF,SH,ave}/1000} \quad \text{inlet HTF temperature to vaporizor after transferring superheat energy to WF} \tag{D.1089}$$

$$H_{vap,1} = \mathrm{h}\left(WF\$,\ \mathrm{T} = TS,\ \mathrm{X} = 0\right) \tag{D.1090}$$

$$H_{vap,2} = \mathrm{h}\left(WF\$,\ \mathrm{T} = TS,\ \mathrm{X} = 1\right) \tag{D.1091}$$

$$H_{vap} = H_{vap,2} - H_{vap,1} \quad \text{ethalpy of vaporization in vaporizor} \tag{D.1092}$$

$$A_{SH} = A_{vap} \cdot \frac{\dot{Q}_{SH}}{\dot{m}_{WF} \cdot H_{vap}} \quad \text{assume that superheat and vaporizor effectiveness are the same to get superheater area} \tag{D.1093}$$

Vaporizer - isobaric heat addition to the working fluid in the quality zone

*

$$\text{call } VAPORIZER\left(\dot{m}_{WF},\ T_{WF,vap,su},\ T_{WF,vap,ex},\ T_{HTF,vap,ex},\ T_{HTF,vap,su},\ v_{HTF},\ WF\$,\ Fluid\$,\ TS : h_{c,vap},\ h_{h,vap},\ Cp_{HTF,vap},\ Cp_{WF,vap}\right) \tag{D.1094}$$

Overall heat transfer coefficient for the vaporizer

$$U_{vap} = \frac{1}{1/h_{h,vap} + 1/h_{c,vap}} \tag{D.1095}$$

$$\dot{Q}_{vap} = H_{vap} \cdot \dot{m}_{WF}\ \text{[kW]} \qquad \text{Power of vaporizor} \tag{D.1096}$$

$$C_{min,vap} = Cp_{WF,vap} \cdot \dot{m}_{WF} \tag{D.1097}$$

$$\epsilon_{vap} = .85 \qquad \text{effectiveness of vaporizor} \tag{D.1098}$$

$$NTU_{vap} = -\ln\left(1 - \epsilon_{vap}\right) \tag{D.1099}$$

The area is found from the definition of NTU.

$$NTU_{vap} = U_{vap} \cdot A_{vap}/C_{min,vap} \tag{D.1100}$$

$$T_{HTF,vap,ex} = T_{HTF,vap,su} - \left(\frac{\dot{Q}_{vap}}{\dot{M}_{HTF} \cdot Cp_{HTF,vap}}\right)\ \text{[C]} \tag{D.1101}$$

$$T_{WF,vap,su} = TS \tag{D.1102}$$

$$T_{WF,vap,ex} = TS \tag{D.1103}$$

$$Pinch_{vap} = T_{HTF,vap,ex} - TS \tag{D.1104}$$

Preheater - isobaric heat addition to the working fluid from the pump liquid discharge to the 2-phase zone

*

$$\text{call } PREHEATER\left(P_{WF,exp,su},\ T_{WF,PRE,su},\ T_{WF,PRE,ex},\ T_{HTF,PRE,ex},\ T_{HTF,PRE,su},\ v_{HTF},\ v_{WF},\ WF\$,\ Fluid\$,\ TS : h_c,\ h_h,\ Cp_{HTF},\ Cp_{WF}\right) \tag{D.1105}$$

Overall heat transfer coefficient for the preheater

$$U = \frac{1}{1/h_h + 1/h_c} \tag{D.1106}$$

$$WF_{vol} = \text{v}\left(WF\$,\ \text{T} = T_{WF,PRE,su},\ \text{p} = P_{WF,exp,su}\right) \qquad \text{specific volume at preheater inlet} \tag{D.1107}$$

$$v_{WF} = WF_{vol} \cdot \dot{M}_{WF}/A_{Cross} \qquad \text{velocity at preheater inlet} \tag{D.1108}$$

by the effectiveness-NTU method.
An energy balance on hot side.

$$\dot{Q}_{pre} = \dot{m}_{HTF} \cdot Cp_{HTF} \cdot \frac{T_{HTF,PRE,su} - T_{HTF,PRE,ex}}{1000} \tag{D.1109}$$

$$\dot{Q}_{pre} = \dot{m}_{WF} \cdot Cp_{WF} \cdot \frac{T_{WF,PRE,ex} - T_{WF,PRE,su}}{1000} \tag{D.1110}$$

The capacitance rates are;

$$C_h = \dot{m}_{HTF} \cdot Cp_{HTF} \tag{D.1111}$$

$$C_c = \dot{m}_{WF} \cdot Cp_{WF} \tag{D.1112}$$

$$C_{min} = min\,(C_h,\ C_c) \tag{D.1113}$$

$$C_{max} = max\,(C_h,\ C_c) \tag{D.1114}$$

The capacitance rate ratio is:

$$C_{min}/C_{max} - 0.000001 = C \tag{D.1115}$$

0.000001 is subtracted so C is always a little less than 1.0 - exactly 1.0 causes problems with eqn for ϵ

The maximum heat transfer is.

$$\dot{Q}_{max} = C_{min} \cdot \frac{T_{HTF,PRE,su} - T_{WF,PRE,su}}{1000} \tag{D.1116}$$

The effectiveness is found from the definition.

$$\epsilon = \dot{Q}_{pre}/\dot{Q}_{max} \tag{D.1117}$$

$$\epsilon = \frac{1 - \exp\,(-NTU \cdot (1 - c))}{1 - c \cdot \exp\,(-NTU \cdot (1 - C))} \tag{D.1118}$$

The preheater area is found from the definition of NTU.

$$NTU = U \cdot A_{pre}/C_{min} \tag{D.1119}$$

Main Variables relating to heat exchange
*

$$T_{HTF,PRE,su} = T_{HTF,vap,ex} \tag{D.1120}$$

$$T_{WF,PRE,ex} = TS - .000001\ [\mathrm{C}] \tag{D.1121}$$

$$\delta_p = 0.001\ [\mathrm{m}] \tag{D.1122}$$

$$k_p = 400\ [\mathrm{W/m \cdot K}] \tag{D.1123}$$

$$A_{Cross} = 0.1 \cdot 0.2 \tag{D.1124}$$

$$\text{call } prop_{htf}\left(fluid\$,\ T_{HTF,PRE,su} : \mu_v,\ \rho_{HTF,v},\ Cp_{HTF,v},\ k_v\right) \tag{D.1125}$$

$$v_{HTF} = \frac{\dot{m}_{HTF}}{A_{cross} \cdot \rho_{HTF,v}} \tag{D.1126}$$

end SUBPROGRAM HEATX ($T_{WF,recupH,ex}$, $P_{WF,exp,su}$, $T_{HTF,Storage,ex}$, $m_{dot,HTF}$, $m_{dot,WF}$, SH, WF$, fluid$:$Q_{dot,pre}$, A_{pre}, A_{vap}, A_{SH}, $T_{HTF,PRE,ex}$) (D.1127)

$$\text{procedure } SCALE\left(RPM_{exp1},\ RPM_{exp2} : Scale1,\ Scale2\right) \tag{D.1128}$$

$$\text{If}\left(RPM_{exp1>12000}\right)\ \text{then} \tag{D.1129}$$

$$Scale1 = 3 \tag{D.1130}$$

$$\text{endif} \tag{D.1131}$$

$$\text{If}\left(RPM_{exp1>6000}\right)\ \text{then} \tag{D.1132}$$

$$Scale1 = 2 \tag{D.1133}$$

else (D.1134)

$$Scale1 = 1 \tag{D.1135}$$

endif (D.1136)

$$\text{If}\left(RPM_{exp2>12000}\right) \text{ then} \tag{D.1137}$$

$$Scale2 = 3 \tag{D.1138}$$

endif (D.1139)

$$\text{If}\left(RPM_{exp2>6000}\right) \text{ then} \tag{D.1140}$$

$$Scale2 = 2 \tag{D.1141}$$

else (D.1142)

$$Scale2 = 1 \tag{D.1143}$$

endif (D.1144)

end Procedure Scale (D.1145)

$$\text{procedure } EPSILONGEN\left(kW,\ Work_{exp} : \epsilon_{gen}\right) \tag{D.1146}$$

$$\epsilon_{gen} := 0.85 \tag{D.1147}$$

end PROCEDURE EPSILONGEN (D.1148)

$$SUBPROGRAMEXPANSION\left(kW,\ WF\$,\ \dot{m}_{WF},\ cc,\ T_{WF,exp,su},\ P_{WF,exp,su} : H_{WF,exp,ex},\ S_{WF,exp,ex},\ T_{WF,exp,ex},\ P_{WF,exp,ex},\ Work_{exp},\ P_{gen},\ RPM,\ Hz,\ \dot{v}_{exp}\right) \tag{D.1149}$$

$V_r = 2.8$ fixed volume ratio of expander (D.1150)

$\epsilon_{exp} = 0.81$ isentropic efficiency of expander (D.1151)

Determine Expander inlet state parameters

Define H high

$$H1 = \text{h}\left(WF\$,\ \text{T} = T_{WF,exp,su},\ \text{P} = P_{WF,exp,su}\right) \tag{D.1152}$$

Define Entropy at initial state

$$S1 = \text{s}\left(WF\$,\ \text{T} = T_{WF,exp,su},\ \text{P} = P_{WF,exp,su}\right) \tag{D.1153}$$

Define the specific volume of the fluid at the start of expansion

$$V1 = \mathrm{v}\left(WF\$,\ \mathrm{T} = T_{WF,exp,su},\ \mathrm{P} = P_{WF,exp,su}\right) \tag{D.1154}$$

Define Internal Energy at initial state

$$U1 = \mathrm{u}\left(WF\$,\ \mathrm{S} = S1,\ \mathrm{H} = H1\right) \tag{D.1155}$$

Expansion

The volume of fluid is increased by $\mathrm{v}_{r,fixed}$

$$V2 = V1 \cdot V_r \tag{D.1156}$$

isentropic pressure

$$P_{exp,ex,s} = \mathrm{P}\left(WF\$,\ \mathrm{S} = S1,\ \mathrm{V} = V2\right) \tag{D.1157}$$

Define isentropic enthalpy at expander exhaust

$$H_S = \mathrm{h}\left(WF\$,\ \mathrm{S} = S1,\ \mathrm{P} = P_{exp,ex,s}\right) \tag{D.1158}$$

Define enthalpy at expander exhaust

$$H_{WF,exp,ex} = H1 - \epsilon_{exp} \cdot (H1 - H_S) \tag{D.1159}$$

Define State at expander exhaust

$$P_{WF,exp,ex} = \mathrm{P}\left(WF\$,\ \mathrm{V} = V2,\ \mathrm{H} = H_{WF,exp,ex}\right) \tag{D.1160}$$

$$T_{WF,exp,ex} = \mathrm{T}\left(WF\$,\ \mathrm{P} = P_{WF,exp,ex},\ \mathrm{H} = H_{WF,exp,ex}\right) \tag{D.1161}$$

$$S_{WF,exp,ex} = \mathrm{s}\left(WF\$,\ \mathrm{P} = P_{WF,exp,ex},\ \mathrm{H} = H_{WF,exp,ex}\right) \tag{D.1162}$$

$$U2 = \mathrm{u}\left(WF\$,\ \mathrm{S} = S_{WF,exp,ex},\ \mathrm{H} = H_{WF,exp,ex}\right) \tag{D.1163}$$

$$Work_{exp} = \dot{M}_{WF} \cdot \left(H1 - H_{WF,exp,ex}\right) \tag{D.1164}$$

$$Work_{exp2} = \dot{m}_{WF} \cdot (U1 - U2) \tag{D.1165}$$

Calculate RPMS

$$min = 60\ [\mathrm{s}] \tag{D.1166}$$

$$\dot{v}_{exp} = \dot{m}_{WF} \cdot V1 \tag{D.1167}$$

$$RPM = \left(\dot{v}_{exp} \cdot min/cc\right) \cdot 1000000 \tag{D.1168}$$

Frequency of the Induction Generator is a linear function of RPMs (R2=0.97)

$$Hz = 0.0056 \cdot RPM + 26.104 \tag{D.1169}$$

Determine generator efficiency

$$\text{call } EPSILONGEN\Big(kW,\ Work_{exp} : \epsilon_{gen}\Big) \tag{D.1170}$$

$$P_{gen} = Work_{exp} \cdot \epsilon_{gen} \tag{D.1171}$$

$$\text{end} \qquad \text{SUBPROGRAM EXPANSION} \tag{D.1172}$$

%%

%% %%% %%
% % % % %
% % % % %
% % % % %
%% % % %%

%%

$$\text{procedure } ORC(TopScroll\$,\ BotScroll\$,\ WF\$,\ fluid\$,\ T_{WF,exp,su},\ SH,\ \dot{m}_{WF},\ T_{amb},\ Pinch_{cond},\ T_{HTF,Storage,ex},\ \dot{m}_{HTF} : T_{HTF,ORC,ex},\ A_{vap},\ A_{pre},\ A_{SH},\ A_{recup},\ P_{exp1},$$

$$P_{exp2},\ Work_{WF,pump,s},\ Work_{ORC,fans},\ vol_{flow,WF},\ Q_{condenser},\ Thermal_{Power,HTF,ORC},\ RPM_{exp1},\ RPM_{exp2},\ Pinch_{vap},\ \dot{v}_{exp1},\ \dot{v}_{exp2})$$

CALCULATE STATE VARIABLES AROUND THE CYCLE

define known T and pressures high and low

$$TS = T_{WF,exp,su} - SH \tag{D.1173}$$

$$P_{WF,exp,su} = \mathrm{P_{sat}}\left(WF\$,\ \mathrm{T} = TS\right) \tag{D.1174}$$

$$T_{WF,cond} = T_{amb} + Pinch_{cond} \tag{D.1175}$$

$$P_{WF,cond} = \mathrm{P_{sat}}\left(WF\$,\ \mathrm{T} = T_{amb} + Pinch_{cond}\right) \tag{D.1176}$$

$$H_{WF,exp,su} = \mathrm{h}\left(WF\$,\ \mathrm{T} = T_{WF,exp,su},\ \mathrm{P} = P_{WF,exp,su}\right) \tag{D.1177}$$

points for T-S diagram Saturation

$$T_{WF,sat0} = TS \tag{D.1178}$$

$$s_{WF,sat0} = \mathrm{s}\left(WF\$,\ \mathrm{T} = TS,\ \mathrm{X} = 0\right) \tag{D.1179}$$

$$T_{WF,sat1} = TS \tag{D.1180}$$

$$s_{WF,sat1} = \mathrm{s}\left(WF\$,\ \mathrm{T} = TS,\ \mathrm{X} = 1\right) \tag{D.1181}$$

points for T-S diagram Saturation Expander Supply

$$S_{WF,exp,su} = \mathrm{s}\left(WF\$,\ \mathrm{T} = T_{WF,exp,su},\ \mathrm{P} = P_{WF,exp,su}\right) \tag{D.1182}$$

FIRST EXPANSION

$$Row = \textbf{Lookup\$row('Copeland'},\ \textbf{'Model'},\ TopScroll\$) \tag{D.1183}$$

$$cc = \textbf{Lookup('Copeland'},\ Row,\ \textbf{'cc/rev'}\ ) \tag{D.1184}$$

$$kW = \textbf{Lookup('Copeland'},\ Row,\ \textbf{'kW'}\ ) \tag{D.1185}$$

call $EXPANSION\left(kW,\ WF\$,\ \dot{m}_{WF},\ cc,\ T_{WF,exp,su},\ P_{WF,exp,su} : H_{WF,exp,ex},\ S_{WF,exp,ex},\ T_{WF,exp,ex},\ P_{WF,exp,ex},\ Work_{exp},\ P_{gen},\ RPM,\ Hz,\ \dot{v}_{exp}\right)$ (D.1186)

assign outputs to first expansion

$$W_{mech,exp1} = Work_{exp} \quad \text{(D.1187)}$$

$$P_{exp1} := P_{gen} \quad \text{(D.1188)}$$

$$RPM_{exp1} := RPM \quad \text{(D.1189)}$$

$$\dot{v}_{exp1} = \dot{v}_{exp} \quad \text{(D.1190)}$$

$$Hz_{exp1} = Hz \quad \text{(D.1191)}$$

points for T-S diagram Exp midpoint

$$T_{WF,exp,mid} = T_{WF,exp,ex} \quad \text{(D.1192)}$$

$$s_{WF,exp,mid} = S_{WF,exp,ex} \quad \text{(D.1193)}$$

assign second stage inputs to first stage outputs

$$T_{WF,exp,su} := T_{WF,exp,ex} \quad \text{(D.1194)}$$

$$P_{WF,exp,su} := P_{WF,exp,ex} \quad \text{(D.1195)}$$

SECOND EXPANSION

$$Row = \textbf{Lookup\$row}(\textbf{'Copeland'},\ \textbf{'Model'},\ BotScroll\$) \quad \text{(D.1196)}$$

$$cc = \textbf{Lookup}(\textbf{'Copeland'},\ Row,\ \textbf{'cc/rev'}) \quad \text{(D.1197)}$$

$$kW = \textbf{Lookup}(\textbf{'Copeland'},\ Row,\ \textbf{'kW'}) \quad \text{(D.1198)}$$

call $EXPANSION\left(kW,\ WF\$,\ \dot{m}_{WF},\ cc,\ T_{WF,exp,su},\ P_{WF,exp,su} : H_{WF,exp,ex},\ S_{WF,exp,ex},\ T_{WF,exp,ex},\ P_{WF,exp,ex},\ Work_{exp},\ P_{gen},\ RPM,\ Hz,\ \dot{v}_{exp}\right)$ (D.1199)

assign outputs to second expansion

$$W_{mech,exp2} = Work_{exp} \quad \text{(D.1200)}$$

$$P_{exp2} := P_{gen} \quad \text{(D.1201)}$$

$$RPM_{exp2} := RPM \quad \text{(D.1202)}$$

$$\dot{v}_{exp2} = \dot{v}_{exp} \quad \text{(D.1203)}$$

$$Hz_{exp2} = Hz \quad \text{(D.1204)}$$

points for T-S diagram Exp2 exhaust

$$T_{WF,exp2,ex} = T_{WF,exp,ex} \quad \text{(D.1205)}$$

$$s_{WF,exp2,ex} = S_{WF,exp,ex} \quad \text{(D.1206)}$$

UNDEREXPANSION/OVEREXPANSION LOSSES

Vapor expands at constant enthalpy to the state at the inlet of recuperator, assume 20kPa pressure drop to P_{cond} (half in recuperator and half in condenser) and 5[C] approach to cond temperature

RECUPERATOR LOW SIDE

points for T-S diagram Recuperator Low side Supply

$$T_{WF,recupL,su} = \mathrm{T}\left(WF\$,\ \mathrm{P} = P_{WF,cond} + 20,\ \mathrm{H} = H_{WF,exp,ex}\right) \tag{D.1207}$$

$$s_{WF,recupL,su} = \mathrm{s}\left(WF\$,\ \mathrm{T} = T_{WF,recupL,su},\ \mathrm{P} = P_{WF,cond} + 20\right) \tag{D.1208}$$

points for T-S diagram Recuperator Low side Exhaust

$$T_{WF,recupL,ex} = T_{WF,cond} + 5 \tag{D.1209}$$

$$s_{WF,recupL,ex} = \mathrm{s}\left(WF\$,\ \mathrm{P} = P_{WF,cond} + 10,\ \mathrm{T} = T_{WF,recupL,ex}\right) \tag{D.1210}$$

$$h_{WF,recupL,su} = \mathrm{h}\left(WF\$,\ \mathrm{T} = T_{WF,recupL,su},\ \mathrm{P} = P_{WF,cond} + 20\right) \tag{D.1211}$$

$$h_{WF,recupL,ex} = \mathrm{h}\left(WF\$,\ \mathrm{T} = T_{WF,recupL,ex},\ \mathrm{P} = P_{WF,cond} + 10\right) \tag{D.1212}$$

$$Power_{recup} = \dot{m}_{WF} \cdot \left(H_{WF,recupL,su} - H_{WF,recupL,ex}\right) \quad \text{Recuperator Power exchange} \tag{D.1213}$$

CONDENSER

$$subcool = 1 \tag{D.1214}$$

points for T-S diagram Condenser Exhaust

$$T_{WF,cond,ex} = T_{amb} + Pinch_{cond} - subcool \tag{D.1215}$$

$$s_{WF,cond,ex} = \mathrm{s}\left(WF\$,\ \mathrm{T} = T_{WF,cond,ex},\ \mathrm{P} = P_{WF,cond}\right) \tag{D.1216}$$

$$h_{WF,cond,ex} = \mathrm{h}\left(WF\$,\ \mathrm{T} = T_{WF,cond,ex},\ \mathrm{P} = P_{WF,cond}\right) \tag{D.1217}$$

$$Q_{condenser} = \dot{M}_{WF} \cdot \left(h_{WF,recupL,ex} - h_{WF,cond,ex}\right) \tag{D.1218}$$

Regression from specs table for WITT air condensers with 10F approach 3-layer 3/8ths tubing

$$A_{cond} = 0.0837 \cdot Q_{condenser} + 0.7903\ \left[\mathrm{m}^2\right] \tag{D.1219}$$

$$Work_{ORC,fans} = 225.37 \cdot \frac{A_{cond}}{1000\ [\mathrm{kW}]} \tag{D.1220}$$

WORKING FLUID PUMP

$$h_{WF,pump,su} = h_{WF,cond,ex} \tag{D.1221}$$

$$s_{WF,pump,su} = s_{WF,cond,ex} \tag{D.1222}$$

$$h_{WF,pump,ex} = \mathrm{h}\left(WF\$,\ \mathrm{s} = s_{WF,pump,su},\ \mathrm{p} = P_{WF,exp,su}\right) \tag{D.1223}$$

$$Work_{WF,pump,s} = \dot{M}_{WF} \cdot \left(h_{WF,pump,ex} - h_{WF,pump,su}\right) \tag{D.1224}$$

$$vol_{WF} = \mathrm{v}\left(WF\$,\ \mathrm{T} = T_{WF,cond,ex},\ \mathrm{S} = s_{WF,cond,ex}\right) \tag{D.1225}$$

$$vol_{flow,WF} = (\dot{m}_{WF} \cdot vol_{WF}) \cdot 1000 \cdot 60 \text{ [LPM]} \tag{D.1226}$$

points for T-S diagram Pump Exhaust

$$T_{WF,pump,ex} = \text{T}\left(WF\$,\ \text{H} = H_{WF,pump,ex},\ \text{P} = P_{WF,exp,su}\right) \tag{D.1227}$$

$$s_{WF,pump,ex} = \text{s}\left(WF\$,\ \text{T} = T_{WF,pump,ex},\ \text{P} = P_{WF,exp,su}\right) \tag{D.1228}$$

RECUPERATOR HIGH SIDE

points for T-S diagram Recuperator High side Exhaust

$$h_{WF,recupH,su} = h_{WF,pump,ex} \tag{D.1229}$$

$$H_{WF,recupH,ex} = Power_{recup}/\dot{m}_{WF} + H_{WF,recupH,su} \tag{D.1230}$$

$$T_{WF,recupH,ex} = \text{T}\left(WF\$,\ \text{P} = P_{WF,exp,su},\ \text{H} = H_{WF,recupH,ex}\right) \tag{D.1231}$$

$$S_{WF,recup,ex} = \text{s}\left(WF\$,\ \text{P} = P_{WF,exp,su},\ \text{H} = H_{WF,recupH,ex}\right) \tag{D.1232}$$

HEATEXCHANGERS PREHEAT AND VAPORIZER

$$\text{call } HEATX\left(TS,\ T_{WF,recupH,ex},\ P_{WF,exp,su},\ T_{HTF,Storage,ex},\ \dot{m}_{HTF},\ \dot{m}_{WF},\ SH,\ WF\$,\ fluid\$: \dot{Q}_{pre},\ A_{pre},\ A_{vap},\ A_{SH},\ T_{HTF,PRE,ex},\ Pinch_{vap}\right) \tag{D.1233}$$

$$T_{HTF,ORC,ex} = T_{HTF,PRE,ex} \tag{D.1234}$$

$$A_{recup} = A_{vap} \cdot Power_{recup}/\dot{Q}_{pre} \qquad \textbf{Area of Recuperator is assumed proporational to area of vaporizor on a heat rate basis} \tag{D.1235}$$

Global ORC parameters

$$T_{HTF,ave} = \frac{T_{HTF,Storage,ex} + T_{HTF,ORC,ex}}{2} \tag{D.1236}$$

$$\text{call } prop_{htf}\left(fluid\$,\ T_{HTF,ave} : \mu_{ave},\ \rho_{ave},\ Cp_{HTF,ave},\ k_{ave}\right) \tag{D.1237}$$

$$Thermal_{Power,HTF,ORC} = \dot{m}_{HTF} \cdot Cp_{HTF,ave} \cdot \frac{T_{HTF,Storage,ex} - T_{HTF,ORC,ex}}{1000 \text{ [kW]}} \tag{D.1238}$$

$$Thermal_{Power,WF,ORC} = \dot{m}_{WF} \cdot \left(H_{WF,exp,su} - H_{WF,recupH,ex}\right) \tag{D.1239}$$

$$\text{end} \qquad \text{PROCEDURE ORC} \tag{D.1240}$$

$$\text{call } WRAPPER(\epsilon_{pump},\ \epsilon_{drive},\ alt,\ lat,\ long,\ \delta_{TGMT},\ Track\$,\ GlazingIntact\$,\ Shadowing_{UD},\ TrackingError_{UD},\ GeomEffects_{UD},\ Reflectivity,$$

$$Dirt_{factor,UD},\ HCEtype\$,\ L_{HCE},\ L_{aperture},\ Width_{UD},\ D_{2,UD},\ D_{3,UD},\ D_{4,UD},\ D_{5,UD},\ SelectiveCoating\$,\ T_{WF,exp,su},\ SH,\ Pinch_{cond},\ TopScroll\$,\ BotScroll\$,\ WF\$,\ fluid\$,\ \dot{m}_{WF},$$

$\dot{v}_{HTF}$, DIA, $Height$: η_{ORC}, η_{sys}, η_{solar}, $Cost_{cond}$, $Cost_{HCE}$, $Cost_{track}$, $Cost_{exp1}$, $Cost_{exp2}$, $Cost_{mat}$, $Cost_{col}$, $Cost_{PB}$, $Cost_{Storage}$,

ORC_{kWh}, Col_{kWh}, $Solar_{kWh}$, $Storage_{kWh}$, $Area_{aperture}$, $P_{ORC,max}$)

Inputs from main:

$$\epsilon_{pump} = 0.85 \tag{D.1241}$$

$$\epsilon_{drive} = 0.85 \tag{D.1242}$$

$$alt = .3 \tag{D.1243}$$

$$long = 26 \tag{D.1244}$$

$$\delta_{TGMT} = 2 \tag{D.1245}$$

$$Track\$ = \text{'E-W'} \tag{D.1246}$$

Collector UD INPUTS

$$fluid\$ = \text{'glycol'} \tag{D.1247}$$

$$\dot{v}_{HTF} = 40 \quad \text{LPM} \tag{D.1248}$$

$$GlazingIntact\$ = \text{'Yes'} \tag{D.1249}$$

$$Shadowing_{UD} = 1 \tag{D.1250}$$

$$TrackingError_{UD} = 1 \tag{D.1251}$$

$$GeomEffects_{UD} = 1 \tag{D.1252}$$

$$Reflectivity = 0.93 \tag{D.1253}$$

$$Dirt_{factor,UD} = 0.96 \tag{D.1254}$$

$$HCEtype\$ = \text{'NEP1200'} \quad \text{STG}_{Pilot}\text{, NEP1200, SopoNova4} \tag{D.1255}$$

$$L_{HCE} = 1 \tag{D.1256}$$

$$L_{aperture} = 60 \tag{D.1257}$$

$$Width_{UD} = 2.5 \tag{D.1258}$$

$$D_{2,UD} = 0.053 \tag{D.1259}$$

$$D_{3,UD} = 0.065 \tag{D.1260}$$

$$D_{4,UD} = 0.08 \tag{D.1261}$$

$$D_{5,UD} = 0.088 \tag{D.1262}$$

$$SelectiveCoating\$ = \text{'Black Chrome'} \tag{D.1263}$$

Storage Tank Size

$$Height = 2.5 \text{ [m]} \tag{D.1264}$$

$$TopScroll\$ = \text{'ZR47'} \tag{D.1265}$$

$$BotScroll\$ = \text{'ZR144'} \tag{D.1266}$$

$$T_{WF,exp,su} = 135 \quad \text{(D.1267)}$$

$$SH = 5 \quad \text{(D.1268)}$$

$$WF\$ = \text{'R245fa'} \quad \text{(D.1269)}$$

$$Pinch_{cond} = 10 \quad \text{(D.1270)}$$

Bibliography

[1] Assessment of Backup Power Needs for Selected Laboratories in Mozambique. Final Report 620-39728, Tetra Tech, Arlington, VA, Ocotber 2010. Prepared for Association of Public Health Laboratories, APHL.

[2] Engen South Africa website. Fuel prices March 2012. Accessed March 25, 2012 at www.engen.co.za/home/apps/content/products_services/fuel_price.

[3] Engineering Toolbox. Air Change Rates for typical Rooms and Buildings. Accessed April 20, 2012 at http://www.engineeringtoolbox.com/airchangerateroomd_867.html.

[4] House Needs website. Forced Convection Radiator retail prices. Accessed March 25, 2012 at http://www.houseneeds.com/shop/atop/radiator-heaters-hydronic-radiator.asp.

[5] Kexin Geyser website. Tankless LPG heater retail prices. Accessed March 25, 2012 at http://www.kexingeysers.co.za.

[6] Liquified Petroleum Gas Safety Association of Southern Africa. fuel prices March 2012. Accessed March 25, 2012 at http://www.lpgas.co.za/page34/page34.html.

[7] MAEEP.org. Small Tonnage Presentation. Accessed March 25, 2012 at www.maeep.org/documents/Small%20Tonnage.ppt.

[8] NASA Atmospheric Science Data Center, Surface meteorology and Solar Energy. Accessed at http://eosweb.larc.nasa.gov/ January 15, 2012.

[9] Photovoltaic Applications in Rural Areas of the Developing World. Technical Paper 21992, Joint UNDP World Bank Energy Sector Management and Assistance Programme, Washington, DC, November 2000.

[10] Plataforma Solar de Almeria Meteorological Facility. Accessed April 10, 2012 at http://www.psa.es/webeng/instalaciones/otros.php.

[11] Powering Up: Costing Power Infrastructure Spending Needs in Sub-Saharan Africa. Africa Infrastructure Country Diagnostic, Background Paper 5 (Phase II) 61811, The International Bank for Reconstruction and Development, Washington, DC, March 2009.

[12] RETScreen International, Clean Energy Project Analysis: Engineering & Cases Textbook. Accessed at www.RETScreen.net January 15, 2012.

[13] Rural Energy and Development: Improving Energy Supplies for 2 Billion People. Best Practice Paper 15912, The World Bank, Washington, DC, July 1996.

[14] Sales of diesel gensets reach new highs. African Review of Business and Technology, April 2008. Accessed on March 25, 2012 at http://tinyurl.com/dieselafrica.

[15] Study on PV Market Chains in East Africa. World bank study, Energy for Sustainable Development, October 2003.

[16] Sustainable.co.za website. Evacuated Tube Solar Water Heater retail prices. Accessed March 25, 2012 at http://www.sustainable.co.za/solarwaterheating/solarheatingcollectors.html.

[17] The Welfare Impact of Rural Electrification: A Reassessment of the Costs and Benefits. IEG Impact Evaluation 45400, The World Bank, Washington, DC, 2008.

[18] U.S.Energy Information Administration. Residential Energy Consumption Survey, 2009. Accessed March 25, 2012 at www.eia.gov/consumption/residential/index.cfm.

[19] Republic of India 2011 Census. Maps of india. http://www.mapsofindia.com/census2011/population-density.html Accessed on May 10, 2012.

[20] J. Aabakken. Power Technologies Energy Data Book. Technical Report 620-39728, National Renewable Energy Laboratory, Golden, CO, August 2006. Fourth Edition.

[21] V.M. Andreev and V.A. Grilikhes. Photovoltaic conversion of concentrated sunlight. *Recherche*, (866):565–566, 1997.

[22] ASHRAE. Standard 62, Ventilation for Acceptable Indoor Air Quality. Technical report, American Society of Heating, Refrigerating and Air Conditioning Engineers, Atlanta GA, 2007.

[23] ASHRAE. Standard 55, Thermal Environmental Conditions for Human Occupancy. Technical report, American Society of Heating, Refrigerating and Air Conditioning Engineers, Atlanta GA, 2010.

[24] F. Assilzadeh, S. Kalogirou, Y. Ali, and K. Sopian. Simulation and optimization of a LiBr solar absorption cooling system with evacuated tube collectors. *Renewable Energy*, (30):1143–1159, 2005.

[25] Thonon B. Recent research and developments in plate heat exchangers. *Fuel and Energy Abstracts*, 36(5):361–361, 1995.

[26] O. Badr and S.D. Probert. Performances of multi-vane expanders. *Applied energy*, 20(3):207–234, January 1985.

[27] R.E. Barber. Current costs of solar powered organic Rankine cycle engines. *Solar Energy*, 20:1–6, 1978.

[28] H. Berument, N. Basak Ceylan, and H. Olgun. Inflation uncertainty and interest rates: is the Fisher relation universal? *Applied Economics*, (39):53–68, 2007.

[29] B. Blunier, G. Cirrincione, Y. Herve, and A. Miraoui. Novel geometrical model of scroll compressors for the analytical description of the chamber volumes. In *International Compressor Engineering Conference*, page Paper 1745, 2006. [8] in paper.

[30] L. Bony, S. Doig, C. Hart, E. Maurer, and S. Newman. Achieving Low-Cost Solar PV: Industry Workshop Recommendations for Near-Term Balance of System Cost Reductions. Technical report, Rocky Mountain Institute, Snowmass, CO, September 2010.

[31] A. Brew-Hammond. Challenges to Increasing Access to Modern Energy Services in Africa. Background paper, Forum of Energy Ministers of Africa, Kwame Nkrumah University of Science and Technology, Kumasi, Ghana, March 2007. Conference on Energy Security and Sustainability.

[32] D. Brosseau, M.J. Kelly, and P.F. Hlava. Testing thermocline filler materials and molten-salt heat transfer fluids for thermal energy storage systems used in parabolic trough solar power plants. Technical Report July, Sandia National Laboratories, Albuquerque, 2004.

[33] J. Brumbaugh. *AUDEL HVAC Fundamentals, Volume 1: Heating Systems, Furnaces, and Boilers*. Wiley Publishing, Inc., Indianapolis, IN, 4^{rth} edition, 2004.

[34] J. C. Bruno, J. López-Villada, E. Letelier, S. Romera, and A. Coronas. Modelling and optimisation of solar organic rankine cycle engines for reverse osmosis desalination. *Applied Thermal Engineering*, 28(17-18):2212–2226, December 2008.

[35] K. Burman, P. Lilienthal, and D. Kline. Web-based solar photovoltaic hybrid design tool for rural clinics in africa. In A. Editor and B. Editor, editors, *Proceedingsof the ISES Solar World Congress: Renewable Energy Shaping Our Future*, pages 910–919. International Solar Energy Society, 2009.

[36] R. Cabraal, D. Barnes, and S. Agarwal. Productive uses of energy for rural development. *Annual Review of Environment and Resources*, (30):117–144, 2005.

[37] J.L. Caillat, S. Ni, and M. Daniels. A computer model for scroll compressors. In *International Compressor Engineering Conference*. Purdue University, 1988.

[38] S. Canada, G. Cohen, R. Cable, D. Brosseau, and H. Price. Parabolic Trough Organic Rankine Cycle Solar Power Plant. Technical Report January, National Renewable Energy Laboratory, Denver, CO, 2005.

[39] Y.A. Cengel. *Heat and Mass Transfer: A Practical Approach*. McGraw-Hill, Inc., New York, NY., 2007. [13] in paper.

[40] S. Chakrabarti and S. Chakrabarti. Rural electrification programme with solar energy in remote region - a case study in an island. *Energy Policy*, (30):33–42, 2002.

[41] D.S.H. Chan and J.C.H. Phang. Analytical methods for the extraction of solar-cell single- and double-diode model parameters from I-V characteristics. *IEEE Transactions on Electron Devices*, 34(2):286–293, February 1987.

[42] P. Charbonneau. An introduction to genetic algorithms for numerical optimization. Technical report, National Center for Atmospheric Research, Boulder, CO, 2002.

[43] A. Chaurey and T.C. Kandpal. A techno-economic comparison of rural electrification based on solar home systems and PVmicrogrids. *Energy Policy*, (38):3118–3129, 2010.

[44] Y. Chen, N.P. Halm, E.A. Groll, and J.E. Braun. Mathematical modeling of scroll compressor part i: Compression process modeling. *Int. J. Refrig.*, 25:731–750, 2002. [10] in paper.

[45] J. Chigwada. Paper presented at the workshop on financing mechanism and business model for pv project. cited in Krause 2004, May 2003. Pretoria, South Africa.

[46] D.A. Clugston and P.A. Basore. PCID Version 5: 32-Bit Solar Cell Modelling on Personal Computers. In *IEEE 26th PVSC*, pages 207–210, Anaheim, CA, 1997.

[47] Lyndon State College. Webpage: Daily temperature variations – net radiation. http://apollo.lsc.vsc.edu/classes/met130/notes/chapter3/daily_trend5.html Accessed on May 10, 2012.

[48] J. S. Coventry. Performance of a concentrating photovoltaic/thermal solar collector. *Solar Energy*, 78(2):211–222, February 2005.

[49] W. De Soto, S.A. Klein, and W.A. Beckman. Improvement and validation of a model for photovoltaic array performance. *Solar Energy*, 80(1):78–88, January 2006.

[50] U. Deichmann, C. Meisner, S. Murray, and D. Wheeler. The Economics of Renewable Energy Expansion in Rural Sub-Saharan Africa. Technical Paper 5193, The World Bank, Washington DC, January 2010.

[51] A. M. Delgado-Torres and L. García-Rodríguez. Comparison of solar technologies for driving a desalination system by means of an organic Rankine cycle. *Desalination*, 216(1-3):276–291, October 2007.

[52] A. M. Delgado-Torres and L. García-Rodríguez. Analysis and optimization of the low-temperature solar organic Rankine cycle (ORC). *Energy Conversion and Management*, 51(12):2846–2856, December 2010.

[53] J. Duffie and W. Beckman. *Solar Engineering of Thermal Processes*. John Wiley and Sons, 2006.

[54] M. Ehsan and S. Bhuiyan. Dual Fuel Performance of a Small Diesel Engine for Applications with Less Frequent Load Variations. *International Journal of Mechanical and Mechatronics Engineering*, 9(10):30–39, December 2009.

[55] K. Emery, J. Burdick, and Y. Caiyem. Temperature dependence of photovoltaic cells, modules and systems. In *25th PVSC*, pages 1275–1278, Washington D.C., 1996.

[56] P. Evans. Rural Africa Looks Beyond The Grid. *Renewable Energy World Magazine*, April 12, 2011.

[57] M. Ezzati, R. Bailis, D. Kammen, T. Holloway, L. Price, L. Cifuentes, B. Barnes, A. Chaurey, and K. Dhanapala. Energy management and global health. *Annual Review of Environment and Resources*, (29):383–419, 2004.

[58] G. Foley. Photovoltaic Applications in Rural Areas of the Developing World. Technical Paper 304, Joint UNDP World Bank Energy Sector Management and Assistance Programme, Washington, DC, November 1995.

[59] R. Forristall. Heat Transfer Analysis and Modeling of a Parabolic Trough Solar Receiver Implemented in Engineering Equation Solver. Technical Report October, National Renewable Energy Laboratory, Golden, CO, 2003.

[60] A. Ghoniem and M. Sorour. Economic Evaluation of Solar Systems. *International Journal of Solar Energy*, 17(4):211–222, 1995.

[61] D. Goncalves. The Solar PV Gold Rush to South Africa . Frost & Sullivan, May 2011. Accessed March 25, 2012 at http://tinyurl.com/d4ajcbl.

[62] J.M. Gordon and M. Huleihil. General performance characteristics of real heat engines. *Journal of applied physics*, 72(3):829–837, 1992.

[63] J. Gravesen and C. Henriksen. The geometry of the scroll compressor. *Society for Industrial and Applied Mathematics*, 43:113–126, 2001. [7] in paper.

[64] J. Guth. Resolving the Paradoxes of Discounting in Environmental Decisions. *Transnational Law & Contemporary Problems*, 18(95):95–114, Winter 2009.

[65] K. Harada. Development of a small scale scroll expander. Master's thesis, Oregon State University, Corvallis, OR., 2010. [2] in paper.

[66] U. Herrmann and D. W. Kearney. Survey of Thermal Energy Storage for Parabolic Trough Power Plants. *Journal of Solar Energy Engineering*, 124(2):145, 2002.

[67] A. Hiwata, A. Ikeda, T. Morimoto, O. Kosuda, and M. Matsui. Axial and radial force control for co2 scroll expander. In *International Compressor Engineering Conference*, page Paper 1849, 2008. [14] in paper.

[68] K.G.T Hollands and G.D. Raithby. Correlation equations for free convection heat transfer in horizontal layers of air and water. *Journal of Heat and Mass Transfer*, 18:879–884, 1975.

[69] Y. Y. Hsieh and T. F. Lin. Evaporation Heat Transfer and Pressure Drop of Refrigerant R-410A Flow in a Vertical Plate Heat Exchanger. *Journal of Heat Transfer*, 125(5):852, 2003.

[70] P.J. Hughes, S.A. Klein, and D.J. Close. Packed bed thermal storage models for solar air heating and cooling systems. *J. Heat Transfer*, 98(2), 1976.

[71] F.P. Incropera and D.P. DeWitt. *Fundamentals of heat and mass transfer*. Wiley, New York, 2002.

[72] Malosh J. and R. Johnson. Part Load Economy of Diesel-Electric Generators. Final report, State of Alaska Department of Transportation and Public Facilities, Fairbanks AK, June 1985. Division of Planning, Research Section.

[73] A. Jimenez and K. Olson. Renewable Energy for Rural Health Clinics. Technical report, National Renewable Energy Laboratory, Golden, CO, September 1998.

[74] L. Jing, P. Gang, and J. Jie. Optimization of low temperature solar thermal electric generation with Organic Rankine Cycle in different areas. *Applied Energy*, 87(11):3355–3365, November 2010.

[75] D. Kammen. An assessment of the environmental impacts of concentrator photovoltaics. Technical paper, Renewable and Appropriate Energy Laboratory, University of California at Berkeley, October 2011.

[76] D. Kammen and C. Kirubi. Poverty, energy and resource use in developing countries: Focus on africa. volume 1136 of *Annals of the New York Academy of Sciences*, pages 348–357, 2008.

[77] M. Kane. *Integration et optimisation thermoeconomique & environomique de centrales thermiques solaires hybrides*. PhD thesis, 2002.

[78] M. Kane. Small hybrid solar power system. *Energy*, 28(14):1427–1443, November 2003.

[79] E. A. Katz, J. M. Gordon, W. Tassew, and D. Feuermann. Photovoltaic characterization of concentrator solar cells by localized irradiation. *Journal of Applied Physics*, 100(4):044514, 2006.

[80] T. Kiceniuk. Development of an organic rankine-cycle power module for a small community solar thermal power experiment. (DOE/JPL-1060-80), 1985.

[81] H.J. Kim, J.M. Ahn, I. Park, and P.C. Rha. Scroll expander for power generation from a low-grade steam source. *Proc. IMechE., Part A: Journal of Power and Energy*, 221(5):705–711, 2007. [5] in paper.

[82] C. Kirubi, A. Jacobson, D. Kammen, and A. Mills. Community-based electric micro grids can contribute to rural devleopment: Evidence from kenya. *World Development*, 37(7):1208–1221, 2009.

[83] S.A. Klein. Engineering Equation Solver EES. F–Chart Software, 2011. Middleton, WI.

[84] A Kolodziej. Staebler-Wronski effect in amorphous silicon and its alloys. *Opto-Electronics Review*, 12(1):21–32, 2004.

[85] D. Kozlowski. Onsite Options. faclitiesnet, 2002. Accessed March 25, 2012 at http://www.facilitiesnet.com/energyefficiency/article/Onsite–Options–1679#.

[86] M. Krause and S. Nordstrom. Solar Photovoltaics in Africa: Experiences with financing and delivery models. Monitoring& Evaluation Report 2, UNDP Global Environment Facility, May 2004.

[87] P. Krugman. Here Comes the Sun. *The New York Times*, November 6, 2011.

[88] Sandia National Laboratories. Sandia, stirling energy systems set new world record for solar-to-grid conversion efficiency. NEWS RELEASE: https://share.sandia.gov/news/resources/releases/2008/solargrid.html Accessed on May 10, 2012.

[89] T. Lambert, P. Gilman, and P. Lilienthal. Micropower System Modeling with HOMER. Chapter 15, Integration of Alternative Sources of Energy, John Wiley & Sons, Inc., 2006. Accessed at www.poweringhealth.org on January 15, 2012.

[90] E. G. Laue. The measurement of solar spectral irradiance at different terrestrial elevations. *Solar Energy*, 13:43–57, 1970.

[91] E.W. Lemmon and R. Span. Short Fundamental Equations of State for 20 Industrial Fluids. *Journal of Chemical & Engineering Data*, 51:785–850, 2006.

[92] V. Lemort. *Contribution to the Characterization of Scroll Machines in Compressor and Expander Modes.* Phd thesis, University of Liege, 2009.

[93] V. Lemort and S. Quoilin. Designing scroll expanders for use in heat recovery rankine cycles. In *International Conference on Compressors and their Systems*, London, 2009. [9] in paper.

[94] V. Lemort and S. Quoilin. Experimental Investigation on a Hermetic Scroll Expander. In *7th International IIR Conference Compressors*, pages 1–7, Papiernicka, 2009.

[95] V. Lemort, S. Quoilin, C. Cuevas, and J. Lebrun. Testing and modeling a scroll expander integrated into an Organic Rankine Cycle. *Applied Thermal Engineering*, 29(14-15):3094–3102, October 2009.

[96] C. Lin. *Feasibility of using power steering pumps in small-scale solar thermal electric power systems.* Bachelor of science thesis, Massachusetts Institute of Technology, 2008.

[97] A. L. Luque and A. Viacheslav. *Concentrator Photovoltaics.* Springer Series in Optical Sciences, 2007.

[98] D. Manolakos, G. Papadakis, S. Kyritsis, and K. Bouzianas. Experimental evaluation of an autonomous low-temperature solar Rankine cycle system for reverse osmosis desalination. *Desalination*, 203(1-3):366–374, February 2007.

[99] G. E. McDonald. Spectral reflectance properties of black chrome for use as a solar selective coating. *Solar Energy*, 17(2):119–122, May 1975.

[100] F. McDonnell. High power density photovoltaics. *Renewable Energy World*, 2002.

[101] A. McMahan. Design and optimization of organic rankine cycle solar thermal powerplants. Master's thesis, University of Wisconsin, Madison, Madison, WI, 2006.

[102] A. McMahan, S. A. Klein, and D. T. Reindl. A Finite-Time Thermodynamic Framework for Optimizing Solar-Thermal Power Plants. *Journal of Solar Energy Engineering*, 129(4):355, 2007.

[103] D. Miller and C. Hope. Learning to lend for off-grid solar power: policy lessons from World Bank loans to India, Indonesia, and Sri Lanka. *Energy Policy*, (28):87–105, 2000.

[104] D. Mills. Advances in solar thermal electricity technology. *Solar Energy*, 76(1-3):19–31, January 2004.

[105] J. Monahan. Development of a 1-kw, organic rankine cycle power plant for remote applications. 1976.

[106] M. Moner-Girona, R. Ghanadan, A. Jacobson, and D. Kammen. Decreasing PV Costs in Africa. *Refocus*, pages 40–45, 2006.

[107] J. Morfeldt. *Optically Selective Surfaces in low concentrating PV/T systems.* Masters thesis, Orebro University, School of Science and Technology, 2009.

[108] B Morgenstern. SOPONOVA Operation and Maintenance Manual, June 2009.

[109] H. Nagata, M. Kakuda, S. Sekiya, M. Shimoji, and T. Koda. Development of a scroll expander for the co2 refrigeration cycle. In *International Symposium on Next-Generation Air Conditioning and Refrigeration Technology*, page Paper 1745, Tokyo, Japan, February 2010. [4] in paper.

[110] United Nations. Millenium development goals. http://www.un.org/millenniumgoals/ Accessed on May 10, 2012.

[111] W. Naude. World Development Report. Technical report, World Bank, Washington, DC, 2009.

[112] J. Nelson. *The Physics of Solar Cells*. Imperial College, London, 2003.

[113] NEP. Technical Data for the PolyTrough 1200. Technical report, NEP Solar Pty Ltd, Warriewood NSW Australia, 2011.

[114] M. Orosz. Solar organic rankine cycle economic (sorce) model, engineering equation solver. *web.mit.edu/mso/www/SORCE.EES Accessed on May 10, 2012.*

[115] M. Orosz. Solar organic rankine cycle economic (sorce) model executable. *web.mit.edu/mso/www/SORCE.EXE Accessed on May 10, 2012.*

[116] M. Orosz. *Thermosolar and Photovoltaic Hybrid Systems for Distributed Power Applications.* PhD Thesis, Massachusetts Institute of Technology, Cambridge, MA, May 2012.

[117] M. Orosz, H. Hemond, and S. Quoilin. SORCE: A design tool for solar Organic Rankine Cycle systems in distributed generation applications. EUROSUN International Solar Energy Society Europe Solar Conference, 2010.

[118] M. Orosz, A. Mueller, and Hemond H. Geometric design of scroll expanders optimized for small organic rankine cycles. *Journal of Gas Turbines, Power and Energy.* (In Review).

[119] M. Orosz, A. Mueller, and S. Quoilin. Small Scale Solar ORC system for distributed power. In *Proc. of the Solar and Chemical Energy Systems (SolarPACES)*, volume 1, 2009.

[120] C.R. Peterson and T.A. Davidson. *Design and analysis of a 1 kw Rankine power cycle, employing a multi-vane expander, for use with a low temperature solar collector.* Bachelor of science thesis, Massachusetts Institute of Technology, 1977.

[121] E. Prabhu. Solar Trough Organic Rankine Electricity System (STORES). Technical Report March, National Renewable Energy Laboratory, Mission Viejo, CA, 2006.

[122] H. Price, E. Lupfert, D. Kearney, E. Zarza, G. Cohen, R. Gee, and R. Mahoney. Advances in Parabolic Trough Solar Power Technology. *Journal of Solar Energy Engineering*, 124(2):109, 2002.

[123] S.D. Probert, M. Hussein, and P.W. O'Callaghan. Design Optimisation of a Solar-Energy Harnessing System for Stimulating an Irrigation Pump. *Applied energy*, 15:299–321, 1983.

[124] S. Quoilin. *Sustainable Energy Conversion Through the Use of Organic Rankine Cycles for Waste Heat Recovery and Solar Applications.* PhD thesis, University of Liege, 2011.

[125] S. Quoilin, S. Declaye, and V. Lemort. Expansion machine and fluid selection for the organic rankine cycle. In *Hefat 2010 - 7th International Conference on Heat Transfer, Fluid Mechanics and Thermodynamics*, Turkey, 2010. [12] in paper.

[126] S. Quoilin and V. Lemort. Technological and economical survey of Organic Rankine Cycle systems. In *5th European Conference on Economics and Management of Energy in Industry*, Vilamoura, Portugal, 2009.

[127] S. Quoilin, V. Lemort, and J. Lebrun. Experimental study and modeling of an Organic Rankine Cycle using scroll expander. *Applied Energy*, 87(4):1260–1268, April 2010.

[128] S. Quoilin, M. Orosz, H. Hemond, and V. Lemort. Performance and design optimization of a low-cost solar organic Rankine cycle for remote power generation. *Solar Energy*, (85):955–966, 2011.

[129] S. Rehman and L. Al-Hadhrami. Study of a solar PVedieselebattery hybrid power system for a remotely located population near Rafha, Saudi Arabia. *Energy*, (35):4986–4995, 2010.

[130] M. Reichler. Modeling of rooftop packaged air conditioning equipment. Master's thesis, University of Wisconsin, 1999.

[131] K. Sagara and N. Nakahara. Thermal Performance and Pressure Drop of Rock Beds with Large Storage Materials. *Solar Energy*, 47(3):157–163, 1991.

[132] J. Saghir. Energy and Poverty: Myths, Links, and Policy Issues. Energy and Mining Sector Board 37481, World Bank, May 2005.

[133] A. Schuster, S. Karellas, E. Kakaras, and H. Spliethoff. Energetic and economic investigation of Organic Rankine Cycle. *Applied Thermal Engineering*, 29(8-9):1809–1817, June 2009.

[134] Enphase Energy M215 Data Sheet. http://enphase.com/ Accessed on May 10, 2012.

[135] N.P.A. Smith. Induction generators for stand-alone micro-hydro systems. In *Power Electronics, Drives and Energy Systems for Industrial Growth, 1996., Proceedings of the 1996 International Conference*, volume 2, pages 669–673. IEEE, 1996.

[136] Solutia. Therminol 55 DataSheet. Technical Report 7239157, Solutia, St. Lous MO, 2008.

[137] D. L. Staebler and C. R. Wronski. Optically induced conductivity changes in discharge-produced hydrogenated amorphous silicon. *Journal of Applied Physics*, 51(6):3262, 1980.

[138] R. Steadman. The Assessment of Sultriness. Part I: A Temperature-Humidity Index Based on Human Physiology and Clothing Science. *Journal of Applied Meteorology*, 18:861–873, July 1979.

[139] J. Stevens and G. Corey. A Study of Lead-Acid Battery Efficiency Near Top of Charge and the Impact on PV System Design. Background paper, Sandia National Laboratories, Alburquerque, NM.

[140] W.J. Stolte. Engineering and economic evaluation of central-station photovoltaic power plants. Technical Report TR–101255, Electrical Power Research Institute, 1992.

[141] R.M. Swanson. The promise of concentrators. *Progress in Photovoltaics Research and Applications*, 111(June 1999), 2000.

[142] B. Taele, K. Gopinathan, and L. Mokhutsoane. The potential of renewable energy technologies for rural development in Lesotho. *Renewable Energy*, (32):609–622, May 2007.

[143] B.F. Tchanche, G. Lambrinos, A. Frangoudakis, and G. Papadakis. Exergy analysis of micro-organic Rankine power cycles for a small scale solar driven reverse osmosis desalination system. *Applied Energy*, 87(4):1295–1306, April 2010.

[144] H. Teng, G. Regner, and C. Cowland. Waste heat recovery of heavy-duty diesel engines by organic rankine cycle. *SAE Technical Papers*, SP-2132, 2007.

[145] USAID. *Powering Health: Energy Management in your Health Facility.* United States Agency for International Development, Washington, DC, 2011. See also www.poweringhealth.org.

[146] Y. V. Vorobiev, J. Gonzalez-Hernandez, and A. Kribus. Analysis of Potential Conversion Efficiency of a Solar Hybrid System With High-Temperature Stage. *Journal of Solar Energy Engineering*, 128(2):258, 2006.

[147] B. Wang, X. Li, and W. Shi. A general geometrical model of scroll compressors based on discretional initial angles of involute. *Int. J. Refrig.*, 28:958–966, 2005. [6] in paper.

[148] H. Wang, R.B. Peterson, and T. Herron. Experimental performance of a compliant scroll expander for an organic rankine cycle. *Proc. IMechE., Part A: Journal of Power and Energy*, 223(7):863–872, 2009. [1] in paper.

[149] J.L. Wang, L. Zhao, and X.D. Wang. A comparative study of pure and zeotropic mixtures in low-temperature solar rankine cycle. *Applied Energy*, 87(11):3366 – 3373, 2010.

[150] L. Wang, B. Sunden, and R.M. Manglik. *Plate heat exchangers: design, applications and performance.* WIT Press, 2007.

[151] X.D. Wang, L. Zhao, J.L. Wang, W.Z. Zhang, X.Z. Zhao, and W. Wu. Performance evaluation of a low-temperature solar Rankine cycle system utilizing R245fa. *Solar Energy*, 84(3):353–364, March 2010.

[152] T. Wendelin. Soltrace: A new optical modeling tool for concentrating solar optics. *ASME Conference Proceedings*, 2003(36762):253–260, 2003.

[153] Witt. Air cooled condenser 550 rpm / flying bird 2 datasheet, http://www.witthtp.com/literature.html, Accessed on December 2nd, 2010.

[154] J.L. Wolpert and S.B. Riffat. Solar-powered Rankine system for domestic applications. *Applied Thermal Engineering*, 16(4):281–289, 1996.

[155] G. Xiaojun, L. Liansheng, Z. Yuanyang, and S. Pengcheng. Research on a scroll expander used for recovering work in a fuel cell. *Int. J. of Thermodynamics*, 7(1):1–8, 2004. [3] in paper.

[156] I. Yaholnitsky. PV panel wholesale prices in South Africa. Personal Communication, March 2012. Director, Bethel Business and Community Development Center.

[157] T. Yamamoto, T. Furuhata, and N. Arai. Design and testing of the organic Rankine cycle. *Energy*, 26(3):239–251, March 2001.

[158] Jeffrey Yang, Arindam Banerjee, Tray Glatfelter, Shuichiro Sugiyama, and Subhendu Guha. Recent Progress in Amorphous Silicon Alloy Leading to 13% Stable Cell Efficiency. In *IEEE 26th PVSC 26th PVSC*, pages 563–568, Anaheim, C.A., 1997.

[159] R. Zanelli. Experimental Investigation of a Hermetic Scroll Expander-Generator. In *International Compressor Engineering Conference*. Purdue University, 1994.

[160] A. Zomers. *Rural Electrification: Utilities Chafe or Challenge*. PhD Thesis, Twente University, Enschede, Pays-Bas, 2001. See also URL `http://doc.utwente.nl/38683`.